



# Towards a Li-ion photo-rechargeable battery

Olivier Nguyen

## ► To cite this version:

Olivier Nguyen. Towards a Li-ion photo-rechargeable battery. Material chemistry. Sorbonne Université, 2018. English. NNT : 2018SORUS437 . tel-02994615

**HAL Id: tel-02994615**

**<https://theses.hal.science/tel-02994615>**

Submitted on 8 Nov 2020

**HAL** is a multi-disciplinary open access archive for the deposit and dissemination of scientific research documents, whether they are published or not. The documents may come from teaching and research institutions in France or abroad, or from public or private research centers.

L'archive ouverte pluridisciplinaire **HAL**, est destinée au dépôt et à la diffusion de documents scientifiques de niveau recherche, publiés ou non, émanant des établissements d'enseignement et de recherche français ou étrangers, des laboratoires publics ou privés.

# Sorbonne Université

Ecole doctorale 397 : Physique et Chimie des Matériaux

*Laboratoire de Chimie de la Matière Condensée de Paris*

## Towards a Li-ion photo-rechargeable battery

By Olivier Nguyen

PhD thesis in Materials Chemistry

Directed by Christel Laberty-Robert

Planned on November 6<sup>th</sup>, 2018

In front of the jury:

Prof. Fabien Miomandre

Professor

Referee

Dr. Jean-Pierre Pereira-Ramos

CNRS Research Director

Referee

Dr. Véronique Balland

Associate Professor

Examiner

Dr. Ivan Lucas

Associate Professor

Examiner

Dr. Natacha Krins

Associate Professor

Co-supervisor

Prof. Christel Laberty-Robert

Professor

Director





## TABLE of CONTENTS

<b>General Introduction .....</b>	<b>9</b>
-----------------------------------	----------

### **Chapter 1 – Solar-powered electrochemical energy storage: state of the art & new approach**

I - Converting and storing solar energy: a new approach.....	19
I.1 - Photovoltaic cells combined with rechargeable batteries .....	19
I.2 - Solar energy storage in capacitors .....	22
I.3 - Solar energy storage in Li-ion intercalative electrodes .....	24
I.4 – Solar energy storage in lithium-ion rechargeable batteries .....	29
I.5 - Solar energy storage in lithium-oxygen rechargeable batteries.....	31
I.6 - Solar energy storage in lithium-sulfur rechargeable batteries.....	33
I.7 - Solar energy storage in lithium-iodide rechargeable batteries .....	34
I.8 - Solar energy storage in dual-liquid redox batteries.....	35
I.9 - State of the art: conclusions .....	41
I.9.1 - Photo-charge or photo-assisted charge? .....	42
I.9.2 – Choice of the electrolyte.....	45
II - Converting and storing solar energy: a new approach.....	48
II.1 - Pioneering works on bifunctional electrodes .....	48
II.2 - The recent and very recent developments on bifunctional electrodes .....	50
III - Thesis objectives and challenges.....	55
Bibliography .....	57

### **Chapter 2 – Mesoporous TiO<sub>2</sub> thin film electrodes: fabrication & characterizations**

I – Introduction .....	69
II – Presentation of the electrodes .....	71
II.1 – Fabrication methods.....	71

II.2 – Control of thin films architecture .....	74
II.2.1 – Thin film thickness .....	74
II.2.2 – Inorganic walls and porous networks .....	76
III – Thin films structural characterizations .....	78
III.1 – Spectroscopic Ellipsometry .....	78
III.1.1 – Adaptation for porous thin films .....	78
III.1.2 – Environmental Ellipsometric Porosimetry .....	79
III.2 – Glancing Angle X-Ray Diffraction .....	85
IV – Reconstruction of TiO <sub>2</sub> electrode energetic diagram.....	92
IV.1 – Band gap determination by UV-Visible Spectroscopy .....	92
IV.2 – Flat-band potential estimated by Mott-Schottky experiment.....	95
V – Conclusion .....	97
Bibliography .....	99

### **Chapter 3 – Mesoporous TiO<sub>2</sub> thin films as photo-rechargeable Li-ion battery electrode materials: photo-electrochemical characterizations**

I – Introduction .....	107
II – Cell design and photo-electrochemical set-up .....	107
III – How light impacts the discharge and charge of the TiO <sub>2</sub> -based battery electrode: observations.....	109
III.1 – Galvanostatic experiments .....	109
III.2 – Cyclic voltammetry experiments .....	113
IV – Evaluation of the photo-current intensity .....	115
IV.1 – Potentiostatic experiments.....	115
IV.2 – Open circuit voltage experiments.....	117
V – Adjusting the rates of simultaneous electrode discharge and photo-recharge.....	119
VI – Conclusion .....	121
Bibliography .....	122

## Chapter 4 – Photo-induced mechanisms: investigation

I - Introduction.....	127
II – Photo-induced mechanisms: dependence on the electrode architecture and role of the electrolyte.....	128
II.1 – Dependence on the electrode architecture.....	128
II.1.1 – Influence of the electrode thickness.....	128
II.1.2 – Influence of the porous network.....	131
II.2 – Role of the electrolyte .....	137
II.2.1 – TiO <sub>2</sub> photo-electrode in an ionic liquid-based electrolyte .....	137
II.2.2 – TiO <sub>2</sub> photo-electrode in a “water-in-salt” electrolyte.....	144
III – <i>Post mortem</i> analysis of the photo-electrode.....	149
III.1 – FEG-SEM and complementary EDX analysis .....	149
III.2 – Probing the electrode surface with XPS .....	154
III.3 – Analysing the electrolyte by NMR spectroscopy.....	162
IV – TiO <sub>2</sub> photo-electrode: <i>operando</i> characterizations .....	168
IV.1 – Electrochemical Impedance Spectroscopy (EIS) .....	168
IV.1.1 – Nyquist plots and equivalent circuits.....	168
IV.1.2 – Results of the fits and analysis .....	171
IV.2 – Investigations by means of Electrochemical Quartz Crystal Microbalance (EQCM) .....	174
IV.2.1 – Principle of Quartz Crystal Microbalance (QCM) .....	174
IV.2 – EQCM and $F(\Delta m/\Delta Q)$ function.....	175
IV.2.3 – EQCM study for Li-ion photo-battery electrode.....	177
V – Conclusion .....	191
Bibliography .....	193
<b>General Conclusion .....</b>	<b>201</b>

## ANNEX

Annex I – Figures .....	V
Annex I.1 – TiO <sub>2</sub> (PB-PEO, TiCl <sub>4</sub> 1M/2M) pore size distribution.....	V
Annex I.2 – FTO and LP30 UV-Visible absorption spectra .....	VI
Annex I.3 – In situ evolution of UV-Vis absorption spectra for anatase TiO <sub>2</sub> electrode (PB-PEO, 2M in TiCl <sub>4</sub> , 10 dipped layers).....	VII
Annex I.4 – CVs in dark and light for different film architecture .....	VIII
Annex I.5 – Chopped potentiostatic experiment in dark and light for different film architecture.....	IX
Annex I.6 – EDX qualitative analysis of TiO <sub>2</sub> electrode surface for different cycling conditions in LP30 electrolyte.....	X
Annex I.7 – Reaction scheme of LiPF <sub>6</sub> degradation suggested by Wiemers-Meyers <i>et al.</i> NMR study .....	XI
Annex I.8 – Nyquist plots fits using RC and Randles circuits.....	XI
Annex I.9 – Nyquist plots fits using equivalent circuit with CPE (dark) .....	XII
Annex I.10 – Nyquist plots fits using equivalent circuit with CPE (light) .....	XIII
Annex I.11 – F(dm/dq) function for TiO <sub>2</sub> film during CVs in LP30 .....	XIV
Annex II – Anatase thin film fabrication .....	XV
Annex III – Technics of characterization .....	XVII
III.1 - Electrochemical and Photo-Electrochemical measurements.....	XVII
III.2 – Glancing Angle X-Ray Diffraction .....	XX
III.3 - Ellipsometry .....	XX
III.4 - Field-Emission-Gun Scanning-Electron-Microscopy and Energy-dispersive X-Ray Spectroscopy.....	XXI
III.5 - X-Ray Photoelectron Spectroscopy .....	XXI
III.6 - Nuclear Magnetic Resonance Spectroscopy .....	XXI
III.7 - UV-Visible spectroscopy .....	XXII
III.8 - Electrochemical Quartz Crystal Microbalance .....	XXIII
Bibliography .....	XXV

## **GENERAL INTRODUCTION**



## General Introduction

The access to Energy has probably become one of the major issues of the 21<sup>st</sup> century and raises crucial questions: how to produce energy, how to consume it, and at what environmental costs?

Supplying the increasing world energy demand while reducing our carbon impact on the planet is indeed a real challenge. Nowadays, fossil fuels provide  $\sim 80\%$  of the primary energy produced in the world (**Figure 1-a**), whereas oil and gas natural reserves should be depleted in  $\sim 50$  years. Besides, growth of the world population along with an increase of the average quality of life could lead to an increase of the global energy consumption from 14 TW today to 28 TW in 2050 (**Figure 1-b**).

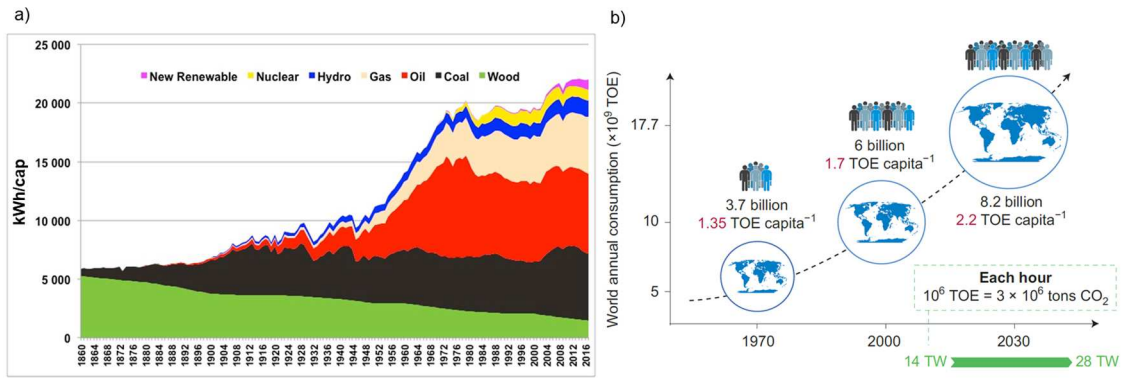


**Figure 1:** Evolution of the average global (primary) energy consumption per capita. Based on Shilling et al. 1977, BP Statistical Review 2018.<sup>1</sup> Evolution and prevision of the world population and its energy consumption, reproduced from Larcher *et al.*<sup>2</sup>

To address these challenges, solutions have already been addressed to reduce our dependency on fossil fuels by diversifying our power sources. Iceland for example relies on fossil fuels only for transportation (15% of its primary energy consumption), while the other 85 % are provided by geothermal energy and hydropower.<sup>3,4</sup> Other countries which do not benefit from such natural resources have minimized their use of fossil fuel for producing electricity (representing  $\sim 20\%$  of the global energy consumption) in favor of the nuclear fission, but this technology also suffers from environmental issues (radioactive wastes, nuclear disasters).

It is therefore necessary to propose development solutions based on abundant and sustainable energy sources, which represents nowadays  $\sim 11\%$  of the produced primary energy.<sup>5</sup> Amongst them, renewable energies such as biomass (whose extensive development may conflict with alimentation issues), wind-, hydro- or solar-power are attractive energy vectors. In particular, solar energy possesses the potential to adequately fulfill the energy demands of the entire world if actual technologies for its



harvesting and supplying were readily available.<sup>6</sup> In fact,  $\sim 0.01\%$  of the solar energy reaching the earth is theoretically sufficient to cover the world energy demand, and could be harvest with an already existing technology of solar panels working with a global efficiency of 10% and covering 0.1% of the planet (which represents more or less Spain area). Despite of this huge potential, the contribution to solar energy to the global energy supply is still less than 1%.<sup>3,5</sup> Amongst other possible technological or geopolitical drawbacks, this technology indeed suffers from the intermittence of the solar radiation. This intrinsic limitation obliges the exploitation of sun light only during a part of the day, and raises the question of the development of electrical “smart grid”, including hybrid structure with energy conversion/storage compartments.

In the case of stationary or domestic applications, photovoltaic devices are generally connected to an electrical grid. The latter receives the produced solar energy from photovoltaic systems, and can in return supply electrical installations when needed. The grid-connected photovoltaic system can also be supplemented with a battery backup, which can store the energy surplus and allow the smoothing between the supply and the demand. However, in some cases, for instance in areas having unreliable or inexistent power from the grid, the need for an energy storage system coupled with the photovoltaic device really becomes essential.

There are many ways to store energy according to its nature (thermal, mechanical, electrical, nuclear, *etc.*). As it also involves electron transfer, the chemical energy is a natural choice to store electricity. “Electrochemistry” is the field encompassing all chemical reactions driven by or resulting from an electrical current flowing at a given potential. It includes numerous technologies dedicated to energy storage, such as fuel cells, supercapacitors and batteries. Amongst them, rechargeable batteries are actively studied due to their wide range of application (**Figure 2**) and their relative high energy density.<sup>7</sup>

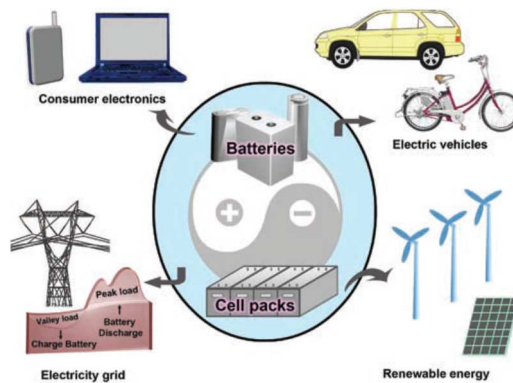


**Figure 2:** Representative applications for rechargeable batteries. Reproduced from Cheng *et al.*<sup>8</sup>

After a fast development at the beginning of the 21<sup>st</sup> century, the battery market had an average growth of  $\sim 8\%$  per year from 2006 to 2016.<sup>9</sup> The market is still dominated by the lead-acid technology, used as start light and ignition batteries, owing to its low cost and long cycle-life (**Figure 3-a**). However, this technology is not suitable for portable applications, in which the gravimetric and volumetric energy densities prevail above all.<sup>4,7</sup> Over one decade, this segment has been conquered by the Li-ion technology, which equips 100% of the portable electronic devices such as cellular, laptops, tablets, cameras, and other handy devices (**Figure 3-b**). Due to the increasing functionalities and resulting energy needs required by such portable devices<sup>10</sup>, seeking for the better autonomy has become one of the major selling argument for the constructors in every domains of the Li-ion battery industry (cell phones, laptops, rechargeable vehicles, *etc.*). This technology is indeed still deeply dependent of the access to an electronic grid, which has become an important strategic issue for example in the electric vehicles industry.

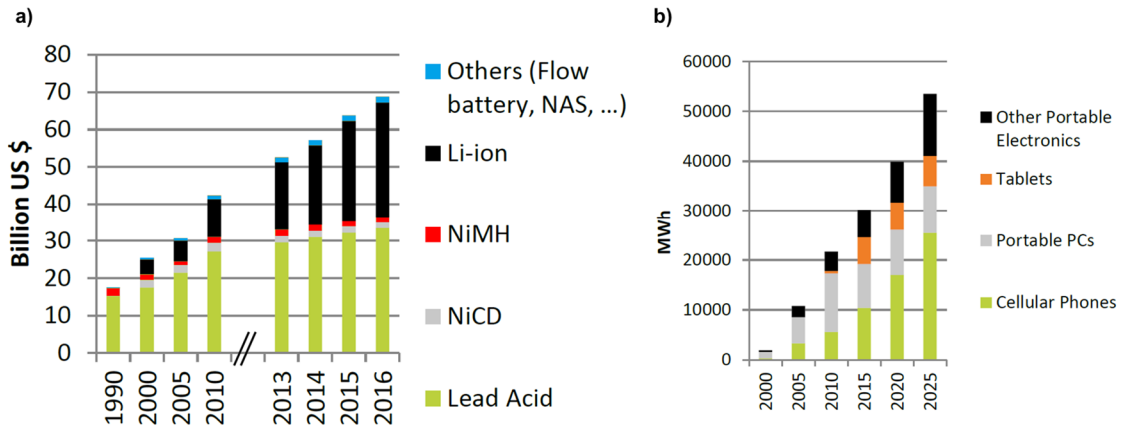


**Figure 3:** The worldwide battery market in 2016 (a) and Li-ion battery forecast for portable electronic devices by application up to 2025 (b). Adapted from Pillot *et al.* for Avicenne Energy 2017 study.<sup>9</sup>

In addition to the appealing scientific dimension, the design of a device that is simultaneously a solar energy convertor and a rechargeable battery therefore represents a paradigm-shifting concept, which could be valuable for both domains of solar energy conversion (need for energy storage due to solar intermittence) and Li-ion battery energy storage (lack of autonomy in regards to increasing energy demands).

In this thesis, Chapter I will be discussing in different approaches considered by the scientific community to convert solar energy and store it simultaneously. The state of the art of solar powered electrochemical energy storage is mainly based on hybrid devices, which address the challenge of converting and storing energy by two separated

compartments. In this work, we will propose to investigate another approach to harvest and store solar energy simultaneously into a single device, using a  $\text{TiO}_2$  bi-functional Li-ion battery photo-electrode. A patent for this system has already been proposed.<sup>11</sup> To go further in the system design, a better understanding of the underlying mechanisms is needed, and will constitute an important part of the work of this thesis.

Chapter II will be dedicated to the fabrication methods of the electrode. We will present the synthesis of the mesoporous thin film electrodes obtained using sol-gel coupled dip-coating process combined with the “evaporation induced self-assembly” (EISA) approach, as well as the associated characterizations (environmental ellipsometric porosimetry, glancing angle X-Ray diffraction, UV-Visible spectroscopy, and Mott Schottky experiments).

In the Chapter III, mesoporous  $\text{TiO}_2$  thin film will be tested as photo-rechargeable Li-ion battery electrode materials. Comparison of the electrochemical response of the electrode in dark conditions and under illumination will allow to discuss the properties of the electrode photo-recharge as well as its mechanism.

In the Chapter IV, photo-induced mechanisms will be further investigated using several ways: (1) by playing with the electrode architecture and the electrolyte in order to analyze their potential influence on the fate of the photo-generated charges (2) by tracking these photo-generated charges and their potential reaction with the electrolyte through *post mortem* analysis of the electrode surface and the electrolyte (3) by realizing *operando* measurements (electrochemical impedance spectroscopy, electrochemical quartz crystal microbalance) to study the electrical and gravimetric properties of the system in real time upon the illumination.

## Bibliography

1. Manicore - URL:<http://www.manicore.com/documentation/energie.html>.
2. Larcher, D. & Tarascon, J.-M. Towards greener and more sustainable batteries for electrical energy storage. *Nat. Chem.* **7**, 19–29 (2015).
3. Connaissance des énergies - URL: <https://www.connaissancedesenergies.org/fiche-pedagogique/chiffres-cles-production-d-energie>.
4. Lepoivre, F. Study and improvement of non-aqueous Lithium-Air batteries via the development of a silicon-based anode. (Université Pierre et Marie Curie-Paris VI, 2016).
5. BP Statistical Review of World Energy June 2017.
6. Kabir, E., Kumar, P., Kumar, S., Adelodun, A. A. & Kim, K.-H. Solar energy: Potential and future prospects. *Renew. Sustain. Energy Rev.* **82**, 894–900 (2018).
7. Tarascon, J.-M. & Armand, M. Issues and challenges facing rechargeable lithium batteries. *Materials for Sustainable Energy* 171–179 (2010).
8. Cheng, F., Liang, J., Tao, Z. & Chen, J. Functional materials for rechargeable batteries. *Adv. Mater.* **23**, 1695–1715 (2011).
9. Pillot, Sanders. The Rechargeable Battery Market and Main Trends 2016-2025 - Avicenne Energy - September 2017.
10. Choi, J. W. & Aurbach, D. Promise and reality of post-lithium-ion batteries with high energy densities. *Nat. Rev. Mater.* **1**, 16013 (2016).
11. Sauvage, F., Andriamiadamanana, C. & Laberty-Robert, C. Photorechargeable battery: turning light energy into chemical energy and then electric energy, French patent. (FR1361775).



## **CHAPTER 1**

**Solar-powered electrochemical energy storage:  
state of the art & new approach**



## TABLE of CONTENTS

I - Converting and storing solar energy: a new approach.....	19
I.1 - Photovoltaic cells combined with rechargeable batteries .....	19
I.2 - Solar energy storage in capacitors .....	22
I.3 - Solar energy storage in Li-ion intercalative electrodes .....	24
I.4 – Solar energy storage in lithium-ion rechargeable batteries .....	29
I.5 - Solar energy storage in lithium-oxygen rechargeable batteries.....	31
I.6 - Solar energy storage in lithium-sulfur rechargeable batteries.....	33
I.7 - Solar energy storage in lithium-iodide rechargeable batteries .....	34
I.8 - Solar energy storage in dual-liquid redox batteries .....	35
I.9 - State of the art: conclusions .....	41
I.9.1 - Photo-charge or photo-assisted charge? .....	42
I.9.2 – Choice of the electrolyte.....	45
II - Converting and storing solar energy: a new approach.....	48
II.1 - Pioneering works on bifunctional electrodes.....	48
II.2 - The recent and very recent developments on bifunctional electrodes .....	50
III - Thesis objectives and challenges.....	55
Bibliography .....	57





## **I - Converting and storing solar energy: a new approach**

The design of a device that is able to simultaneously convert solar energy and store it like a battery represents a paradigm-shifting energy storage concept that allows charging a battery without any external power supply.<sup>1-3</sup>

The first solar-powered electrochemical energy storage (SPEES) was proposed in 1976 by Hodes *et al.*<sup>4</sup> using a three-electrode system composed of cadmium selenide/sulfur/silver sulfide (CdSe/S/Ag<sub>2</sub>S). Since then, different combinations of solar cells and storage devices have been developed. In such hybrid systems, research has been mostly focused on combining dye-sensitized solar cells (DSSCs) for the photo-conversion, and capacitors or tungsten trioxide-based electrodes for the energy storage. More recently, other hybrid devices combining photo-electrodes with Li-ion batteries, Li-S batteries, Li-O<sub>2</sub> batteries and redox-flow batteries have also been investigated.

In this section, we first propose to describe the state of the art of SPEES systems, which are based until very recently and to the best of our knowledge almost exclusively on separate technologies.

### **I.1 - Photovoltaic cells combined with rechargeable batteries**

The most well-known technology to convert solar energy into electric energy is the silicon-based solar cell. Solar cells using crystalline silicon can achieve efficiencies of about 25 % and dominate at the moment the field of commercial photovoltaic modules.<sup>5,6</sup> However, the intermittency of solar energy has been a major drawback conflicting the permanent electric energy needs.

On the other side, even Li-ion batteries, which stand as the most established rechargeable accumulators, still suffer from their lack of autonomy in regards to increasing energy demands.<sup>7</sup>

Therefore, it seems quite natural, as a first approach to overcome their respective weaknesses, to try to combine the two most reliable and commercialized technologies for energy conversion (silicon photovoltaic cells) and storage (Li-ion rechargeable batteries), using electrical wiring.

In 2006, Kan *et al.*<sup>8</sup> observed that the direct charging of a Li-ion battery takes longer for a solar cell (about 4 times longer for their system in comparison to an electrical charge). The battery capacity also decreases faster than in standard use. In order to improve the energy transfer, the authors propose to add supercapacitors between the

photovoltaic cell and the accumulator. The energy is first quickly collected by the capacitors, then slowly restored to the batteries. The capacitors act as a buffer against the photovoltaic current variations induced by the fluctuated incident solar radiations. This control over the current restitution should thus improve the lifetime of the battery. However, the authors note that this advantage is only possible at the expense of increased weight and volume of the storage system.

In order to test the performances of a battery designed for electric vehicles, Gibson *et al.*<sup>9</sup> investigated for General Motors the charge of iron phosphate-based Li-ion cells using externally wired amorphous silicon photovoltaic modules. The whole system could be charged at a rate of up to 1.5 C (theoretical discharge completed in 60 / 1.5 h) with an average voltage of 3.4 V. The optimized solar charging system reaches a 14.5 % efficiency by combining a photovoltaic system with 15 % solar to electric efficiency and a nearly 100 % storage efficiency battery module. This high system efficiency is achieved with no intervening electronics. It is obtained by matching the photovoltaic maximum power point voltage to the battery charging voltage at the desired maximum state of charge for the battery using an optimum 15-cell battery module (**Figure 1**).

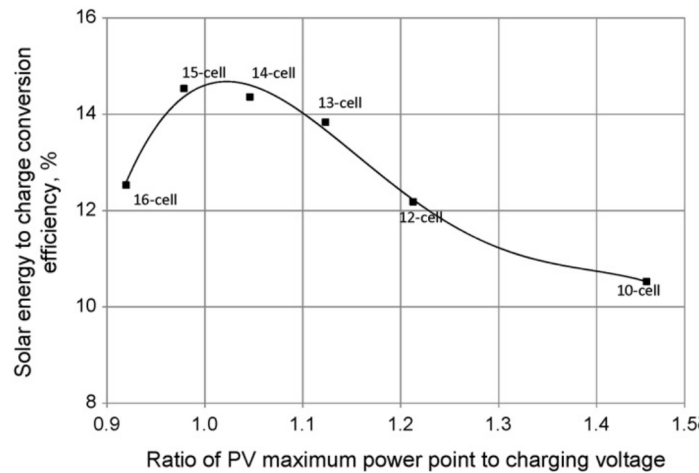


**Figure 1:** Solar energy to battery charge conversion efficiency comparison for 10-, 12-, 13-, 14-, 15-, and 16-cell modules. The optimum efficiency was approximately 14.5 % when the battery charge voltage was equal to the photovoltaic maximum power point ( $V_{mpp}/V_{battery}$  charging near unity).<sup>9</sup>

Thus, working on the optimal match between the photovoltaic system and the battery is a very important step to optimize the system overall performances, and could limit the addition of increasing weight electronics.

In 2015, Xu *et al.*<sup>10</sup> demonstrated the use of perovskite solar cells (PSC) packs with four single  $\text{CH}_3\text{NH}_3\text{PbI}_3$ -based solar cells connected in series to photo-charge a lithium-ion battery (LIB) assembling a  $\text{LiFePO}_4$  cathode and a  $\text{Li}_4\text{Ti}_5\text{O}_{12}$  anode (**Figure 2**).

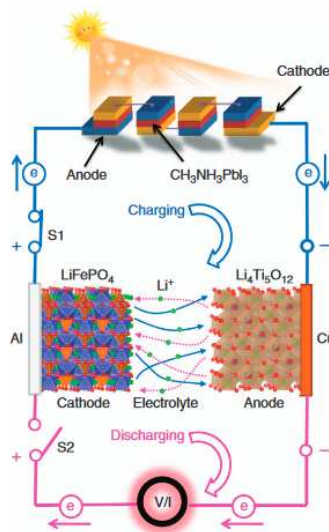


**Figure 2:** Schematic diagram of the PSC-LIB system.<sup>10</sup>

The authors show a maximal overall photo-electric conversion and storage efficiency of 7.8 % at 0.1 C and about 7 % at 0.5 C, and a discharging capacity decreasing from 140.4  $\text{mAh.g}^{-1}$  to 111.6  $\text{mAh.g}^{-1}$  (79.5 % of initial capacity) after 10 cycles. In order to further improve the efficiency of such perovskite-powered systems, Gurung *et al.*<sup>11</sup> firstly introduced in 2017 a direct current-direct current (DC-DC) boost converter into the PSCs for photo-charging a  $\text{Li}_4\text{Ti}_5\text{O}_{12}$ - $\text{LiCoO}_2$  battery. The converter boosts the low input voltage of a single junction solar cell to charge the lithium ion cell, which leads to a high overall efficiency of 9.4 % and average storage efficiency of 77.2 % at 0.5 C. In addition, the discharging capacity decreases from 151.3  $\text{mAh.g}^{-1}$  to 134.4  $\text{mAh.g}^{-1}$  (89 % of initial capacity) after 10 cycles.

The wire-connected strategy has many advantages including the freedom of selecting the type of individual units and their assembly. However, although associations with external solar cells have achieved feasible conversion and storage of solar energy in rechargeable batteries, there are still some challenges in these systems for the practical applications. As major drawback, the extra photovoltaic modules and external wires considerably enlarge the volume and weight of the entire device in comparison to a single rechargeable battery. They also increase the cost of energy storage.<sup>12</sup>

To avoid this issue, both energy conversion and storage parts could be integrated into one hybrid device. Researchers have been focusing on integrating capacitors and intercalative electrode into DSSCs (**section I.2-I.3**), or photo-electrodes into

rechargeable batteries (**sections I.4-I.8**). In this chapter, there will be no mention of organic- or polymer-based SPEES systems,<sup>1,2,12,13</sup> we will focus on the advances on inorganic-based SPEES, which are particularly relevant to our own approach of the SPEES. In each section, we will illustrate some examples of representative devices in order to highlight their specificities. They will be summarized in **section I.9**.

## I.2 - Solar energy storage in capacitors

The DSSC is the most commonly used photo-converter in SPEES devices. Presenting energy conversion efficiencies up to 11 %<sup>14</sup> and good performances under diffuse and low intensity light conditions,<sup>15</sup> this technology allows a low cost alternative to common silicon based solar cells.<sup>9</sup> DSSC are also attractive due to their potential to be flexible and lightweight, and the design opportunities they offer due to their transparency or multicolour options (for example for building integration).<sup>16</sup> Their typical basic configuration is as follows<sup>16</sup> (**Figure 3**): at the heart of the device is the mesoporous oxide layer composed of a network of TiO<sub>2</sub> nanoparticles that have been sintered to establish good electronic contact. Typically, the film thickness is ca. 10  $\mu\text{m}$  and the nanoparticle size 10-30 nm in diameter. The porosity is 50-60 %. The mesoporous layer is deposited on a transparent conducting oxide on a glass or plastic substrate. The most commonly used substrate is glass coated with fluorine-doped tin oxide (FTO). Attached to the surface of the nanocrystalline film is a monolayer of the charge-transfer dye.

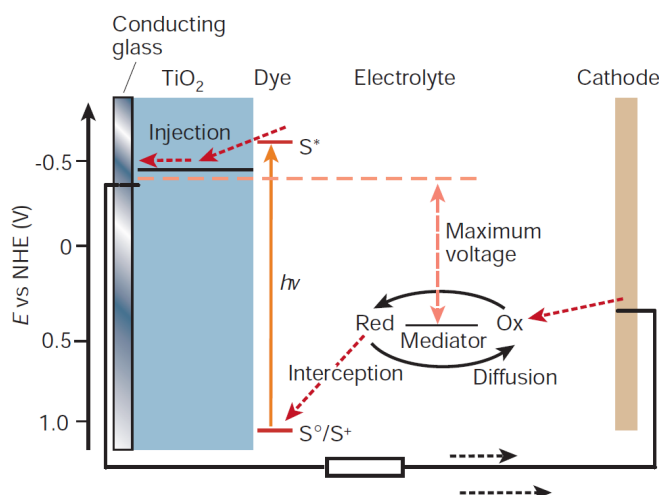


**Figure 3:** Schematic of operation of the dye-sensitized electrochemical photovoltaic cell.<sup>17</sup>

Photo-excitation of the latter results in the injection of an electron into the conduction band of the oxide, leaving the dye in its oxidized state. The dye is restored to its ground state by an electron transfer from the electrolyte, usually an organic solvent

containing the iodide ( $I^-$ )/ triiodide ( $I_3^-$ ) redox system. The  $I_3^-$  ions, formed by oxidation of  $I^-$  ions, diffuse along a short distance ( $<50\ \mu\text{m}$ ) through the electrolyte to the counter electrode, which is coated with a thin layer of platinum catalyst. The regenerative cycle is completed by the reduction of  $I_3^-$  to  $I^-$  at the counter electrode, the circuit being completed via electron migration through the external load.

By combining the DSSC with an electron storage device, the electrons can be stored after photo-generation. In 2004, Miyasaka *et al.*<sup>18</sup> developed a device combining a photo-electrode made of dye sensitized  $\text{TiO}_2$  nanoparticles and an activated carbon double layer with a specific surface area of about  $1000\text{--}2500\ \text{m}^2\text{g}^{-1}$  (**Figure 4**). After photo-generation of electron-hole pairs, electrons and holes are accumulated at each of the two activated carbon electrodes (AC layer). These two carbon layers are separated by an organic electrolyte of high concentration ( $(\text{CH}_3\text{CH}_2)_4\text{NBF}_4$ , 15 wt% in propylene carbonate), which provides the counter-ions needed for the charge compensation at the carbon surface.

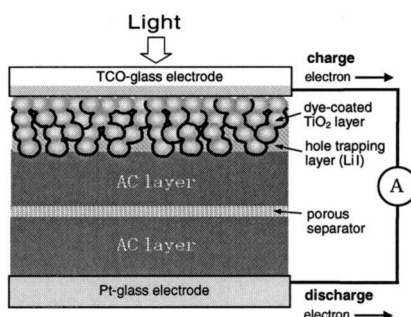


**Figure 4:** Schematic illustration for the two-electrode photo-capacitor.<sup>18</sup>

At charged state, the photo-capacity provides a voltage of 0.45 V for a discharge capacitance of  $43\ \text{F.g}^{-1}$  ( $0.69\ \text{F.cm}^{-2}$  for 16 mg of activated carbon at the counter electrode). It is comparable to carbon-based electrode material reported in the literature, which roughly presents capacities between  $10\ \text{F.g}^{-1}$  and  $300\ \text{F.g}^{-1}$  depending on the nature of the electrode (typically  $40\ \text{F.g}^{-1}$  for activated carbon).<sup>19,20</sup> However, this two-electrode system suffers from a big internal resistance: electrons returning to the photo-electrode should go through the space charge Schottky barrier at the  $\text{TiO}_2$  layer, which delays the discharge process. For this reason, Miyasaka *et al.* improved the device using a three-electrode device<sup>21</sup> to obtain energy densities 5 times higher than the 2-electrode one for a delivered voltage of 0.8 V (**Figure 5**).

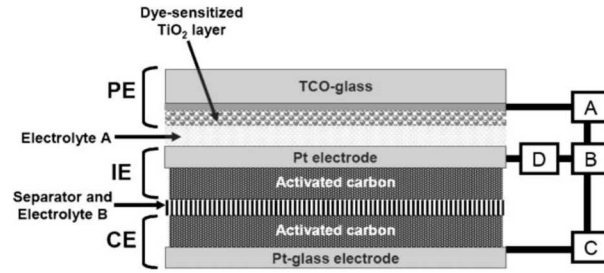


**Figure 5:** Structure of the three-electrode photo-capacitor. The cell consists of a dye-sensitized  $\text{TiO}_2$  photo-electrode (PE), a Pt-plate inner electrode (IE) and a Pt-coated glass counter-electrode (CE) covered with activated carbon (AC), spacer, separator, and redox (A) and redox-free (B) electrolytes.<sup>21</sup>

Instead of activated carbon, carbon nanotubes have also been used for the storage in these hybrid systems. In 2013, Yang *et al.*<sup>22</sup> published a study on a system comparable to the 2-electrode device proposed by Miyasaka. Films of multi-wall carbon nanotubes are aligned to form the 2 electric storage layers. The authors obtain a photo-electric conversion efficiency of 6.1 %, a specific capacitance of  $48 \text{ F.g}^{-1}$ , a storage efficiency of 84 % for a global photo-electric conversion and storage conversion of about 5.1 %. When introducing polyaniline in the carbon nanotubes, the specific capacitance goes to  $208 \text{ F.g}^{-1}$ , but the storage efficiency goes down to about 70 % for a global efficiency of 4.3 %. The authors explain this efficiency decrease by the chemical reactions that occurred within the carbon-polyaniline composite during the charge / discharge process. In the context of developing flexible and lightweight photo-capacitors for mobile or wearable electronic devices<sup>23</sup>, researchers have investigated wire-shaped electrode design instead of the classical planar structure: braided fibers<sup>24</sup>, multi-wall fibers<sup>25</sup> or braided sheath / core fibers<sup>26</sup> have thus been developed to be integrated into textiles or other deformable structures for self-powering applications. Performances of the described solar capacitors are resumed in **Table 1** (page 28).

### I.3 - Solar energy storage in Li-ion intercalative electrodes

The energy produced by a DSSC can also be stored by another way. Photo-generated electrons can be driven to an insertion electrode material able to accommodate small metallic cations (typically  $\text{Li}^+$ ). During the photo-charge, the electrode material reduction (induced by the electrons flow) is electrically compensated by cations insertion. During the discharge, the spontaneous opposite electron flow induces the re-oxidation of the storage material and the de-insertion of the cations. This way, the photo-generated electrons can be stored by charge compensation thanks to a host lattice electrode able to reversibly intercalate cations.

The first example of such hybridization was published by Hauch *et al.* in 2002.<sup>27</sup> The authors adopt a 2-electrode system, which integrates an intermediate storage layer of  $\text{WO}_3$ , electroactive with regards to lithium ion intercalation. The  $\text{WO}_3$  layer is directly in contact with the photo-active sensitized  $\text{TiO}_2$  layer (**Figure 6**). These mesoporous layers are deposited by screen-printing by analogy with DSSC fabrication process.

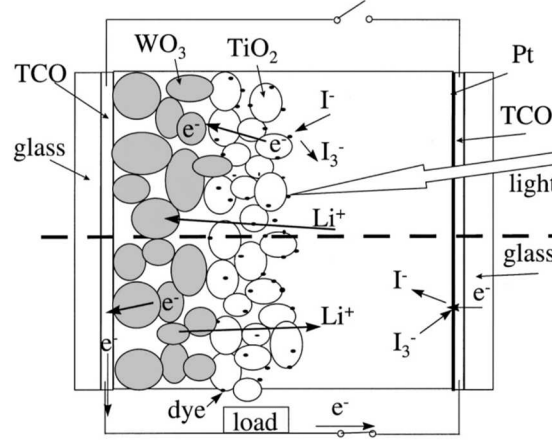


**Figure 6:** Schematic diagram of the proposed 2 electrode tungsten photo-capacitor.<sup>27</sup>

During the open circuit photo-charge process, electrons provided after illumination of the photo-active sensitized  $\text{TiO}_2$  layer are transferred and stored into  $\text{WO}_3$ , which is able to be reduced ( $\text{W}^{6+}$  into  $\text{W}^{5+}$ ) while inserting  $\text{Li}^+$  to form  $\text{Li}_x\text{WO}_3$  (**equation 1**).



During the discharge, an external circuit connects the two electrodes. The current induces  $\text{W}^{5+}$  oxidation into  $\text{W}^{6+}$  in  $\text{Li}_x\text{WO}_3$ , together with  $\text{Li}^+$  extraction and the  $\text{I}_2$  regeneration at the counter electrode.

After one hour of photo-charge ( $1000 \text{ W.m}^{-2}$ ), the device provides an open current voltage of 0.6 V and a discharge capacity of  $1.8 \text{ C.cm}^{-2}$ . After conversion, this capacity corresponds to  $0.5 \text{ mAh.cm}^{-2}$ , *i.e.*  $28 \text{ mAh.g}^{-1}$  for a  $50 \mu\text{m}$ -thick electrode and a theoretical density of  $7.16 \text{ g.cm}^{-3}$  for  $\text{WO}_3$ , which is around five times smaller than usual Li-ion battery capacities. The authors estimate that the accumulator capacity is limited by the low concentration of  $\text{Li}^+$  in the electrolyte. They attribute the observed self-discharge process to the electron transfer from  $\text{TiO}_2$  or  $\text{WO}_3$  in the electrolyte. The authors also highlight the colour change between  $\text{WO}_3$  and  $\text{Li}_x\text{WO}_3$ , which could be a useful property for a photo-electrochromic device.<sup>28</sup>



In 2011, Cannavale *et al.*<sup>29</sup> proposed a photo-voltachromic device, which takes advantages of the tungsten oxide colour change (i) to produce a smart modulation of the optical transmittance and, at the same time, (ii) to generate electrical power by means of solar energy conversion. They describe a system very closed to a DSSC, where  $\text{WO}_3$  capture the photo-induced electron at the counter electrode (**Figure 7**), while I is oxidized in  $\text{I}_3^-$ . This reaction induces lithium-ion insertion and a change in the electrode colour. At open circuit,  $\text{Li}_x\text{WO}_3$  is oxidized back in  $\text{WO}_3$ , I is regenerated and the system becomes transparent. At closed circuit, the counter electrode turns to blue. The control of the state of charge and the optical transmittance is thus achieved using the external circuit. By tailoring the iodine concentration from 0.05 M to 0.005 M, the authors improve the efficiency of the coloration and the photovoltaic conversion efficiency from 3.26 % to 6.55 %.

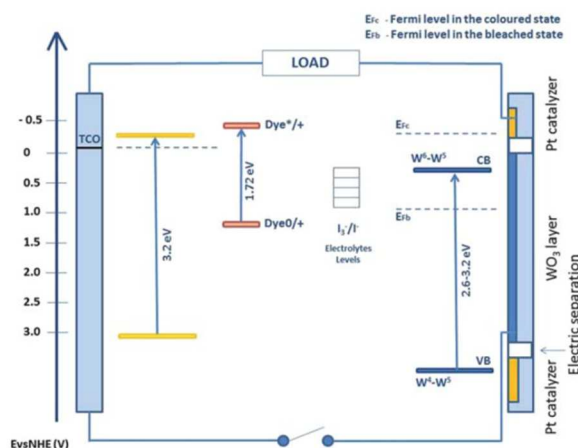


**Figure 7:** Schematic representation of the energy levels in a photo-voltachromic cell.<sup>29</sup>

In 2009, Segawa's team optimized Hauch *et al.* system using a 3-electrode device.<sup>30</sup> A conversion compartment A is separated from a storage compartment B by a lithium-ion permeable Nafion membrane. They focused their efforts on the charge storage electrode (**Figure 8**). A surface-oxidized WO<sub>3</sub> (so-WO<sub>3</sub>) electrode is obtained by annealing the tungsten substrate at ambient atmosphere. Compared to a WO<sub>3</sub> made of monoclinic nanocrystals (nc-WO<sub>3</sub>), the so-WO<sub>3</sub> presents higher open current voltage and better cycling abilities, which is explained by a good lithium-ion diffusion at different intercalation levels. The authors obtain an open current voltage of 0.4 V and a discharge capacity of 10 to 20 mAh.g<sup>-1</sup>, which is 5-10 times lower than for a classical Li-ion battery.

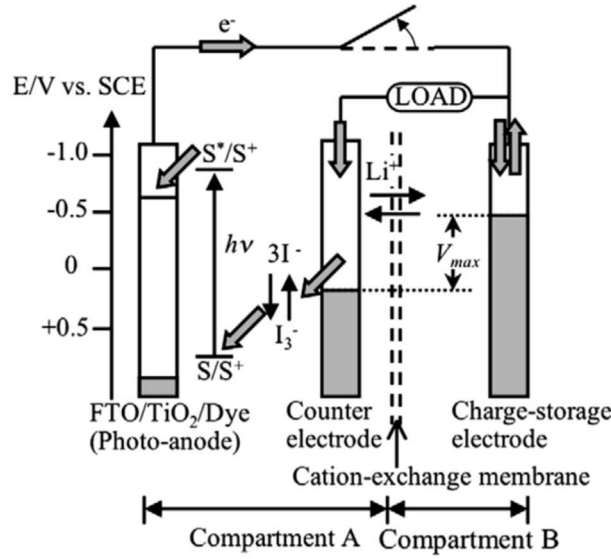


**Figure 8:** Operation scheme of the 3-electrode ES-DSSC system. Compartment A is the DSSC section, and compartment B is the section containing the charge-storage electrode.<sup>30</sup>

In 2012, Yan *et al.*<sup>31</sup> proposed a comparable battery where the Pt counter electrode is replaced by a Ti counter electrode covered by TiN nanotubes, and where the storage electrode is made in combining so-WO<sub>3</sub> and carbone nanotubes (**Figure 9**). After the photo-charge, they obtain a discharge capacity of 0.124 mAh.cm<sup>-2</sup> against 0.2 mAh.cm<sup>-2</sup> after a classical electrochemical charge, which corresponds to a complete photo-charge efficiency of 69.5 %. Performances of the described devices are resumed in **Table 1** (page 28).

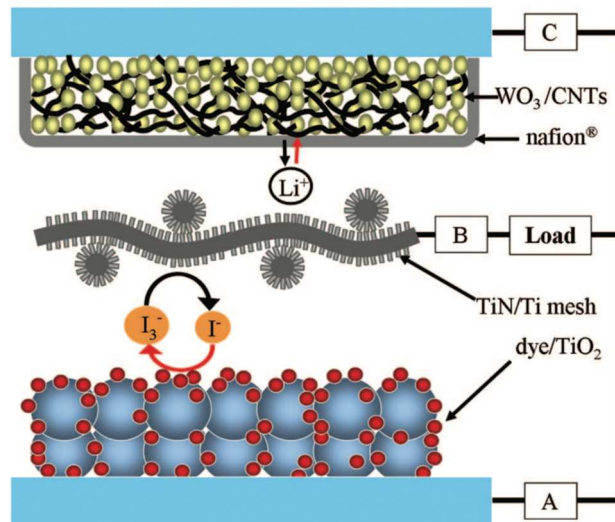


**Figure 9:** Schematic illustration of the 3-electrode DSSC // Ti/TiN // WO<sub>3</sub>/CNTs system.<sup>31</sup>

**Table 1:** Summary of reported solar capacitors and intercalative electrodes

Solar cell type	Energy storage device	Active material (storage)	Electrolyte (storage)	Device geometry	Discharge voltage	Capacity / Energy density	Tested cycling numbers	Conversion efficiency	Storage efficiency	Ref
DSSC	capacitor	activated carbon on Pt electrode	propylene carbonate	2 electrodes	~0.4 V	0.69 F.cm <sup>-2</sup> , (43 F.g <sup>-1</sup> )	10 cycles ~86 % capa. retention	-	59 %	18
		activated carbon on Pt electrode	propylene carbonate	3 electrodes	~0.72 V	0.09 mW.h.cm <sup>-2</sup> 0.65 F.cm <sup>-2</sup> , (41 F.g <sup>-1</sup> )	-	-	42 %	21
		Carbon nanotubes	PVA/H <sub>3</sub> PO <sub>4</sub>	3 electrodes	~0.75 V	0.47 mW.h.cm <sup>-2</sup> 48 F.g <sup>-1</sup>	100 cycles ~80 % capa. retention	6.1 %	84 %	22
		Carbon nanotubes	PVA/H <sub>3</sub> PO <sub>4</sub>	Braided fibers	~0.6 V	0.6 mF.cm <sup>-2</sup> / 1.5.10 <sup>-7</sup> W.h.cm <sup>-2</sup>	-	2.2 %	68.4 %	24
		Carbon nanotubes	PVA/H <sub>3</sub> PO <sub>4</sub>	Multi-wall fibers	~0.63 V	3.32 mF.cm <sup>-2</sup> / 0.27 mW.cm <sup>-2</sup>	1000 cycles 88.2 % efficiency retention	2.73 %	75.7 %	25
DSSC	Intercalative electrode	Carbon nanotubes	PVA/H <sub>3</sub> PO <sub>4</sub>	Braided sheath / core	~0.7 V	~20 F.g <sup>-1</sup>	50 cycles under 20 % strain	1.8 % (global efficiency)	-	26
		WO <sub>3</sub>	propylene carbonate	2 electrodes	~0.6 V	1.8 C.cm <sup>-2</sup> (0.5 mAh.cm <sup>-2</sup> 28 mAh.g <sup>-1</sup> )	-	-	-	27
		WO <sub>3</sub>	acetonitrile	2 electrodes	~0.7 V	-	-	6.55 %	-	29
		so-WO <sub>3</sub> / Pt coated W	3-methoxypropionitrile	3 electrodes	~0.4 V	~20 mAh.g <sup>-1</sup>	-	-	-	30
		WO <sub>3</sub> CNTs/ TiN, Ti mesh	propylene carbonate	3 electrodes	~0.7 V	0.124 mAh.cm <sup>-2</sup>	10cycles ~86 % capa. retention	-	-	31

## I.4 – Solar energy storage in lithium-ion rechargeable batteries

Lithium-ion battery (LIBs) has been developed as one of the most efficient devices for the electrical energy storage. LIB technology has now surpassed other previously competitive battery because of their high gravimetric energy density and long cycle durability.<sup>7</sup> During the charge step, LIB electrodes can store the provided electrical current via reversible  $\text{Li}^+$  intercalation. If an additional photo-electrode can now harvest light and convert incident photon energy into electrochemical energy, the converted photo-energy could be used to directly recharge the battery.

In 2012, Guo *et al.*<sup>32</sup> reported for the first time a device where a DSSC is directly associated with a Li-ion battery. The device is based on a common bifacial titanium electrode, which is shared by the DSSC and the battery. This electrode is functionalized on both sides by  $\text{TiO}_2$  nanotubes, which are perpendicularly grown to the electrode surface (**Figure 10**). Here, it is important to note that the photo-electrode and the battery electrode are nevertheless distinct electrodes, even if they share the same current collector.

This study echoed Mor *et al.* work on a titanium sheet anodization to fabricate stiff or flexible dye-sensitized cells.<sup>33</sup> In these systems, it has been shown that reducing the photo-electrode particles size can lead to an enhancement of the efficiency of photo-induced charge collection.<sup>34</sup>

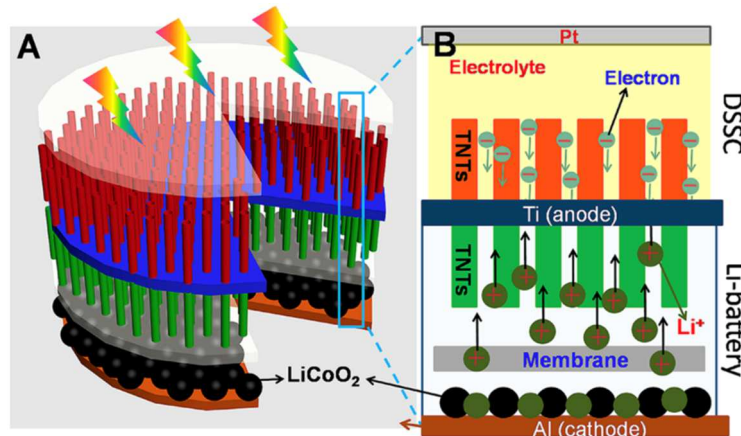


**Figure 10:** Schematic representation of an integrated power pack system based on double-sided  $\text{TiO}_2$  nanotube arrays.<sup>32</sup>

When sunlight irradiates the DSSC, the photo-generated electrons from the light-absorbing dye are injected into the conduction band of  $\text{TiO}_2$  nanotubes and transported along the Ti foil to the  $\text{TiO}_2$  anode of lithium-ion battery (**Figure 10**). In the meantime, the photo-generated holes accumulate at the Pt electrode. At the anode, the

excited electrons induce the following chemical process:  $\text{TiO}_2 + x\text{Li}^+ + xe^- \rightarrow \text{Li}_x\text{TiO}_2$ . At the cathode, the reaction  $\text{LiCoO}_2 \rightarrow \text{Li}_{1-x}\text{CoO}_2 + x\text{Li}^+ + xe^-$  releases free electrons that flow to the counter electrode of the DSSC through an external circuit to combine with the holes in the Pt electrode. By using this hybrid structure, the system delivers a 2 V voltage for a discharge capacity of about 39  $\mu\text{Ah}$  under a discharge current density of 100  $\mu\text{A}$ . The total energy and storage efficiency is reported up to 0.82 %. Performances of all the described systems in this section have been summarized in **Table 2** pages 39-40.

In 2015, Li *et al.*<sup>35</sup> reported a novel photo-assisted chargeable Li-ion battery consisting of a  $\text{LiFePO}_4$  cathode, a metallic lithium anode and a  $\text{TiO}_2$  photo-electrode coupled with an iodide ion redox shuttle for saving electric energy (**Figure 11**).

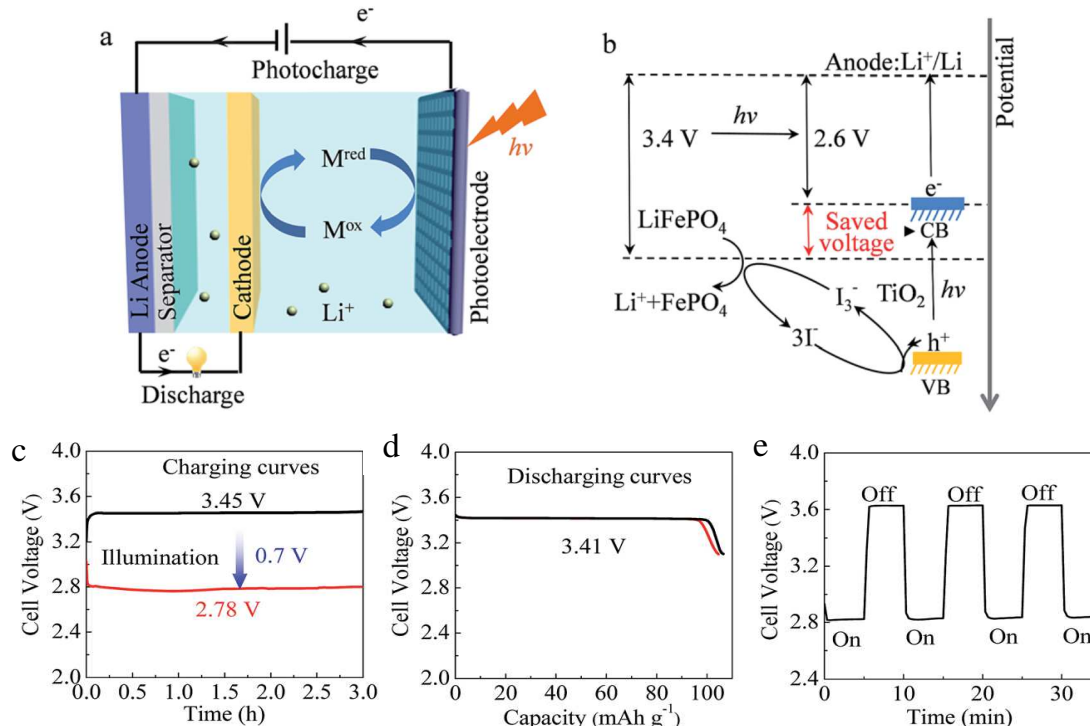


**Figure 11:** (a) Schematic illustration and (b) energy diagram of a photo-assisted chargeable LIB with a three-electrode system. (c) The charge curves of the photo-assisted chargeable LIB (red line) and the LIB (black line) at a current density of 0.02  $\text{mA}\cdot\text{cm}^{-2}$ . (d) The discharge curves of the photo-assisted chargeable LIB (red line) and the LIB (black line) at a current density of 0.01  $\text{mA}\cdot\text{cm}^{-2}$ . (e) The light response of the charging voltage of a photo-assisted chargeable LIB when illumination was switched from “on” to “off”.<sup>35</sup>

During the photo-assisted charging process, the photo-excited electrons of  $\text{TiO}_2$  are transferred to the anode, reducing  $\text{Li}^+$  to  $\text{Li}$  metal using an extra applied voltage to compensate the actual required charging voltage. Meanwhile, the  $\text{I}^-$  redox mediator is oxidized to  $\text{I}_3^-$  by the photo-excited holes and then, in turn, oxidizes the  $\text{LiFePO}_4$ . In the process,  $\text{I}_3^-$  is reduced back to  $\text{I}^-$ . Due to the contribution of the photo-voltage, the

charging voltage of the  $\text{LiFePO}_4$  cathode is experimentally reduced to 2.78 V, which is lower than the discharge voltage of 3.41 V, resulting in about 19% input electric energy saving. Interestingly, this photo-assisted rechargeable battery exhibits a fast photo-response behaviour and could be discharged at a stable voltage plateau of 3.41 V after 10 cycles. If this system allows energy saving, it is to mention that it is not fully autonomous, in contrast to the previous example.

## I.5 - Solar energy storage in lithium-oxygen rechargeable batteries

The use of  $\text{O}_2$  molecules from the air as an active material, instead of solid materials, promises a drastic improvement in the energy density ( $\sim 3550 \text{ Wh.kg}^{-1}$ ).<sup>12</sup> Typically, a Li- $\text{O}_2$  battery is composed of a lithium metal anode, a porous carbon cathode and a  $\text{Li}^+$  ion conductive electrolyte. Li- $\text{O}_2$  cells operate in both aqueous and non-aqueous electrolytes on the basis of two governing reactions:  $2 \text{Li}^+ + 2 \text{e}^- + \frac{1}{2} \text{O}_2 + \text{H}_2\text{O} \rightarrow 2 \text{LiOH}$ ,  $E = 3.45 \text{ V}$  vs  $\text{Li}^+/\text{Li}$  (aqueous) and  $2 \text{Li}^+ + 2\text{e}^- + \text{O}_2 \rightarrow \text{Li}_2\text{O}_2$ ,  $E = 2.96 \text{ V}$  vs  $\text{Li}^+/\text{Li}$  (non-aqueous).<sup>7</sup>

In 2014, Yu *et al.*<sup>36</sup> introduced the approach of using a redox shuttle to couple a photo-electrode with the oxygen electrode in non-aqueous Li- $\text{O}_2$  batteries, which enables photo-assisted charging process. The device integrates a dye-sensitized  $\text{TiO}_2$  photo-electrode with the oxygen electrode via the linkage of the triiodide/iodide redox shuttle. On charging under illumination, the photo-electrode generates triiodide ions that subsequently diffuse to the oxygen electrode surface and oxidize  $\text{Li}_2\text{O}_2$  (**Figure 12**).

The main interest of this system is to deliver a tension corresponding to the energy difference between the  $\text{Li}^+/\text{Li}$  and  $\text{O}_2/\text{Li}_2\text{O}_2$  redox couples while only paying the energy cost corresponding to the difference between  $\text{Li}^+/\text{Li}$  redox potential and the quasi-Fermi level of electrons in  $\text{TiO}_2$ . This way, the photo-voltage generated on the  $\text{TiO}_2$  photo-electrode allows the system to be charged at an input voltage of 2.8 V under illumination instead of 4.0 V in a conventional Li- $\text{O}_2$  battery.

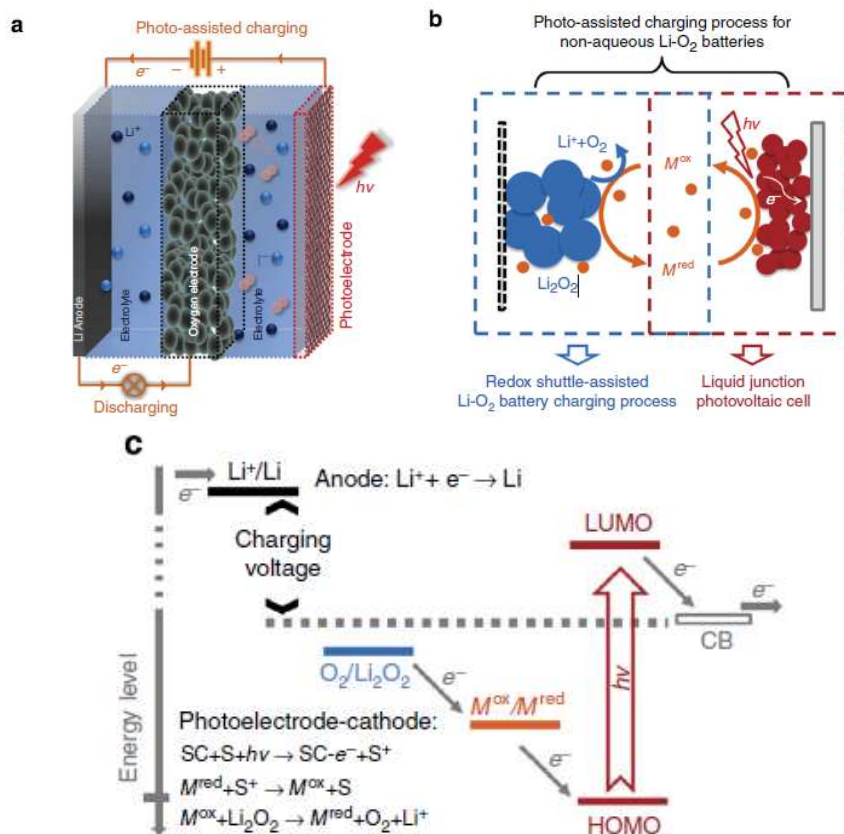


**Figure 12:** a) Schematic illustration of a photo-assisted chargeable Li-O<sub>2</sub> battery with TiO<sub>2</sub> as photo-electrode b) representative scheme of the photo-assisted process c) Energy diagram of the photo-assisted recharge.<sup>36</sup>

Based on a similar mechanism, Liu *et al.*<sup>37</sup> presented in 2015 a photo-assisted rechargeable Li-O<sub>2</sub> battery by integrating carbon nitride on carbon paper as photo-catalyst instead of TiO<sub>2</sub> photo-electrode (**Figure 13**). Upon charging under illumination, the I<sup>-</sup> ions in the electrolyte are oxidized to I<sub>3</sub><sup>-</sup> ions by photo-excited holes from the g-C<sub>3</sub>N<sub>4</sub> photo-catalyst. The resultant I<sub>3</sub><sup>-</sup> ions subsequently diffuse to the oxygen electrode and oxidize Li<sub>2</sub>O<sub>2</sub> to Li<sup>+</sup> and O<sub>2</sub>. Meanwhile, the photo-excited electrons of g-C<sub>3</sub>N<sub>4</sub> are transferred to the anode to reduce Li<sup>+</sup> to Li with the help of a charging voltage of 1.9V. This charging voltage is lower than the discharging voltage (effective discharge voltage of 2.7 V).



Owing to the potential photo/thermal instability of the redox shuttle in electrolytes, Liu *et al.*<sup>38</sup> suggested further improvements by demonstrating that g-C<sub>3</sub>N<sub>4</sub>-carbon paper photo-catalyst could realize the direct photo-oxidation of Li<sub>2</sub>O<sub>2</sub> without any redox mediators. With the suitable design, this system reduces the charge voltage of the Li–O<sub>2</sub> battery to 1.96 V without any redox mediator, which could pave the way for the design of photo-charging all-solid state batteries.

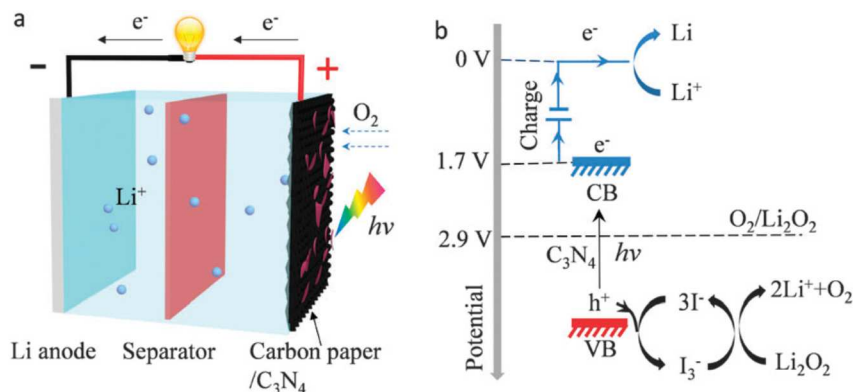


**Figure 13:** Schematic illustration of a photo-rechargeable Li–O<sub>2</sub> battery with g-C<sub>3</sub>N<sub>4</sub> as photo-electrode.<sup>37</sup> Theoretical photo-charging voltage is 1.7 V, effective photo-charging voltage of 1.9 V was achieved.

## I.6 - Solar energy storage in lithium-sulfur rechargeable batteries

Sulfur is one of the most promising active materials because of its high theoretical capacity (1675 mAh.g<sup>-1</sup>), low cost and natural abundance<sup>7</sup>. Sulfur undergoes series of structural changes described by the redox reaction of  $S_8 + 16 Li \rightarrow 8 Li_2S$  (~2.15 V vs. Li/Li<sup>+</sup>) during the discharging and charging processes.<sup>39</sup>

In 2015, Li *et al.*<sup>40</sup> reported a prototype of a solar-driven chargeable lithium-sulfur battery, which enabled photo-assisted charging process. The capture and storage of solar energy is realized by oxidizing S<sup>2-</sup> ions to polysulfide ions in aqueous solution with a Pt-modified CdS photo-catalyst (**Figure 14**). After 2 h of photo-charge, the battery can deliver a specific capacity of 792 mAhg<sup>-1</sup> with a discharge potential of around 2.53 V. A specific capacity of 199 mAhg<sup>-1</sup>, reaching the level of conventional lithium-ion batteries, can be achieved after only 10 min of photo-charge. The charging process of the battery is also accompanied with hydrogen generation. The produced gas is monitored and quantified by gas chromatography, but the discrepancy of the hydrogen evolution rate measured from the photocatalytic water splitting system and that calculated from the stored electrons in the Li-S battery is not well understood. The system presents a capacity retention of 92.5 % after 10 cycles, but the capacity decreases with a prolonged irradiation. As explanation, the authors suggest the



generation of solid-state  $S_8$ , which is a consequence of the over-oxidation of  $S^{2-}$  ions by Pt/CdS photo-catalyst. The insoluble  $S_8$  species would not allow recovering electrons from the current collector and can consequently cause the capacity loss. Therefore, overcharging should be avoided by controlling the optimal light irradiation time, which is determined to be 2 h in this study.

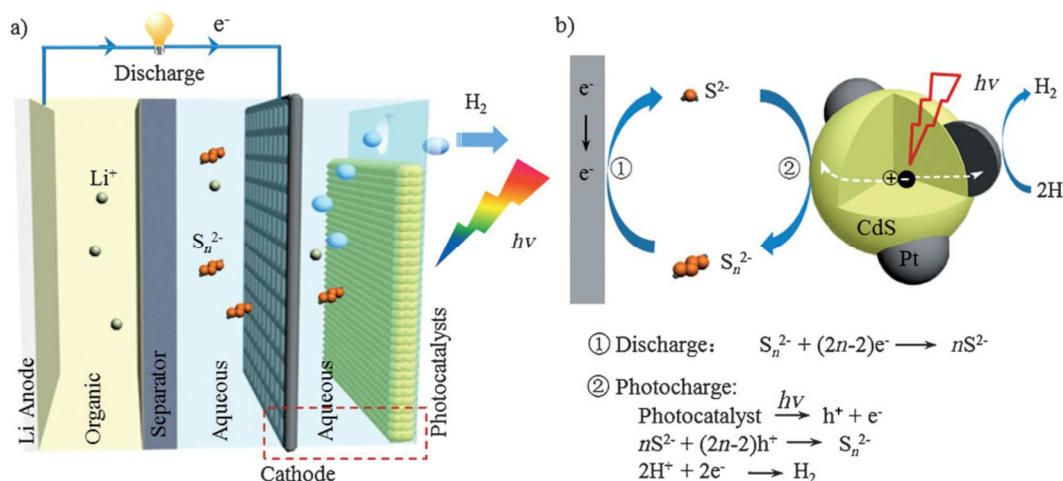


**Figure 14:** a) Schematic illustration of a photo-rechargeable Li-S battery b) representative scheme of discharge and photo-charge processes.<sup>40</sup>

## I.7 - Solar energy storage in lithium-iodide rechargeable batteries

In the continuity of their work on  $Li-O_2$ ,<sup>36</sup> Yu *et al.*<sup>41</sup> demonstrated in 2015 the photo-assisted charging concept for a solar-powered Li-I flow battery by incorporation of a dye sensitized  $TiO_2$  photo-electrode into a Li-I redox flow battery (**Figure 15**). The Li anode and  $I_3^-/I^-$  catholyte are separated by a ceramic Li-ion conductive separator. The catholyte composition includes guanidine thiocyanate and chenodeoxycholic acid additives, which facilitate the surface-wetting between the hydrophilic  $I_3^-/I^-$  catholyte and the hydrophobic dye sensitized. To the best of our knowledge, it is the first time that a DSSC photo-electrode is immersed into an aqueous catholyte, which constitutes an important step towards the coupling of this electrode with redox-flow systems.

The discharging process is similar to that of conventional Li-I batteries: electrochemical oxidation of Li to  $Li^+$  on the anode side and reduction of  $I_3^-$  to  $I^-$  on the counter-electrode side give an electricity output of 3.3 V. Upon illumination, dye molecules, which are chemically adsorbed on the  $TiO_2$  semiconductor surface, get photo-excited and inject electrons into the conduction band of  $TiO_2$  (steps 1 and 2 in **Figure 15.c**). The oxidation of  $I^-$  to  $I_3^-$  then takes place by regenerating oxidized dye

molecules (step 3 in **Figure 15.c**). By applying an additional external voltage,  $\text{Li}^+$  ions pass meanwhile through the ceramic separator and are reduced to metallic Li on the anode side (step 4 in **Figure 15.c**), completing the full photo-assisted charging process.

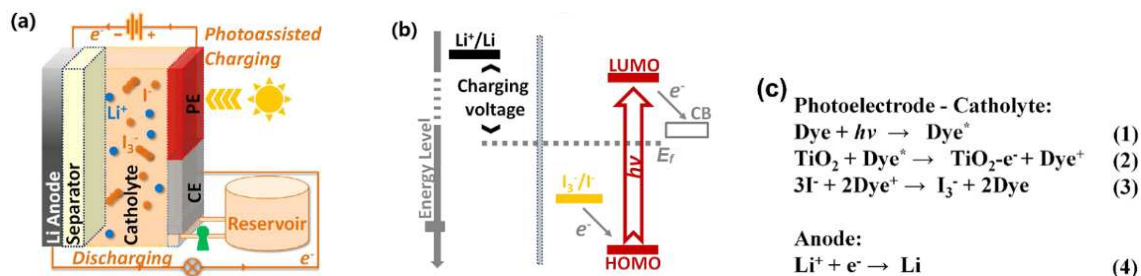


**Figure 15:** (a) Schematic of a Li-I flow battery with the three-electrode configuration (b) energy diagram for the photo-assisted charging process (c) photo-electrochemical half reactions.<sup>41</sup>

Similar to previously described photo-assisted charging devices in Li- $\text{O}_2$  technology, the main interest of this system is to deliver a tension corresponding to the energy difference between the  $\text{Li}^+/\text{Li}$  and  $\text{I}_3^-/\text{I}^-$  redox couples while only paying the energy cost corresponding to the difference between  $\text{Li}^+/\text{Li}$  redox potential and the quasi-Fermi level of electrons in  $\text{TiO}_2$ . This way, the device could be discharged at 3.3 V while being charged at 2.9 V, thus allowing energy savings up to 20 %. This system shows a good cycling ability with a stable charging voltage plateau conserved after 25 cycles, but presents a slow rate of photo-charge (16.8 hours for 0.1 mL of catholyte).

In 2016, Nikiforidis *et al.*<sup>42</sup> demonstrated photo-assisted lithium–iodine redox cells integrated with a hematite photo-electrode replacing the  $\text{TiO}_2$  dye sensitized photo-electrode. The energy efficiency for the photo-assisted charge process is  $\sim 95.4\%$ , which is  $\sim 20\%$  higher than that in the absence of illumination at a current rate of  $0.075 \text{ mA}\cdot\text{cm}^{-2}$ . The hematite is remarkably stable in aqueous  $\text{I}_3^-/\text{I}^-$  catholyte and exhibits over 600 hours of cycling without noticeable performance decay and photo-corrosion. Nevertheless, the expensive LISICON separator and the durability for effectively avoiding the redox-shuttle have still to be developed in these systems.<sup>12</sup>

## I.8 - Solar energy storage in dual-liquid redox batteries

In contrast with other rechargeable batteries employing the solid or gas materials on the active electrodes, the dual-liquid redox batteries enable to store electrical energy via two liquid redox-couple electrolytes (anolyte and catholyte). This option avoids safety issues for the use of metal anode (Li, Na and K etc.). Besides, dual electrolytes can be stored in external reservoirs for different volumes.<sup>12</sup> Redox batteries can be interesting for their flexibility, high lifetimes, high reliability, relatively low operation

costs, as well as the potential to store a large amount of energy. Furthermore, the power and energy output are independent of the storage capacity, which offers a separate control over the energy and the power, resulting in a highly flexible system.<sup>2</sup>

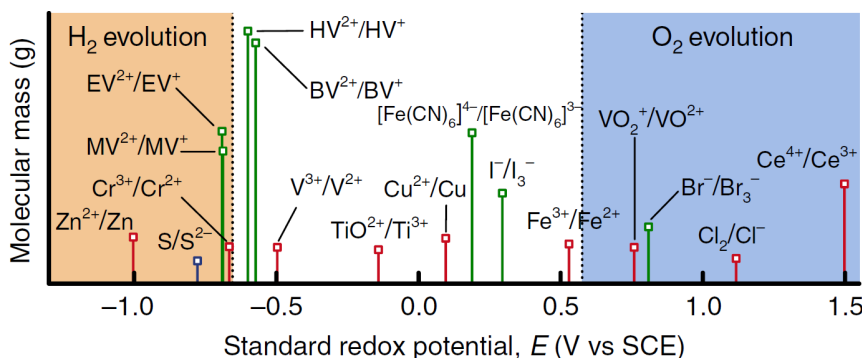


**Figure 16:** Reduction potentials of some couples considered relative to their thermodynamic stability window of water at neutral pH (white region). The lines coloured in red, green and blue are for couples stable in acidic (1M acid), neutral and basic (1M base) conditions, respectively. BV, benzyl viologen; EV, ethyl viologen; HV, heptyl viologen; MV, methyl viologen; SCE, standard calomel electrode.<sup>43</sup>

The redox potentials of common redox-couples are shown in **Figure 16**.<sup>43</sup> The first solar battery was introduced in a redox battery with the  $\text{Ag}_2\text{S}/\text{Ag}$  and  $\text{S}/\text{S}^{2-}$  respectively as anode and cathode active materials, with a CdSe photo-electrode integrated in the catholyte's compartment in 1976<sup>4</sup>. Since then, different kinds of redox-couples have been investigated for photo-rechargeable redox-flow batteries. All vanadium systems,<sup>44-48</sup> iodide-,<sup>49-51</sup> quinone-<sup>52-54</sup> and polysulfide-based<sup>55,56</sup> systems are amongst the most studied redox couples for photo-assisted recharge. Detailed device descriptions can be found in recent reviews.<sup>1,2,12</sup> Performances of few of these systems have been summarized in **Table 2** pages 39-40.

Here, we will only illustrate the photo-rechargeable redox-flow batteries technology using a typical all-vanadium system based on the aqueous couples  $\text{V}^{3+}/\text{V}^{2+}$  (- 0.26 V vs ESH) and  $\text{VO}_2^+/\text{VO}^{2+}$  (1.0 V vs ESH). These redox couples present high charge transfer kinetics and count among the most used and studied redox couples for stationary storage energy applications.<sup>57</sup>

In 2012, Liu *et al.* studied the effect of vanadium redox species on the photo-electrochemical behavior of  $\text{TiO}_2$  and hybrid  $\text{TiO}_2/\text{WO}_3$  photo-electrodes in a photo-water splitting cell.<sup>44</sup> They observe a strong improvement of the electrode photo-response when  $\text{VO}^{2+}$  is added to the aqueous electrolyte. They attribute this phenomenon to the redox properties of  $\text{VO}^{2+}$ , which would trap holes and limit exciton recombinations. On the basis of this study, Wei *et al.*<sup>45</sup> proposed a cell integrating a  $\text{TiO}_2$  photo-electrode into an all-vanadium redox-flow battery (**Figure 17**).

During the photo-charge, the photo-generated holes diffuse from  $\text{TiO}_2$  electrode to the photo-electrode/electrolyte interface and oxidized  $\text{VO}^{2+}$ , whereas electrons get transported through external circuit to reduce  $\text{V}^{3+}$  at the Pt counter-electrode. In the dark, the battery discharges as a regular redox battery with  $\text{V}^{2+}$  oxidation and  $\text{VO}_2^+$  reduction. A Nafion membrane allows the separation of the two compartments and ensures the ionic conductivity by protons transfer into an aqueous electrolyte ( $\text{H}_2\text{SO}_4$ , 3 mol.L<sup>-1</sup>). Even if it is thermodynamically possible to decompose water in this device, the required multi-electronic reactions are too slow in comparison to the single electron transfer process involved in the vanadium couples redox reactions (**Figure 17**).

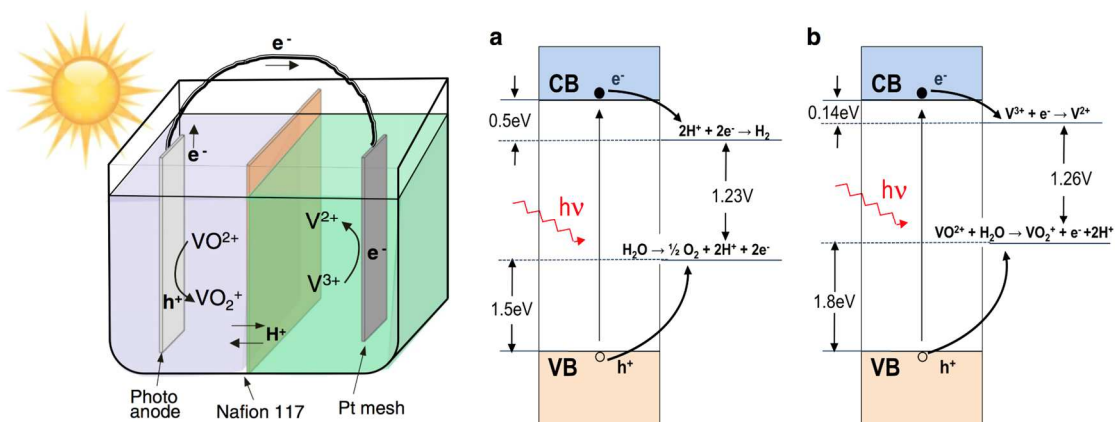


**Figure 17:** (left) Schematic illustration of the all-vanadium redox PEC storage cell (right) band positions of  $\text{TiO}_2$  and corresponding photo-electrochemical reactions in a) photo-catalytic water splitting and b) an all-vanadium redox PEC storage cell. CB and VB refer to conduction band and valence band, respectively. The energy differences between the semiconductor band edges and thermodynamic redox reactions are indicated in the figures.<sup>45</sup>

This battery can be continuously photo-recharged for long time (>25 h) and delivers a 0.8 V open circuit voltage in the dark. Compared to other photo-electrodes materials,  $\text{TiO}_2$  shows a remarkable stability in acid conditions and allows a good electric conversion efficiency of 12 % at 350 nm. However, its large band gap (3.2 V) in absence of dye limits the light absorption at shorter wavelengths.

In another study, the same authors replace the  $\text{TiO}_2$  electrode by a hybrid electrode  $\text{TiO}_2/\text{WO}_3$ .<sup>48</sup> Because  $\text{WO}_3$  band gap is smaller (2.6 V) than  $\text{TiO}_2$ , its association with  $\text{TiO}_2$  aims to extend the photo-electrode absorption window. Besides, the  $\text{WO}_3$  valence and conduction bands position are such that electrons and holes should naturally be transferred from  $\text{TiO}_2$  to  $\text{WO}_3$  (**Figure 18**).

In this system, the photo-generated charge carriers can follow different paths at the semiconductor/electrolyte interface. Electrons and holes can reduce  $V^{3+}$  and oxidize  $VO^{2+}$ , or they can recombine. Electron transfer can also occur from  $TiO_2$  to  $WO_3$  reducing  $W^{6+}$  in  $W^{5+}$  and forming  $H_xWO_3$ ,  $H^+$  can be reversibly extracted from this structure. This formation of  $H_xWO_3$  can be interpreted as an additional storage for the electrons, which could be then given back during the discharge. The higher photo-currents were observed with 12% mass percentage in  $WO_3$ . For smaller percentages,  $WO_3$  content would not offer enough insertion sites for the electrons to avoid recombination, whereas for higher  $WO_3$  mass content,  $H_xWO_3$  formation would compete with vanadium redox reactions.

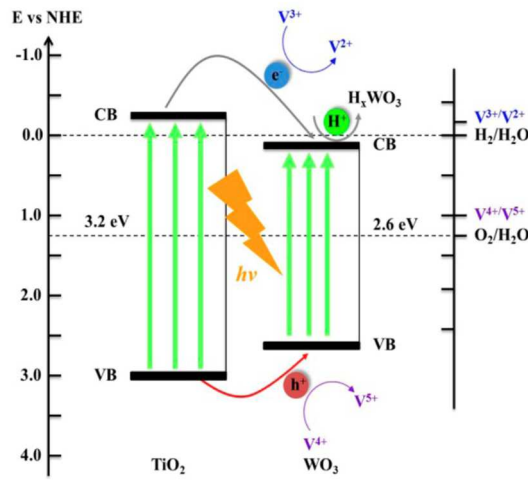


**Figure 18:** Schematic representation of proposed electron storage mechanism and charge transfer pathways for the hybrid  $WO_3/TiO_2$  electrode in the all-vanadium photo-electrochemical storage cell.<sup>48</sup>

**Table 2:** Summary of reported solar batteries (1/2)

Battery type	Photo-electrode	Active material in anode / cathode	Electrolyte	Separator	Discharge / charge voltage (photo-assisted charge voltage)	Capacity	Tested cycling numbers	Global efficiency	Energy saving <sup>1</sup>	Ref
Li-ion batteries	DSSC	TiO <sub>2</sub> /LiCoO <sub>2</sub>	3-methoxy-pionitrile /LP30	PE	~2 V	39 µAh	3 cycles (>100 % capacity retention)	0.82 %	-	32
	TiO <sub>2</sub>	Li/LiFePO <sub>4</sub>	EC,DMC/H <sub>2</sub> O	LISICON	3.41 V / 3.45 V (2.78 V)	137 mAh.g <sup>-1</sup>	10 cycles (~97 % capacity retention)	-	19 %	35
Li-S batteries	CdS/Pt	Li/S	EC,DMC/H <sub>2</sub> O	LISICON	2.53 V	792 mAh.g <sup>-1</sup>	10 cycles (~92.5 % capacity retention)	-	-	40
Li-O <sub>2</sub> batteries	DSSC	Li/LiFePO <sub>4</sub>	DMSO	Glassy fiber	~2.8 V / 3.4 V (2.72 V)	-	4 cycles (photo-assisted charge voltage)	-	20 %	36
	C <sub>3</sub> N <sub>4</sub>	Li/LiFePO <sub>4</sub>	Tetraglyme	Glassy fiber	2.74 V / 3.61 V (1.96 V)	600 mAh.g <sup>-1</sup>	2.72 V → 3.10 V 70 cycles (photo-assisted charge voltage: 1.96 V → 2.35 V)	-	46 %	38
Li-I batteries	DSSC	Li/ I <sub>3</sub> <sup>-</sup> ,I <sup>-</sup>	H <sub>2</sub> O	LISICON	3.3 V / 3.6 V (2.91 V)	32600 mAh.L <sup>-1</sup>	25 cycles (photo-assisted charge voltage: 2.91 V → 2.93 V)	-	19 %	41
	αFe <sub>2</sub> O <sub>3</sub>	Li/ I <sub>3</sub> <sup>-</sup> ,I <sup>-</sup>	EC,DMC/H <sub>2</sub> O	LISICON	3.3 V / 3.84 V (3.4 V)	192 mAh.g <sup>-1</sup>	22 cycles (>99 % capacity retention)	-	11 %	42

<sup>1</sup> Calculated as  $(V_{\text{charge}} - V_{\text{photo-charge}}) / V_{\text{charge}}$

Table 3: Summary of reported solar batteries (2/2)

Battery type	Photo-electrode	Active material in anode / cathode	Electrolyte	Separator	Discharge / charge voltage (photo-assisted charge voltage)	Capacity	Tested cycling numbers	Global efficiency	Energy saving <sup>1,2</sup>	Ref
Redox-flow batteries	TiO <sub>2</sub>	V <sup>3+</sup> , V <sup>2+</sup> /VO <sub>2</sub> <sup>+</sup> , VO <sub>2</sub> <sup>2+</sup>	H <sub>2</sub> O (H <sub>2</sub> SO <sub>4</sub> 3M)	Nafion 117	~0.8 V	0.0042 μmol.h <sup>-1</sup>	-	12 %	-	45
	TiO <sub>2</sub>	V <sup>3+</sup> , V <sup>2+</sup> /VO <sub>2</sub> <sup>+</sup> , VO <sub>2</sub> <sup>2+</sup>	H <sub>2</sub> O (H <sub>2</sub> SO <sub>4</sub> or MSA 3M)	Nafion 117	-	-	60 h (89.5 % photo-current retention)	45.6 %	-	47
	TiO <sub>2</sub> /WO <sub>3</sub>	V <sup>3+</sup> , V <sup>2+</sup> /VO <sub>2</sub> <sup>+</sup> , VO <sub>2</sub> <sup>2+</sup> , H <sub>x</sub> WO <sub>3</sub>	H <sub>2</sub> O (H <sub>2</sub> SO <sub>4</sub> 3M)	Nafion 117	-	-	-	-	-	48
	DSSC <sup>2</sup>	Li <sub>2</sub> WO <sub>4</sub> , Li <sub>2+x</sub> WO <sub>4</sub> /I <sub>3</sub> <sup>-</sup> , I <sup>-</sup>	H <sub>2</sub> O/PC	LISICON	~0.5 V	0.0195 mAh.mL <sup>-1</sup>	10 cycles (98.6 % capa. retention)	-	-	49
	DSSC	DMFc <sup>+</sup> , DMFc <sup>-</sup> / I <sub>3</sub> <sup>-</sup> , I <sup>-</sup>	MPN/PC	LISICON	~0.3 V	~39 μAh	10 cycles (~79 % capa. retention)	0.05 %	-	50
	DSSC	AB5-type hydrogen storage alloy / I <sub>3</sub> <sup>-</sup> , I <sup>-</sup>	H <sub>2</sub> O (KOH 5M)/PC	Modified Nafion 117	~0.6 V	26.7 mAh.g <sup>-1</sup>	20 cycles (88 % capa. retention)	0.4 %	-	51
	αFe <sub>2</sub> O <sub>3</sub>	AQDS/FeCN <sup>3-</sup> , FeCN <sup>4-</sup>	H <sub>2</sub> O (NaOH 1M)	Nafion 117	~0.74 V	-	-	0.06-0.08 %	-	52
	Dual-silicon	AQDS/Br <sup>-</sup> , Br <sup>3-</sup>	H <sub>2</sub> O (H <sub>2</sub> SO <sub>4</sub> 1M)	Nafion 115	0.78 V	730 mAh.L <sup>-1</sup>	10 cycles (~98 % capa. retention)	3.2 %	-	53
	Silicon solar cells	AQDS/BQDS	H <sub>2</sub> O	Nafion 212	~0.41 V	3500 mAh.L <sup>-1</sup>	10 cycles (~91 % current retention)	1.7 %	-	54
	TiO <sub>2</sub>	S <sub>4</sub> <sup>2-</sup> , S <sup>2-</sup> / I <sub>3</sub> <sup>-</sup> , I <sup>-</sup>	H <sub>2</sub> O (NaOH 1M)	Nafion 117	0.83 V/0.86 V (0.08 V)	110 mAh.g <sup>-1</sup>	20 cycles (~90 % capa. retention)	-	91 %	55
	DSSC	S <sub>4</sub> <sup>2-</sup> , S <sup>2-</sup> / I <sub>3</sub> <sup>-</sup> , I <sup>-</sup>	AcN/THF (2:1 v/v)	CML-7000	0.8 V	240 μAh.cm <sup>2</sup>	10 cycles (78 % efficiency)	1.7 %	-	56

<sup>1</sup> Calculated as  $(V_{\text{charge}} - V_{\text{photo-charge}}) / V_{\text{charge}}$

<sup>2</sup> “DSSC” : TiO<sub>2</sub> + dye

## I.9 - State of the art: conclusions

The strategy, which consists in externally wiring a battery with solar cells in order to recharge it, is up to now the most mature technology. In fact, it benefits from two well-known and established technologies for conversion (solar cell technology) and storage (Li-ion battery technology). Good performances could be reached by working on the good match (buffer against the photovoltaic current variations<sup>8</sup>, matching the photovoltaic maximum power point voltage to the battery charging voltage<sup>9</sup>, boost converter<sup>11</sup>) between solar cells and storage devices (when optimized, up to 14.5 % of overall efficiencies for amorphous silicon photovoltaic modules<sup>9</sup> and 9 % for perovskite solar cells).<sup>10,11</sup> However, it has shown practical limitations: the extra photovoltaic modules and external wires considerably enlarge the volume and weight of the entire device, and increase the cost of energy storage.<sup>12</sup> In fact, no work has been undertaken on the system design to try to make the device more suitable for portable applications.

In order to design an appropriate compact device for both converting and storing energy, two main strategies have been described in this chapter.

The first strategy consists in hybridizing a DSSC with capacitors in order to directly store the photo-generated energy. Compared to solar batteries, solar capacitors responsiveness to photo-current storage is expected to be quicker because of the inherent fast-charging nature of the capacitor component.<sup>1</sup> In this strategy, research has mostly been focused on the engineering aspects of designing more efficient, compact, portable, and flexible devices. Performances of these devices (reported in **Table 1** (page 28)) show that amongst the different tested geometries to assemble conversion and storage compartments, the three-electrode device with carbon nanotubes<sup>22</sup> seems to remain highly performing system in regards to discharge voltage, conversion and storage efficiencies. Flexibility<sup>24-26</sup> has thus a little cost in terms of performances, even if all the systems roughly have similar performances.

The second strategy consists in introducing photo-electrodes into lithium-based rechargeable battery in order to allow either a photo-charge or a photo-assisted charge. One more time, DSSC are quite commonly used. Storage capacities and output voltage are coherent with what could be expected from battery technologies: high voltage for Li-based batteries, and high capacities for post-lithium technologies (Li-S and Li-O<sub>2</sub>) and redox-flow batteries. In these systems, report of the conversion and storage efficiencies is far from being systematic. Very little information is given more specifically on the global efficiency of lithium-based photo-batteries.



It can be useful to remind here that almost all the reported devices have been published within the last 5 years. Hence, instead of comparing efficiencies of devices still far from their maturity point, it may be more relevant to analyse and compare the operation principle of these SPEES devices.

### I.9.1 - Photo-charge or photo-assisted charge?

The nature of the charge under light exposure (photo-charge or photo-assisted charge) depends on the amount of energy required to reverse the spontaneous reactions occurring between the cathode (or catholyte) and the anode (or anolyte). The energy diagram in **Figure 19** is representative for systems where typically a DSSC is coupled with a storage electrode.

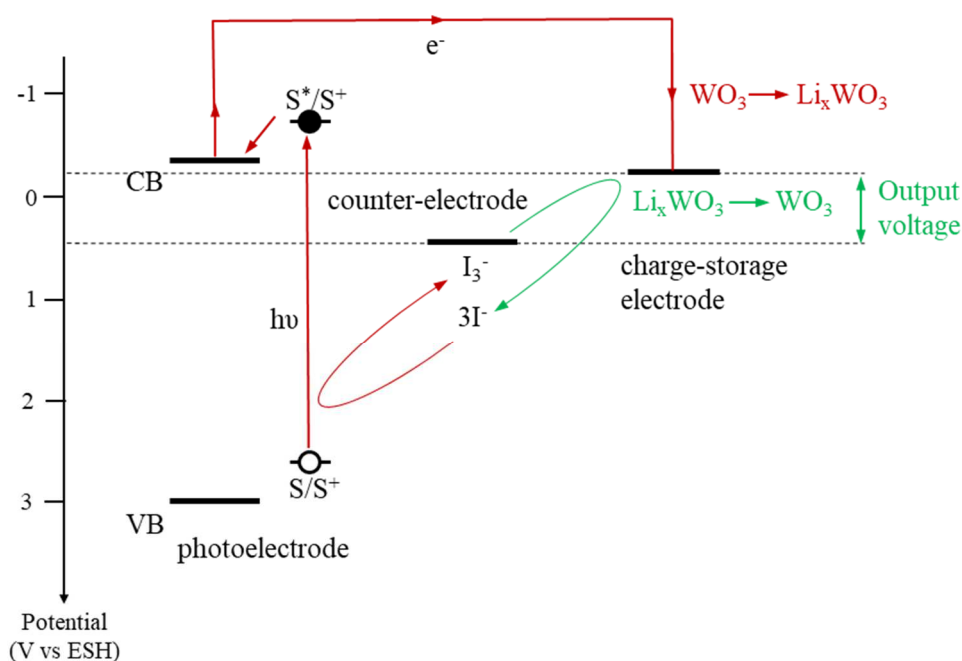


**Figure 19:** Schematic energy diagram for the photo-charging (in red) and discharge (in green) processes of a typical {DSSC + WO<sub>3</sub>} system.

After illumination, photo-generated electrons flow from the photo-electrode (typically TiO<sub>2</sub>) to the counter electrode (typically WO<sub>3</sub>, or polymers like PEDOT<sup>58,59</sup>), where it is stored through ion intercalation. The obtained output discharge voltage corresponds to the difference between the Fermi level of the chosen active storage material (typically WO<sub>3</sub>, or polymers like PEDOT<sup>58,59</sup>) and the potential of the mediator redox potential (I<sup>-</sup> / I<sub>3</sub><sup>-</sup> in a DSSC). In this case, the discharge voltage (also called output voltage) is limited by the position of the conduction band of the photo-electrode, which determines the electron highest energy level. It is the reason why the discharge voltage

in the {DSSC + capacitors system} system generally don't exceed 0.6-0.7 V ( $E_{CB, TiO_2} \sim -0.2$  V vs ESH,<sup>60</sup>  $E_{\text{Iodine / iodide}} \sim 0.4$  V vs ESH<sup>16</sup>). In this configuration, no additional voltage needs to be applied for the photo-charge.

The energy diagram in **Figure 20** is representative for systems working with a metallic Li electrode as counter electrode (typically in Li-O<sub>2</sub>,<sup>36-38</sup> Li-S,<sup>40</sup> Li-I batteries,<sup>41,42</sup> or in a half cell Li-ion battery configuration<sup>35</sup>). In this case, the output voltage is generally high (around 2-3 V against 0.7 V generally in a {DSSC + capacitors system}), and light exposure doesn't bring enough energy to realize a complete photo-charge. However, it allows a photo-assisted charge by reducing the charging voltage under light exposure.

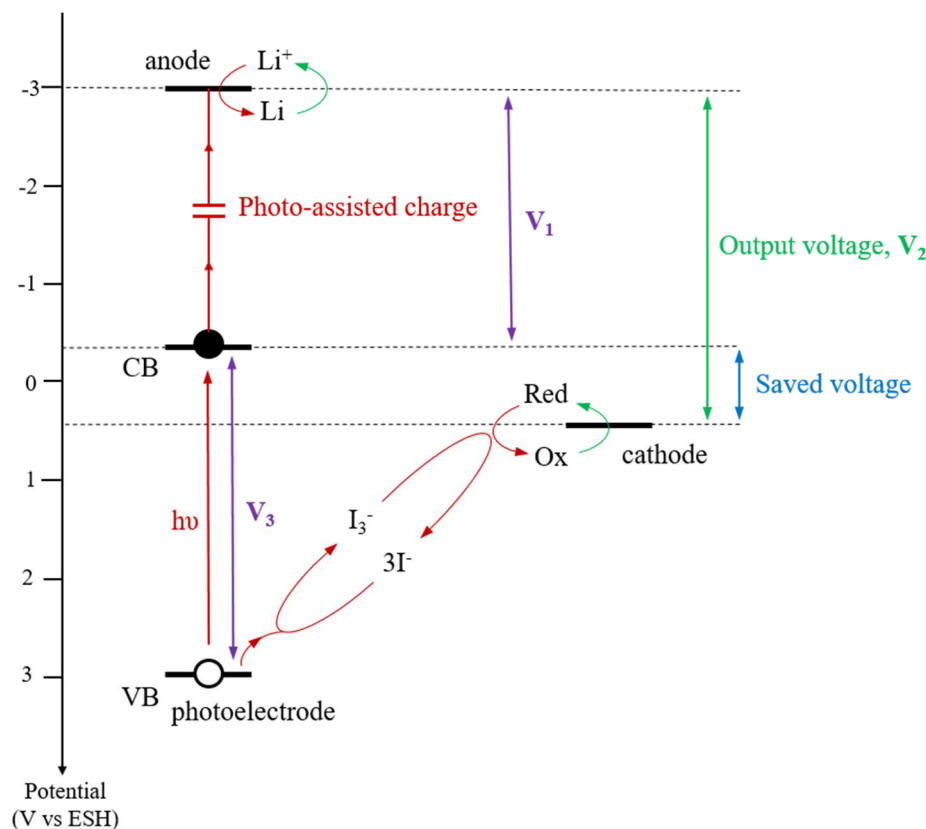


**Figure 20:** Schematic energy diagram for the photo-assisted charging (in red) and discharge (in green) processes of systems typically working with a metallic Li electrode as counter electrode.

The main interest of these systems is to deliver a tension corresponding to the energy difference between Li<sup>+</sup>/Li and the redox active material at the cathode / catholyte while only paying the energy cost corresponding to the difference between Li<sup>+</sup>/Li redox potential and the quasi-Fermi level of electrons in the photo-electrode (TiO<sub>2</sub>,<sup>35,36,41,55</sup> αFe<sub>2</sub>O<sub>3</sub>,<sup>42</sup> or C<sub>3</sub>N<sub>4</sub>,<sup>37,38</sup>).

In most cases,  $I^- / I_3^-$  redox couple is used as mediator to transfer photo-generated holes from the photo-electrode allowing the mediated oxidation of the cathode / catholyte during the photo-assisted charge. In some cases, the photo-oxidation is unmediated, as in Li-I systems where  $I^- / I_3^-$  is the catholyte<sup>41,42</sup> itself or in a Li-O<sub>2</sub> battery study.<sup>38</sup> For cathode / catholyte as LiFePO<sub>4</sub>, Li<sub>2</sub>O<sub>2</sub> or I<sub>3</sub><sup>-</sup>, which have comparable reduction potential around 0.4 V vs ESH, the charging voltage is expected to be reduced from 0.6-0.7 V for TiO<sub>2</sub>, 0.45 V for  $\alpha$ -Fe<sub>2</sub>O<sub>3</sub> and 1.65 V for C<sub>3</sub>N<sub>4</sub> photo-electrodes (see **Table 2** pages 39-40). The ideal energy alignment should thus minimize the energy difference ( $V_1$ ) between the anode and the quasi-Fermi level of electrons in the photo-electrode for smaller photo-assisted charge voltage, maximize ( $V_2$ ) the energy difference between the anode and the cathode for larger discharge voltage output, but also minimize ( $V_3$ ) the photo-electrode band-gap for a better sunlight harvesting.

The last energy diagram (**Figure 21**) is typical for redox-flow batteries, where no additional voltage needs to be applied for the photo-charge. After illumination, both photo-generated holes and electrons have to react with the discharged redox species to ensure a complete photo-recharge. The ideal catholyte-photo-electrode alignment should maximize ( $V_2$ ) =  $E_{\text{anolyte}} - E_{\text{catholyte}}$  for larger discharge voltage output, meanwhile minimize photo-electrode band gap ( $V_1$ ) for better sunlight harvesting.<sup>1</sup>

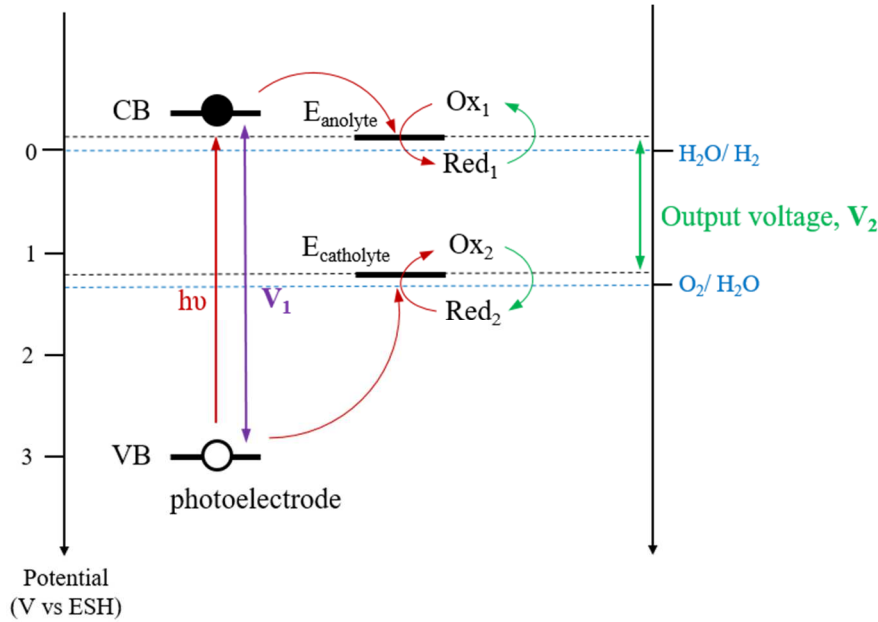


**Figure 21:** Schematic energy diagram for the photo-charging (in red) and discharge (in green) processes of redox-flow batteries employing two soluble redox species.

### I.9.2 – Choice of the electrolyte

The choice of the electrolyte and of the eventual associated dissolved species is a real challenge in order to develop solar powered electrochemical energy storage devices. In fact, they should (1) be adapted for the usual charges and discharges of the chosen battery technology, but also (2) be adapted to operate under light exposure.

#### *(1) to be adapted for usual charges and discharges of the battery*

Amongst many criteria, the solvent should have an adapted electrochemical window, so that electrolyte degradation would not occur within the range of the working potentials of both the cathode and the anode. In this regard, organic solvents or ionic liquids can provide wide electrochemical windows in comparison to aqueous solvents, which are not suitable for high voltage application (see the 1.23V-limited water stability window in **Figure 21**). Nevertheless, compared to organic solvents, aqueous solvents can be an interesting solution in regards to their low toxicity, low cost and higher evaporation temperature.

Obviously, criterion (1) strongly depends on the battery technology. For instance, for the post-lithium-ion batteries, which promise high energy densities such as Li-S or Li-O<sub>2</sub> batteries, designing a suitable electrolyte is already a big challenge, even under dark conditions.

In Li-S batteries for example, unlike those in traditional lithium-ion batteries, the charge and discharge processes of a lithium-S system involve series of intermediate redox polysulfide species, which are highly soluble into liquid electrolytes.<sup>7,61</sup> Under the working conditions (for charge and discharge) of lithium-sulfur batteries, the soluble polysulfide species tend to migrate from the cathode through the porous separator to chemically react with lithium metal at the anode. This polysulfide shuttle behavior severely lowers the cycling efficiency of the cells and induces capacity fade during cycling.<sup>62</sup>

As studied alternatives, polymer and solid-state electrolytes are more favorable than liquid electrolytes in terms of their capability of reducing the solubility of polysulfides and blocking the shuttle of polysulfides in Li-S batteries. Besides, they could protect the lithium metal anode and minimize dendrite formation, which is beneficial for improving the safety and life cycle of Li-S batteries. However, polymer and solid-state electrolytes usually have low ionic conductivity because of the high viscosity of polymers and high energy barrier for Li-ion transport in solid-state electrolytes.<sup>61</sup>

In Li-O<sub>2</sub> batteries, the electrolyte is also key component and one of the main challenges at present. It must be stable both to O<sub>2</sub> and its reduced species, as well as to the LiO<sub>x</sub> compounds that form on discharge; it must exhibit sufficient Li<sup>+</sup> conductivity, O<sub>2</sub> solubility and diffusion to ensure satisfactory rate capability, as well as wet the electrode surface and possess low volatility to avoid evaporation at the cathode.

In the aqueous operation, the discharging process produces a soluble product, LiOH, which does not readily decompose during charging and can also precipitate<sup>63,64</sup> above ~5 M, impairing the energy density and cyclability.

Electrolytes based on organic carbonates (for example, LiPF<sub>6</sub> in propylene carbonate) have so far been widely used in non-aqueous Li-O<sub>2</sub> cells, because of their low volatility, compatibility with Li metal and high oxidation stability (>4.5 V vs. Li<sup>+</sup>/Li). However, studies also show that organic carbonates are vulnerable to the nucleophilic attack reduced O<sub>2</sub> species.<sup>63</sup>

Hence, design of suitable electrolytes is already a tough challenge for technologies as Li-O<sub>2</sub> and Li-S for example.

## *(2) to be adapted to operate under light exposure*

As SPEES systems are meant to work under light exposure, it seems important to figure out if created excitons could trigger unexpected degradative side reactions. In the described SPEES devices (**sections I.2-I.8**), information is often given concerning the battery capacity retentions after illumination, but up to now, very little information is given concerning the effect of light illumination during the photo-(assisted)-charge on the eventual degradation of the constitutive elements of the battery.

Many SPEES devices are based on DSSC technology whose stability under light has already been discussed.<sup>65,66</sup> The most commonly used electrolyte is the iodide/triiodide redox couple in an organic matrix, generally acetonitrile. Experimental studies indicated that exposure of DSSCs to UV light can degrade their performance during long-term operation as it can generate a number of degradation mechanisms. For instance, UV light can cause TiO<sub>2</sub> direct band excitation, which may lead to oxidation of the dye.<sup>67,68</sup> Using optical spectroscopy, it was found that UV light can cause irreversible reaction of iodine leading to the bleaching of the electrolyte.<sup>67</sup> Furthermore, electrolyte bleaching was also reported resulting in the high temperatures (T > 50 °C) under one Sun illumination even in the absence of UV light and under both indoor and outdoor ageing conditions in the presence of UV filter with a cut-off wavelength at 397 nm.<sup>69</sup> Also, active oxygen species (such as hydroxyl groups and OH radicals), water or

other impurities in the electrolyte and sublimation of iodine due to inadequate sealing barriers are the other factors in the  $I_3^-$  degradation mechanisms.<sup>70</sup>

Hence, we could yet keep in mind that dye and dissolved redox species can be particularly sensible to light exposure. Finding a way to limit their utilization could then conduct to more stable devices.

## II - Converting and storing solar energy: a new approach

Up to now, the challenge of combining solar energy harvesting and energy storage have been addressed in hybridizing two separated technologies. In fact, conversion and energy storage compartments have been externally wired,<sup>9,8,10,11</sup> or have been incorporated into a two compartments device sharing a common electrode as described in **section I**.

In this work, we propose a different approach to harvest and store the solar energy into a single device. The idea here is to explore the possibility of converting and storing the solar energy within a single bifunctional electrode. In fact, such a bifunctional electrode could be integrated into photo-rechargeable Li-ion batteries, where intercalating storage electrodes could be directly recharged by light irradiation. As developed, photo-rechargeable Li-ion batteries could offer several advantages.

First, they are inherently simple systems since they do not require complex installation for the storage and distribution of fuels, e.g., solar fuels. Second, they are potential energy efficient devices in that they utilize a single material photo-active host electrode for the dual functionalities of energy harvesting and storage, thereby eliminating any possibility of energy losses associated with charge transfer. Third, they can be highly robust if they are developed as small and portable energy devices with capacities to bridge the energy needs of a day and night cycle.<sup>71</sup>

### II.1 - Pioneering works on bifunctional electrodes

The concept of solar intercalation batteries was first introduced by Tributsch *et al.* in the 1980s on the basis of theoretical considerations and supporting experiments.<sup>72-76</sup> In his pioneering work published in 1980,<sup>72</sup> zirconium- and hafnium-dichalcogenides are used as *p*-type semiconductors in HCl aqueous electrolyte (for H<sup>+</sup> insertion) or in LiClO<sub>4</sub>·3H<sub>2</sub>O containing acetonitrile (for Li<sup>+</sup> insertion). Under light exposure, an additional cathodic photo-current is observed. As layer-type transition metal compounds of Groups IV.B and V.B are well-known to intercalate ions, the author attribute this phenomenon to cation insertion. At this early stage, experimental efforts did not conduct to a working photo-intercalation solar cell due to the insufficient *p*-type conductivity of transition metal dichalcogenides. Besides, aqueous electrolytes are little suited to ion exchange with this kind of host materials. In fact, co-intercalation of water products make intercalation partially irreversible and lead to corrosion. In addition, host electrodes could be partially reduced with formation of H<sub>2</sub>S and H<sub>2</sub>Se. However, this pioneering work shows the feasibility of inserting cations under light exposure when using *p*-type semiconductor photo-electrode.

During the search for new materials with which these difficulties can be avoided, Betz *et al.*<sup>75</sup> chose to further work on  $\text{TiO}_2(\text{B})$  for its reasonable stability in water, and its improved conditions for cation insertion and transport. Using this *n*-type semiconductor photo-electrode, Tributsch's group demonstrates the possibility of extracting cations under light exposure when using *n*-type semiconductor photo-electrode (**Figure 22**).

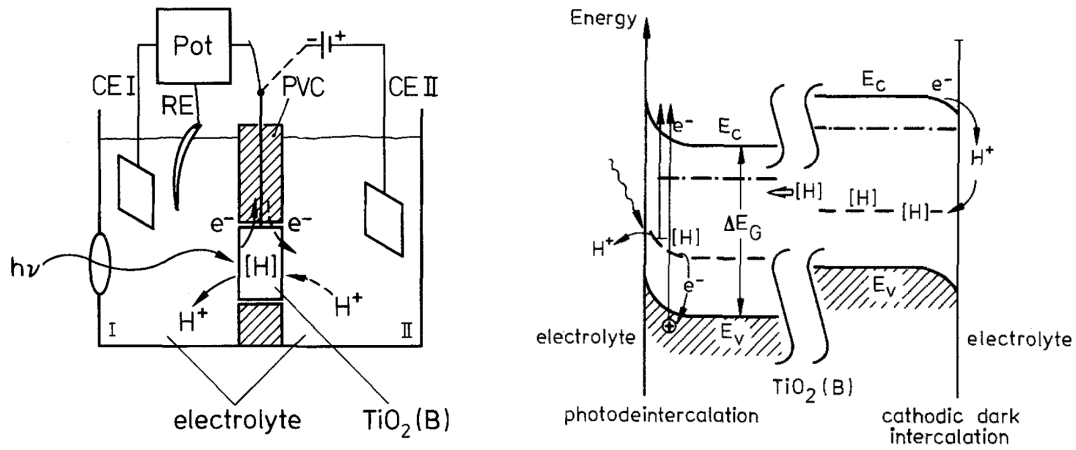


**Figure 22:** (left) Schematic representation of the two compartment electrochemical set-up (right) Energy band scheme of proton electrochemical insertion and photo-extraction.<sup>75</sup>

The authors propose a two-compartment photo-electrochemical cell, which integrates  $\text{TiO}_2(\text{B})$  as ceramic photo-electrochemical membrane. In this cell, the compartment (I) corresponds to the photo-electrochemical part of the system. The compartment (II) is a regular electrochemical cell, where it is possible to pre-insert protons into  $\text{TiO}_2(\text{B})$  by applying cathodic potential, thus preparing  $\text{TiO}_2(\text{B})$  to the photo-electrochemical experiment. The two compartments are separated by a PVC plate, and  $\text{TiO}_2(\text{B})$  sample is put onto a hole in the centre of the PVC plate. Isolation is made so that electronic and ionic currents as well as elements from compartment (II) pass from one cell to the other solely through the  $\text{TiO}_2(\text{B})$  electrode (**Figure 22**).

The experiments show a photo-current, which is explained by two reactions: proton photo-insertion and water photo-oxidation. The proposed mechanism to explain these reactions is described as followed: under illumination, photo-generated electrons pass in the conduction band and are collected by the external circuit. For their part, photo-generated holes migrate to the semiconductor surface and oxidized  $\text{Ti}^{3+}$  (from  $\text{H}_x\text{TiO}_2$ ) into  $\text{Ti}^{4+}$ , which lead to proton extraction. Nonetheless, holes could also oxidize water to give  $\text{O}_2$ .



Interestingly, colour changes are observed during proton insertion (the electrode goes from white to blue). This coloration could allow the reduced phase to absorb light in the visible range, thus increasing the light absorbance at cathodic potentials. These phenomenons of electrochemical insertion and photo-extraction are summarized in **Figure 22**.

## II.2 - The recent and very recent developments on bifunctional electrodes

To our knowledge, after Tributsch's works, this particular aspect of photo-electrochemistry has received very little research attention in the energy domain, compared to the global research interest on fuel-producing photo-electrochemical reactions (e.g.  $H_2$  from watersplitting<sup>77</sup> or more complex hydrocarbons from  $CO_2$  reduction<sup>78</sup>).

In 2013, F. Sauvage, C. Andriamiadamanana and C. Laberty-Robert<sup>79</sup> patented the idea of using a single transparent photo-rechargeable electrode that can simultaneously store energy and be recharged under illumination (**Figure 23**). The imagined device comprises a positive electrode based on  $TiO_2$  anatase nanoparticles, a negative electrode based on metallic lithium, and  $LiPF_6$  (1M) dissolved in a mixture of ethylene carbonate / dimethyl carbonate (1:1 vol) as electrolyte.

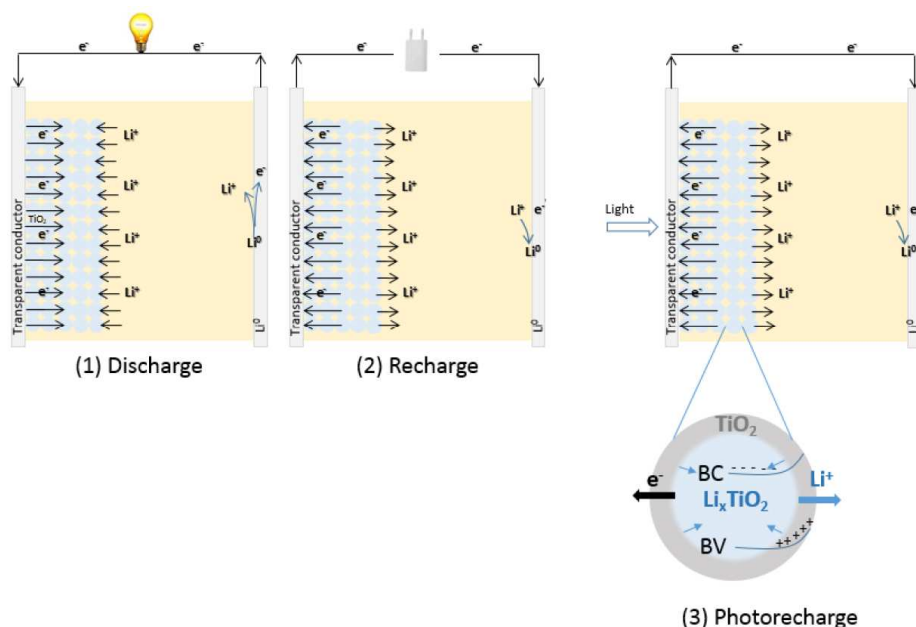


**Figure 23:** Operation scheme of a single transparent photo-rechargeable electrode that could simultaneously store energy and be recharged under illumination.<sup>79</sup>

The authors elaborate preliminary electrochemical experiments to test the impact of light on lithiated  $\text{TiO}_2$  electrodes. Observed photo-currents under illumination have been interpreted using Tributsch mechanistic hypothesis, where photo-generated holes oxidize  $\text{Ti}^{3+}$  (from  $\text{Li}_x\text{TiO}_2$ ) into  $\text{Ti}^{4+}$ , which lead to lithium-ion extraction. Nonetheless, the theoretical knowledge of photo-electrochemical behaviour of insertion materials is still limited. Amongst other issues, fate of generated photo-charges and electrolyte potential degradation still have to be addressed.

Very recently, some reports have been published on bifunctional electrodes, showing the new-born interest of this approach to address the issue of converting and storing energy in a single electrode.

In 2017, Paoella *et al.*<sup>80</sup> introduce a two-electrode system involving direct photo-oxidation of  $\text{LiFePO}_4$  nanocrystals by light irradiation in the presence of the N719 dye as hybrid photo-cathode and metal Li as anode (**Figure 24**).

Using regular lithium hexafluorophosphate in carbonate-based electrolyte, the photo-electrode is studied as positive electrode in a Li-ion battery half-cell configuration. According to the authors, dye-sensitization generates electron-hole pairs with the holes aiding the delithiation of lithium iron phosphate (LFP), thus photo-charging the cathode. On their side, photo-generated electrons might be involved in the formation of a solid electrolyte interface at the metal Li anode via oxygen reduction and peroxide formation in the electrolyte.

The overall two-electrode cell efficiency for energy conversion and storage is calculated to be in the range of 0.06-0.08 %. Such low current efficiency has been attributed by the authors to the large charge recombination losses at the LFP/dye/electrolyte interface, and still needs to be addressed. As expected for an LFP cathode material, the device offers high output voltage (3.4 V), but the voltage plateau decreases to 2.8 V after the 5<sup>th</sup> cycle.

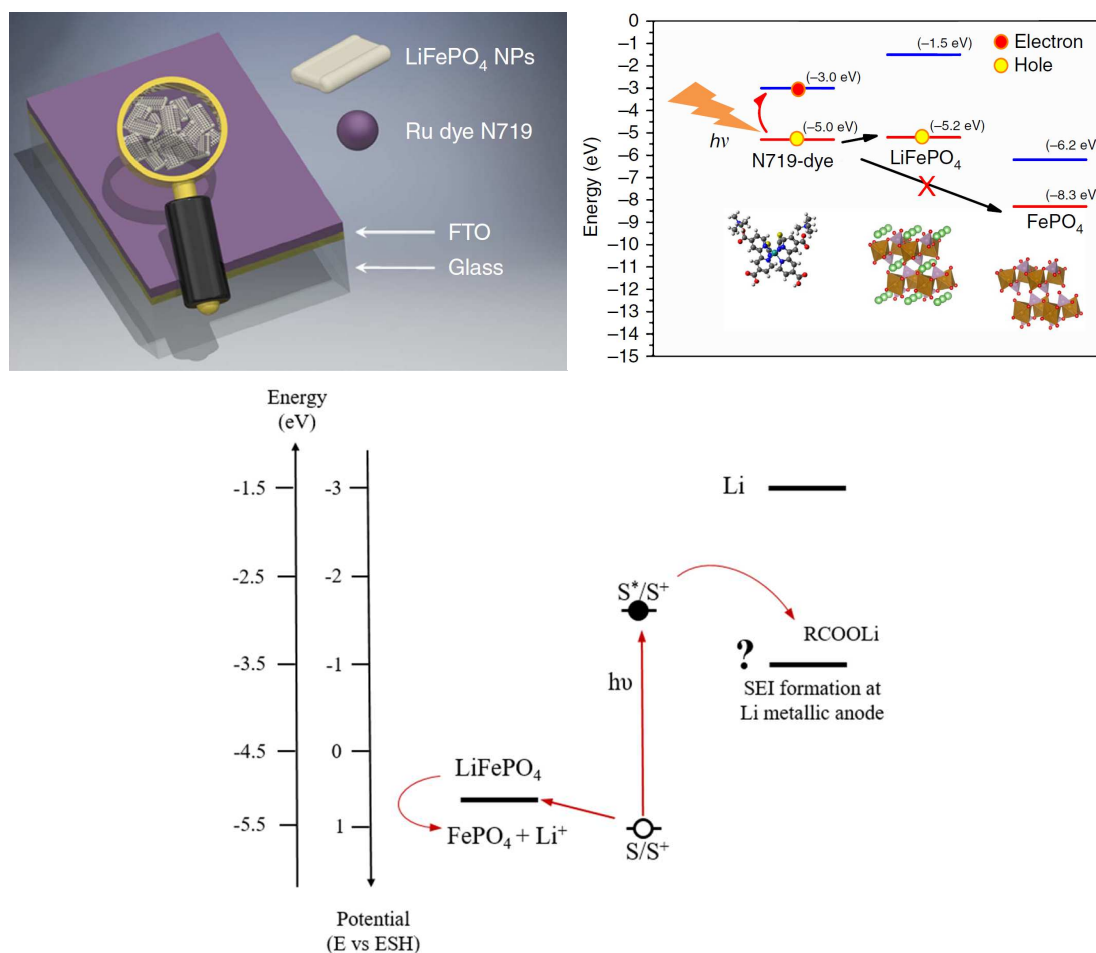


**Figure 24:** (left) Schematic representation of the FTO/LFP NPs/DYE electrode (right) energy band alignment of the photo-cathode components<sup>80</sup> (bottom) schematic representation of LFP photo-recharge (Li-ion photo-extraction) and hypothesis on the fate of the electron.

A few months later, Lou *et al.*<sup>71</sup> proposed a bifunctional material for solar-rechargeable Sodium-ion battery applications. Interestingly, the authors worked on a negative photo-electrode ( $\text{MoO}_3$ ) in association with a  $\text{MnO}_2$  positive electrode in an aqueous solvent (**Figure 25**).

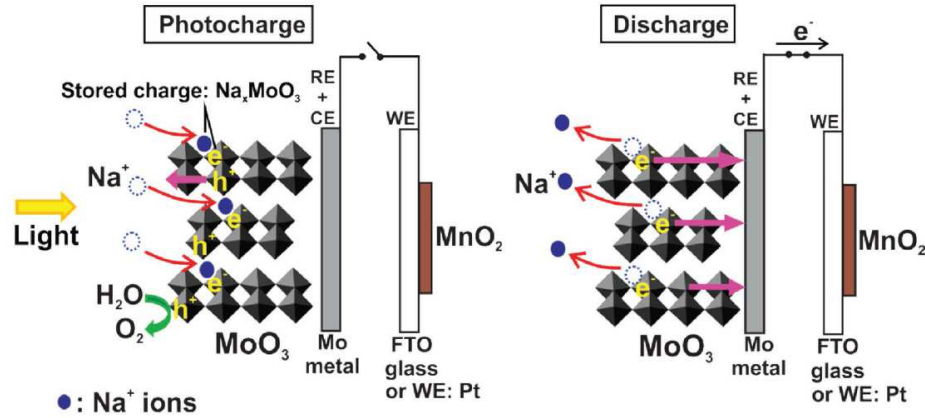
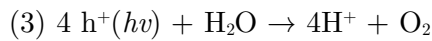
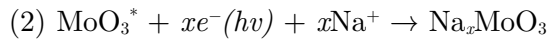


**Figure 25:** Photo-charging and discharging mechanisms in an aqueous Na-ion solar-intercalation battery, with  $\text{MoO}_3$  as negative photo-electrode and  $\text{MnO}_2$  as positive electrode.<sup>71</sup>

When illuminated under the sun,  $\text{MoO}_3$  undergoes photo-excitation and generated electron-hole pairs (**Equation (1)**). The photo-generated electrons are neutralized and stored in the lattice structure of the  $\text{MoO}_3$  through the intercalation of  $\text{Na}^+$  ions (**Equation (2)**). Photo-generated holes migrate to the electrode surface where they oxidize water to oxygen (**Equation (3)**). During the discharge process, electrons flow from  $\text{MoO}_3$  electrode to the  $\text{MnO}_2$  or Pt electrode simultaneously extracting  $\text{Na}^+$  ions (**Equation (4)**). During a discharge at 10  $\mu\text{A}$ , the potential gradually decreases from around 0.6 V to 0.4 V in 2h.



This mechanism is proposed by studying the structural evolution of  $\text{MoO}_3$  during light-induced intercalation processes and during de-intercalation process. The demonstrated feasibility of nanocrystalline  $\text{MoO}_3$  as photo-intercalating host material could here pave the way for aqueous Na-ion photo-batteries based on bifunctional electrodes.

Metal oxides are not the only materials that have been investigated as bifunctional electrode. In 2018, Podjsaki *et al.*<sup>81</sup> reported a 2D cyanamide ( $\text{NCN}^-$ )-functionalized

polyheptazine imide (NCN-PHI) as negative photo-electrode, which is described by the authors as a pseudo-capacitor able to store light-induced charge for hours in the form of trapped electrons (**Figure 26**). After light exposure, photo-generated electrons reduce the carbon nitride backbone. Charge compensation is then realized by adsorbing alkali metal ions within the NCN layers.

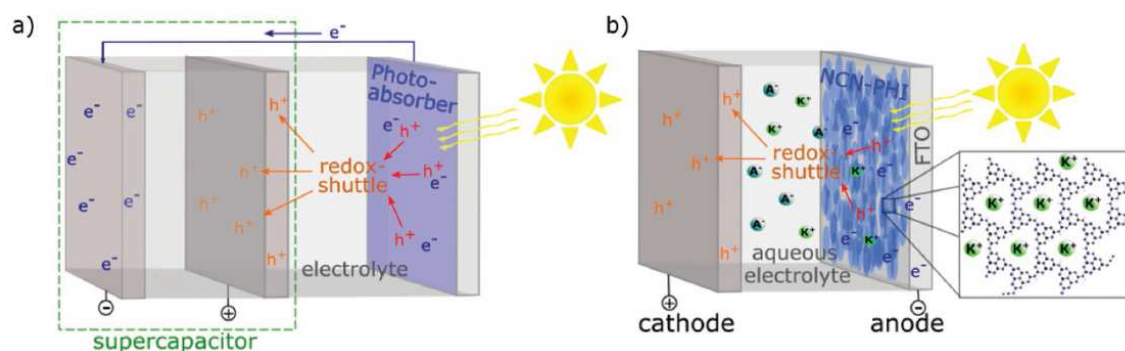


**Figure 26:** a) Concept of a traditional solar battery or solar photocapacitor. b) Proposed monolithic solar battery based on NCN-PHI. Photoabsorption and electron storage occurs within the same material.<sup>81</sup>

The photo-anode is here studied in a half cell configuration: in order to mimic a cathode that swiftly takes up the photo-generated holes, the authors extract them chemically by using aqueous 4-methylbenzyl alcohol as sacrificial reducing agent. Interestingly here, the material band gap of 2.76 eV is presented as a reasonable trade-off between visible light absorption and output cell voltage (0.7 V).

### III - Thesis objectives and challenges

The pioneering work of Tributsch showed the feasibility of photo-extracting protons out of bulk  $\text{TiO}_2(\text{B})$  material<sup>75</sup>. However, the observed photo-currents were very low, and until very recently,<sup>71,79–81</sup> the process was not further explored as a potential technology for converting and storing solar energy.

So far, the challenge of combining solar energy harvesting and energy storage has been addressed in hybridizing two distinct technologies. In this project, our goal is to develop a bifunctional Li-ion battery electrode able to simultaneously convert and store solar energy.

Since the selected electrode active material should be able to harvest light energy and store it as a Li-ion battery electrode, our strategy is to use transition metal oxide-based semiconductors. These semiconductors are primary candidates because their oxidation/reduction can be driven by light, and some of them offer crystallographic sites for cation accommodation ( $\text{Li}^+/\text{Na}^+$ ).<sup>74,82,83</sup> Amongst the various transition metal oxide-based semiconductors,<sup>84–86</sup>  $\text{TiO}_2$  has demonstrated to combine both good light absorption and the ability to reversibly host  $\text{Li}^+$ .<sup>87</sup> On one hand, in rechargeable Li-ion storage devices,  $\text{TiO}_2$  is a well-known candidate for the negative electrode<sup>88–90</sup> because it exhibits cycling stability at a high charging rate and reasonable capacity. In particular, among the numerous titania polymorphs, anatase  $\text{TiO}_2$  is known to be an efficient electroactive host for Li intercalation-deintercalation.<sup>88,91</sup>

On the other hand, for photo-electrochemical applications anatase  $\text{TiO}_2$  is also a very attractive electrode material due to its band gap of 3.2 eV, allowing 4% of the incident solar energy to be absorbed.<sup>92</sup> In addition, the electron mobility of  $\text{TiO}_2$  in a nanoparticle-based film is about  $0.01 \text{ cm}^2\text{V}^{-1}\text{s}^{-1}$ ,<sup>95</sup> which is high compared to that of other semi-conductors.

As the chosen photo-electrode will undergo  $\text{Li}^+$  insertion during the battery charge and discharge cycles, it is important to mention that making the choice of  $\text{TiO}_2$  will imply to deal with titania lithiated phases. In fact, studies have shown that during Li insertion, the bulk anatase  $\text{TiO}_2$  spontaneously phase separates into a Li-rich phase ( $\text{Li}_{\sim 0.5+y}(\text{TiO}_2)$ ) and Li-poor phase ( $\text{Li}_{\sim 0.01}(\text{TiO}_2)$ ) on a scale of several tens of nanometers in the material.<sup>96,97,90,91</sup> This two-phase equilibrium is maintained until all of the Li-poor phase is converted into the Li-rich phase up to the completion of Li insertion.<sup>88</sup> As the lithium rich phase ( $\text{Li}_{0.5+y}\text{TiO}_2$ ) is expected to absorb light in the visible range and to be a better electronic conductor,<sup>98,99</sup> we could therefore take

advantage of the  $\text{TiO}_2$  optoelectronic modifications during lithiation to increase the light harvesting and the electronic transport.

Taking into account all of these attributes, anatase  $\text{TiO}_2$  has been selected as a potential electrode material for photo-rechargeable Li-ion battery.

In this work, the full electrochemical device investigated will use  $\text{TiO}_2$  as a positive electrode, while metallic lithium or graphite carbon is used as the negative electrode. This unusual choice for the positive electrode has been made to study the  $\text{TiO}_2$  electrode in a configuration where the  $\text{Li}^+$  extraction at the  $\text{TiO}_2$  electrode corresponds to the charging reaction. In fact, as the feasibility of photo-extracting protons from  $\text{TiO}_2$  has been shown, we would like to study the  $\text{Li}^+$  photo-extraction reaction as the photo-charging reaction, which implies to consider  $\text{TiO}_2$  as the positive electrode ( $\text{Ti}^{3+}$  oxidation and simultaneous  $\text{Li}^+$  extraction during the charge step).

The resulting voltage in this system is thus lower than in usual Li-ion batteries. However, the high operating potential of  $\text{TiO}_2$  is relatively high compared to that of graphite. Therefore, it should allow output voltage around 1.75 V vs.  $\text{Li}^+/\text{Li}^0$ , which is still high compared to most SPEES systems limited around 0.7 V vs.  $\text{Li}^+/\text{Li}^0$  (see **Table 2** pages 39-40).

At this early stage of the bifunctional electrode technology, one of the main goal of this project is also to better understand the mechanisms behind the observed cations photo-insertion / photo-extraction. In fact, it is worth noting that the reaction sequence involving photo-generated excitons (**Figure 22**) has been proposed as hypothesis to account for the experimental observations. And even in the very recent developments on the subject,<sup>71,80</sup> the fate of photo-generated charges often remains a real challenge.

The second big challenge comes from the constant reorganization of the lithiated / non lithiated interface during the battery operation depending on the state of charge during  $\text{Li}^+$  insertion / extraction. In fact, when studying the light effect on a material (for example in watersplitting or photo-catalysis), the photo-electrode usually has a unique composition. Here on the contrary, photo-analysis will be performed on a composition changing electrode due to the lithiation / delithiation. Optoelectronic properties of the material will therefore probably depend on the state of charge of the electrode.

In the next chapter, we will present the fabrication methods and characterizations of the mesoporous  $\text{TiO}_2$  thin film electrodes, which will be used and studied in the following chapters as photo-rechargeable Li-ion battery electrode.

## Bibliography

1. Yu, M. *et al.* Solar-powered electrochemical energy storage: an alternative to solar fuels. *J. Mater. Chem. A* **4**, 2766–2782 (2016).
2. Schmidt, D., Hager, M. D. & Schubert, U. S. Photo-Rechargeable Electric Energy Storage Systems. *Adv. Energy Mater.* **6**, 1500369 (2016).
3. Zhu, Y. G. *et al.* Proton enhanced dynamic battery chemistry for aprotic lithium–oxygen batteries. *Nat. Commun.* **8**, 14308 (2017).
4. Hodes, G., Manassen, D. & Cahen, D. G. Hodes, J. Manassen and D. Cahen, Nature, 1976, 261, 403–404. *Nature* **261**, 403–404 (1976).
5. Gaudiana, R. Third-Generation Photovoltaic Technology – The Potential for Low-Cost Solar Energy Conversion. *J. Phys. Chem. Lett.* **1**, 1288–1289 (2010).
6. Olivares-Amaya, R. *et al.* Accelerated computational discovery of high-performance materials for organic photovoltaics by means of cheminformatics. *Energy Environ. Sci.* **4**, 4849 (2011).
7. Choi, J. W. & Aurbach, D. Promise and reality of post-lithium-ion batteries with high energy densities. *Nat. Rev. Mater.* **1**, 16013 (2016).
8. Kan, S. Y., Verwaal, M. & Broekhuizen, H. The use of battery–capacitor combinations in photovoltaic powered products. *J. Power Sources* **162**, 971–974 (2006).
9. Gibson, T. L. & Kelly, N. A. Solar photovoltaic charging of lithium-ion batteries. *J. Power Sources* **195**, 3928–3932 (2010).
10. Xu, J., Chen, Y. & Dai, L. Efficiently photo-charging lithium-ion battery by perovskite solar cell. *Nat. Commun.* **6**, (2015).
11. Gurung, A. *et al.* Highly Efficient Perovskite Solar Cell Photocharging of Lithium Ion Battery Using DC-DC Booster. *Adv. Energy Mater.* **7**, 1602105 (2017).
12. Li, Q., Liu, Y., Guo, S. & Zhou, H. Solar energy storage in the rechargeable batteries. *Nano Today* **16**, 46–60 (2017).
13. Luo, B., Ye, D. & Wang, L. Recent Progress on Integrated Energy Conversion and Storage Systems. *Adv. Sci.* **4**, (2017).
14. Yum, J.-H., Chen, P., Grätzel, M. & Nazeeruddin, M. K. Recent Developments in Solid-State Dye-Sensitized Solar Cells. *ChemSusChem* **1**, 699–707 (2008).
15. Bomben, P. G., Borau-Garcia, J. & Berlinguette, C. P. Three is not a crowd: efficient sensitization of TiO<sub>2</sub> by a bulky trichromic trisheteroleptic cycloruthenated dye. *Chem. Commun.* **48**, 5599 (2012).
16. Grätzel, M. Dye-sensitized solar cells. *J. Photochem. Photobiol. C Photochem. Rev.* **4**, 145–153 (2003).
17. Grätzel, M. Photoelectrochemical cells. *nature* **414**, 338 (2001).



18. Miyasaka, T. & Murakami, T. N. The photocapacitor: An efficient self-charging capacitor for direct storage of solar energy. *Appl. Phys. Lett.* **85**, 3932–3934 (2004).
19. Zhang, Y. *et al.* Progress of electrochemical capacitor electrode materials: A review. *Int. J. Hydrog. Energy* **34**, 4889–4899 (2009).
20. Gu, W. & Yushin, G. Review of nanostructured carbon materials for electrochemical capacitor applications: advantages and limitations of activated carbon, carbide-derived carbon, zeolite-templated carbon, carbon aerogels, carbon nanotubes, onion-like carbon, and graphene: Nanostructured carbon materials for electrochemical capacitor applications. *Wiley Interdiscip. Rev. Energy Environ.* **3**, 424–473 (2014).
21. Murakami, T. N., Kawashima, N. & Miyasaka, T. A high-voltage dye-sensitized photocapacitor of a three-electrode system. *Chem. Commun.* 3346 (2005).
22. Yang, Z. *et al.* An integrated device for both photoelectric conversion and energy storage based on free-standing and aligned carbon nanotube film. *J Mater Chem A* **1**, 954–958 (2013).
23. Jost, K., Dion, G. & Gogotsi, Y. Textile energy storage in perspective. *J. Mater. Chem. A* **2**, 10776 (2014).
24. Chen, T. *et al.* An Integrated ‘Energy Wire’ for both Photoelectric Conversion and Energy Storage. *Angew. Chem. Int. Ed.* **51**, 11977–11980 (2012).
25. Chen, X. *et al.* A novel ‘energy fiber’ by coaxially integrating dye-sensitized solar cell and electrochemical capacitor. *J Mater Chem A* **2**, 1897–1902 (2014).
26. Yang, Z. *et al.* Self-Powered Energy Fiber: Energy Conversion in the Sheath and Storage in the Core. *Adv. Mater.* **26**, 7038–7042 (2014).
27. Hauch, A., Georg, A., Krašovec, U. O. & Orel, B. Photovoltaically Self-Charging Battery. *J. Electrochem. Soc.* **149**, A1208 (2002).
28. Hauch, A., Georg, A., Baumgärtner, S., Krašovec, U. O. & Orel, B. New photoelectrochromic device. *Electrochimica Acta* **46**, 2131–2136 (2001).
29. Cannavale, A. *et al.* Highly efficient smart photovoltachromic devices with tailored electrolyte composition. *Energy Environ. Sci.* **4**, 2567 (2011).
30. Saito, Y., Uchida, S., Kubo, T. & Segawa, H. Surface-oxidized tungsten for energy-storable dye-sensitized solar cells. *Thin Solid Films* **518**, 3033–3036 (2010).
31. Yan, N. F., Li, G. R., Pan, G. L. & Gao, X. P. TiN nanotube arrays as electrocatalytic electrode for solar storable rechargeable battery. *J. Electrochem. Soc.* **159**, A1770–A1774 (2012).
32. Guo, W., Xue, X., Wang, S., Lin, C. & Wang, Z. L. An Integrated Power Pack of Dye-Sensitized Solar Cell and Li Battery Based on Double-Sided TiO<sub>2</sub> Nanotube Arrays. *Nano Lett.* **12**, 2520–2523 (2012).

33. Mor, G. K., Shankar, K., Paulose, M., Varghese, O. K. & Grimes, C. A. Use of Highly-Ordered TiO<sub>2</sub> Nanotube Arrays in Dye-Sensitized Solar Cells. *Nano Lett.* **6**, 215–218 (2006).
34. Sauvage, F. *et al.* Hierarchical TiO<sub>2</sub> Photoanode for Dye-Sensitized Solar Cells. *Nano Lett.* **10**, 2562–2567 (2010).
35. Li, Q., Li, N., Ishida, M. & Zhou, H. Saving electric energy by integrating a photoelectrode into a Li-ion battery. *J. Mater. Chem. A* **3**, 20903–20907 (2015).
36. Yu, M., Ren, X., Ma, L. & Wu, Y. Integrating a redox-coupled dye-sensitized photoelectrode into a lithium–oxygen battery for photoassisted charging. *Nat. Commun.* **5**, 5111 (2014).
37. Liu, Y. *et al.* Reducing the charging voltage of a Li–O<sub>2</sub> battery to 1.9 V by incorporating a photocatalyst. *Energy Environ. Sci.* **8**, 2664–2667 (2015).
38. Liu, Y. *et al.* Lowering the charge voltage of Li–O<sub>2</sub> batteries via an unmediated photoelectrochemical oxidation approach. *J. Mater. Chem. A* **4**, 12411–12415 (2016).
39. Liao, K. *et al.* Stabilization of polysulfides via lithium bonds for Li–S batteries. *J. Mater. Chem. A* **4**, 5406–5409 (2016).
40. Li, N., Wang, Y., Tang, D. & Zhou, H. Integrating a Photocatalyst into a Hybrid Lithium-Sulfur Battery for Direct Storage of Solar Energy. *Angew. Chem. Int. Ed.* **54**, 9271–9274 (2015).
41. Yu, M. *et al.* Aqueous Lithium–Iodine Solar Flow Battery for the Simultaneous Conversion and Storage of Solar Energy. *J. Am. Chem. Soc.* **137**, 8332–8335 (2015).
42. Nikiforidis, G., Tajima, K. & Byon, H. R. High Energy Efficiency and Stability for Photoassisted Aqueous Lithium–Iodine Redox Batteries. *ACS Energy Lett.* **1**, 806–813 (2016).
43. Chun, S.-E. *et al.* Design of aqueous redox-enhanced electrochemical capacitors with high specific energies and slow self-discharge. *Nat. Commun.* **6**, (2015).
44. Liu, D., Liu, F. & Liu, J. Effect of vanadium redox species on photoelectrochemical behavior of TiO<sub>2</sub> and TiO<sub>2</sub>/WO<sub>3</sub> photo-electrodes. *J. Power Sources* **213**, 78–82 (2012).
45. Wei, Z., Liu, D., Hsu, C. & Liu, F. All-vanadium redox photoelectrochemical cell: An approach to store solar energy. *Electrochem. Commun.* **45**, 79–82 (2014).
46. Liu, D., Wei, Z., Hsu, C., Shen, Y. & Liu, F. Efficient Solar Energy Storage Using A TiO<sub>2</sub>/WO<sub>3</sub> Tandem Photoelectrode in An All-vanadium Photoelectrochemical Cell. *Electrochimica Acta* **136**, 435–441 (2014).
47. Liu, D. *et al.* Ultra-long electron lifetime induced efficient solar energy storage by an all-vanadium photoelectrochemical storage cell using methanesulfonic acid. *J. Mater. Chem. A* **3**, 20322–20329 (2015).

48. Liu, D. *et al.* Reversible Electron Storage in an All-Vanadium Photoelectrochemical Storage Cell: Synergy between Vanadium Redox and Hybrid Photocatalyst. *ACS Catal.* **5**, 2632–2639 (2015).
49. Yan, N. F., Li, G. R. & Gao, X. P. Solar rechargeable redox flow battery based on  $\text{Li}_2\text{WO}_4/\text{LiI}$  couples in dual-phase electrolytes. *J. Mater. Chem. A* **1**, 7012 (2013).
50. Liu, P. *et al.* A Solar Rechargeable Flow Battery Based on Photoregeneration of Two Soluble Redox Couples. *ChemSusChem* **6**, 802–806 (2013).
51. Lei, B., Li, G.-R., Chen, P. & Gao, X.-P. A solar rechargeable battery based on hydrogen storage mechanism in dual-phase electrolyte. *Nano Energy* **38**, 257–262 (2017).
52. Wedege, K., Azevedo, J., Khataee, A., Bentien, A. & Mendes, A. Direct Solar Charging of an Organic-Inorganic, Stable, and Aqueous Alkaline Redox Flow Battery with a Hematite Photoanode. *Angew. Chem. Int. Ed.* **55**, 7142–7147 (2016).
53. Liao, S. *et al.* Integrating a dual-silicon photoelectrochemical cell into a redox flow battery for unassisted photocharging. *Nat. Commun.* **7**, 11474 (2016).
54. Li, W. *et al.* Integrated Photoelectrochemical Solar Energy Conversion and Organic Redox Flow Battery Devices. *Angew. Chem. Int. Ed.* **55**, 13104–13108 (2016).
55. Li, Q., Li, N., Liu, Y., Wang, Y. & Zhou, H. High-Safety and Low-Cost Photoassisted Chargeable Aqueous Sodium-Ion Batteries with 90% Input Electric Energy Savings. *Adv. Energy Mater.* **6**, 1600632 (2016).
56. Mahmoudzadeh, M. A. *et al.* A high energy density solar rechargeable redox battery. *J. Mater. Chem. A* **4**, 3446–3452 (2016).
57. Weber, A. Z. *et al.* Redox flow batteries: a review. *J. Appl. Electrochem.* **41**, 1137–1164 (2011).
58. Chen, H.-W. *et al.* Plastic dye-sensitized photo-supercapacitor using electrophoretic deposition and compression methods. *J. Power Sources* **195**, 6225–6231 (2010).
59. Liu, P., Yang, H. X., Ai, X. P., Li, G. R. & Gao, X. P. A solar rechargeable battery based on polymeric charge storage electrodes. *Electrochem. Commun.* **16**, 69–72 (2012).
60. Kapilashrami, M., Zhang, Y., Liu, Y.-S., Hagfeldt, A. & Guo, J. Probing the Optical Property and Electronic Structure of  $\text{TiO}_2$  Nanomaterials for Renewable Energy Applications. *Chem. Rev.* **114**, 9662–9707 (2014).
61. Manthiram, A., Fu, Y., Chung, S.-H., Zu, C. & Su, Y.-S. Rechargeable Lithium–Sulfur Batteries. *Chem. Rev.* **114**, 11751–11787 (2014).
62. Manthiram, A., Yu, X. & Wang, S. Lithium battery chemistries enabled by solid-state electrolytes. *Nat. Rev. Mater.* **2**, 16103 (2017).
63. Bruce, P. G., Freunberger, S. A., Hardwick, L. J. & Tarascon, J.-M.  $\text{Li-O}_2$  and  $\text{Li-S}$  batteries with high energy storage. *Nat. Mater.* **11**, 19–29 (2012).

64. Shao, Y. *et al.* Making Li-Air Batteries Rechargeable: Material Challenges. *Adv. Funct. Mater.* **23**, 987–1004 (2013).
65. Asghar, M. I. *et al.* Review of stability for advanced dye solar cells. *Energy Environ. Sci.* **3**, 418 (2010).
66. Mozaffari, S., Nateghi, M. R. & Zarandi, M. B. An overview of the Challenges in the commercialization of dye sensitized solar cells. *Renew. Sustain. Energy Rev.* **71**, 675–686 (2017).
67. Hinsch, A. *et al.* Long-term stability of dye-sensitised solar cells. *Prog. Photovolt. Res. Appl.* **9**, 425–438.
68. Sommeling, P. M., Späth, M., Smit, H. J. P., Bakker, N. J. & Kroon, J. M. Long-term stability testing of dye-sensitized solar cells. *J. Photochem. Photobiol. Chem.* **164**, 137–144 (2004).
69. Macht, B. *et al.* Patterns of efficiency and degradation in dye sensitization solar cells measured with imaging techniques. *Sol. Energy Mater. Sol. Cells* **73**, 163–173 (2002).
70. Figgemeier, E. & Hagfeldt, A. Are dye-sensitized nano-structured solar cells stable? An overview of device testing and component analyses. *International Journal of Photoenergy* (2004).
71. Lou, S. N. *et al.* An Operando Mechanistic Evaluation of a Solar-Rechargeable Sodium-Ion Intercalation Battery. *Adv. Energy Mater.* **7**, 1700545 (2017).
72. Tributsch, H. Photo-intercalation: Possible application in solar energy devices. *Appl. Phys.* **23**, 61–71 (1980).
73. Tributsch, H. Photoelectrochemical energy conversion involving transition metal d-states and intercalation of layer compounds. in *Solar Energy Materials* 127–175 (Springer, 1982).
74. Tributsch, H. Photo-electrochemical studies on intercalation and semiconducting intercalation compounds. *Solid State Ion.* **9**, 41–57 (1983).
75. Betz, G., Tributsch, H. & Marchand, R. Hydrogen insertion (intercalation) and light induced proton exchange at TiO<sub>2</sub> (B)-electrodes. *J. Appl. Electrochem.* **14**, 315–322 (1984).
76. Tributsch, H. Interfacial processes involving strong electronic interactions in solar energy conversion and storage. *J. Photochem.* **29**, 89–113 (1985).
77. Walter, M. G. *et al.* Solar Water Splitting Cells. *Chem. Rev.* **110**, 6446–6473 (2010).
78. Kumar, B. *et al.* Photochemical and Photoelectrochemical Reduction of CO<sub>2</sub>. *Annu. Rev. Phys. Chem.* **63**, 541–569 (2012).
79. Sauvage, F., Andriamiadamanana, C. & Laberty-Robert, C. Photorechargeable battery: turning light energy into chemical energy and then electric energy, French patent. (FR1361775).

80. Paolella, A. *et al.* Light-assisted delithiation of lithium iron phosphate nanocrystals towards photo-rechargeable lithium ion batteries. *Nat. Commun.* **8**, 14643 (2017).
81. Podjaski, F., Kröger, J. & Lotsch, B. V. Toward an Aqueous Solar Battery: Direct Electrochemical Storage of Solar Energy in Carbon Nitrides. *Adv. Mater.* 1705477 (2018).
82. Judeinstein, P., Chemseddine, A. & Sanchez, C. Propriétés photoélectrochimiques des gels d'oxyde de tungstène. *J. Chim. Phys.* **89**, 1469–1476 (1992).
83. Zhai, T. *et al.* Centimeter-Long  $V_2O_5$  Nanowires: From Synthesis to Field-Emission, Electrochemical, Electrical Transport, and Photoconductive Properties. *Adv. Mater.* **22**, 2547–2552 (2010).
84. Chen, S. & Wang, L.-W. Thermodynamic Oxidation and Reduction Potentials of Photocatalytic Semiconductors in Aqueous Solution. *Chem. Mater.* **24**, 3659–3666 (2012).
85. Li, J. & Wu, N. Semiconductor-based photocatalysts and photoelectrochemical cells for solar fuel generation: a review. *Catal. Sci. Technol.* **5**, 1360–1384 (2015).
86. Zhao, J., Wang, X., Xu, Z. & Loo, J. S. C. Hybrid catalysts for photoelectrochemical reduction of carbon dioxide: a prospective review on semiconductor/metal complex co-catalyst systems. *J. Mater. Chem. A* **2**, 15228 (2014).
87. van de Krol, R., Goossens, A. & Schoonman, J. Spatial Extent of Lithium Intercalation in Anatase  $TiO_2$ . *J. Phys. Chem. B* **103**, 7151–7159 (1999).
88. Reddy, M. V., Subba Rao, G. V. & Chowdari, B. V. R. Metal Oxides and Oxysalts as Anode Materials for Li Ion Batteries. *Chem. Rev.* **113**, 5364–5457 (2013).
89. Kim, C., Buonsanti, R., Yaylian, R., Milliron, D. J. & Cabana, J. Carbon-Free  $TiO_2$  Battery Electrodes Enabled by Morphological Control at the Nanoscale. *Adv. Energy Mater.* **3**, 1286–1291 (2013).
90. Wagemaker, M., Borghols, W. J. H. & Mulder, F. M. Large Impact of Particle Size on Insertion Reactions. A Case for Anatase  $Li_xTiO_2$ . *J. Am. Chem. Soc.* **129**, 4323–4327 (2007).
91. Yang, Z. *et al.* Nanostructures and lithium electrochemical reactivity of lithium titanites and titanium oxides: A review. *J. Power Sources* **192**, 588–598 (2009).
92. O'Regan, B. & Grätzel, M. A low-cost, high-efficiency solar cell based on dye-sensitized colloidal  $TiO_2$  films. *Nature* **353**, 737–740 (1991).
93. Fujishima, A. & Honda, K. Electrochemical Photolysis of Water at a Semiconductor Electrode. *Nature* **238**, 37–38 (1972).
94. Krol, R. van de, Liang, Y. & Schoonman, J. Solar hydrogen production with nanostructured metal oxides. *J. Mater. Chem.* **18**, 2311–2320 (2008).

95. Hendry, E., Koeberg, M., O'Regan, B. & Bonn, M. Local Field Effects on Electron Transport in Nanostructured TiO<sub>2</sub> Revealed by Terahertz Spectroscopy. *Nano Lett.* **6**, 755–759 (2006).
96. Lunell, S., Stashans, A., Ojamäe, L., Lindström, H. & Hagfeldt, A. Li and Na Diffusion in TiO<sub>2</sub> from Quantum Chemical Theory versus Electrochemical Experiment. *J. Am. Chem. Soc.* **119**, 7374–7380 (1997).
97. Wagemaker, M., Kentgens, A. P. M. & Mulder, F. M. Equilibrium lithium transport between nanocrystalline phases in intercalated TiO<sub>2</sub> anatase. *Nature* **418**, 397–399 (2002).
98. Dinh, N. N., Oanh, N. T. T., Long, P. D., Bernard, M. C. & Hugot-Le Goff, A. Electrochromic properties of TiO<sub>2</sub> anatase thin films prepared by a dipping sol–gel method. *Thin Solid Films* **423**, 70–76 (2003).
99. Özer, N. Reproducibility of the coloration processes in TiO<sub>2</sub> films. *Thin Solid Films* **214**, 17–24 (1992).
100. He, T. & Yao, J.-N. Photochromism in transition-metal oxides. *Res. Chem. Intermed.* **30**, (2004).



## **CHAPTER 2**

### **Mesoporous TiO<sub>2</sub> thin film electrodes: fabrication & characterizations**





## TABLE of CONTENTS

I – Introduction .....	69
II – Presentation of the electrodes .....	71
II.1 – Fabrication methods.....	71
II.2 – Control of thin films architecture .....	74
II.2.1 – Thin film thickness .....	74
II.2.2 – Inorganic walls and porous networks .....	76
III – Thin films structural characterizations .....	78
III.1 – Spectroscopic Ellipsometry.....	78
III.1.1 – Adaptation for porous thin films .....	78
III.1.2 – Environmental Ellipsometric Porosimetry .....	79
III.2 – Glancing Angle X-Ray Diffraction .....	85
IV – Reconstruction of TiO <sub>2</sub> electrode energetic diagram .....	92
IV.1 – Band gap determination by UV-Visible Spectroscopy .....	92
IV.2 – Flat-band potential estimated by Mott-Schottky experiment.....	95
V – Conclusion .....	97
Bibliography .....	99



## I – Introduction

Li-ion battery electrodes are usually synthesized in mixing electrode active material with carbon to enhance the electrode electronic conductivity. A binder is usually added to hold the active material within the electrode together and maintain a good connection between the electrode and the contacts. The resulting electrode presents various interfaces, together with uncontrolled porosity and interconnections between the particles.

By contrast to a conventional battery electrode, we have chosen to work with a model electrode, whose composition is as simple as possible. In fact, the aim is to study the photo-electrochemical behavior of such an electrode and previous studies<sup>1</sup> generally add to their electrode composition carbon for the conductivity and dye for the photo-absorbance, which could complicate the analysis of the photo-electrochemical behavior of the electrode. In this study, the TiO<sub>2</sub> electrode is carbon- and dye-free. As the lithium rich phase (Li<sub>0.5+y</sub>TiO<sub>2</sub>) is expected to absorb light in the visible range and to be a better electronic conductor,<sup>2,3</sup> we could therefore take advantage of the TiO<sub>2</sub> optoelectronic modifications during lithiation to increase the light harvesting and the electronic transport without additional carbon or dye.

The recombination, diffusion, or reaction processes of the photo-generated charges could be particularly influenced by parameters such as TiO<sub>2</sub> crystallites size, particles connectivity, or by their distance to the current collector. Therefore, the electrode architecture, on which such parameters depend, should also be as well-defined as possible. For this reason, we have chosen to work with mesoporous thin film electrodes using sol-gel coupled dip coating process combined with the “evaporation induced self-assembly” (EISA) approach, which allows to easily tune the architectural properties of the electrode.

In section II, the fabrication methods are presented. The conditions of the multilayer dip-coating process and the various films obtained using different co-polymers as templating agents or different titania concentration are described.

In section III, structural characterization of the architecture-controlled TiO<sub>2</sub> electrode is then addressed using techniques adapted for mesoporous thin film characterization, as environmental ellipsometric porosimetry (EEP) and glancing angle X-Ray diffraction (G-XRD). Thin film thickness, porosity, specific surface area, crystallite size and their homogeneity in the whole film are investigated.

In section IV, energy diagram of TiO<sub>2</sub> electrode is determined, using UV-Visible spectroscopy (band-gap determination) and Mott Schottky experiment (flat-band

potential). Knowledge of the energy diagram could indeed constitute an important starting point to consider reactivity of the photo-generated charges at the TiO<sub>2</sub> electrode / electrolyte interface.

## II – Presentation of the electrodes

Mesoporous TiO<sub>2</sub> thin film electrodes are obtained by combining sol-gel chemistry with the dip-coating process and the “evaporation induced self-assembly” (EISA) approach. Sol-gel solutions are solutions made of metal salts dissolved in organic solvent. Through a careful control of pH, aging time, water content, solvent and concentration in the sol-gel solution, hydrolysis and condensation reactions occur to form a starting sol that can be deposited by dip coating, but also by spin coating, drop casting or doctor blade.<sup>4-8</sup> Block co-polymers and organic additives such as polybutadiene-b-ethylene oxide (PB-PEO) can be added to the solution to form and tune a nano/mesoporous microstructure. Upon final heat treatment, metal oxide is calcined and carbon elements of the block co-polymer are decomposed, leaving physical vacancies and thus forming a porous microstructure. Its decomposition should occur after the crystallization of the inorganic network occurs otherwise, the porous network could collapse. The size of the pore and the inorganic wall can be tuned changing various parameters including the nature of the block-co-polymer (the contrast between hydrophilic/hydrophobic blocks and their respective size), the nature of the solvent and the inorganic precursor concentration.<sup>9</sup>

### II.1 – Fabrication methods

In our case, a solution containing the TiCl<sub>4</sub> precursor is first prepared by mixing TiCl<sub>4</sub> and ethanol (EtOH) with a molar ratio 1(TiCl<sub>4</sub>):5(EtOH), and will be referred as “precursor solution”. When stored at 4°C, this precursor solution can be used for several months. Then, 100 mg of Poly(1,4-butadiene)-b-poly(ethylene oxide) (PB-b-PEO:P4515-BdEO, M.W. (PB)=11800 g.mol<sup>-1</sup> and M.W. (PEO)=13500 g.mol<sup>-1</sup>) is dissolved in a mixture of 5.0 g EtOH and 0.4 g H<sub>2</sub>O. Referred in this thesis as “PB-PEO” polymers, P4515-BdEO polymers was purchased from Polymer Source and was used without any further purification. Polydispersity of the chosen polymers should be small enough (typically 1.15) to avoid dissolution issues and obtain homogenous solutions. A heat treatment of 70°C for 2 hours is necessary to complete the dissolution. After cooling at room temperature, the inorganic precursor solution containing TiCl<sub>4</sub> precursor is added dropwise into the solution of PB-PEO. The concentration of TiCl<sub>4</sub> in the final solution is typically around 1-2 mol.L<sup>-1</sup> in titanium (0.8-1.6 g of precursor solution). The as-prepared solution is aged for 1 night under stirring to generate hydrolyzed, slightly condensed hybrid species. This step could be necessary to pre-organize the titanium clusters around the block copolymers in the starting sol (inorganic precursors are coordinated by the PEO functions of the polymer polar chains). In such solution using voluminous PB-PEO polymers, concentration in

surfactants has already reached the equivalent of a critical micellar concentration, and hybrid micelles are pre-formed in solution.

Deposition of the sol-gel is done by dip-coating because it is a relatively simple, reproducible and low energy synthesis. As the mesoporous thin films will be dedicated to photo-electrochemical applications, fluorine-doped tin oxide (FTO) - coated substrates are used. These conductive and transparent substrates were purchased from SOLEMS (YSUB/ASASHI 120/1: 10 x 30 mm / resistivity: 80  $\Omega\cdot\text{cm}^{-2}$ , thickness of the FTO layer: 80 nm). The substrates are first cleaned with EtOH and acetone, then dipped into a fully filled small tank containing around 2 mL of the sol-gel solution in a dry atmosphere (<5% relative humidity) at ambient temperature. A withdrawal speed of 2.5 mm.s<sup>-1</sup> is applied to deposit the hybrid solution on top of the FTO substrate. Upon withdrawal, the organic volatile solution evaporates, triggering the self-assembly process: micelles are stacked and evaporation of HCl (and resulting pH increase) induces the full condensation of the inorganic network. The dry atmosphere favours the fast evaporation of HCl, EtOH and H<sub>2</sub>O.

The hybrid, homogenous film is then placed for 1h in a furnace at 500°C in air (static atmosphere) to (i) induce crystallization of the anatase and (ii) decompose the block-copolymer. The different steps of the formation of the films are summarized in **Figure 1**.

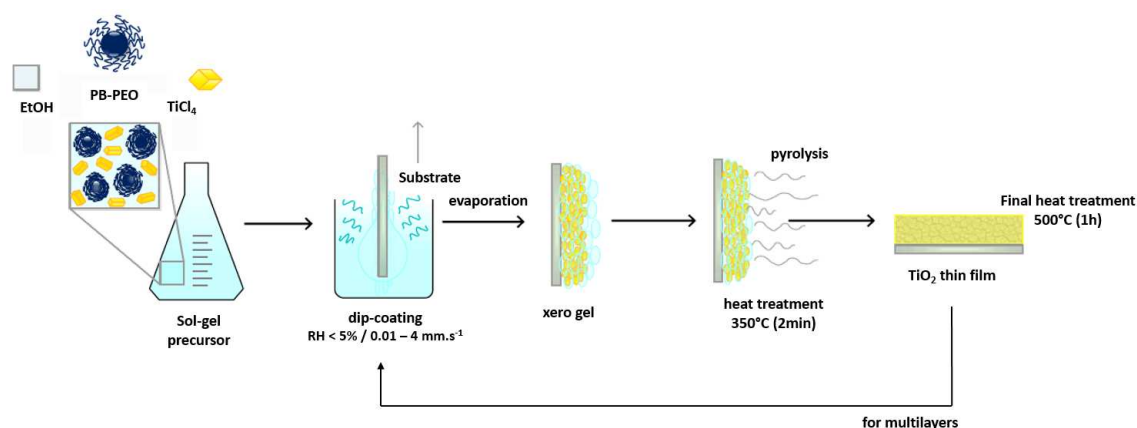


**Figure 1:** Sol-gel dip coating thin film fabrication process. Adapted from Hilliard.<sup>9</sup>

After final heat treatment, mesoporous thin films can be observed by FEG-SEM in order to image the porous network (planar and cross sections observations) and estimate the film thickness (cross sections observations). **Figure 2** shows a typical TiO<sub>2</sub> mesoporous thin film obtained at 1 mol.L<sup>-1</sup> (1M) in titanium precursors. The three-dimensionally interconnected porosity develops a well-defined electrode-electrolyte interface. Anatase TiO<sub>2</sub> nanocrystals (detailed XRD characterization in section III.2)

constitute a continuous inorganic backbone coupled with a homogenous, crack-free porous network (characterized by environmental ellipsometric porosimetry in section III.1) according to SEM-FEG images.

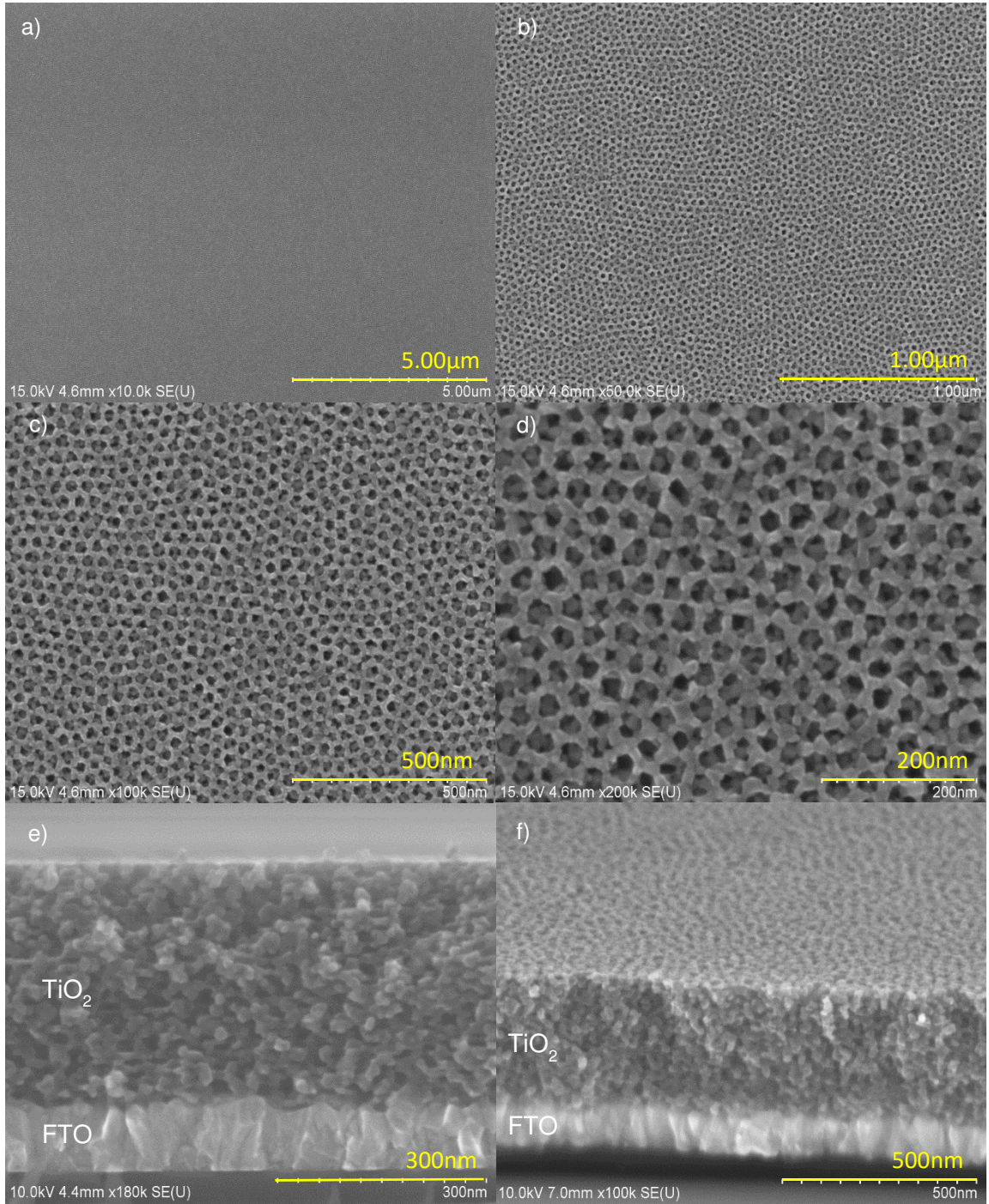


**Figure 2:** FEG-SEM pictures of the same  $\text{TiO}_2$  thin film ( $\text{TiCl}_4$  at 1M, 5 layers, calcined for 1h at  $500^\circ\text{C}$ ) with planar observations for 4 different magnifications (a)-(d), cross section (e) and tilted cross section (f) observations.



## II.2 – Control of thin films architecture

The recombination, diffusion, or reaction processes of the photo-generated charges could be particularly influenced by parameters such as TiO<sub>2</sub> crystallites size, particles connectivity, or by their distance to the current collector. Therefore, the electrode architecture on which such parameters depend, could be important to control. In this section, we present how thin film thickness and porous network can be controlled by combining sol-gel chemistry with the dip-coating process and the “evaporation induced self-assembly” (EISA) approach.

### II.2.1 – Thin film thickness

The film thickness depends on multiple controllable parameters: withdrawal speed, temperature, humidity, and inorganic precursor concentration in the starting sol-gel solution.

Thickness of the thin film can also be increased by consecutively dipping the substrate in the solution. Between each film, an intermediate heat-treatment is applied to favor layer adhesion between each deposition and avoid the last dipped film to re-dissolve in the sol-gel solution.

Recently, it has been demonstrated in the laboratory that the tank configuration and filling level can have a strong impact on the film thickness and optical quality when coating large substrates. These geometrical parameters influence the solvent relative pressure gradients (coming from solvent evaporation).<sup>10</sup> Consequently, the same tank has been used for all the dips. As the solution filling level decreases during the dip coating process, the solution should be theoretically refilled after each dip to guarantee an ideal reproducibility between each dipped layer. In practice, as the FTO substrate is quite small (dipped part: around 2 cm x 1 cm), the filling level is not drastically modified after each dip, contrary to large substrates. Every 5 dips, fresh sol-gel solution is stirred with the remaining one from the tank under smooth heating for a few minutes. The latter solution is then used to refill the tank for the next 5 dips. Between each successive dipped layer, the back of the substrate is cleaned with ethanol in order to only dip the face of the substrate coated with FTO.

The intermediate heat-treatment has been chosen in order to avoid cracks and inhomogeneities between each layers. Decreasing the intermediate heat-treatment from 450°C for 5 min to 350°C for 3 min gave homogeneous thin films (**Figure 3**).

By using a multi-layering process, mesoporous thin films were obtained with a thickness ranging between 110 nm (1 layer) and 1500 nm (14 layers) (**Figure 4**) when using the sol-gel solution at  $2 \text{ mol.L}^{-1}$  in titanium precursor. As the relation between the number of dipped layers and the film thickness is almost linear, it is quite easy, using this process, to choose and predict the films thickness.

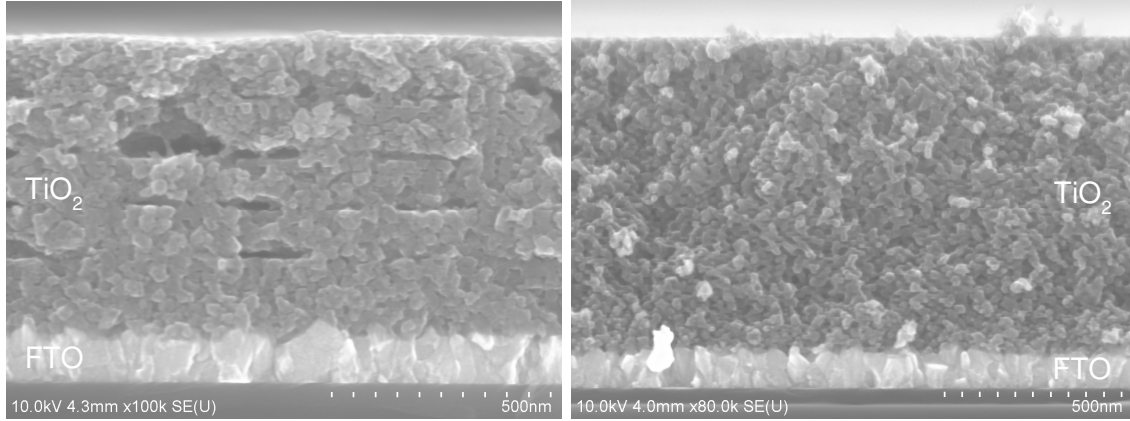


**Figure 3:** FEG-SEM pictures of  $\text{TiO}_2$  thin films (2M, 6 dipped layers) after final heat treatment ( $500^\circ\text{C}$ , 1h) with intermediate heat treatments between each dipped layer of 5 min at  $450^\circ\text{C}$  (left) and of 3 min at  $350^\circ\text{C}$  (right) cross sections.

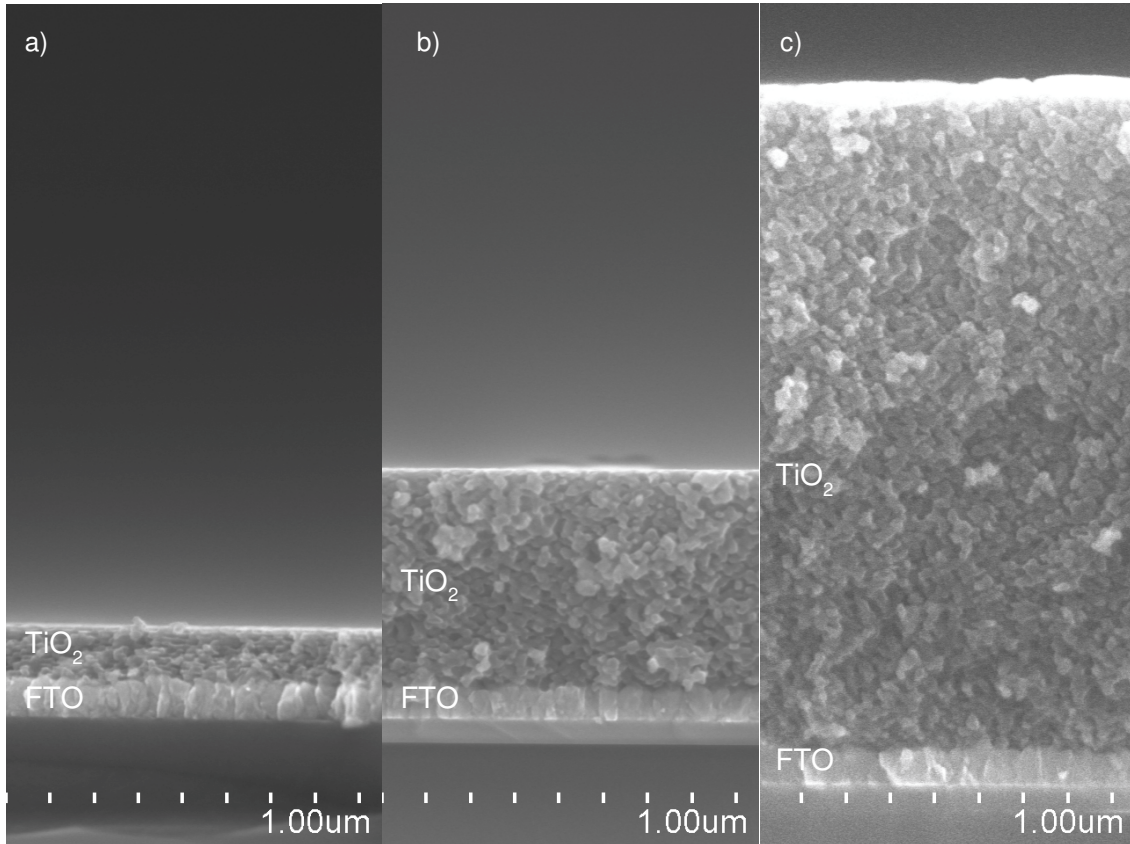


**Figure 4:** FEG-SEM pictures of  $\text{TiO}_2$  thin films ( $2 \text{ mol.L}^{-1}$ ) cross sections. The film thickness is 110 nm for 1 layer (a), 520 nm for 5 layers (b), 1500 nm for 14 layers (c).

## II.2.2 – Inorganic walls and porous networks

Thickness of the titania inorganic walls as well as porous network can be controlled by changing the structuring agent or the titanium precursor concentration. In **Figure 5** is reported the influence of the nature of the block-copolymer and of the titanium precursor concentration. Films were prepared with PB-PEO using titania precursors solution at 1 mol.L<sup>-1</sup> (a) and 2 mol.L<sup>-1</sup> (b), with Pluronic F127 (TiCl<sub>4</sub> 1M) (c) and without any polymers (d).

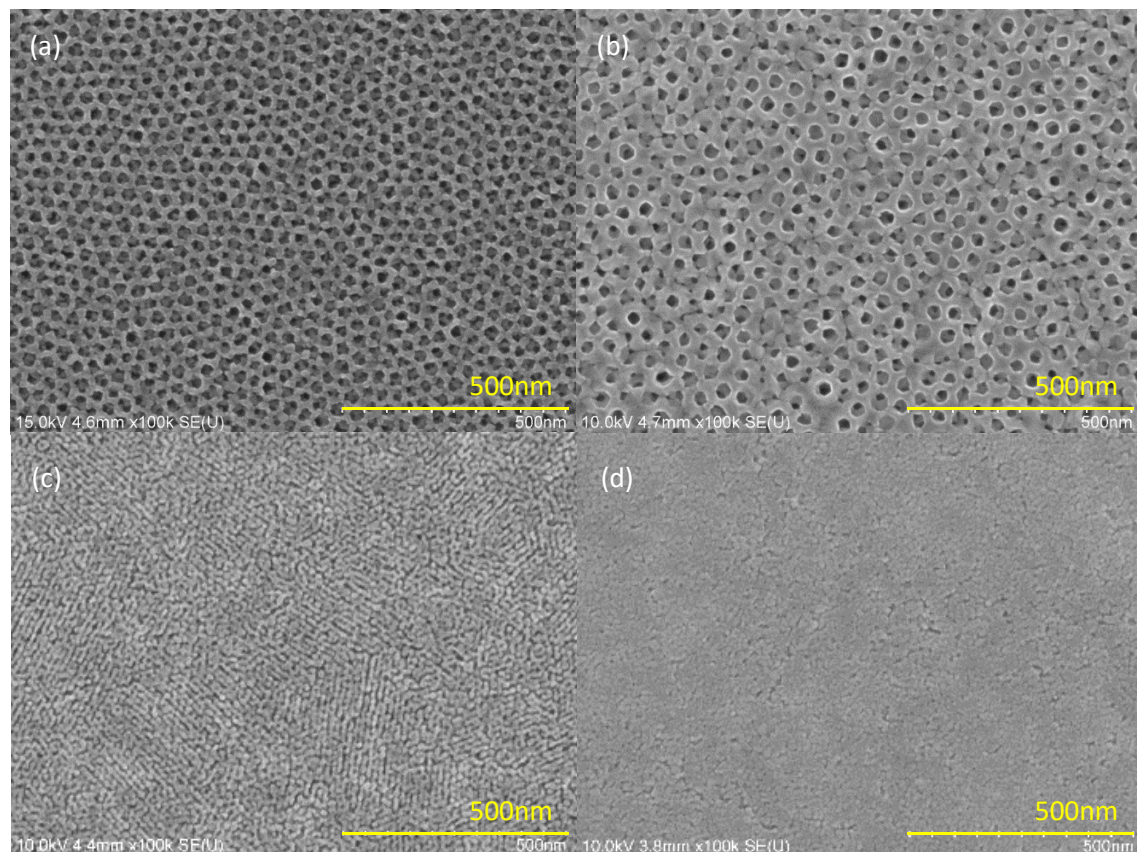


**Figure 5:** FEG-SEM pictures of TiO<sub>2</sub> planar using block-copolymer PB-PEO with titania precursors solution at 1M (a), 2M (b), with Pluronic F127 (TiCl<sub>4</sub> 1M) (c), without polymer (d).

By modifying the concentration from 1 mol.L<sup>-1</sup> to 2 mol.L<sup>-1</sup>, the thickness of the inorganic walls went from around 12 (a) to 25 nm (b), with pores diameter around 26 nm<sup>1</sup>. It also changes the thickness of the film, which doubles from 50-60 nm (at 1 mol.L<sup>-1</sup>) to 100-110 nm (at 2 mol.L<sup>-1</sup>) for one layer.

<sup>1</sup> Average values evaluated with IMAGE-J on FEG-SEM photos (**Figure 5**) for samples of 623 points (1M) and 2181 points (2M). Pore size distribution are presented in **Annex Figure A.1.1**.

The **Figure 6** shows that films with equivalent thickness can be obtained when using PB-PEO with titania precursors solution at 1M for 4 dipped layers, and at 2M for 2 dipped layers.

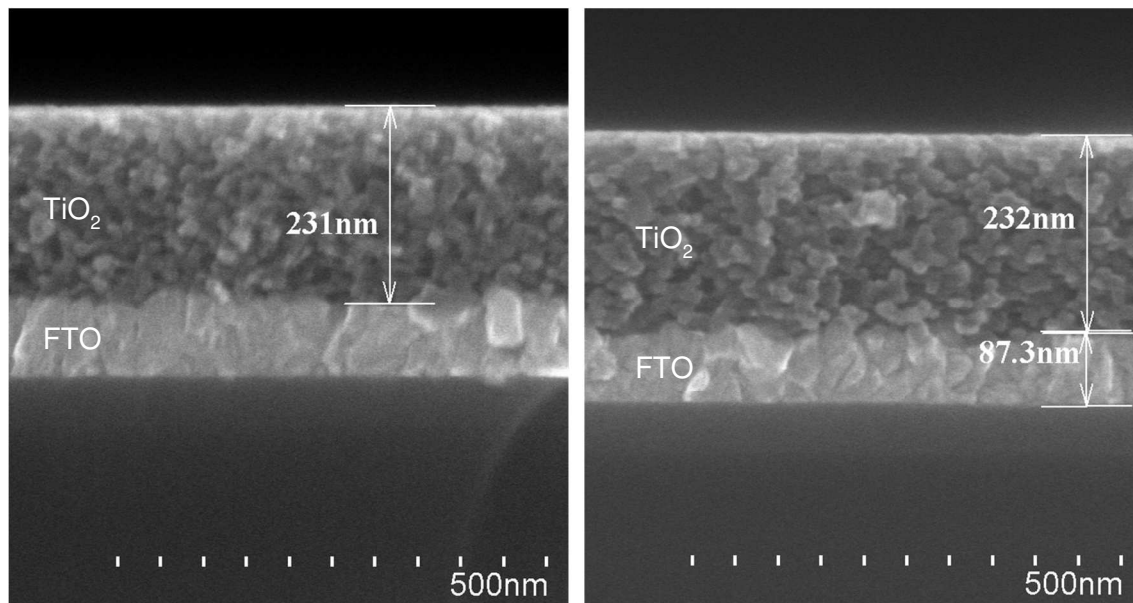


**Figure 6:** FEG-SEM pictures of  $\text{TiO}_2$  planar using block-copolymer PB-PEO with titania precursors solution at 1M for 4 dipped layers (left) and at 2M for 2 dipped layers (right).

### III – Thin films structural characterizations

In this section, structural characterizations of the architecture-controlled TiO<sub>2</sub> electrode are addressed using environmental ellipsometric porosimetry (EEP) and glancing angle X-Ray diffraction (G-XRD). Thin film thickness, porosity, specific surface area, crystallite size and their homogeneity in the whole film are investigated.

#### III.1 – Spectroscopic Ellipsometry

The refractive index and the thickness of final films were measured, after the stabilizing thermal treatment, by spectroscopic ellipsometry performed on a UV-IR (240 1000 nm) variable angle spectroscopic ellipsometer (VASE) M2000DI from Woollam. Data analysis was performed with the CompleteEASE software.

Ellipsometry is an optical technique where a polarized light wave changes its polarization state when reflected by a surface. This change depends of the optical properties of the reflecting material, which can be extrapolated from the ellipsometric measurement. This can be done using an optical dispersion model of the analyzed film. Its parameters are varied to match the experimental data as closely as possible. For dielectric transparent materials, the most common employed model is a Cauchy dispersion, described by the equation (1):

$$n = A + \frac{B}{\lambda^2} \quad (1)$$

where A and B are the variable parameters and n is the refractive index. This model will be used in this thesis to describe the titania thin films deposited on silicon or FTO substrates.

##### III.1.1 – Adaptation for porous thin films

Porous thin films are a composite material, they alternate the backbone material with empty volume (pores filled with air). Therefore, Effective Medium Approximations (EMA) model can be applied to calculate the porous volume of the layer. EMA treats the optical layer properties as a mix of the properties of its constituents, considering the respective volume fractions, and allows the linear approximation described by equation (2):

$$\tilde{\epsilon} = f_A \cdot \tilde{\epsilon}_A + f_B \cdot \tilde{\epsilon}_B \quad (2)$$

where  $f_A$  and  $f_B$  are the relative volumetric fractions of two materials A and B of known dielectric constants  $\tilde{\epsilon}_A$  and  $\tilde{\epsilon}_B$  within a volume unit of measured dielectric constant  $\tilde{\epsilon}$ .

The Bruggemann-EMA is frequently used for the determination of the relative volumetric fractions  $f_A$  and  $f_B$ . This equation (3) is very accurate for a two component system<sup>11</sup>:

$$f_A \cdot \frac{\tilde{\epsilon}_A - \tilde{\epsilon}}{\tilde{\epsilon}_A + 2\tilde{\epsilon}} + f_B \cdot \frac{\tilde{\epsilon}_B - \tilde{\epsilon}}{\tilde{\epsilon}_B + 2\tilde{\epsilon}} = 0 \quad (3)$$

Now let's consider a porous titania thin film ( $\tilde{\epsilon}$ ) composed of pores ( $\tilde{\epsilon}_A$ ) and TiO<sub>2</sub> backbone material ( $\tilde{\epsilon}_B$ ). The dielectric constant of the porous film  $\tilde{\epsilon}$  can be measured by ellipsometry under dry air atmosphere. The dielectric function  $\tilde{\epsilon}_A$  simply equals to the one of dry air, whereas  $\tilde{\epsilon}_B$  can be measured on a dense film of TiO<sub>2</sub> material. The porous volume of the mesoporous thin layer can therefore be determined with the Bruggeman-EMA by fitting the volumetric fractions of air,  $f_A$ , and of the inorganic matrix,  $f_B$ , within the mesoporous film.

This methodology has been employed to estimate the porous volume for different architectures of TiO<sub>2</sub> thin films, whose synthesis has been described in section II. Results are presented in the next section.

### III.1.2 – Environmental Ellipsometric Porosimetry

Environmental Ellipsometric Porosimetry (EEP) is a characterization technique adapted for the analysis of thin porous films, which monitors *in situ* gas sorption within the film (**Figure 7**). From refractive index and thickness variations, it is possible to estimate open porosity, pore radius distribution and film specific surface area.

Flowing wet air in the atmosphere, water adsorbs in the pores forming a multi-layer coverage, until the water capillary condensation occurs. The Kelvin equation (4):

$$RT \cdot \ln \frac{P}{P_0} = -\gamma \cdot V_L \cdot \cos \theta \cdot \frac{G}{r_m} \quad (4)$$

where  $P/P_0$  is the partial pressure, assumed equal to atmospheric relative humidity RH, gives the value of  $P/P_0$  for which water condenses inside the pores, in a process called capillary condensation. When  $P/P_0 = 1$  the pores are completely full of liquid water. In



the Kelvin equation,  $\gamma$  is the surface tension,  $V_L$  is the molar volume of water,  $\theta$  is the wetting angle and  $r_m$  is the curvature radius of the liquid/vapor interface.  $G$  is a geometric factor accounting for the pores shape, it has a value of 2 for a sphere and 1 for a cylinder. The geometric factor can be calculated also for elliptic pores, knowing their anisotropy factor, as reported by Boissière et al.<sup>11</sup>

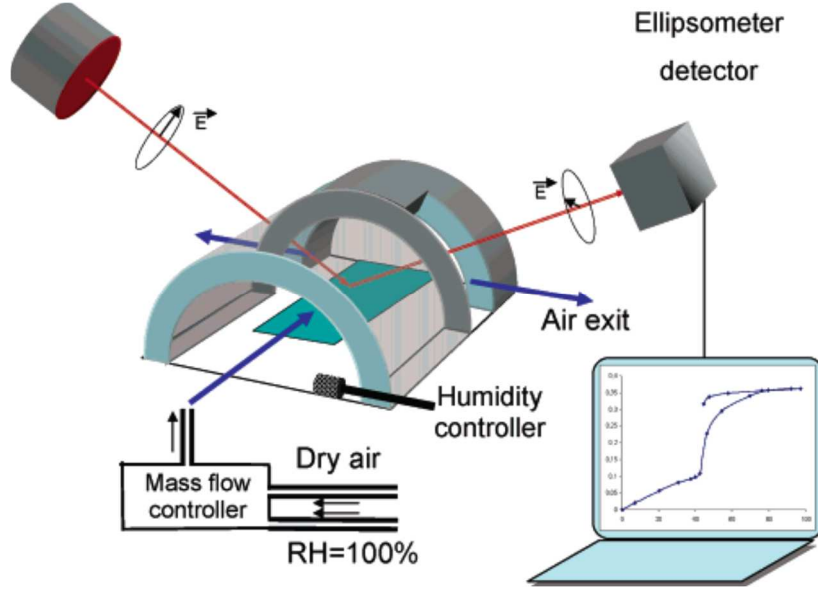


**Figure 7:** Experimental setup employed in environmental ellipsometric porosimetry, reproduced from Boissière et al.<sup>11</sup>

The measured radius  $r_m$  is not exactly equal to the pore radius,  $r$ , since the capillary condensation occurs only after the adsorption of a water layer covering completely the pore walls. The thickness,  $t$ , of this deposit can be measured on non-porous samples of the analyzed material. The pore radius,  $r$ , can be calculated as follow:  $r = r_m + t$ .

The evolution of the film refractive index,  $n$ , and the thickness,  $d$ , as a function of the environmental relative humidity ( $RH = P/P_0$ ), are measured by EEP. The capillary condensation pressure  $P/P_0$  is measured and the pore radius distribution can be obtained using the Kelvin equation. Isotherms usually present hysteresis, meaning that two different values of  $P/P_0$  are associated with adsorption and desorption (**Figure 8**).

Hysteresis is originated from the fact that the interface curvature is not the same during adsorption and desorption. After capillary condensation, a liquid meniscus is formed inside the pores, and it has a different curvature compared to the starting adsorbed layer. Therefore, the desorption curve is shifted towards smaller  $P/P_0$ .

Another reason that causes hysteresis in the porosimetry curves is that in many cases the access to larger pores is limited by smaller pores and they are not drained until the desorption condition of the bottleneck is met. Then, both the neck and the large pore

are rapidly emptied. From the desorption isotherm, it is thereby possible to obtain the pore radius of the restrictions that access the larger cavities, also called bottlenecks.

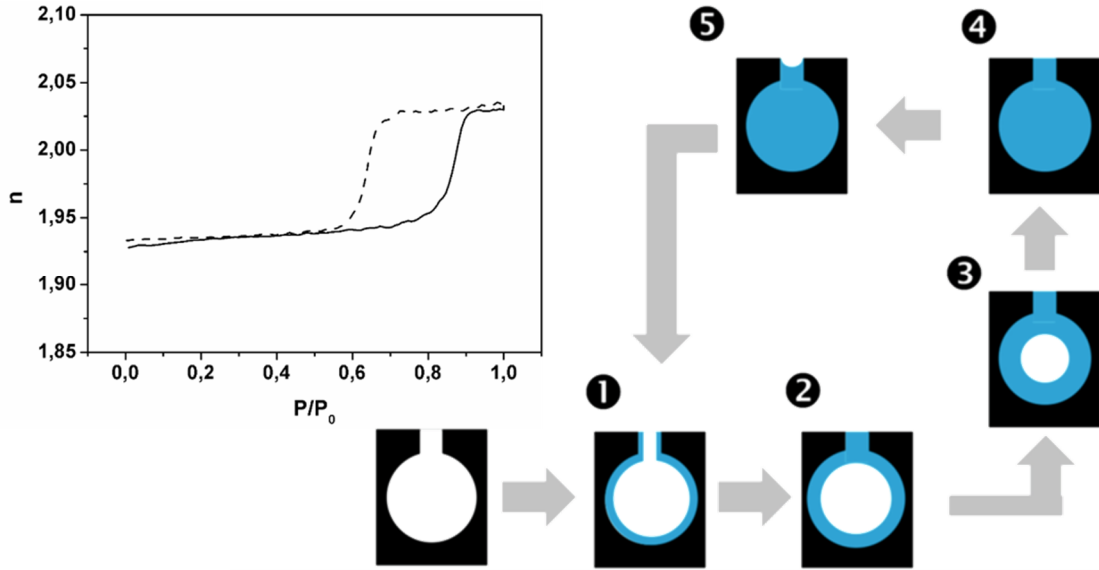


**Figure 8:** Representation of sorption isotherms and scheme of respective situation in the pore system. Adsorption cycle is in solid lines, desorption cycle in dashed lines. The capillary condensation corresponds to phase 3. Adapted from Löbmann<sup>12</sup>.

From EEP data, the surface area values can be estimated by taking into account the total mesoporous volume and pores dimensions. With a geometrical model of a spherical pore with 4 connections per pore, specific surface area  $S$  can be estimated using equation (5):

$$S = \frac{V_p}{V_{pore}} \cdot (S_{pore} - 4 \cdot S_{bottlenecks}) \quad (5)$$

Ratio between the porous volume  $V_p$  and the volume of one pore  $V_{pore}$  gives the number of pores. The geometrical volume of a pore,  $V_p$ , the surface of a pore,  $S_{pore}$ , and of an inter-pore connection,  $S_{bottlenecks}$ , are determined from the EEP determination of the pores and bottlenecks dimensions. Surface area values obtained with this methodology are presented in the next section.

In our study, analysis of our electrodes by Environmental Ellipsometric Porosimetry (EEP) measurements led to isotherms (**Figure 9** and **Figure 10**) presenting phenomenon of capillary condensation characteristic of mesoporous materials. Adsorption-desorption cycles were performed with water for F127 films and with isopropanol for PB-PEO films (for PB-PEO big pores, isopropanol surface tension is more adapted to measure  $P/P_0$  at capillary condensation).



Analysis of these isotherms showed that mesoporous films have an average porous volume ranging between  $\simeq 12\%$  and  $\simeq 36\%$  (**Table 1**). These values were obtained as the ratio between the volumic fraction of air,  $f_A$ , and of TiO<sub>2</sub>,  $f_B$ , using equation (3) (section III.1.1), with  $\tilde{\varepsilon}$  (porous titania thin) and  $\tilde{\varepsilon}_B$  (dense itania) measured for  $P/P_0 = 0$  (dry air).

PB-PEO thin films prepared with a higher Ti/polymers ratio (1M vs. 2M) are denser, which could be expected for films with thicker titania walls (**II.2.2 Figure 5**). At fixed titania precursor concentration, a thicker film has a higher average density. In fact, a more precise EEP analysis realized in the laboratory<sup>13</sup> using a 3 layers model for a similar mesoporous 280-thick film showed a porosity gradient along the film, where inner layers are significantly denser than surface layer.<sup>13</sup> Indeed, as the films are dipped using a multi-layering process, we could expect that layer number,  $n$ , is partially filled with sol-gel solution when dipping the layer number  $n+1$ . Besides, in comparison to surface layers, first dipped layers undergo multiple intermediate heat treatments, which could also possibly reduce the porous volume due to crystallite growth.

The determination of  $P/P_0$  at capillary condensation during the adsorption cycle (**Figure 9**, solid lines) allows the estimation of pore diameters, which are found  $\simeq 10$  nm for F127 films, and  $\simeq 26$  nm, whatever the conditions for PB-PEO films. These dimensions are in a good agreement with those evaluated by FEG-SEM analysis (section II.2.2).

The determination of  $P/P_0$  at capillary condensation during the desorption cycle (**Figure 9**, dashed lines) allows the estimation of pore bottleneck dimensions, whose dimension could be crucial in terms of electrolyte diffusion. Pore restrictions seem to slightly decrease when increasing the Ti/polymers ratio or the thickness of PB-PEO films ( $\simeq 10$ -13 nm), and is smaller for F127 films ( $\simeq 8$  nm).

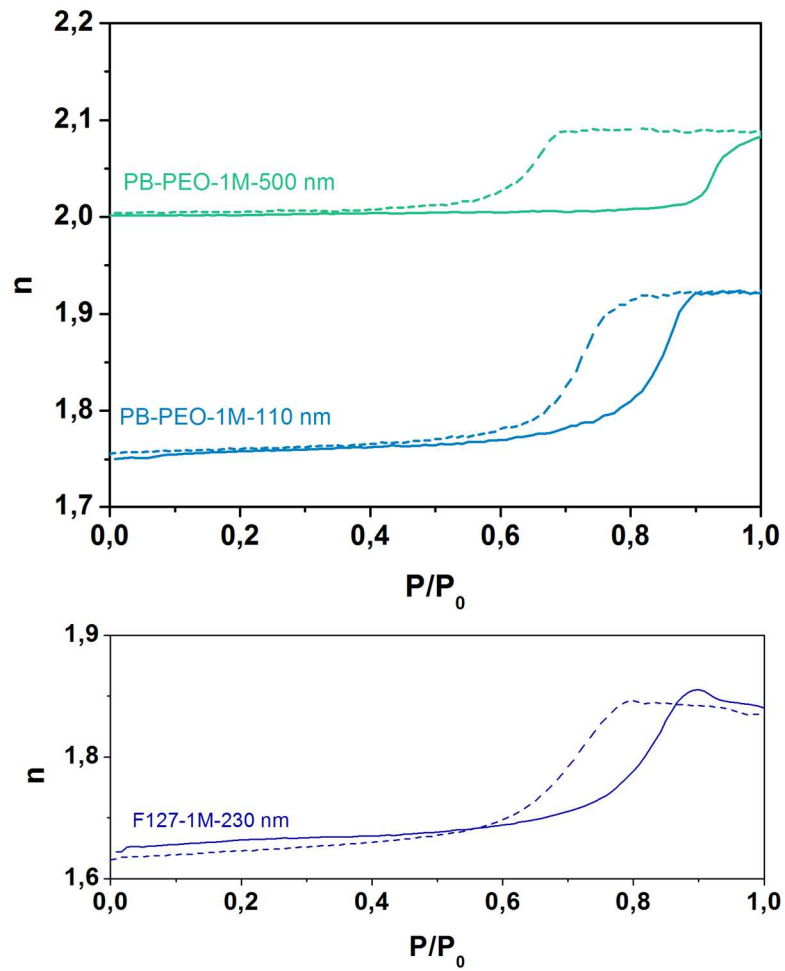


**Figure 9:** Evolutions of refractive index  $n$  of mesoporous titania films (TiCl<sub>4</sub>, 1M) as a function of  $P/P_0$ . Adsorption (solid lines)-desorption (dashed lines) cycles were performed with isopropanol for PB-PEO films and with water for F127 films. Thickness of the film are indicated in the sample name.

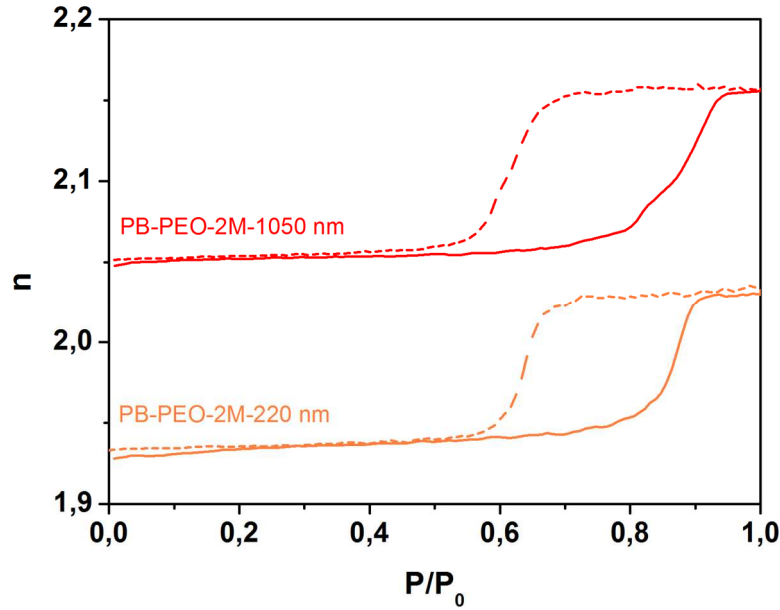


**Figure 10:** Evolutions of refractive index  $n$  of mesoporous titania films (TiCl<sub>4</sub>, 2M) as a function of  $P/P_0$ . Adsorption (solid lines)-desorption (dashed lines) cycles were performed with isopropanol. Thickness of the film are indicated in the sample name.

Polymers	[TiCl <sub>4</sub> ]	Thickness [nm] (number of dipped layers)	Porous volume [%]	Pore/bottleneck diameter [nm]	Specific surface area [m <sup>2</sup> .cm <sup>-3</sup> ]/[m <sup>2</sup> .g <sup>-1</sup> ]
PB-PEO	1M	110 (2)	30	26 / 13	60 / 20
		500 (10)	15	27 / 11	40 / 10
	2M	230 (2)	20	26 / 11	50 / 15
		1050 (10)	12	26 / 10	30 / 10
F127	1M	230 (1)	36	10 / 8	220 / 80

**Table 1:** Results of spectroscopic ellipsometry measurements. Porous volume is determined using Bruggeman-EMA (III.1.1) pore and restriction size through EEP measurements and specific surface area through a geometrical determination.

The specific surface can then be calculated from EEP measurements using geometrical model described in the previous section. Specific surface evolves from  $\approx 10 \text{ m}^2.\text{g}^{-1}$  for the denser and thicker films, to  $\approx 20 \text{ m}^2.\text{g}^{-1}$  for the thinner and more porous one, which is an order of magnitude smaller than what can be expected from mesoporous films.<sup>11</sup>

Compared to the PB-PEO-templated films, F-127 mesoporous thin films develop higher porous volume and higher specific surface area due to their more tortuous worm-like porous network. Pores and necks are also significantly smaller. Analysis of the photo-electrochemical behavior of such films compared to PB-PEO films could therefore give

information on the eventual key parameters (connectivity between the crystallites, crystallite size, distance the charges have to overcome to reach the current collector, *etc.*) governing the photo-induced mechanisms of the electrode, and will be addressed in chapter IV.

### III.2 – Glancing Angle X-Ray Diffraction

TiO<sub>2</sub> thin films were deposited on Fluorine-doped Tin Oxide (FTO)-coated glass substrates to be photo-electrochemically analyzed. The structure of TiO<sub>2</sub>/FTO films are characterized using glancing XRD to optimize TiO<sub>2</sub>/FTO signal. Grazing-incidence diffraction is a scattering geometry combining the Bragg condition with the conditions for X-ray total external reflection from crystal surfaces.<sup>14</sup>

Parallel, monochromatic X-ray beam falls on the sample surface at a fixed angle of incidence ( $\alpha_i$ ) and diffraction profile is recorded. Since the refractive index in the sample is less than unity, total external reflection of X-rays occurs below the critical angle of incidence  $\alpha_c$ . At small incident angles, diffracted and scattered signals at the angle  $2\theta$  arise mainly from a limited depth below the surface of the sample.

XRD analysis was done for incidence angles between 0.4° and 2°. Observed broadening of the peaks at smaller incident angles is due to the geometrical configuration and to the beam footprint, which increases at smaller incident angle. For an incident angle,  $\alpha_c$ , instrumental broadening is given by the following equation (6) and is about 5 times bigger at  $\alpha_c = 0.4^\circ$  (1.64°) than for  $\alpha_c = 2.0^\circ$  (0.33°):

$$W_{instru.} = \frac{0.05}{\sin(\alpha_c)} \cdot \frac{180}{250 \cdot \pi} \quad (6)$$

For TiO<sub>2</sub> films treated for 1h at 500°C, spectra displayed peaks of solely anatase phase (**Figure 11**). TEM photos in dark field/bright field confirmed that the film is mostly crystalline (**Figure 12**).

Crystallites size and lattice parameters of TiO<sub>2</sub> anatase were determined for different film architectures and thicknesses (**Table 2**). It is to mention that for most thin films (typically 50-100 nm), the grazing angle configuration was not enough to completely mask the FTO substrate diffraction signal. As silicon substrates presented the advantage not to overshadow the titania X-ray diffraction contribution (no signal is expected from Si), refinements were compared for the same thin film (5 layers, 2M TiCl<sub>4</sub>) deposited on FTO or silicon substrates, and no significant differences were

observed (**Table 2**). Values of crystallite size and lattice parameters can therefore be reasonably compared on FTO or silicon substrates.

After final heat treatment (1h, 500°C), films obtained with Pluronic F127 and PB-PEO polymers for the same TiCl<sub>4</sub> concentration (1M) gave comparable crystallite size (about 7-8 nm). For the electrode prepared at 2M in TiCl<sub>4</sub>, crystallite size was bigger and slightly increased with the film thickness (12-15 nm).

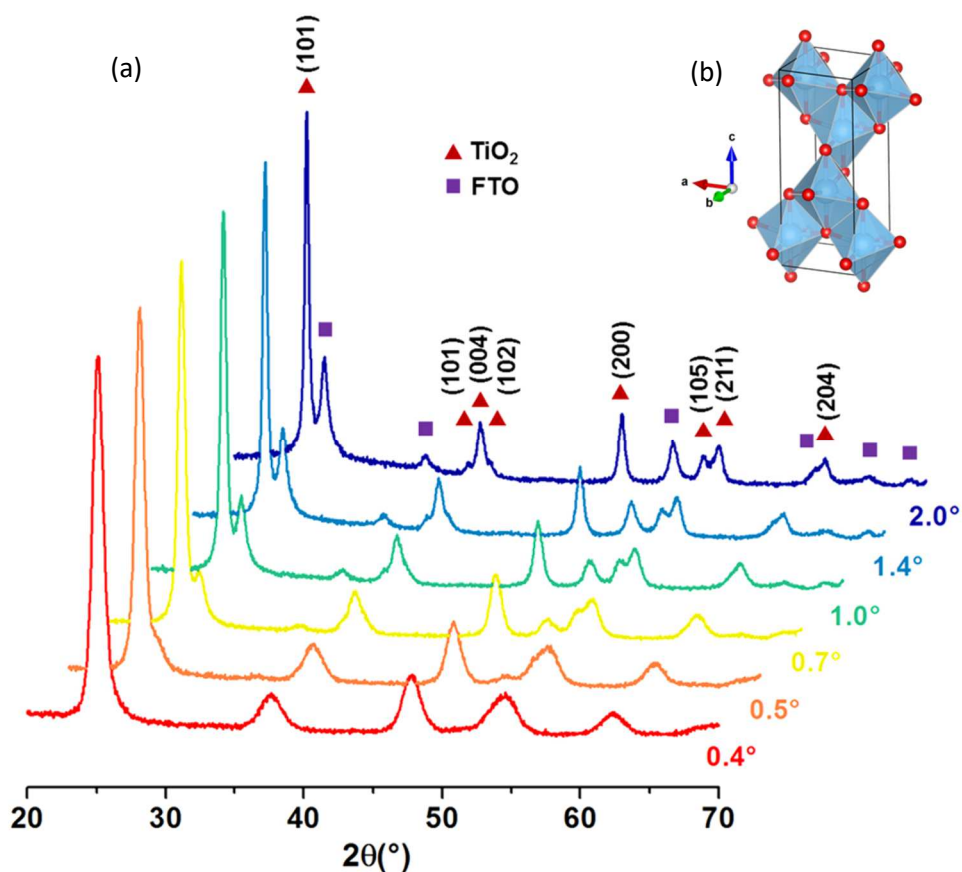


**Figure 11:** XRD diagram of mesoporous PB-PEO TiO<sub>2</sub> (2M, 520 nm-thick) for incident angle from 0.4° to 2.0° (a) and anatase crystal structure (b).

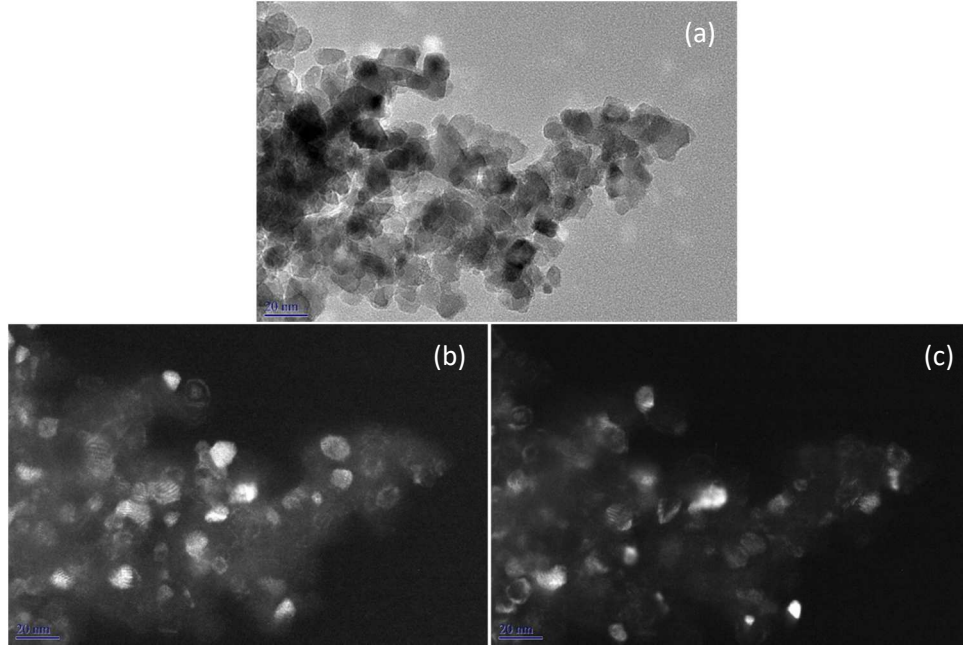


**Figure 12:** TEM pictures of TiO<sub>2</sub> particles (TiCl<sub>4</sub> 1M, 4 dipped layers, treated 1h at 500°C) (a). The electrode was first scratched; obtained particles were then dispersed in ethanol, and dropped on TEM grid. The same zone analyzed in bright field / dark field (b)-(c) confirmed that the film is mostly crystalline.

Lattice parameters were very similar to micrometric TiO<sub>2</sub> anatase<sup>15</sup> (no particular deformation observed).

	Crystallite size (nm)	a,b (Å)	c (Å)	z <sub>0</sub> (Å)
<b>TiO<sub>2</sub>-F127-100 nm-1M</b>	6.51 ± 0.07*	3.772*	9.490*	0.204*
<b>TiO<sub>2</sub>-PBPEO-110 nm-1M</b>	7.96 ± 0.13*	3.768*	9.476*	0.203*
<b>TiO<sub>2</sub>-PBPEO-230 nm-2M</b>	12.79 ± 0.15	3.782	9.513	0.204
<b>TiO<sub>2</sub>-PBPEO-520 nm-2M (0.4°)</b>	12.91 ± 0.13	3.774	9.504	0.203
	13.01 ± 0.16*	3.776*	9.502*	0.203*
<b>TiO<sub>2</sub>-PBPEO-1000 nm-2M (0.7°)</b>	14.36 ± 0.12	3.774	9.500	0.204
<b>Micrometric TiO<sub>2</sub><sup>15</sup></b>	100-200	3.785	9.514	0.208

**Table 2:** Crystallites size and lattice parameters of TiO<sub>2</sub> anatase thin films after heat treatment (1h, 500°C). Indicated concentrations correspond to TiCl<sub>4</sub> concentration in the initial sol-gel solution. Values with (\*) were determined using silicon substrates instead of FTO substrates.

The more the incident angle increased, the more X-ray diffracted signal of FTO substrate became visible (**Figure 11**). For each incidence angle, the X-rays penetration depth into the sample can be estimated.

First, critical angle  $\alpha_C$  of the sample was determined by X-Ray Reflectivity (XRR) using the Fresnel equation<sup>13</sup>. At  $2 \alpha_C$ , the corresponding reflectivity value is  $I_{\max}/2$ , where  $I_{\max}$  is the maximum of the reflectivity plateau. For example, for a typical mesoporous PB-PEO thin films (TiCl<sub>4</sub> 2M, 230 nm-thick),  $\alpha_C$  is found to be 0.243° (**Figure 13**).

By using small angle approximation in Snell law,  $\alpha_C$  can be expressed as a linear function of the square root of the material density. As the theoretical density of anatase and the corresponding  $\alpha_C$  (0.297°) are known, density of the sample was then estimated using equation (7). For example, the density of PB-PEO mesoporous thin films (TiCl<sub>4</sub> 2M, 230 nm-thick) was estimated at  $\simeq 67\%$ , which was in good agreement with the  $\simeq 30\%$  porosity estimated though ellipsometric measurements (see section III.1.2).

$$\rho_{sample} = \rho_{theoretical} \cdot \left( \frac{\alpha_{c,sample}}{\alpha_{c,theoretical}} \right)^2 \quad (7)$$

Knowing  $\alpha_C$  and titania density, X-Ray attenuation length as a function of the incident glancing angle can finally be determined using tabulated values<sup>14</sup> (**Figure 12**). The attenuation length  $L_{att}$  corresponds to the depth into the material measured along the surface normal where the intensity of X-rays falls to  $1/e$  of its value at the surface (Beer-Lambert law). In other terms, 67% of the X-rays are stopped at this depth. At  $4 L_{att}$ , 98% of the X-rays (attenuation of  $1/e^4$ ) are stopped. For a given incident glancing angle, we could consider that the probed depth of the sample corresponds to about 4 times the attenuation length. Above a depth of  $4 L_{att}$ , the X-Ray diffraction signal is almost entirely attenuated (diffracted signal intensity less than 2% of its value at the surface).

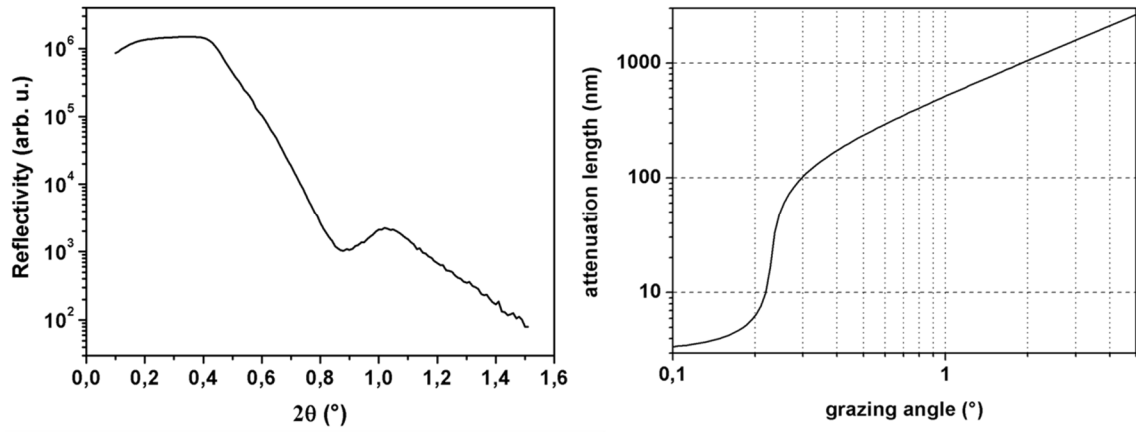


**Figure 13:** Reflectivity of mesoporous PB-PEO TiO<sub>2</sub> (TiCl<sub>4</sub> 1M, 230 nm-thick), deducted value of  $\alpha_c$  is found to be 0.243° (left). Attenuation length as a function of the incident glancing angle for mesoporous PB-PEO TiO<sub>2</sub> (TiCl<sub>4</sub> 2M, 230 nm-thick) (right).

Multilayered mesoporous films were therefore probed at multiple incident angles to allow selective analysis of the material on a depth of hundreds of nanometers. In particular, homogeneity of the crystal structure and of the crystallite size was checked for the thicker films, which have been synthesized by a multi-layering process using sometimes more than 10 layers.

**Figure 14** shows XRD analysis of a 1000 nm-thick film for incidence angles between 0.4° and 1°. The probed depth was about 450 nm at 0.4°, 660 nm at 0.5°, 1000 nm at 0.7° and 1480 nm at 1°. The probed depth values correspond to 4  $L_{att}$  for each incident angle. FTO signal was clearly visible at 1°. Refinements at 0.4°, 0.5°, 0.7° and 1° showed monophasic anatase with very similar crystallite size and lattice parameters (**Table 3**).



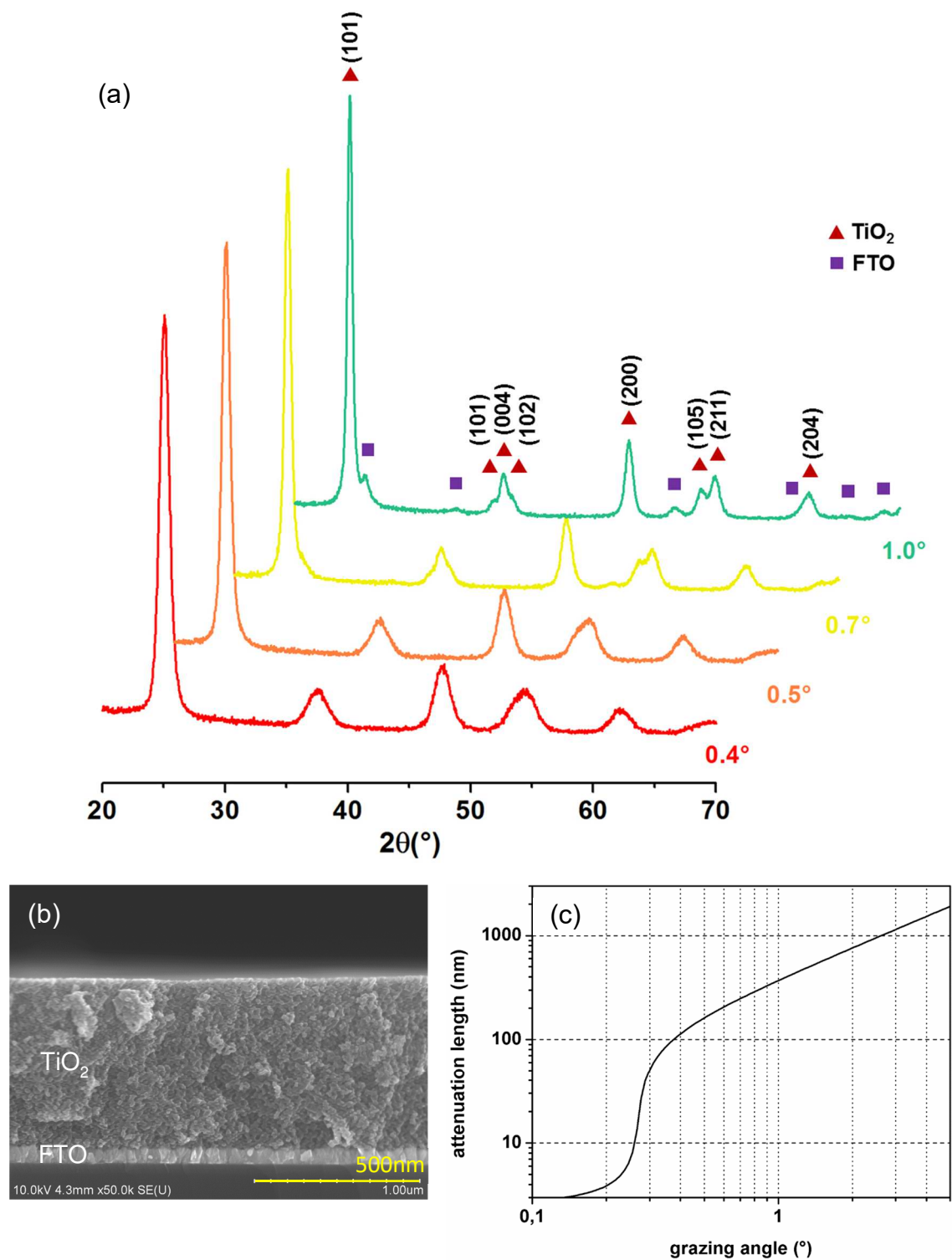


**Figure 14:** XRD diagram of mesoporous PB-PEO TiO<sub>2</sub> (2M, 1  $\mu\text{m}$ --thick) for incident angle from 0.4° to 1.0° (a). Corresponding FEG-SEM cross section (b). Corresponding attenuation length function for a density of 85% ( $\alpha_c = 0.273^{\circ}$ ) (c).

Incident angle (°)	Probed depth (nm)	Crystallite size (nm)	a,b (Å)	c (Å)	z <sub>0</sub> (Å)
0.4	450	13.63 ± 0.12	3.773	9.506	0.204
0.5°	660	14.36 ± 0.12	3.775	9.503	0.204
0.7°	1000	14.75 ± 0.13	3.775	9.495	0.203
1°	1480	15.47 ± 0.13	3.775	9.488	0.202

**Table 3:** Crystallites size and lattice parameters for the same 1 µm-thick TiO<sub>2</sub> anatase thin film (PB-PEO, TiCl<sub>4</sub> 2M) after heat treatment (1h, 500°C) for different incident angles. The given probed depth values correspond to 4 L<sub>att</sub> for each incident angle.

## IV – Reconstruction of TiO<sub>2</sub> electrode energetic diagram

In this section, energy diagram of TiO<sub>2</sub> electrode is determined. Band-gap is first evaluated by UV-Visible spectroscopy. The flat-band potential is then estimated by means of Mott Schottky measurements. The knowledge of the energy diagram could constitute an important starting point to consider reactivity of the photo-generated charges at the TiO<sub>2</sub> electrode / electrolyte interface in the following chapters.

### IV.1 – Band gap determination by UV-Visible Spectroscopy

The bandgap of semiconductor materials can be determined by measurement of optical transitions using following equation (8):

$$A = \frac{B(h\nu - E_g)^m}{h\nu} \quad (8)$$

where A is the absorption coefficient, B a constant,  $h\nu$  the light energy from Planck's constant ( $h$ ) and frequency ( $\nu$ ) determined by the speed of light ( $3 \times 10^8$  m.s<sup>-1</sup>) over the wavelength ( $\lambda$  in nm) by the Planck-Einstein relation. For direct semiconductors  $m = \frac{1}{2}$ , whereas for indirect,  $m = 2$ . Extrapolation of  $(A h\nu)^{1/m}$  vs.  $h\nu$  yields a Tauc plot, indicating the band gap value from the x-axis intercept from the linear feature of the absorption edge.<sup>16</sup>

In order to determine the band gap of TiO<sub>2</sub> thin film as a function of lithium content in the electrode, UV-Vis absorption spectroscopy was acquired *in situ* for different potentials imposed during a CV experiment in a two-electrode configuration, using an argon-tight cuvette designed and fabricated for the experiment (**Figure 15**). Absorbance is measured on an Agilent Technologies Cary Series 5000 spectrophotometer in a double beam configuration with another cuvette containing an FTO/glass film in the used electrolyte as a zero. Absorbance of the substrate and the electrolyte separately are presented in **Annex Figure A.1.2**.

The **Figure 16** presents the evolution of absorbance of a TiO<sub>2</sub> electrode (PB-PEO, 1M in TiCl<sub>4</sub>, 5 dipped layers) during lithiation (2.6 V to 1.4 V vs. Li<sup>+</sup>/Li<sup>0</sup>, 2 mV.s<sup>-1</sup>) and delithiation (1.4 V to 2.6 V vs. Li<sup>+</sup>/Li<sup>0</sup>, 2 mV.s<sup>-1</sup>) in LP30.

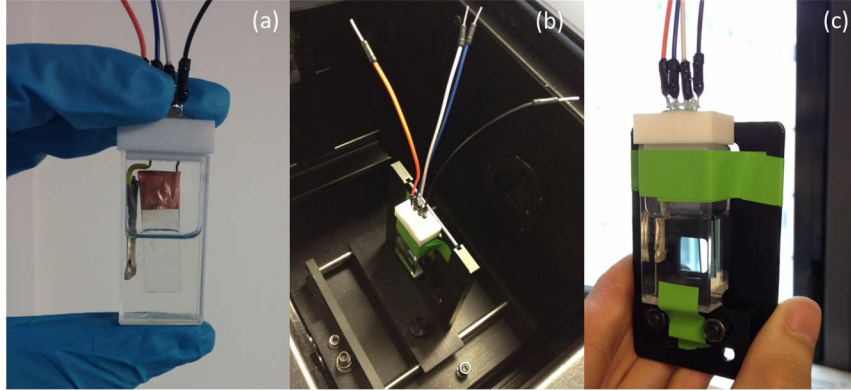


**Figure 15:** TiO<sub>2</sub> thin film (used as working electrode) and Li foil (used as counter- and ref. electrode) in argon-tight cuvette containing LP30 electrolyte (a) same cell in UV-Vis spectrophotometer (b) observed blue color of TiO<sub>2</sub> film after film lithiation (c).

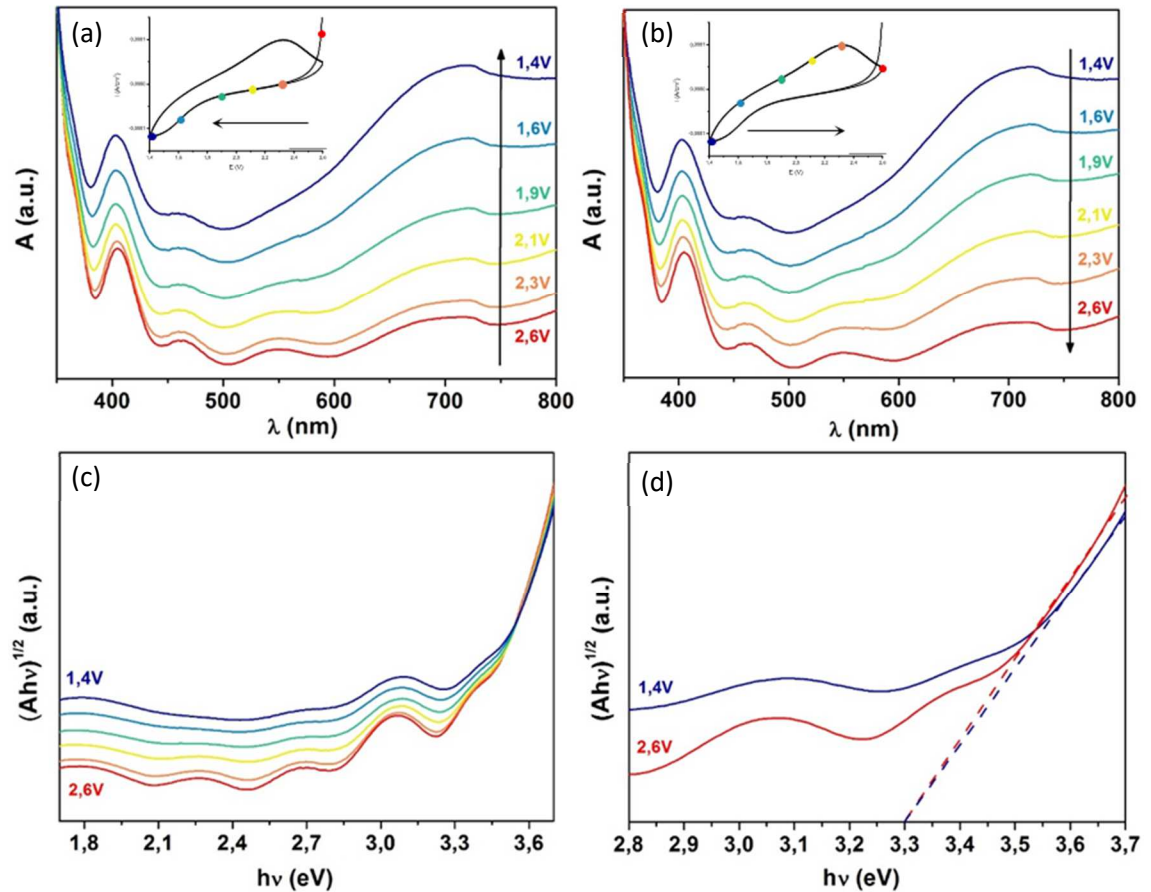


**Figure 16:** *In situ* evolution of UV-Vis absorption spectra for anatase TiO<sub>2</sub> electrode (PB-PEO, 1M in TiCl<sub>4</sub>, 5 dipped layers) during Li<sup>+</sup> insertion (CV from 2.6 V to 1.4 V) (a) and Li<sup>+</sup> extraction (CV from 1.4 V to 2.6 V) (b) in LP30 using air-tight cuvette in a two-electrode configuration. Associated CV experiment between 2.6 V to 1.4 V vs. Li<sup>+</sup>/Li<sup>0</sup> at 2 mV.s<sup>-1</sup> (insert) and Tauc plots corresponding to the discharge experiment (c)-(d).

Modification in the electrode color was observed visually (**Figure 15**): the electrode changes from transparent color (unlithiated) to dark blue after discharge (lithiated) and returned to a transparent color after charge (delithiated). This electrochromic effect is due to the charge compensating electron that enters the material with the Li ion. However, the exact nature of the electronic transition responsible for blue color is much debated.<sup>17–21</sup> Some studies have attributed this coloration to absorption by nearly-free electrons, either compensating for intercalated Li-ions or for Li-ions accumulated at the liquid/solid interface.<sup>22–24</sup> This interpretation suggests a delocalized nature of the highest occupied electron states.<sup>18</sup> Other authors have attributed the color to polaron absorption by electrons localized on Ti<sup>3+</sup> centers in the lattice and occupying the 3d metal orbitals,<sup>25–27</sup> or to electrons trapped in surface states.<sup>28</sup> A “semi-localized” nature of the electron has also been proposed<sup>17</sup> based on the study of anatase TiO<sub>2</sub> electronic conductivity during lithium intercalation; authors suggested that electrons could be free or nearly-free at low lithiation content (consistent with the observed conductivity increase during e<sup>−</sup> injection), but become localized at higher lithium content, when the phase transformation to Li<sub>0.5</sub>TiO<sub>2</sub> takes place (a high free-electron concentration would have induced a metallic conduction, whereas in contrary, a diminution of the conductivity is observed). Owing to the nano-size of the particles, light absorption could also possibly come from electron localized in the antibonding O 2p/Ti 4s hybridized orbitals.<sup>29</sup>

As deduced from linear extrapolation from the absorption edge on Tauc plots **Figure 16**, we found that the electrode band-gap value is always  $\simeq 3.3$  eV, regardless of the lithium content into the electrode. This TiO<sub>2</sub> band-gap value is in relative good agreement with the one found in the literature ( $\simeq 3.2$  eV).<sup>19,30–32</sup>

Blue color of the electrode upon lithiation is correlated to the increased broad absorption around 720 nm in the visible-near-infrared region.<sup>17</sup> The absorbance peak around 425 nm could be attributed to the possible presence surface states trapping the electrons.<sup>19,33</sup> The exact nature of the trap states is still discussed, but have been generally located between 0.04 eV to 1 eV under the conduction energy band<sup>19,30,33–39</sup>. In our case, owing to the position of the TiO<sub>2</sub> absorption edge ( $\simeq 375$  nm), these surface trap states could be possibly located about 0.4 eV below the conduction band edge.

Fringes observed on the absorbance curves at 2.6 V are probably due to the light refraction between layers and pores within mesoporous TiO<sub>2</sub> in absence of intercalating lithium, or for a very low lithium content.<sup>9,40</sup> This observation has been confirmed in a second similar experiment using a thicker TiO<sub>2</sub> electrode (PB-PEO, 2M in TiCl<sub>4</sub>, 10 dipped layers), for which an important refraction phenomenon was observed at delithiated state. This complementary experiment and resulting Tauc plots also led to

same conclusions concerning the unchanged TiO<sub>2</sub> anatase band-gap upon electrode lithiation, regardless to the electrode thickness, and the used electrolyte (PYR<sub>13</sub>TFSI, 0.2M in LiTFSI) (see **Annex Figure A.1.3**).

## IV.2 – Flat-band potential estimated by Mott-Schottky experiment

In order to complete the energy diagram of the TiO<sub>2</sub> thin film electrode, value of flat-band potential can be calculated by means of electrochemical impedance spectroscopy (EIS). The double layer capacity at the semiconductor/electrolyte interface can be measured as a function of the applied potential. The flat band potential ( $E_{fb}$ ) can then be extrapolated using the Mott-Schottky relation described by equation (9):

$$\frac{1}{C^2} = \left( \frac{2}{e\epsilon_0\epsilon_r N A^2} \right) \left[ (V - E_{fb}) - \frac{k_B T}{e} \right] \quad (9)$$

where  $C$  is the differential capacitance of the space-charge region,  $e$  the elementary charge ( $1.60 \times 10^{-19}$  C),  $\epsilon_0$  the permittivity of vacuum ( $8.85 \times 10^{-12}$  F.m<sup>-1</sup>),  $\epsilon_r$  the dielectric constant of the semiconductor,  $N$  the doping density,  $A$  the surface area of the sample,  $V$  the electrode potential,  $E_{fb}$  the flat-band potential,  $k_B$  the Boltzmann constant ( $1.38 \times 10^{-23}$  J.K<sup>-1</sup>) and  $T$  the absolute temperature (293 K).

Mott-Schottky plot at 1 kHz for TiO<sub>2</sub> electrode (PB-PEO, TiCl<sub>4</sub> 1M, 5 layers) is presented in **Figure 17**. Positive slope of  $1/C^2$  graph as a function of the potential shows the n-type of the semiconductor. Intercept to the potential axis obtained by extrapolation of the linear part of the  $1/C^2$  function gives an estimation of the flat band potential  $E_{fb} \simeq 2.84$  V vs. Li<sup>+</sup>/Li<sup>0</sup>, with an additional incertitude  $k_B T$  (0.025 eV at 293 K).

It is to mention that a small frequency dependence phenomenon on the Mott-Schottky experiments has been experienced inducing an additional incertitude of  $\simeq 0.1$  eV. In addition to the experimental error, it could be due to several parameters, which are not considered in the Mott-Schottky model, as the nano-crystalline nature of the semiconductor, its mesoporous structure, the presence of surface states, or even the influence of the conductive substrate.<sup>41–43</sup>

The flat-band potential of the mesoporous TiO<sub>2</sub> electrode is thus estimated at  $E_{fb} \simeq -0.16 \text{ V} \pm 0.125 \text{ V}$  vs. NHE, which is close from values  $\simeq -0.5 \text{ V}$  to  $0 \text{ V}$  vs. NHE found in the literature (generally reported in water for watersplitting application, with a dependence to pH or to the presence of surface states).<sup>42–45</sup>

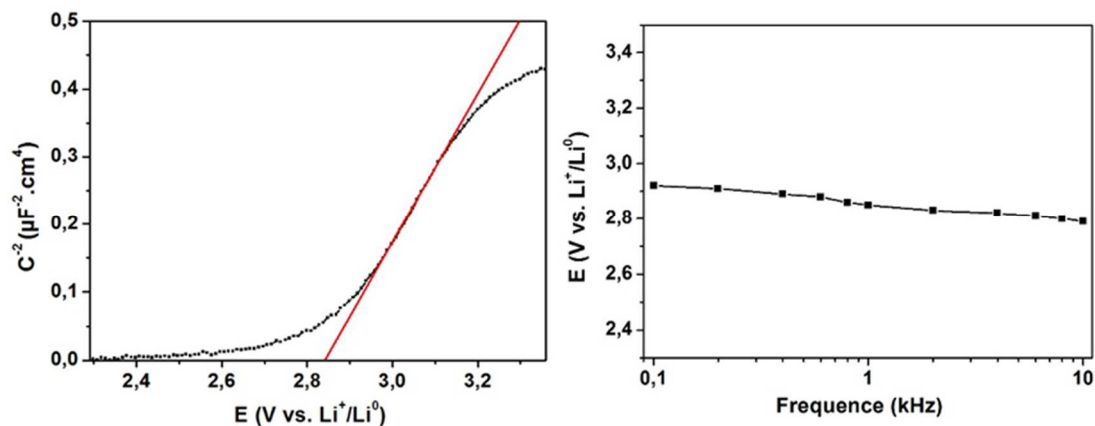


**Figure 17:** Mott-Schottky experiment at 1 kHz ( $5 \text{ mV} \cdot \text{s}^{-1}$ ) for TiO<sub>2</sub> electrode (PB-PEO,  $\text{TiCl}_4$  1M, 5 layers) in LP30 (left). Frequency dependence on the flat-band potential (right).

Combined with band-gap determination through UV-Vis measurements determined in section IV.1, the energy diagram of TiO<sub>2</sub> anatase electrode is drawn (see **Figure 18**). The knowledge of the energy diagram of our electrode could constitute an important starting point to consider reactivity of the photo-generated charges at the TiO<sub>2</sub> electrode / electrolyte interface.

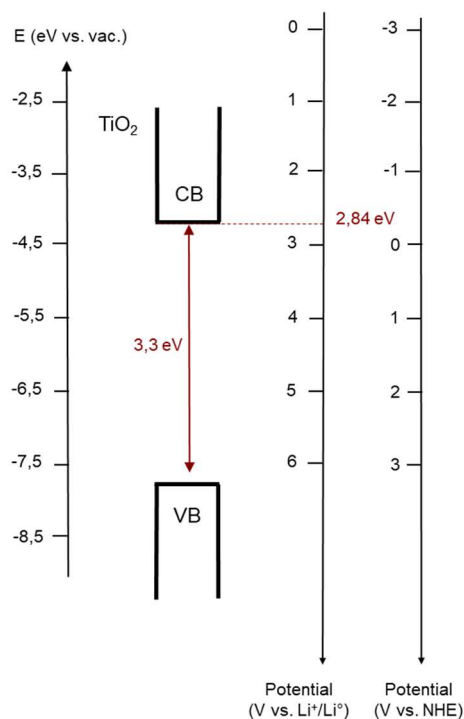


**Figure 18:** Schematic energetic diagram of TiO<sub>2</sub>. Band gap value is deduced from UV-Vis measurements and flat band potential from Mott-Schottky experiment at 1 kHz.

## V – Conclusion

In this chapter, we have presented the synthesis of TiO<sub>2</sub> mesoporous thin film electrode using multilayer dip coating process. By contrast to a conventional battery electrode, the mesoporous film is not composed of any binder, which could prevent excessive light trapping and avoiding possible carrier deceleration across multiple interfaces.

PB-PEO-templated thin films have been characterized using ellipsometric spectroscopy, glancing-angle X-ray diffraction, TEM and FEG-SEM analysis. They present a three-dimensionally interconnected porosity, which develops a well-defined electrode–electrolyte interface.

TiO<sub>2</sub> nanocrystals constitute the inorganic backbone of the photo-electrode and are connected to form a continuous network, according to FEG-SEM images. For the same final heat treatment (500°C, 1h), their size can vary from 7 nm for the thinner electrode and the less concentrated in titania precursors one, to 15 nm for the thicker and more concentrated one.

If pores diameter is quite constant (about 26 nm), porous volume (30 to 12%) pore restrictions (13 to 10 nm) and specific surface (20 to 10 m<sup>2</sup>.g<sup>-1</sup>) decrease when the film is getting thicker and when the ratio between titania precursors/polymers increases. More precisely, gradient in porosity has been observed across the film, where inner layers are getting denser as at the surface. When carefully controlled (ambient humidity and temperature, filling of the tank) the multilayer dip-coating process presents the advantage of being predictive and tunable concerning the film thickness. Crystallite size seems to be quite homogeneous along the film, which could indicated that the main reason of the porosity gradient is the filling of the first dipped layers with the sol-gel solution during the multilayer process rather than crystallite growth due to the additional heat treatments.

F127-templated thin films present a worm-like porous network with smaller pore size. This more tortuous porous architecture thus provides higher porous volume and smaller bottlenecks size. It could therefore constitute an interesting alternative to PB-PEO films to test the eventual geometrical limiting factors for the electrolyte impregnation and photo-charge carrier transport.

In the last section, we have reconstructed the energy diagram of TiO<sub>2</sub> mesoporous thin film electrode (PB-PEO, 1M in TiCl<sub>4</sub>, 5 layers), which is comparable to the energy diagram expected for anatase TiO<sub>2</sub>.<sup>19,30–32</sup> The deduced schematic energetic diagram will be used in particular in chapter IV to consider reactivity of the photo-generated charges at the TiO<sub>2</sub> electrode / electrolyte interface.



In the next chapter, PB-PEO-templated mesoporous  $\text{TiO}_2$  thin film (200/500 nm-thick,  $\text{TiCl}_4$  1M/2M) will be photo-electrochemically tested and studied in LP30 electrolyte as photo-rechargeable Li-ion battery electrode materials.

## Bibliography

1. Paolella, A. *et al.* Light-assisted delithiation of lithium iron phosphate nanocrystals towards photo-rechargeable lithium ion batteries. *Nat. Commun.* **8**, 14643 (2017).
2. Dinh, N. N., Oanh, N. T. T., Long, P. D., Bernard, M. C. & Hugot-Le Goff, A. Electrochromic properties of TiO<sub>2</sub> anatase thin films prepared by a dipping sol-gel method. *Thin Solid Films* **423**, 70–76 (2003).
3. Özer, N. Reproducibility of the coloration processes in TiO<sub>2</sub> films. *Thin Solid Films* **214**, 17–24 (1992).
4. Lu, Y. *et al.* Continuous formation of supported cubic and hexagonal mesoporous films by sol-gel dip-coating. *Nature* **389**, 364–368 (1997).
5. Sanchez, C. *et al.* ‘Chimie douce’: A land of opportunities for the designed construction of functional inorganic and hybrid organic-inorganic nanomaterials. *Comptes Rendus Chim.* **13**, 3–39 (2010).
6. Grosso, D. *et al.* Fundamentals of Mesostructuring Through Evaporation-Induced Self-Assembly. *Adv. Funct. Mater.* **14**, 309–322 (2004).
7. Grosso, D. *et al.* Periodically ordered nanoscale islands and mesoporous films composed of nanocrystalline multimetallic oxides. *Nat. Mater.* **3**, 787–792 (2004).
8. Krins, N. *et al.* NbVO<sub>5</sub> Mesoporous Thin Films by Evaporation Induced Micelles Packing: Pore Size Dependence of the Mechanical Stability upon Thermal Treatment and Li Insertion/Extraction. *Chem. Mater.* **23**, 4124–4131 (2011).
9. Hilliard, S. Water Splitting Photoelectrocatalysis. (2016).
10. Bindini, E., Naudin, G., Faustini, M., Grosso, D. & Boissière, C. Critical Role of the Atmosphere in Dip-Coating Process. *J. Phys. Chem. C* **121**, 14572–14580 (2017).
11. Boissiere, C. *et al.* Porosity and Mechanical Properties of Mesoporous Thin Films Assessed by Environmental Ellipsometric Porosimetry. *Langmuir* **21**, 12362–12371 (2005).
12. Löbmann, P. Characterization of sol-gel thin films by ellipsometric porosimetry. *J. Sol-Gel Sci. Technol.* **84**, 2–15 (2017).
13. Nguyen, O. *et al.* Shedding light on the light-driven lithium ion de-insertion reaction: towards the design of a photo-rechargeable battery. *J. Mater. Chem. A* **5**, 5927–5933 (2017).
14. Stepanov, S. Grazing-incidence X-ray diffraction. *3rd Autumn Sch. X-Ray Scatt. Surf. Thin Layers* 1–4 (1997).
15. Structural and thermal parameters for rutile and anatase - Howard - 1991 - Acta Crystallographica Section B - Wiley Online Library.
16. Tauc, J., Grigorovici, R. & Vancu, A. Optical Properties and Electronic Structure of Amorphous Germanium. *Phys. Status Solidi B* **15**, 627–637 (1966).
17. van de Krol, R., Goossens, A. & Meulenkamp, E. A. Electrical and optical properties of TiO<sub>2</sub> in accumulation and of lithium titanate Li<sub>0.5</sub>TiO<sub>2</sub>. *J. Appl. Phys.* **90**, 2235–2242 (2001).
18. Structure and dynamics of lithium in Anatase TiO<sub>2</sub>: study of interstitial Li-ion intercalation in anatase TiO<sub>2</sub> at the atomic level - Wagemaker M. thesis, 2003.

19. Ardo, S. & Meyer, G. J. Photodriven heterogeneous charge transfer with transition-metal compounds anchored to TiO<sub>2</sub> semiconductor surfaces. *Chem Soc Rev* **38**, 115–164 (2009).
20. Khomenko, V. M., Langer, K., Rager, H. & Fett, A. Electronic absorption by Ti<sup>3+</sup> ions and electron delocalization in synthetic blue rutile. *Phys. Chem. Miner.* **25**, 338–346 (1998).
21. Naldoni, A. *et al.* Effect of Nature and Location of Defects on Bandgap Narrowing in Black TiO<sub>2</sub> Nanoparticles. *J. Am. Chem. Soc.* **134**, 7600–7603 (2012).
22. Enright, B. & Fitzmaurice, D. Spectroscopic Determination of Electron and Hole Effective Masses in a Nanocrystalline Semiconductor Film. *J. Phys. Chem.* **100**, 1027–1035 (1996).
23. Boschloo, G. & Fitzmaurice, D. Electron accumulation in nanoporous-nanocrystalline TiO<sub>2</sub> electrodes. *Proc Electrochem Soc* **97–20**, 84–87 (1997).
24. Kavan, L. Nanocrystalline TiO<sub>2</sub> (Anatase) Electrodes: Surface Morphology, Adsorption, and Electrochemical Properties. *J. Electrochem. Soc.* **143**, 394 (1996).
25. Cao, Y., Chen, Y., Sun, X., Zhang, Z. & Mu, T. Water sorption in ionic liquids: kinetics, mechanisms and hydrophilicity. *Phys. Chem. Chem. Phys.* **14**, 12252 (2012).
26. Södergren, S. *et al.* Lithium intercalation in nanoporous anatase TiO<sub>2</sub> studied with XPS. *J. Phys. Chem. B* **101**, 3087–3090 (1997).
27. Wagemaker, M., Lützenkirchen-Hecht, D., van Well, A. A. & Frahm, R. Atomic and Electronic Bulk versus Surface Structure: Lithium Intercalation in Anatase TiO<sub>2</sub>. *J. Phys. Chem. B* **108**, 12456–12464 (2004).
28. Kang, T.-S. Time-Dependent Electrochromism of Nanocrystalline TiO<sub>2</sub> Films in Propylene Carbonate Solution of LiClO<sub>4</sub>. *J. Electrochem. Soc.* **145**, 1982 (1998).
29. Vayssieres, L., Persson, C. & Guo, J.-H. Size effect on the conduction band orbital character of anatase TiO<sub>2</sub> nanocrystals. *Appl. Phys. Lett.* **99**, 183101 (2011).
30. Berger, T., Monllor-Satoca, D., Jankulovska, M., Lana-Villarreal, T. & Gómez, R. The Electrochemistry of Nanostructured Titanium Dioxide Electrodes. *ChemPhysChem* **13**, 2824–2875 (2012).
31. Chen, S. & Wang, L.-W. Thermodynamic Oxidation and Reduction Potentials of Photocatalytic Semiconductors in Aqueous Solution. *Chem. Mater.* **24**, 3659–3666 (2012).
32. Kapilashrami, M., Zhang, Y., Liu, Y.-S., Hagfeldt, A. & Guo, J. Probing the Optical Property and Electronic Structure of TiO<sub>2</sub> Nanomaterials for Renewable Energy Applications. *Chem. Rev.* **114**, 9662–9707 (2014).
33. Boschloo, G. & Fitzmaurice, D. Spectroelectrochemical Investigation of Surface States in Nanostructured TiO<sub>2</sub> Electrodes. *J. Phys. Chem. B* **103**, 2228–2231 (1999).
34. Bisquert, J. *et al.* A review of recent results on electrochemical determination of the density of electronic states of nanostructured metal-oxide semiconductors and organic hole conductors. *Inorganica Chim. Acta* **361**, 684–698 (2008).

35. Westermarck, K. *et al.* Determination of the electronic density of states at a nanostructured TiO<sub>2</sub>/Ru-dye/electrolyte interface by means of photoelectron spectroscopy. *Chem. Phys.* **285**, 157–165 (2002).
36. Fabregat-Santiago, F., Mora-Seró, I., Garcia-Belmonte, G. & Bisquert, J. Cyclic Voltammetry Studies of Nanoporous Semiconductors. Capacitive and Reactive Properties of Nanocrystalline TiO<sub>2</sub> Electrodes in Aqueous Electrolyte. *J. Phys. Chem. B* **107**, 758–768 (2003).
37. Wagemaker, M. *et al.* Thermodynamics of spinel Li<sub>x</sub>TiO<sub>2</sub> from first principles. *Chem. Phys.* **317**, 130–136 (2005).
38. Jankulovska, M., Berger, T., Lana-Villarreal, T. & Gómez, R. A comparison of quantum-sized anatase and rutile nanowire thin films: Devising differences in the electronic structure from photoelectrochemical measurements. *Electrochimica Acta* **62**, 172–180 (2012).
39. Jankulovska, M., Berger, T., Wong, S. S., Gómez, R. & Lana-Villarreal, T. Trap States in TiO<sub>2</sub> Films Made of Nanowires, Nanotubes or Nanoparticles: An Electrochemical Study. *ChemPhysChem* **13**, 3008–3017 (2012).
40. Hong, W. Q. Extraction of extinction coefficient of weak absorbing thin films from special absorption. *J. Phys. Appl. Phys.* **22**, 1384 (1989).
41. Rajeshwar, K. Fundamentals of semiconductor electrochemistry and photoelectrochemistry. *Encycl. Electrochem.* (2007).
42. Ge, H. *et al.* Influence of Surface States on the Evaluation of the Flat Band Potential of TiO<sub>2</sub>. *ACS Appl. Mater. Interfaces* **6**, 2401–2406 (2014).
43. Cardon, F. & Gomes, W. P. On the determination of the flat-band potential of a semiconductor in contact with a metal or an electrolyte from the Mott-Schottky plot. *J. Phys. Appl. Phys.* **11**, L63 (1978).
44. Radecka, M., Rekas, M., Trenczek-Zajac, A. & Zakrzewska, K. Importance of the band gap energy and flat band potential for application of modified TiO<sub>2</sub> photoanodes in water photolysis. *J. Power Sources* **181**, 46–55 (2008).
45. Krol, R. van de, Goossens, A. & Schoonman, J. Mott-Schottky Analysis of Nanometer-Scale Thin-Film Anatase TiO<sub>2</sub>. *J. Electrochem. Soc.* **144**, 1723–1727 (1997).



## **CHAPTER 3**

**Mesoporous TiO<sub>2</sub> thin films as photo-rechargeable  
Li-ion battery electrode materials:  
photo-electrochemical characterizations**



## TABLE of CONTENTS

I – Introduction .....	107
II – Cell design and photo-electrochemical set-up .....	108
III – How light impact the discharge and charge of the $\text{TiO}_2$ -based battery electrode: observations.....	109
III.1 – Galvanostatic experiments .....	109
III.2 – Cyclic voltammetry experiments .....	113
IV – Evaluation of the photo-current intensity .....	115
IV.1 – Potentiostatic experiments.....	115
IV.2 – Open circuit voltage experiments.....	117
V – Adjusting the rates of simultaneous electrode discharge and photo-recharge.....	119
VI – Conclusion .....	121
Bibliography .....	122





## I – Introduction

Based on their observations of the effect of light on pre-protoned  $\text{TiO}_2(\text{B})$ , Tributsch et al.<sup>1</sup> proposed a mechanism, where photo-generated holes oxidize  $\text{Ti}^{3+}$  (from  $\text{H}_x\text{TiO}_2$ ) into  $\text{Ti}^{4+}$ , which lead to lithium-ion extraction. This interpretation has also been adopted by Zaghbi et al.<sup>2</sup> in their recent study on lithium iron phosphate as photo-rechargeable electrode.

In the case of our study, analysing how light impacts the electrochemical response of the battery electrode for different electrochemical experiments could provide essential information about the characteristics and the mechanisms of the  $\text{TiO}_2$  electrode photo-recharge. By using a more simple composition of the electrode (carbon- and dye-free electrode) in comparison to the usual Li-ion battery systems or dye-sensitized systems, we hope to facilitate the comprehension of the observed light-induced phenomena, which will be compared to Tributsch mechanistic hypothesis.

In this chapter, mesoporous  $\text{TiO}_2$  thin film is tested as a photo-rechargeable Li-ion battery electrode materials. As regards to the choice of the experiments, it is to mention that in the case of photo-rechargeable battery testing, a precise methodology is not established (in comparison to the one in Li-ion battery domain for example).

At this very early stage of development of the bifunctional electrode technology, the few reported photo-recharge experiments<sup>2,3</sup> are essentially based on the analysis of open current voltage experiments under illumination. In this study, we will try to play with other simple experiments, which are more inspired by the methodology applied in other domains studying effects of illumination (*e.g.* photo-water splitting), using chopped illumination for example.

In the first section, we will describe the cell and the photo-electrochemical set-up. The following sections report our observations and deductions on the electrochemical response of  $\text{TiO}_2$  electrode upon illumination for different electrochemical experiments (galvanostatic, cyclic voltammetry, open current voltage, potentiostatic under chopped illumination experiments).

## II – Cell design and photo-electrochemical set-up

Electrochemical measurements were performed in a three-electrode cell, made of a sealed glass container (transparent in the visible range), assembled in an Ar-glove box ( $\text{H}_2\text{O}$  content  $< 0,1\text{ppm}$ ). Two foils of lithium were used as counter and reference electrodes respectively. The mesoporous anatase  $\text{TiO}_2$  film on FTO substrate was used as working electrode and was oriented such as the  $\text{TiO}_2$  film faces the light. The electrolyte was 1M  $\text{LiPF}_6$  EC/DMC=50/50 (v/v) (LP30). Cyclic voltammograms (CV), chronopotentiometric (charge-discharge) and chronoamperometric experiments were performed in the electrochemical window of 2.6 V-1.4 V vs  $\text{Li}^+/\text{Li}^\circ$  using Solartron Analytical Modulab potentiostat. The illumination of the electrochemical cell was performed with a Xenon lamp (Oriel) operating at 280 W, coupled with a water-filled Spectra-Physics 6123 NS liquid filter to eliminate infra-red radiations. The spectrum of the lamp is presented in **Annex III.1**. The distance between the lamp and the cell was set to 45 cm. Dark conditions were obtained by wrapping the cell into an aluminum foil. For prolonged exposure to light, a water-cooled glass cell was used to prevent the illumination to heat the cell (**Figure 1**).

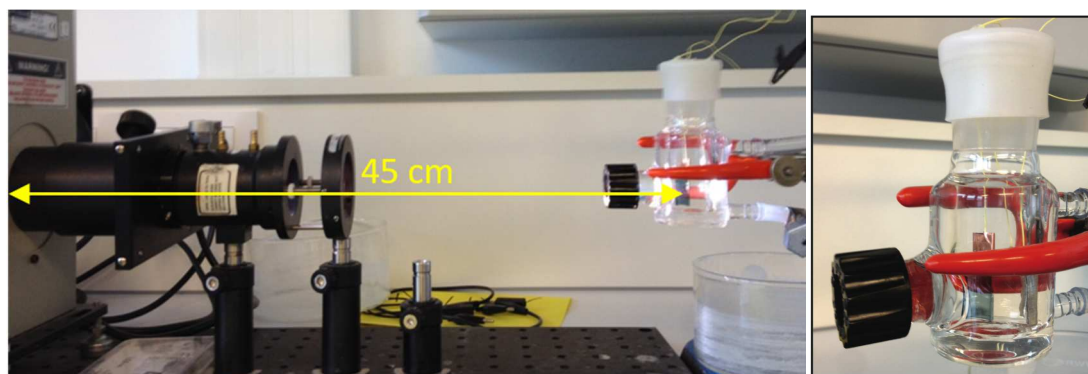


**Figure 1:** Experimental set-up. Optical bench (left) and water-cooled glass cell (right).

### III – How light impacts the discharge and charge of the TiO<sub>2</sub>-based battery electrode: observations

In all following experiments, prior to comparing successively the dark- and light-behavior of TiO<sub>2</sub> versus lithium insertion, the working electrode was electrochemical stabilized in dark conditions using the following experiment: 10 cyclic voltammograms (CVs) from 2.6 V to 1.4 V vs Li<sup>+</sup>/Li<sup>0</sup> at 0.5 mV.s<sup>-1</sup> (see **Figure 2**) in order to reach a stable electrochemical signal upon cycling. The important reduction observed during the first cycle could be due to a solid electrolyte interface SEI formation by degradation of the LP30 electrolyte for reductive potentials.

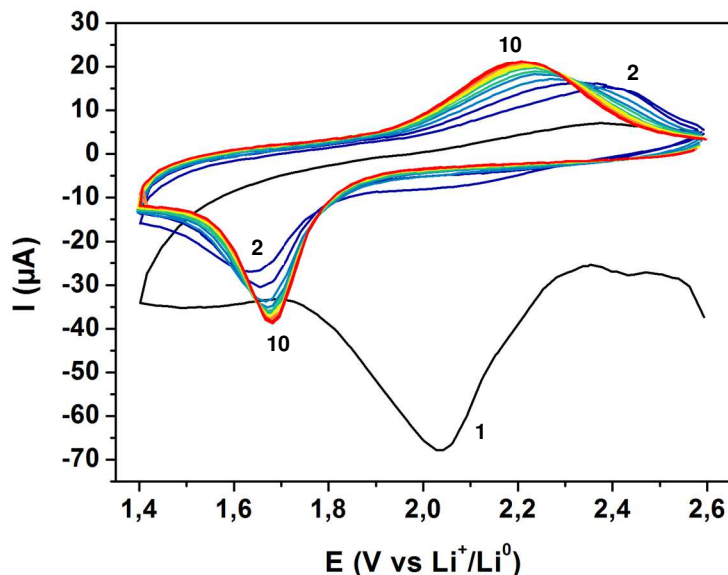


**Figure 2:** First ten cyclic voltammograms at scan rate 0.5 mV.s<sup>-1</sup> of mesoporous anatase TiO<sub>2</sub> thin film (stabilization treatment). The number of the cycle is indicated in the graph as reference (1<sup>st</sup> cycle in dark, 10<sup>th</sup> in red).

#### III.1 – Galvanostatic experiments

The **Figure 3-a** shows discharge-charge curves of anatase TiO<sub>2</sub> (230 nm-thick, PB-PEO, 1M TiCl<sub>4</sub>) at a rate of 2C, *i.e.* 0.5 Li<sup>+</sup>/TiO<sub>2</sub> inserted in 30 min<sup>i</sup>. These experiments were performed on stabilized samples first in dark conditions, then under illumination. Both dark and light discharge curves exhibit the three expected regions

<sup>i</sup> With a cut-off voltage of 1.4 V, it is very unlikely to expect the LiTiO<sub>2</sub> phase to be formed (theoretical capacity 335 mAh.g<sup>-1</sup>). In this work, the ‘C-rate’ refers to the arbitrary Li<sub>0.5</sub>TiO<sub>2</sub> composition (168 mAh.g<sup>-1</sup>).

for TiO<sub>2</sub> anatase inserting lithium ions.<sup>4</sup> First, a large voltage decrease (I) associated to both insertion of a small amount of Li<sup>+</sup> within the anatase phase to form Li<sub>0.1</sub>TiO<sub>2</sub>. Second, a plateau region (II) at around 1,75 V is the electrochemical signature of a biphasic process due to the coexistence of a Li-poor phase (tetragonal Li<sub>α</sub>TiO<sub>2</sub>) and a Li-rich phase (orthorhombic Li<sub>0.5</sub>TiO<sub>2</sub>).<sup>5,6</sup> Third, the slope region (III) after the plateau indicates the addition of extra Li<sup>+</sup> to the Li-rich phase.

In this work, the use of an FTO-based substrate limits the discharge voltage to a rather high cut-off voltage of 1.4 V in order to prevent SnO<sub>2</sub> reduction to Sn<sup>0</sup>. Consequently, it is not expected to access the full theoretical capacity of nano-sized anatase TiO<sub>2</sub>, reported as LiTiO<sub>2</sub> (335 mAh.g<sup>-1</sup>).<sup>7</sup>

The charge curves highlight the reversibility of processes (I), (II) and (III), through the regions (I')-sloped increase potential, (II')-plateau at 1.95 V and (III')-sloped increase up to the voltage cut at 2.6 V. Thanks to the present set-up (as opposed to coin cells or Swagelok-type cells), we were also able to observe the reversible color changes of the electrode: from a completely transparent state to a dark blue state (**Figure 3-b, c, d**). The blue color is clearly assigned to the presence of Ti<sup>3+</sup> centers resulting from Li<sup>+</sup> insertion, however the nature of the electronic transition responsible for the absorption in the orange range is yet unclear.<sup>8,9</sup>

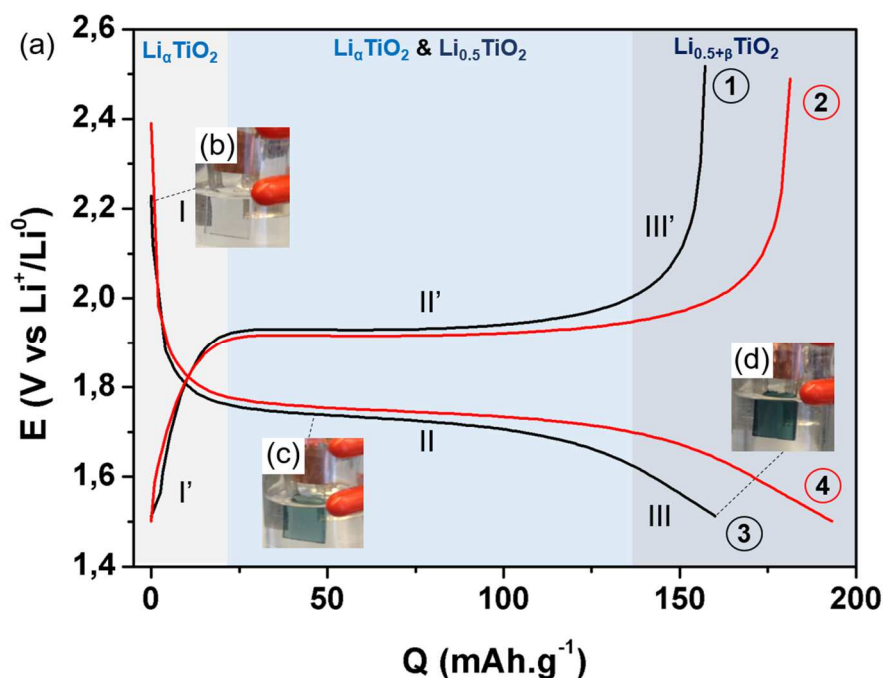


**Figure 3:** (a) Potential versus Capacity evolution (discharge-charge at 2C-rate) of TiO<sub>2</sub> mesoporous films (230 nm-thick, PB-PEO, 1M TiCl<sub>4</sub>) in dark condition (black) and under light (red). (b, c, d) Pictures of the cell at the beginning of zone II and at the end of zone III. Li<sub>0.5</sub>TiO<sub>2</sub> corresponds to a capacity of 168 mAh.g<sup>-1</sup>.

According to **Figure 3-a** illumination appears to impact the total charge stored: 193 mAh.g<sup>-1</sup> under light (**curve n°2**) against 160 mAh.g<sup>-1</sup> in the dark (**curve n°1**). The “dark” capacity at 2C is very close to the theoretical capacity for Li<sub>0.5</sub>TiO<sub>2</sub> (168 mAh.g<sup>-1</sup>).

The impact of light on the capacity is yet important ( $\simeq 21\%$  of extra capacity). The higher capacity mainly results from the increase in the plateau’s length in both charge and discharge curves (regions II and II’, respectively), suggesting that the extra-capacity comes from the lithiation/delithiation of TiO<sub>2</sub>. Expected light-induced reactions are presented in **Figure 4**.

Upon photon-excitation, electron-hole pairs are created at the electrode surface (**Figure 4-eq. 1**). The separation of excitons then occurs in the space charge layer and the charge carriers diffuse, either to the electrode/electrolyte interface for the hole, or to the electrode/substrate interface for the electron. The holes are expected to be responsible for the light-induced oxidation of Ti<sup>3+</sup> to Ti<sup>4+</sup> (**Figure 4-eq. 2**), which results in lithium ions photo-extraction.

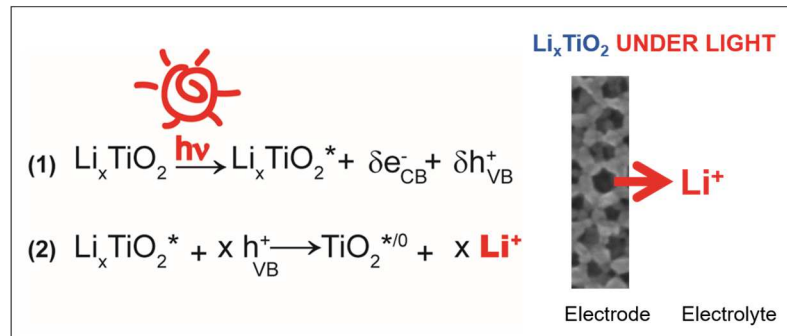


**Figure 4:** Expected reactions responsible for Li-ion photo-extraction at the positive electrode in TiO<sub>2</sub>//Li<sup>0</sup> electrochemical cell.

When charging the TiO<sub>2</sub> electrode under light (**Figure 3-curve n°2**), two phenomena should happen simultaneously (**Figure 5**):

- 1) Li-ion extraction, imposed by the electrochemical charge process,
- 2) Li-ion photo-extraction, induced by the illumination (as described in **Figure 4**).

The polarization between the discharge and charge curves is reduced upon illumination: from 190 to 160 mV (**Figure 3-a**). This mostly results from the decrease in potential of the “light charge plateau” (II’), suggesting a faster charging process. In terms of light-matter interactions, these observations directly witness the participation of photo-carriers in the processes involved in charge storage. The photo-generated charges would allow faster Li<sup>+</sup> and/or e<sup>-</sup> transport across the nanoparticles, which could enhance the

overall charge kinetics and/or the reversibility of the system. Li<sup>+</sup> de-insertion is thereby photo-assisted, and extra charge capacity under illumination results from the extra Li-ion photo-extraction.

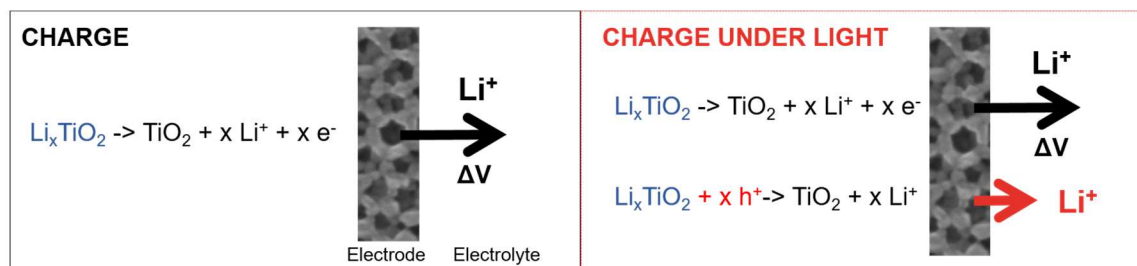


**Figure 5:** Expected reactions upon charge in dark (left) and under illumination (right).

When discharging the TiO<sub>2</sub> electrode under light (**Figure 3-curve n°4**), two phenomena should happen simultaneously (**Figure 6**):

- 1) Li-ion insertion, imposed by the electrochemical discharge process,
- 2) Li-ion photo-extraction, induced by the illumination.

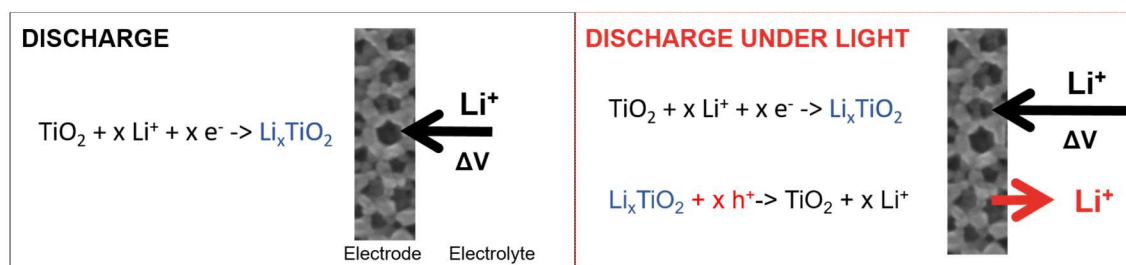


**Figure 6:** Expected reactions upon discharge in dark (left) and under illumination (right).

The position in potential of the discharge plateau (II) does not seem to be as much affected by light as the charge plateau, although the light discharge capacity is much higher than in the dark. This observation tends to indicate that (i) discharge kinetics is not significantly affected, and (ii) that new accessible sites for Li<sup>+</sup> are being created. If the above light-induced charge mechanism is the only one involved, the extra positions for Li<sup>+</sup> would come from lithium ions being simultaneously photo-extracted and thus leaving empty sites for further Li<sup>+</sup> insertion. These are now available for extra Li<sup>+</sup> to enter the electrode material (**Figure 6**). Electrochemically induced reduction/ Li<sup>+</sup> insertion and Li<sup>+</sup> photo-extraction/Ti<sup>3+</sup> photo-oxidation would then happen simultaneously.

The fact that the discharge kinetics is not affected by illumination tends to show that photo-generated carriers do not impact Ti<sup>4+</sup> reduction process or Li<sup>+</sup> insertion

transport. In conclusion, among the photo-generated charge, holes appear to play a predominant role in photo-charging, through Ti<sup>3+</sup> oxidation and Li<sup>+</sup> extraction kinetics enhancement.

### III.2 – Cyclic voltammetry experiments

The analysis of CVs performed at 0.5 mV.s<sup>-1</sup> in dark and under illumination (**Figure 7**) highlights the same conclusions concerning the improved behavior under light. The oxidation peak (Ti<sup>3+</sup> in Ti<sup>4+</sup>) associated with Li<sup>+</sup> extraction also increases in intensity, and its position shifts towards lower potential (dark: 2.24 V to light: 2.16 V). This 80mV-shift points towards improved kinetics for the oxidation process/ Li<sup>+</sup> extraction process under light stimulation.

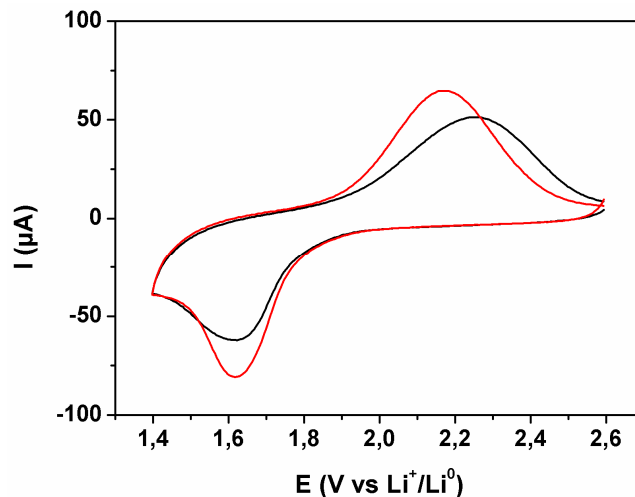


**Figure 7:** Cyclic voltammograms (CV) at 0.5 mV.s<sup>-1</sup> under dark (black) and light (red) conditions with TiO<sub>2</sub> (230 nm-thick, PBPEO, 1M TiCl<sub>4</sub>) as working electrode.

On the other hand, the reduction peak (Ti<sup>4+</sup> in Ti<sup>3+</sup>), which corresponds to Li-insertion (1.61 V), increases in intensity under light, while its position remains unchanged, suggesting no improvement in Li<sup>+</sup> transport kinetics upon lithium ion insertion but “extra Li<sup>+</sup> inserted”.

Similarly to the discharge-charge experiment, we expect the enhancement of the reduction peak intensity to result from extra Li<sup>+</sup> insertion into sites freed during the simultaneous Li<sup>+</sup> photo-extraction. It is to mention that the CV was performed in water-cooled cell, showing that an increase in temperature cannot be fully responsible for improved kinetics.



The impact of the sweep rate onto charge–discharge processes was studied under dark and light conditions (**Figure 8**).

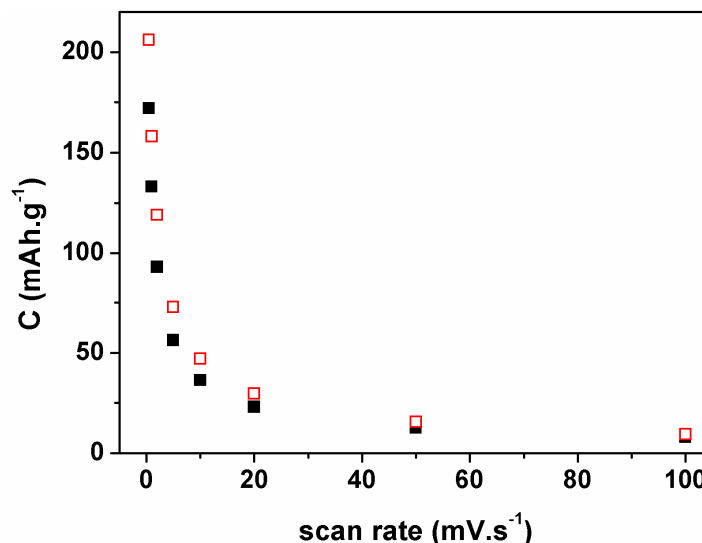


**Figure 8:** Specific charge inserted as a function of CV scan rate.

As expected, in the dark, the evolution of the capacity as function of scan rate exhibits two distinct regions: (i) at low scan rate (below 10 mV/s), the capacity is dominated by the faradaic-insertion reactions and lithium insertion into the anatase structure and (ii) at a high scan rate (higher than 10 mV/s) the capacity represents the contribution of capacitive charge storage. Under light, these two distinct regions are also present but the impact of light is solely observed for low sweep rates, where charge storage is mainly due to faradaic contribution. At high sweep rate, the cell resistance becomes too large, mostly due to the slow diffusion of Li<sup>+</sup> in the electrolyte, and the photo-generated electrons cannot compensate for the kinetic limitations.<sup>10</sup> This result could indicate that here light affects the insertion capacity and not the capacitive charge storage.

## IV – Evaluation of the photo-current intensity

### IV.1 – Potentiostatic experiments

The contribution of anodic and cathodic photocurrent was also highlighted through potentiostatic experiments where light was switched on/off every 1 min (**Figure 9**). Starting from the fully lithiated state  $\text{Li}_{0.5+y}\text{TiO}_2$ , the potential was set to 1.95 V (**Figure 9-curve n°1**). This value corresponds to the beginning of the oxidation peak observed on the CV curve (**Figure 7**).

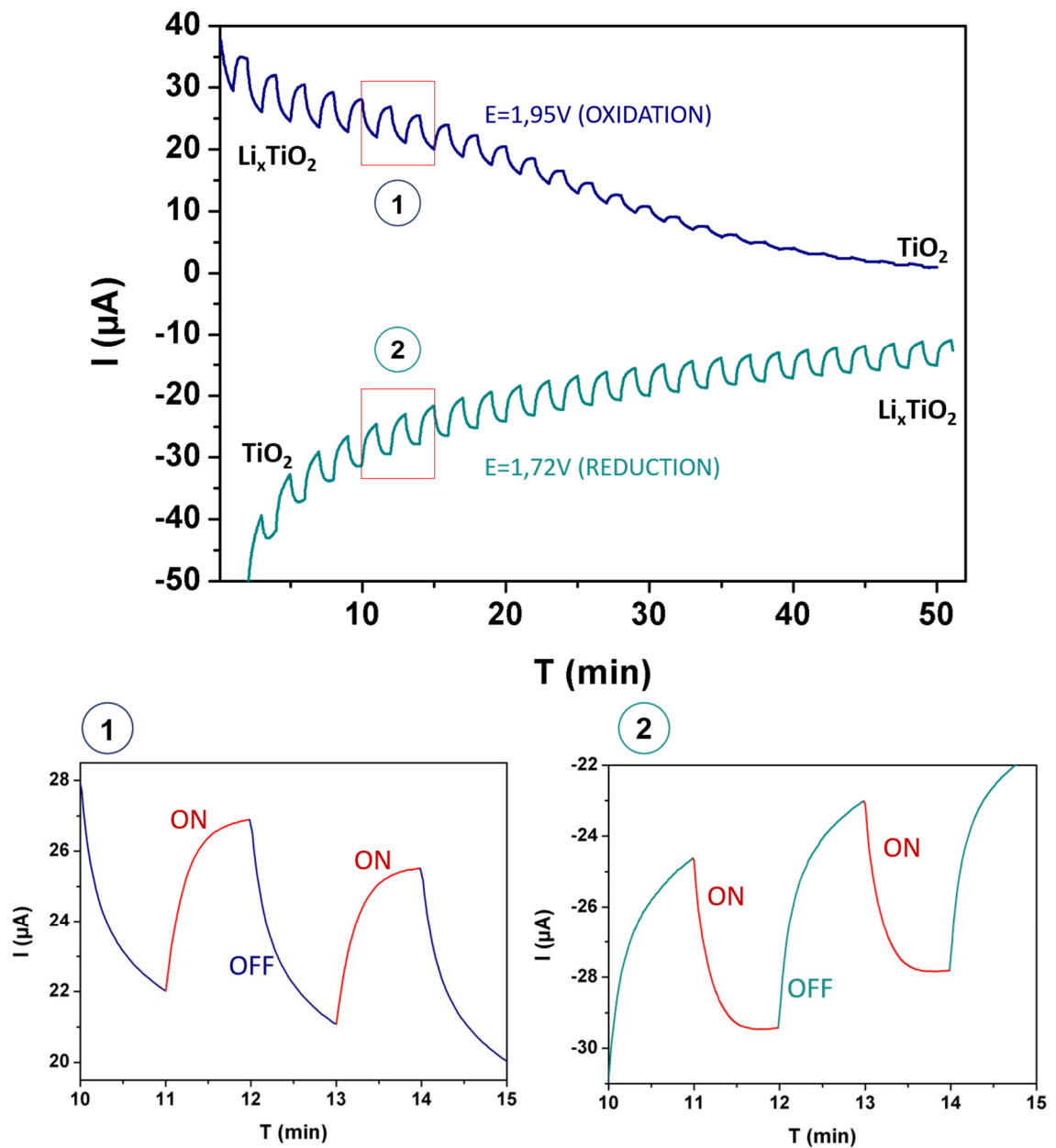


**Figure 9:** Potentiostatic experiments under chopped illumination, light is switch on and off every 1 min for  $E$  set at 1.95 V (blue) and 1.72 V (green).

An oxidation current corresponding to Li<sup>+</sup> extraction was observed, and the film got progressively transparent. When the light was switched on, the current increased quickly in about 25 sec. and tended to reach saturation after 1 min.

This observation can again be explained by the fact that under illumination, holes are generated and participate to the oxidation of Ti<sup>3+</sup> to Ti<sup>4+</sup>, accelerating thereby the kinetic of Li<sup>+</sup> extraction.<sup>11</sup> When the film got progressively transparent during the Li<sup>+</sup> extraction and photo-extraction, photo-currents progressively decreased. In fact, as the light promoted Li<sup>+</sup> photo-extraction, light effects became inexistent when the anatase electrode got progressively fully delithiated.

Starting from the lithium anatase poor phase, the potential was set to 1.72 V (Figure 9-curve n°2). A reduction current was observed as expected for Ti<sup>4+</sup> to Ti<sup>3+</sup> reduction and the film got progressively blue. When light was switched on, the current increased and reached a maximum value after about 25 s of illumination.

Photo-generated holes are expected to participate to the extraction of Li<sup>+</sup>, whereas in this case the applied potential encourages Li<sup>+</sup> insertion. The photo-extraction of Li<sup>+</sup> releases new sites, which are now available to be electrochemically filled, therefore giving rise to larger reduction current, which is coherent with the galvanostatic and CV experiments previously analyzed.

Photo-current intensities can be exploited in order to estimate the amount of photo-extracted Li<sup>+</sup> during 1 minute of illumination for a 500 nm-thick PB-PEO (TiCl<sub>4</sub> 2M) mesoporous anatase electrode. By integration (Figure 10), the average photo-capacity for 1 minute under light is estimated at 0.3 mC, which is 8.10<sup>-5</sup> mAh (**Table 1**). This value represents  $\approx 0.3\%$  of the total electrode capacity, when Li<sub>0.5</sub>TiO<sub>2</sub> is taken as the 100% lithiated reference (**Table 2**). If Li<sup>+</sup> photo-extraction is the only phenomenon responsible for the observed photo-current, it means that  $\approx 0.3\%$  of the total amount of lithium in Li<sub>0.5</sub>TiO<sub>2</sub> is extracted in 1 min under illumination. On the base of this quick estimation, a 500 nm-thick anatase electrode Li<sub>0.5</sub>TiO<sub>2</sub> could thus be fully delithiated in about 6.2 h under illumination.

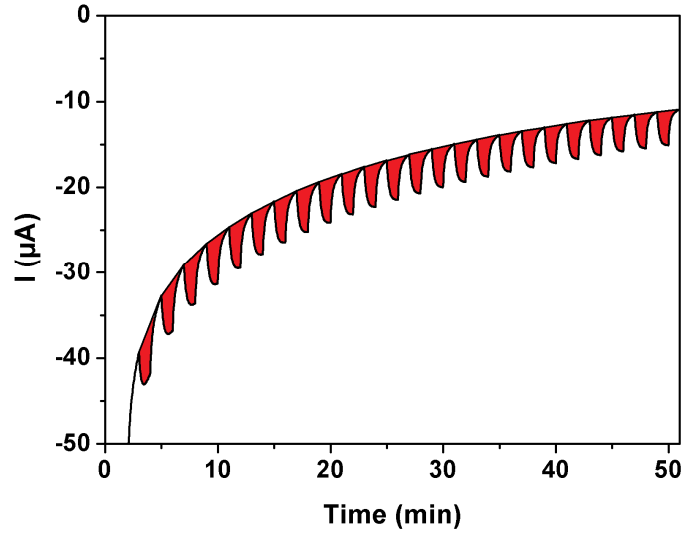


**Figure 10:** Potentiostatic experiments under chopped illumination, light is switch on and off every 1 min for E set at 1.72 V. Red area corresponds to the integrated photo-charge.

Photo-capacity for 1 min under light	0.3 mC/8.10 <sup>-5</sup> mAh
Photo-current	5 μA

**Table 1:** Estimation of the average photo-capacity and photo-current based on the integration of the photo-current for a 50 min potentiostatic experiment at 1.72 V.

Electrode thickness	500 nm
Electrode surface	1.0 cm <sup>2</sup>
Electrode porosity	≈ 15%
Electrode mass	0.18 mg
Li <sub>0.5</sub> TiO <sub>2</sub> theoretical capacity	168 mAh.g <sup>-1</sup>
Electrode capacity	3.10 <sup>-2</sup> mAh

**Table 2:** Electrode characteristics and calculated electrode capacity.

## IV.2 – Open circuit voltage experiments

In order to test this estimation, Open Circuit Voltage (OCV) experiment was performed under illumination after a sequence of discharge-charge-discharge galvanostatic experiment at  $\pm 30 \mu\text{A}$  (**Figure 11**). During relaxation under light (**Figure 11-curve n°1**), Li<sup>+</sup> got photo-extracted, potential of lithiated anatase got from 1.5 V to 2.5 V in about 8 h, with a coexistence of lithium rich phase and poor phase during about 4 h (*cf.* the plateau potential **Figure 11**). This 500 nm-thick electrode (1 cm<sup>2</sup>, TiCl<sub>4</sub> 2M) can therefore be photo-recharged in a period of time which is

coherent in regards to the estimated photo-capacity under chopped illumination (6.2 h). Relaxation in dark conditions (**Figure 11-curve n°2**) allows the electrode to reach 2.1 V in about 1 day, which is probably due to the self-delithiation of the system.

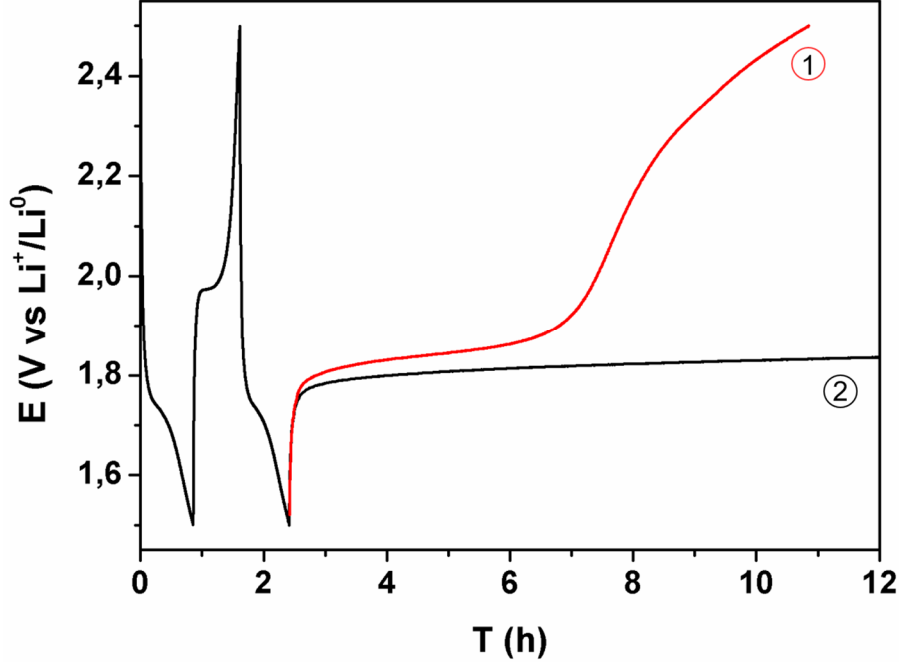


**Figure 11:** Open Circuit Voltage (OCV) experiment under illumination (curve n°1) and in dark conditions (curve n°2) after a discharge-charge-discharge galvanostatic experiment at  $\pm 30 \mu\text{A}$ . Experiment is realized in a water-cooled glass cell.

The average photo-current  $I_{\text{light}}$  ( $\approx 5 \mu\text{A}$ ) was estimated as followed:

$$I_{\text{light}} = \frac{C_{\text{light},60\text{sec}}}{60} \quad (7)$$

where  $C_{\text{light},60\text{sec}}$  (in  $\mu\text{C}$ ) is the photo-capacity obtained during 60 sec. under light based on the integration of the photo-current for a 50 min potentiostatic experiment at 1.72V.

## V – Adjusting the rates of simultaneous electrode discharge and photo-recharge

If this estimation is correct ( $I_{\text{light}} \simeq 5 \mu\text{A}$  for a 500 nm-thick electrode of 1 cm<sup>2</sup> using titania precursor solution at 2M, *i.e.*  $\simeq 0.3 \text{ mA.g}^{-1}$ ), and if the described two coexisting reactions (*i.e.* Li<sup>+</sup>-electrochemical insertion and Li<sup>+</sup>-photo-extraction) do happen during the discharge under illumination (**Figure 6**), it means that we could adjust the discharge rate to be exactly compensated by the photo-charge of the electrode.

At  $-8 \mu\text{A}$  ( $\simeq C/2.5$ ) (**Figure 12**), comparison of the galvanostatic experiments under dark (**Figure 12-curve n°1**) and light (**Figure 12-curve n°2**) clearly indicates a drastic enhancement of the capacity under light ( $375 \text{ mAh.g}^{-1}$ ).

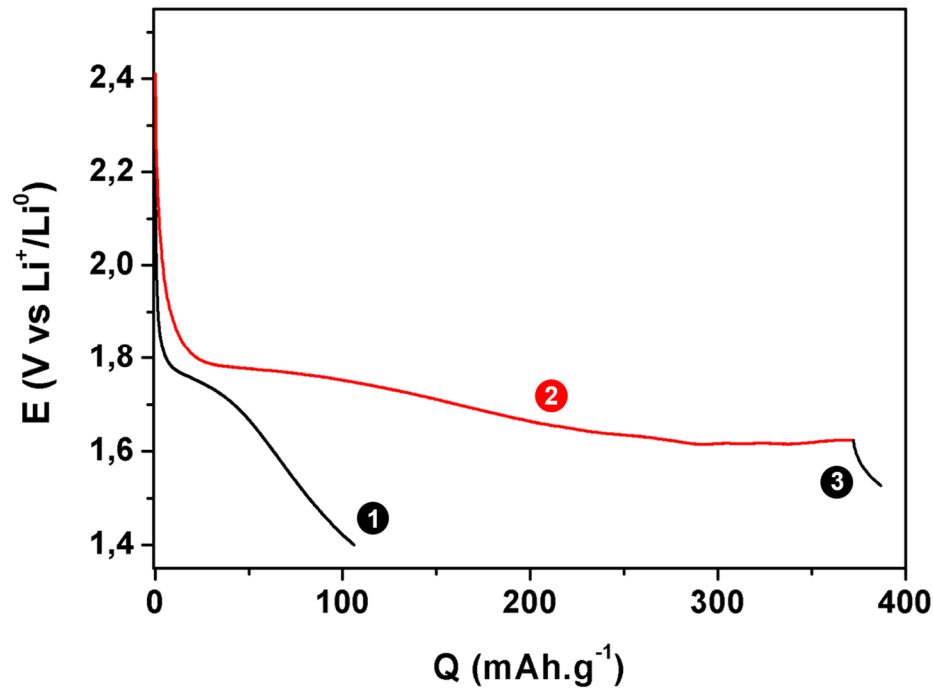


**Figure 12:** Galvanostatic experiment at  $-8 \mu\text{A}$  ( $\simeq C/2.5$ ) under dark (1) and light (2) conditions for a 520 nm-thick TiO<sub>2</sub> mesoporous electrode. Illumination is stopped during step (3). Experiment is realized in a water-cooled glass cell.

This capacity even exceeds the theoretical capacity of LiTiO<sub>2</sub> ( $335 \text{ mAh.g}^{-1}$ ), which could anyway not be reached at this reduction potential. For this slower discharge rate ( $-8 \mu\text{A}$ ), Li<sup>+</sup> photo-extraction is fast enough to compensate for the Li<sup>+</sup>-electrochemical insertion. In these conditions, the photo-charge of the electrode can thus counterbalance the slow discharge of the electrode. After about 8 h under light, the

illumination is then stopped (3), and discharge can be completed down to 1.5 V vs  $\text{Li}^+/\text{Li}$ .

In order to check the stability of the electrode, charge-discharge cycles at  $\pm 20 \mu\text{A}$  have been compared before and after the galvanostatic experiment at  $-8 \mu\text{A}$  under light (Figure 13).

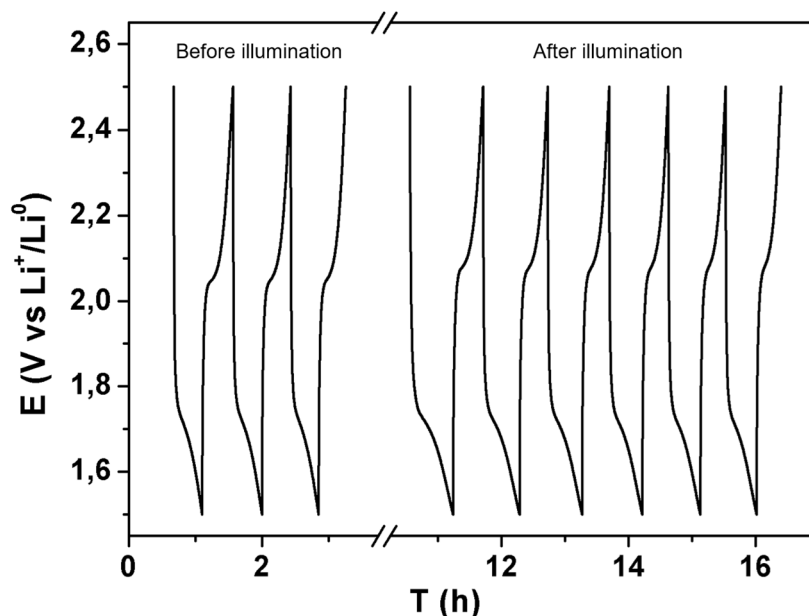


**Figure 13:** Galvanostatic discharge-charge experiment ( $\pm 20 \mu\text{A}$ ) before and after slow discharge under light ( $-8 \mu\text{A}$ ) for a 520 nm-thick  $\text{TiO}_2$  mesoporous electrode.

The observed unchanged capacities do not show particular signs of electrode modifications or degradations. FEG-SEM observation of the film after the experiment also tends to confirm the good conservation of the film porous structure, which did not collapse during the charge-discharge sequences (Figure 14).

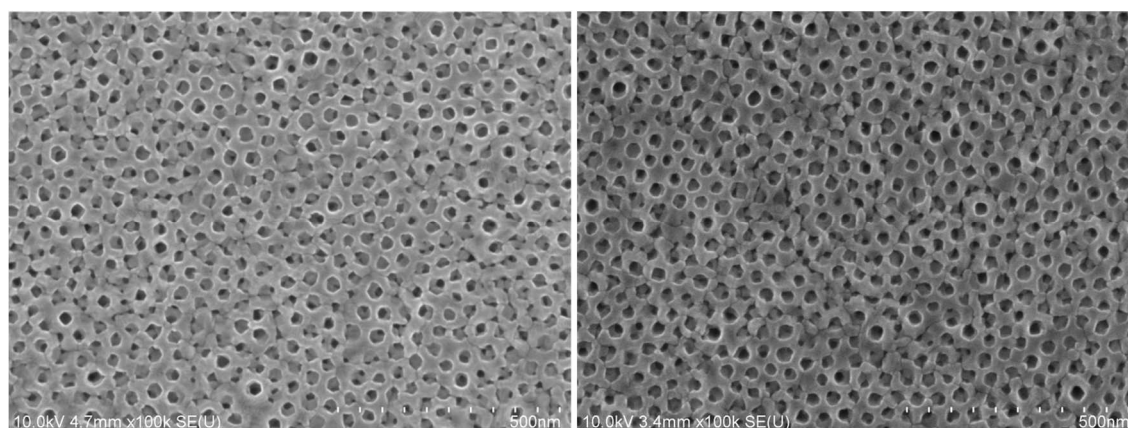


**Figure 14:** FEG-SEM pictures of  $\text{TiO}_2$  thin films planar sections before (left) and after (right) stabilization step and galvanostatic experiments. Electrodes were washed using water and flushed with  $\text{N}_2$  for 10 sec. before analysis. Be aware that potential SEI degradation products are here not visible due to their solubilization in water.

## VI – Conclusion

In this chapter, we have performed experiments to characterize the photo-electrochemical behavior of TiO<sub>2</sub> electrode considered as a positive electrode in a 3-electrode configuration (TiO<sub>2</sub> // LP30 // Li, Li).

Comparison of the electrochemical studies performed under light and dark conditions clearly indicates that light enhances the electrochemical charge/discharge properties. These results highlight that photo-induced de-insertion mechanism has been achieved for carbon- and dye-free TiO<sub>2</sub> based mesoporous film electrode. Light induces the formation of electron/hole pairs and those charge carriers influence the mobility of lithium ion and/or participate in the oxidation of Ti<sup>3+</sup> and facilitate Li<sup>+</sup> de-insertion.

Order of magnitude of photo-currents intensities ( $I_{\text{light}} \simeq 5 \mu\text{A}$  for a 500 nm-thick electrode of 1 cm<sup>2</sup> using titania precursor solution at 2M and PB-PEO, *i.e.*  $\simeq 30 \text{ mA.g}^{-1}$ ) has been estimated through potentiostatic experiments under chopped illumination and have been confirmed by OCV experiments and galvanostatic experiments under light. In fact, by adjusting the estimated kinetics of the photo-charge (Li<sup>+</sup>-photo-extraction) to an equivalent opposite Li<sup>+</sup>-electrochemical insertion (electrochemical discharge), apparent “infinite” capacity could be achieved during galvanostatic experiments under light (**Figure 12**). This phenomenon validates, in a simple and efficient way, the hypothesis of the compensation of the electrode electrochemical discharge by the photo-induced electrode recharge, and thereby confirms the mechanism of Li-ion photo-induced extraction for TiO<sub>2</sub> mesoporous electrode.

Nonetheless, in this chapter, we have not considered yet the eventual reaction of the photo-generated charges with the electrolyte. Can for example TiO<sub>2</sub> also plays the role of a photo-catalyst for the electrolyte? More broadly, what parameters could influence the photo-induced phenomena (from the generation to the recombination/reaction) and what could be the consequences for the TiO<sub>2</sub> photo-recharge?

In the next chapter, photo-induced mechanisms are therefore further investigated using several ways: (1) by playing with the electrode architecture and the electrolyte in order to analyze their influence on the fate of the photo-generated charges (2) by probing the electrode and the electrolyte through *post mortem* analysis to find eventual traces of electrolyte degradation (3) by realizing *operando* measurements to study the system in real time upon illumination.



## Bibliography

1. Betz, G., Tributsch, H. & Marchand, R. Hydrogen insertion (intercalation) and light induced proton exchange at TiO<sub>2</sub> (B)-electrodes. *J. Appl. Electrochem.* **14**, 315–322 (1984).
2. Paoella, A. *et al.* Light-assisted delithiation of lithium iron phosphate nanocrystals towards photo-rechargeable lithium ion batteries. *Nat. Commun.* **8**, 14643 (2017).
3. Lou, S. N. *et al.* An Operando Mechanistic Evaluation of a Solar-Rechargeable Sodium-Ion Intercalation Battery. *Adv. Energy Mater.* **7**, 1700545 (2017).
4. Guo, Y.-G., Hu, Y.-S. & Maier, J. Synthesis of hierarchically mesoporous anatase spheres and their application in lithium batteries. *Chem. Commun.* **0**, 2783–2785 (2006).
5. Wagemaker, M., Lützenkirchen-Hecht, D., van Well, A. A. & Frahm, R. Atomic and Electronic Bulk versus Surface Structure: Lithium Intercalation in Anatase TiO<sub>2</sub>. *J. Phys. Chem. B* **108**, 12456–12464 (2004).
6. Lafont, U., Carta, D., Mountjoy, G., Chadwick, A. V. & Kelder, E. M. In Situ Structural Changes upon Electrochemical Lithium Insertion in Nanosized Anatase TiO<sub>2</sub>. *J. Phys. Chem. C* **114**, 1372–1378 (2010).
7. van de Krol, R., Goossens, A. & Schoonman, J. Spatial Extent of Lithium Intercalation in Anatase TiO<sub>2</sub>. *J. Phys. Chem. B* **103**, 7151–7159 (1999).
8. Khomenko, V. M., Langer, K., Rager, H. & Fett, A. Electronic absorption by Ti<sup>3+</sup> ions and electron delocalization in synthetic blue rutile. *Phys. Chem. Miner.* **25**, 338–346 (1998).
9. Naldoni, A. *et al.* Effect of Nature and Location of Defects on Bandgap Narrowing in Black TiO<sub>2</sub> Nanoparticles. *J. Am. Chem. Soc.* **134**, 7600–7603 (2012).
10. Augustyn, V. *et al.* High-rate electrochemical energy storage through Li<sup>+</sup> intercalation pseudocapacitance. *Nat. Mater.* **12**, 518–522 (2013).
11. Usui, H., Miyamoto, O., Nomiya, T., Horie, Y. & Miyazaki, T. Photo-rechargeability of TiO<sub>2</sub> film electrodes prepared by pulsed laser deposition. *Sol. Energy Mater. Sol. Cells* **86**, 123–134 (2005).

## **CHAPTER 4**

### **Photo-induced mechanisms: investigation**



## TABLE of CONTENT

I - Introduction.....	127
II – Photo-induced mechanisms: dependence on the electrode architecture and role of the electrolyte.....	128
II.1 – Dependence on the electrode architecture.....	128
II.1.1 – Influence of the electrode thickness.....	128
II.1.2 – Influence of the porous network.....	131
II.2 – Role of the electrolyte .....	137
II.2.1 – TiO <sub>2</sub> photo-electrode in an ionic liquid-based electrolyte .....	137
II.2.2 – TiO <sub>2</sub> photo-electrode in a “water-in-salt” electrolyte.....	144
III – <i>Post mortem</i> analysis of the photo-electrode.....	149
III.1 – FEG-SEM and complementary EDX analysis .....	149
III.2 – Probing the electrode surface with XPS .....	154
III.3 – Analysing the electrolyte by NMR spectroscopy.....	162
IV – TiO <sub>2</sub> photo-electrode: <i>operando</i> characterizations.....	168
IV.1 – Electrochemical Impedance Spectroscopy (EIS) .....	168
IV.1.1 – Nyquist plots and equivalent circuits.....	168
IV.1.2 – Results of the fits and analysis .....	171
IV.2 – Investigations by means of Electrochemical Quartz Crystal Microbalance (EQCM) .....	174
IV.2.1 – Principle of Quartz Crystal Microbalance (QCM) .....	174
IV.2 – EQCM and $[F(\Delta m/\Delta Q)]$ function.....	175
IV.2.3 – EQCM study for Li-ion photo-battery electrode.....	177
V – Conclusion .....	191
Bibliography .....	193



## I - Introduction

The fate of the photo-generated charges results from the competition between charge recombination and charge diffusion and/or reaction. It is expected to be strongly influenced by (1) the electrode architecture (crystallite size, crystallite connectivity, grain boundaries, electrode thickness, *etc.*), or by (2) the choice of the electrolyte (which imposes the species at the electrode/electrolyte interface). In this first section, we will first propose to play with the electrode architecture in order to identify structural parameters that could directly influence the  $\text{Li}^+$  photo-extraction. This study is allowed by the mesoporous electrode, whose architecture is well-defined and easily tunable using sol-gel coupled dip coating process combined with the “evaporation induced self-assembly” (EISA) approach. We will then compare the photo-electrochemical behavior of the electrode in three different kinds of electrolyte (organic, ionic liquid, “water-in-salt”-based electrolytes). In each case, photo-induced phenomena at the electrode/electrolyte interface is discussed in order to yield a more consistent picture of the fate of generated-excitons.

Illumination of the electrode upon cycling could potentially led to electrolytes degradation. In the second section, *post mortem* analyses are performed on both the electrode and the electrolyte in order to detect the possible species formed in dark and light conditions. Electrode surfaces are analyzed at different steps of the electrode (photo)-electrochemical cycling by means of FEG-SEM, EDX, and XPS techniques. Evolution of the electrolyte is also complementarily probed by NMR spectroscopy. The adequation of the *post mortem* study with the analysis made in the first section is discussed.

In the third section, photo-induced mechanisms are investigated in real time by means of *operando* measurements. The system is first analyzed by EIS measurements, in order to probe the electrical properties of the material in dark conditions, and compare them under illumination. We then propose a preliminary work dedicated to the analysis of the gravimetric response of a  $\text{TiO}_2$ -coated piezoelectric substrate ( $\text{GaPO}_4$ ) when coupled to electrochemical and photo-electrochemical measurements. Here, a new specially designed experimental setup is proposed to study the nature of species involved at the electrode/electrolyte interface upon photo-electrochemical cycling.

## II – Photo-induced mechanisms: dependence on the electrode architecture and role of the electrolyte

### II.1 – Dependence on the electrode architecture

#### II.1.1 – Influence of the electrode thickness

Electrochemical and photo-electrochemical responses of titania films were compared for different electrode thicknesses obtained using the multilayered dip-coating process described in Chapter 2.II.1. For this purpose, photo-electrodes were performed in a 3-electrode configuration using  $\text{TiO}_2$  as working electrode, metallic lithium foils as reference and counter-electrodes, and LP30 as electrolyte.

Anatase  $\text{TiO}_2$  thin films were prepared with PB-PEO at 2M in  $\text{TiCl}_4$  with thicknesses varying between 110 nm and 1500 nm (**Figure 1**).

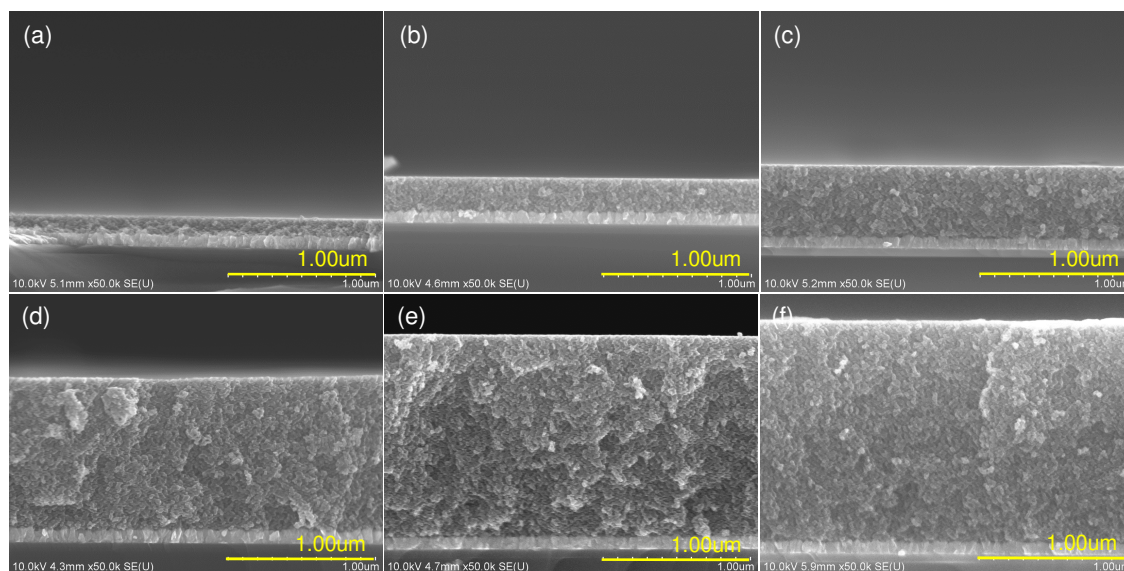


**Figure 1:** FEG-SEM photos of  $\text{TiO}_2$  (PBPEO, 2M in  $\text{TiCl}_4$ ) cross-sections. The film thickness in nm and the number of dipped layers (in brackets) are: 110 (1), 230 (2), 520 (5), 1050 (10), 1320 (12), 1500 (14) (from (a) to (f)).

Capacities under dark (black) and light (red) conditions were evaluated by integration of the  $i(t)$  function ( $i$  for current intensity), which was deduced from cyclic voltammetry experiments performed at  $0.5 \text{ mV.s}^{-1}$  between 2.6 V and 1.4 V versus  $\text{Li}^+/\text{Li}^0$ .

In **Figure 2**, dark capacities are plotted as a function of the  $\text{TiO}_2$  film thickness, with a normalization by the electrode mass.<sup>i</sup> For the same scan rate ( $0.5 \text{ mV.s}^{-1}$ ), mass capacities were reduced by a factor 2.5 ( $155$  to  $62 \text{ mAh.g}^{-1}$ ) when the electrode thickness is multiply by a factor 14 ( $110$  to  $1500 \text{ nm}$ ). This diminution could be due (1) to the more important distance that electrons have to overcome from the current collector to the electrode/electrolyte interface when increasing the film thickness, or (2) to restricted diffusion of the electrolyte into the first dipped  $\text{TiO}_2$  layers of the film, near the FTO (referred as “inner layers”). In fact, as inner layers are expected to be less porous than the surface layers ( $9\%$  vs.  $26\%$  for example for a  $280 \text{ nm}$ -thick  $\text{TiO}_2$  film dipped with 5 layers<sup>1</sup>), their accessibility for the electrolyte could limit the complete development of the electrode/electrolyte interface in the entire thickness of the film.

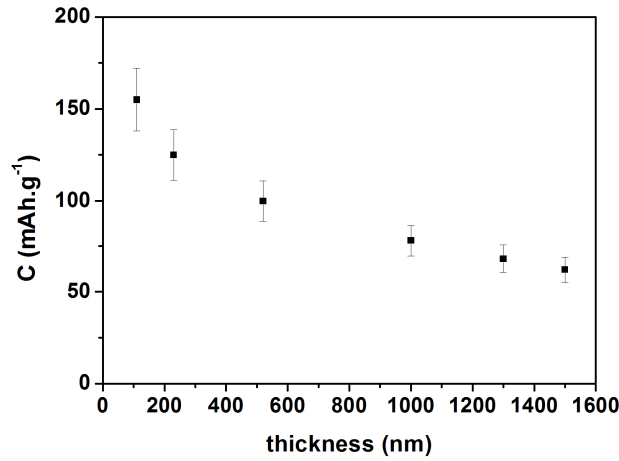


**Figure 2:** Mass discharge capacity calculated from CVs at  $0.5 \text{ mV.s}^{-1}$  ( $2.6 \text{ V}$  to  $1.4 \text{ V}$  vs.  $\text{Li}^+/\text{Li}^0$ ) under dark conditions, plotted as a function of the film thickness.

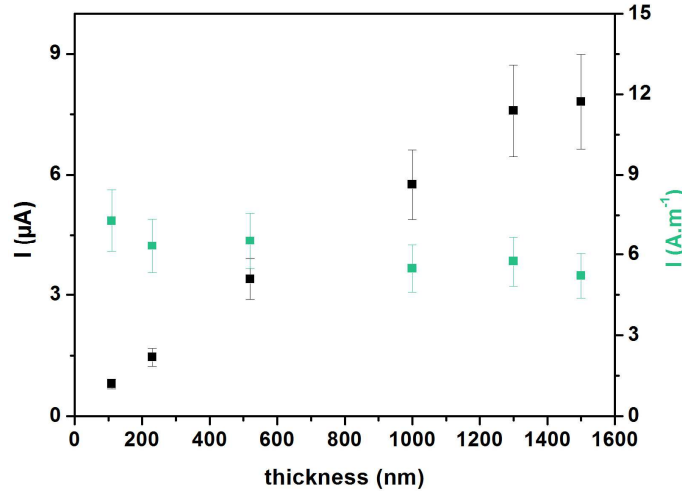
Photo-current intensities (**Figure 3**, in black) and photo-current normalized by the electrode thickness (**Figure 3**, in green) were calculated from potentiostatic experiments ( $1.72 \text{ V}$  vs.  $\text{Li}^+/\text{Li}^0$ ) under chopped illumination (light on/off every  $30 \text{ sec.}$ ).

Photo-current intensities (in dark) increase with the film thickness, but do not evolve linearly; the photo-current for a  $1500 \text{ nm}$ -thick electrode ( $\approx 8 \mu\text{A}$ ) is not 14 time higher than photo-current for a  $110 \text{ nm}$ -thick electrode ( $\approx 1 \mu\text{A}$ ). Additionally, a slight

<sup>i</sup> Plotted error bars report the standard deviation obtained for a film thickness of  $230 \text{ nm}$  (sample of 4 different films). The corresponding error percentage ( $\approx 11\%$  here *e.g.* for the capacities) is then reported for all the other thickness values to approximate the standard deviation for each thickness. The same methodology will be applied for others functions (capacity enhancement under light, photo-currents, *etc.*)



decrease of the normalized intensities (green) ( $\simeq 7 \mu\text{A}.\mu\text{m}^{-1}$  at 110 nm vs.  $\simeq 5.5 \mu\text{A}.\mu\text{m}^{-1}$  at 1.5  $\mu\text{m}$ ) is observed.



**Figure 3:** Photo-current (dark) and photo-current normalized by the electrode thickness (green) calculated from potentiostatic experiment (1.72 V vs.  $\text{Li}^+/\text{Li}^0$ ) under chopped illumination (light on/off every 30 sec.) plotted as a function of the film thickness.

In order to interpret the evolution of the photo-currents as a function of the electrode thickness, it may be worth to remind that intensity of photo-currents depends of the amount of lithiated phase of  $\text{TiO}_2$ . In fact, the lithiated phase of  $\text{TiO}_2$  is expected to be the photo-active phase, due to the presence of  $\text{Ti(III)}$  sites for the reaction with photo-generated holes. Therefore, it should be taken under consideration that if a film A has a lower mass capacity in dark than a film B (*i.e.* a lower proportion of lithiated phase), photo-currents are expected to be lower for film A than for film B.

Hypotheses can be formulated to explain the no linearity and the normalized photo-current decrease. This decrease could (1) simply results from the fact that capacities of thick films were smaller than thin films (which implies a lower proportion of photo-active lithiated phase) (see **Figure 2**), and/or, (2) be due to a decrease of the intensity of the photo-induced phenomena for thicker  $\text{TiO}_2$  films (decrease of the photo-charges generation, or increase of photo-charges recombinations for instance).

In order to address this question, we have plotted the gain in capacity under illumination when compared to the capacities in dark conditions, in %, (referred as “capacity enhancement under illumination”).

The **Figure 4** presents the capacities obtained under dark (black) and light (red) conditions and the capacity enhancement under illumination (in %, green) as a function

of the electrode thickness. Results show that gain in capacities are higher for films with a thickness above  $\approx 500$  nm (capacities enhancement of  $\approx 30$ -35%) than for film with a thickness below  $\approx 500$  nm (capacities enhancement of  $\approx 15$ -20%). As thicker films are in average denser than thin films (porous volume of  $\approx 12\%$  for a 1  $\mu\text{m}$ -thick film and  $\approx 20\%$  for a 200 nm-thick electrode, see chapter 1 section III.1.2), this increased density could maybe promote a better photo-charges separation (leading to a better photo-electron evacuation for example) and eventually explain the higher gains.

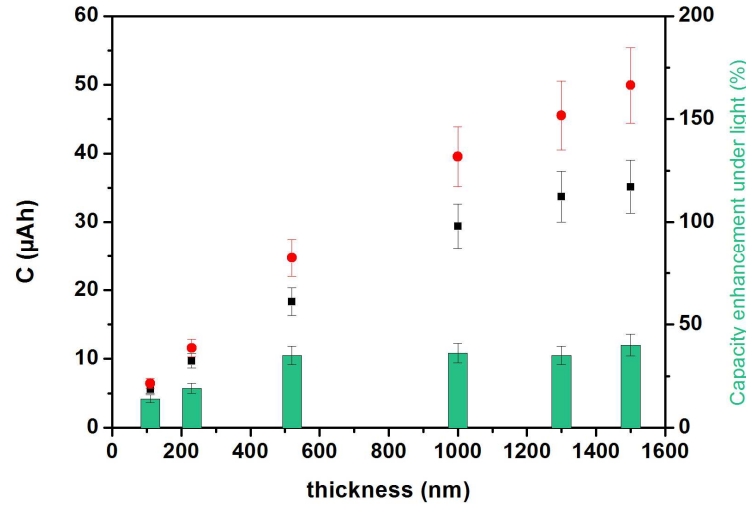


**Figure 4:** Capacity calculated from CVs at  $0.5 \text{ mV.s}^{-1}$  (2.6 V to 1.4 V vs.  $\text{Li}^+/\text{Li}^0$ ) under dark (black) and light (red) conditions are plotted as a function of the film thickness for electrode of  $1 \text{ cm}^2$ . Capacity enhancement under illumination (green) is calculated as the gain in capacity (%) when comparing capacities in light vs. in dark.

Hence, in order to study the electrodes with sufficiently high photo-currents (thick films), but also with limited electrolyte/photo-charges diffusion eventual issues (thin films), we will typically work with films between 200 nm and 500 nm.

Based only on these first observations, we could also mention that in order to develop the “ideal” bi-functional electrode for energy conversion storage, thickness compromises will probably need to be found to obtain both high dark capacity and high photo-current. For example, in our case, thin films are better candidates to reach high specific capacity, but thick film seem more interesting to get higher photo-currents. Thick films could also be more adapted if the surface capacity matters (rather than mass capacity for example), depending on targeted application.

### II.1.2 – Influence of the porous network

Photo-electrochemical response was also compared for different kind of porous networks (**Figure 5**). Anatase  $\text{TiO}_2$  thin films were prepared with PB-PEO at 1M in  $\text{TiCl}_4$

(4 dipped layers), at 2M in  $\text{TiCl}_4$  (2 dipped layers) and with Pluronic F127 (2 dipped layer) polymers. By adapting the number of dipped layers for each polymer and  $\text{TiCl}_4$  concentration used, films were compared at a fixed thickness of 230 nm (**Figure 5** and **Figure 6**). Films characteristics are presented in **Table 1**. The potential influence of the porous network on the photo-electrochemical response can thereby be de-correlated from the electrode thickness.

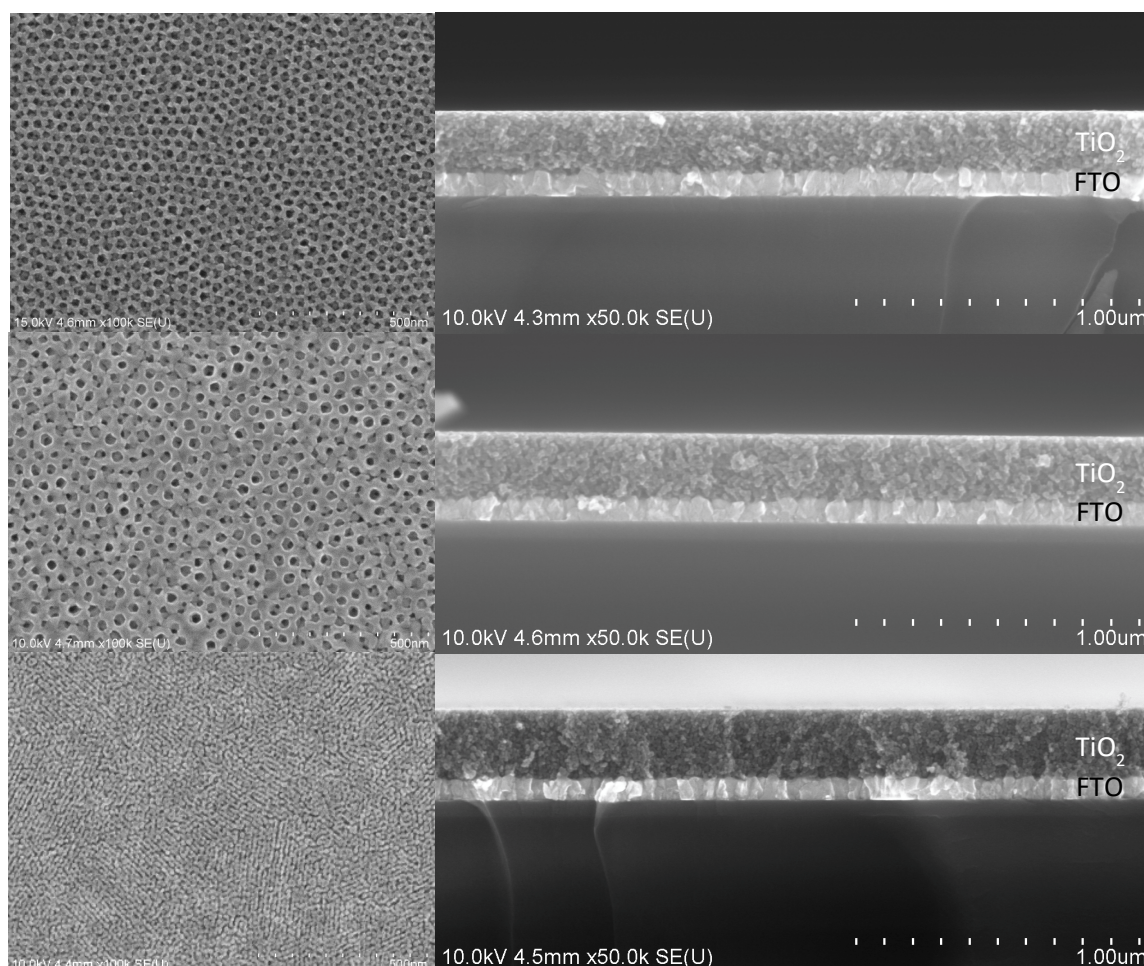


**Figure 5:** FEG-SEM photos of  $\text{TiO}_2$  planar and cross-sections prepared with PB-PEO at 1M in  $\text{TiCl}_4$  dipping 4 layers (top), at 2M in  $\text{TiCl}_4$  dipping 2 layers (middle) and with Pluronic F127 dipping 2 layers (down).

Polymers	$[\text{TiCl}_4]$	Thickness [nm]	Crystallites size [nm]	Porous volume [%]	Pore diameter [nm]
PB-PEO	2M	230	12.8	20	26
	1M	230	8.2	24	26
F127	1M	230	6.8	32	10

**Table 1:** Characteristic of the  $\text{TiO}_2$  films. Thickness is determined by FEG-SEM analysis, porous volume, pore/bottleneck diameters and specific surface area are estimated by

ellipsometric measurements. Crystallite size are determined by glancing angle XRD using silicon substrates instead of FTO substrates.

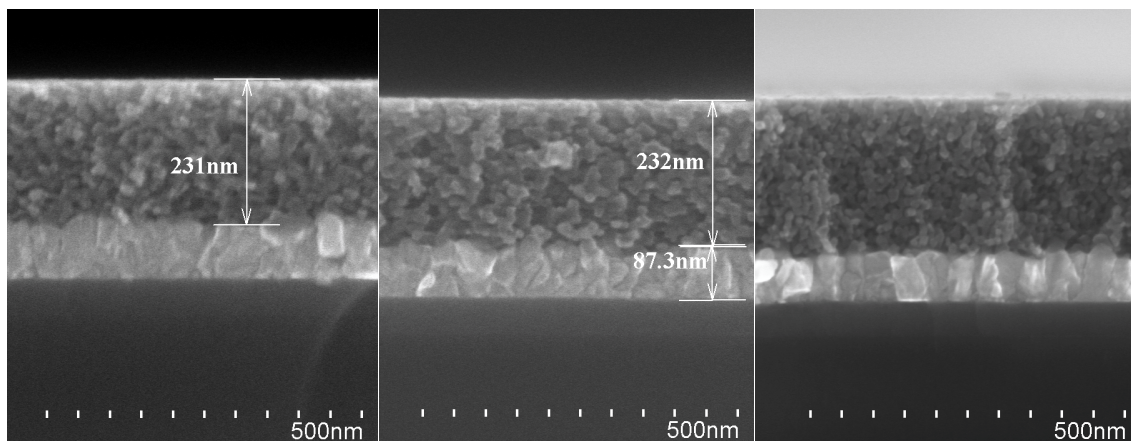


**Figure 6:** FEG-SEM photos of  $\text{TiO}_2$  cross-sections prepared with PB-PEO at 1M in  $\text{TiCl}_4$  dipping 4 layers (left), at 2M in  $\text{TiCl}_4$  dipping 2 layers (middle) and with Pluronic F127 dipping 2 layers (right). Very similar thickness was obtained with success.

Capacities under dark and light conditions (**Figure 7**) were evaluated by means of integration of CV experiments performed at  $0.5 \text{ mV.s}^{-1}$  between 2.6 V and 1.4 V versus  $\text{Li}^+/\text{Li}^0$  (**Annex Figure A.1.4**). Results show that capacity enhancement under light ( $\simeq 20\%$ ) is similar for the three different films. Photo-current intensities were also estimated through potentiostatic experiments (**Annex Figure A.1.5**). No significantly different values ( $\simeq 20 \text{ mA.g}^{-1}$ ) were found for the three porous architectures, which confirms the results of the CV experiments.

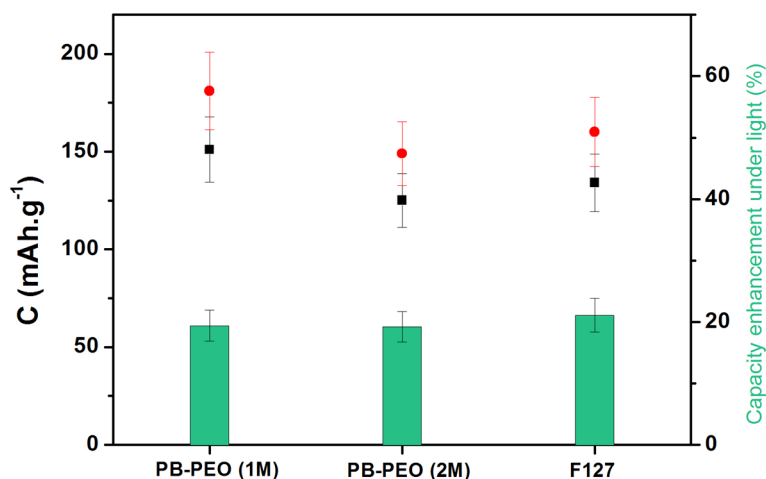


**Figure 7:** Capacity calculated from CVs at  $0.5 \text{ mV.s}^{-1}$  (2.6 V to 1.4 V vs.  $\text{Li}^+/\text{Li}^0$ ) under dark (black) and light (red) conditions plotted for 230 nm-thick anatase films prepared with PB-PEO (1M and 2M in  $\text{TiCl}_4$ ) and with F127. Capacity enhancement under illumination (green) is calculated as the gain in capacity (%) when comparing capacities in light vs. in dark.

These experiments show that the  $\text{Li}^+$  photo-extraction has comparable efficiencies in these 3 different kinds of porous networks. It could show that (1) porous architecture in this studied range of parameters is not critical for the intensity of photo-induced mechanisms, or (2) parameters, which could have opposite effects on the photo-extraction, simultaneously change from one film to another. For example, when the film density increases from F127 to PBPEO ( $\text{TiCl}_4$  2M) to PBPEO ( $\text{TiCl}_4$  1M) films (see **Table 1**), crystallite size also simultaneously decreases.

If we make the hypothesis that a higher film density allows higher photo-currents (as it has been suggest in the previous section), comparable efficiencies for the 3 films could suggest that bigger crystallite size reduces the efficiency  $\text{Li}^+$  photo-extraction.

It is indeed generally thought that the smaller the particle, the wider the charge depletion layer and thereby the more space it occupies within the all  $\text{TiO}_2$  nanoparticle volume. As the electric field generated in the depletion zone allows the separation of the photo-charges, the number of photo-carriers involved in the redox mechanism should be maximized for small particles<sup>2</sup>, which could even become smaller than the hole diffusion length (as order of magnitude, it has been estimated at around 10 nm for rutile  $\text{TiO}_2$  single crystals<sup>3</sup>).

In order to give some response elements, three different heat treatments (1h, 2h and 3h at  $500^\circ\text{C}$ ) were applied to anatase  $\text{TiO}_2$  thin films (PB-PEO, 2M in  $\text{TiCl}_4$ ) in order to see the possible influence of the crystallite size on the photo-extraction efficiency. A crystallite size augmentation was observed for prolonged heat treatment (see refinements results in **Table 1**). It could be due to a possible reorganization and fusion of the crystallites during the prolonged heat treatment (see **Figure 8**).

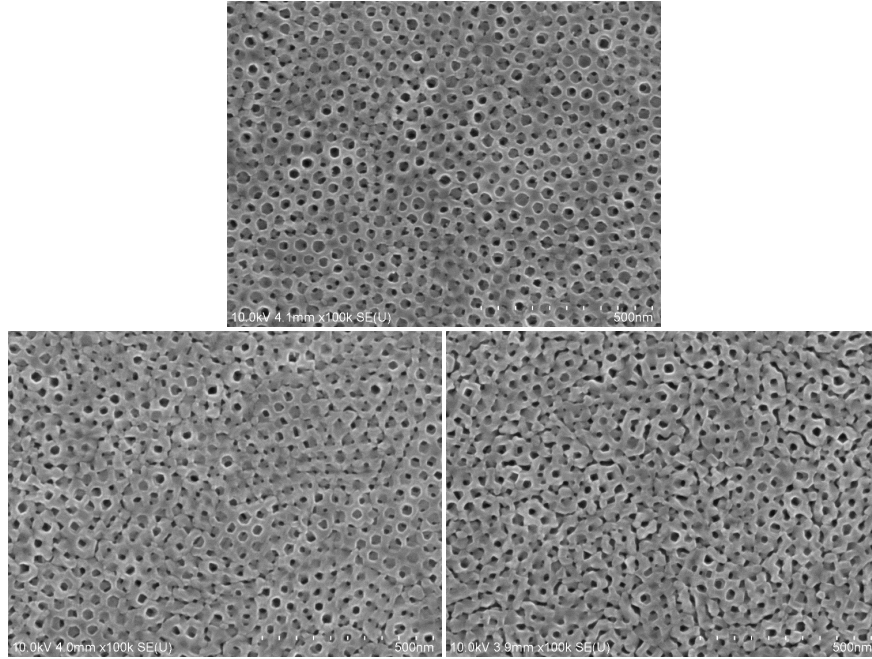


**Figure 8:** FEG-SEM photos of anatase  $\text{TiO}_2$  (PB-PEO, 2M in  $\text{TiCl}_4$ ) treated for 1h (up), 2h (left) and 3h (right) at  $500^\circ\text{C}$ .

CV experiments and deduced capacity enhancement under light showed that photo-capacities significantly decreased with extending the heat treatment (see **Figure 9**).

These result could confirm the fact that small crystallites are more adapted for a more efficient use of light. Nonetheless, crystallite size is not the only factor changing when prolonging the heat treatment. In order to get a more consistent picture of the electrode evolution, further investigations and film characterization could be useful to figure out how the connectivity between the particles (grain boundaries), the specific surface area, or the films density change during the heat treatment.

	1h $500^\circ\text{C}$	2h $500^\circ\text{C}$	3h $500^\circ\text{C}$
<b>Crystallite size (nm)</b>	$12.5 \pm 0.2$	$18.8 \pm 0.2$	$25.6 \pm 0.2$

**Table 1:** Results of the refinements after X-Ray diffraction measurements. Films were dipped on silicon substrates for the XRD analysis.

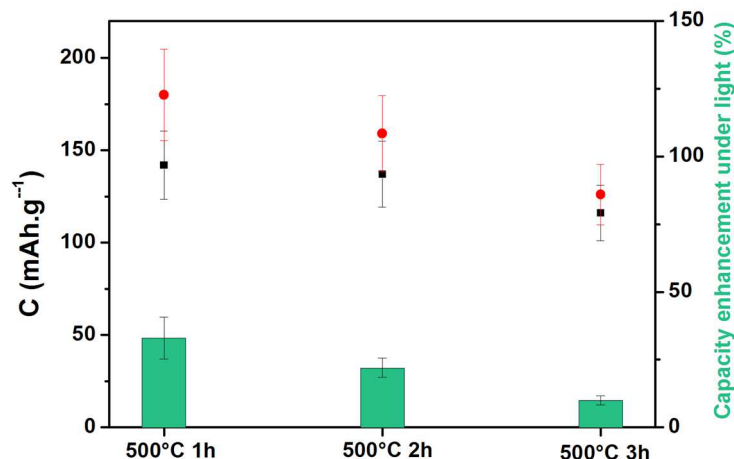


**Figure 9:** Capacity calculated from CV experiments at  $0.5 \text{ mV.s}^{-1}$  (2.6 V to 1.4 V vs.  $\text{Li}^+/\text{Li}^0$ ) under dark (black) and light (red) conditions plotted for anatase films (PB-PEO, 2M in  $\text{TiCl}_4$ ) treated for 1h, 2h and 3h at  $500^\circ\text{C}$ . Photo-capacity is calculated as the difference between light and dark capacity.

In this section, we have tried to play with the electrode structure in order to see how much it could impact the photo-induced mechanisms. No drastic differences were observed in the range of mesoporous architectures used in this work. For the future investigations, use of dense  $\text{TiO}_2$  (without polymers) or complete different architectures could be considered to study the active material differently shaped.

When analyzing the fate of photo-generated charges, which depends on the competition between charge recombination, diffusion and/or reaction at an electrode/electrolyte interface, it seems also crucial to picture the electrode in interaction with the surrounding electrolyte. In the next section, our investigations will be focused on the role played by the electrolyte during photo-induced mechanisms.



## II.2 – Role of the electrolyte

### II.2.1 – TiO<sub>2</sub> photo-electrode in an ionic liquid-based electrolyte

Up to now, in this study, LP30 was the electrolyte. LP30 solvent is a widely used electrolyte in Li-ion battery. It is composed of LiPF<sub>6</sub> salts (1M) dissolved in a mixture of ethylene carbonate and dimethyl carbonate (50/50 in volume). Alkyl carbonates are generally chosen due to their acceptable anodic stability for the 4 V cathodes used in Li-ion batteries, together with other properties such as high polarity and good conductivity of their solutions, a reasonable temperature range between freezing and boiling points and acceptable toxicity.<sup>4</sup> The LiPF<sub>6</sub> salt is known to present well-balanced properties when evaluated against the requirements that battery environment places on electrolyte components (solubility, mobility, electrochemical stability).<sup>5</sup> Nonetheless, LiPF<sub>6</sub> salt is also known to decompose in LiF and PF<sub>5</sub>, and the latter readily hydrolyzes to form HF and POHF<sub>3</sub>.<sup>4,6,7</sup> These two hydrolysis products are highly reactive and their unavoidable presence in LiPF<sub>6</sub> solutions has a detrimental impact on the electrode performances.<sup>8</sup>

Besides, safety concerns still surround the use of these flammable electrolytes.<sup>9</sup> Improvement could be expected by excluding liquids and using solvent-free, polymer electrolytes. However, the battery in a solid-state version operates well only at temperatures higher than 50°C, which limits their range of application.<sup>10</sup>

Hence, the use of ionic liquids is generally presented as an interesting alternative, as they are practically non-flammable and have high thermal stability. Apart from the fact that these characteristics could be valuable for photo-rechargeable battery application, in our case, this electrolyte is studied above all with the aim of investigating the fate of the photo-charges in an other electrolyte than LP30.

Ionic liquids are low-temperature molten salts, i.e. liquids composed of ions only. The salts are characterized by weak interactions, owing to the combination of a large cation and a charge delocalized anion. This combination gives a fluid with an ion conductivity comparable to many organic electrolyte solutions and an absence of decomposition up to about 300-400°C. As lithium salts have high solubility in ionic liquids, their association as electrolyte have become very interesting in Li-ion batteries applications.<sup>9</sup>

In order to observe the photo-electrochemical response of TiO<sub>2</sub> electrode in a completely different electrolyte, TiO<sub>2</sub> photo-electrode was electrochemically tested in ionic liquid using the same methodology as the previous study in LP30 electrolyte. Electrolyte was prepared by dissolving lithium bis(trifluoromethanesulfonyl)imide salt



(LiTFSI, 0.2M) in N-Propyl-N-methyl-pyrrolidinium bis(trifluoromethanesulfonyl)imide ionic liquid (PYR<sub>13</sub>TFSI) (**Figure 10**).

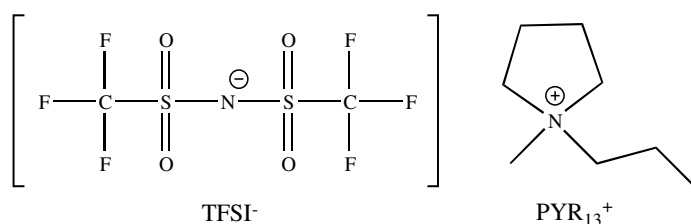


**Figure 10:** N-Propyl-N-methyl-pyrrolidinium bis(trifluoromethanesulfonyl)imide ionic liquid (PYR<sub>13</sub>TFSI) chemical formula

Compared to experiments in LP30, preliminary CV stabilization step was not necessary in ionic liquid. The first CV was already well-defined and did not show other peaks than the one for the reduction (1.62 V) and oxidation (2.12 V) of TiO<sub>2</sub> (**Figure 11-a**). CVs performed under illumination at 0.5 mV.s<sup>-1</sup> between 2.5 V and 1.4 V showed increased intensities and shifted oxidation peak, which is very comparable to similar experiments conducted in LP30 solvent (**Figure 11-b**).

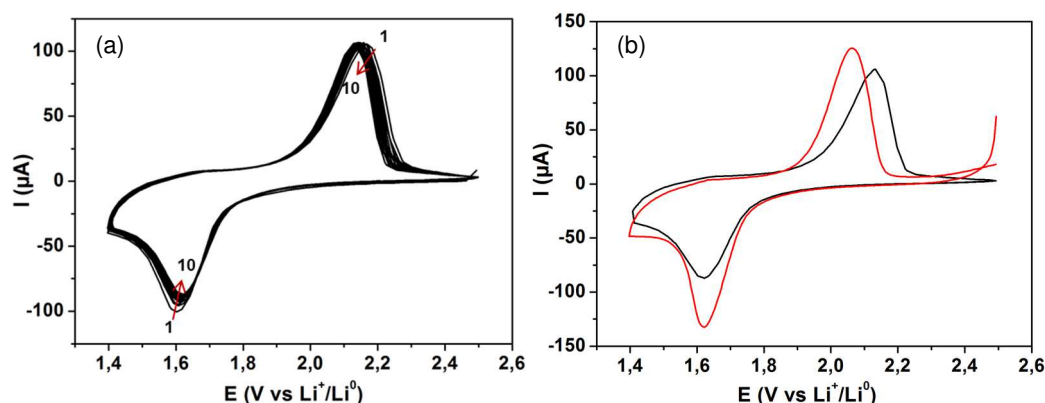


**Figure 11:** First ten cyclic CVs at scan rate 0.5 mV.s<sup>-1</sup> of mesoporous anatase TiO<sub>2</sub> thin film (PB-PEO, 1M in TiCl<sub>4</sub>, 4 dipped layers) in ionic liquid (LiTFSI 0.2M in PYR<sub>13</sub>TFSI). The number of the cycle is indicated in the graph as reference (a). CVs performed under dark (black) and light conditions (red) (b).

The **Figure 12** reports the position of the TiO<sub>2</sub> reduction and oxidation peaks during CVs performed at 0.5 mV.s<sup>-1</sup> under dark (black) and light (red) conditions for different conditions.

The difference between TiO<sub>2</sub> oxidation and reduction peaks is comparable, if not reduced, in ionic liquid in comparison to LP30 ( $\approx 0.5$  mV vs.  $\approx 0.6$  mV for a 230 nm-thick TiO<sub>2</sub> electrode prepared with PB-PEO at 1M in TiCl<sub>4</sub>, comparison in **Figure 12**, black frames).

In ionic liquid, capacities in dark are comparable, if not better, to those in LP30 (see **Figure 13**). Comparison between organic electrolyte and ionic liquids for their use in Li-ion battery has already been reported. Authors have for example compared the performances of LTO anode in LP30 vs. LiTFSI-PYR<sub>14</sub>TFSI<sup>11,12</sup> or TiO<sub>2</sub> in LiTFSI-EC/DEC vs. LiTFSI-PYR<sub>13</sub>TFSI.<sup>12,13</sup> Results show very comparable surtensions and capacities, sometimes slightly better in ionic liquids, especially after the 10<sup>th</sup> cycle or at higher temperature.

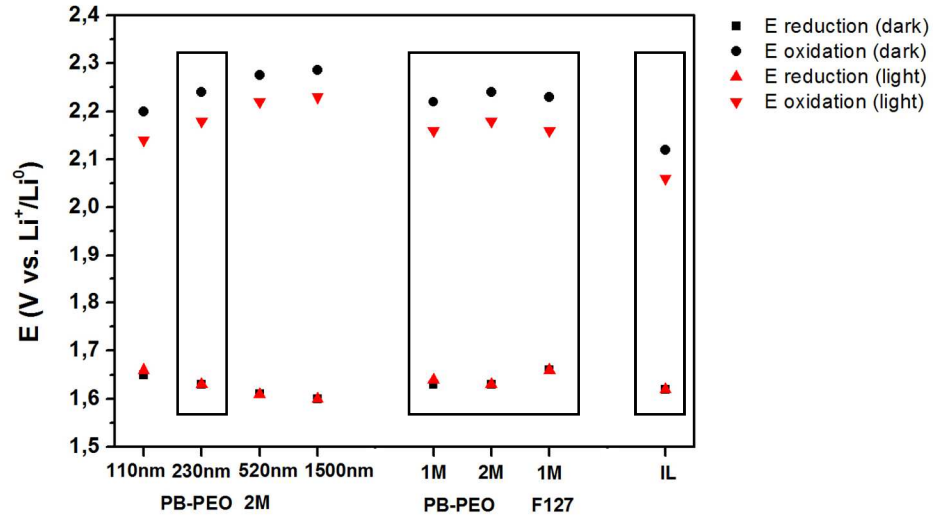


**Figure 12:** Comparison of TiO<sub>2</sub> oxidation and reduction peak position during CVs (0.5 mV.s<sup>-1</sup>) performed under dark (black) and light (red) conditions. Data are reported for TiO<sub>2</sub> photoelectrode in LP30 (PB-PEO, 2M in TiCl<sub>4</sub>, 110 nm-thick to 1500 nm-thick) (230 nm-thick for PBPEO at 1M/2M and F127 at 1M in TiCl<sub>4</sub>) and in PYR<sub>13</sub>TFSI (LiTFSI 0.2M) (230 nm-thick, PB-PEO, 1M in TiCl<sub>4</sub>). Films with comparable thickness (230 nm) are in black frames.

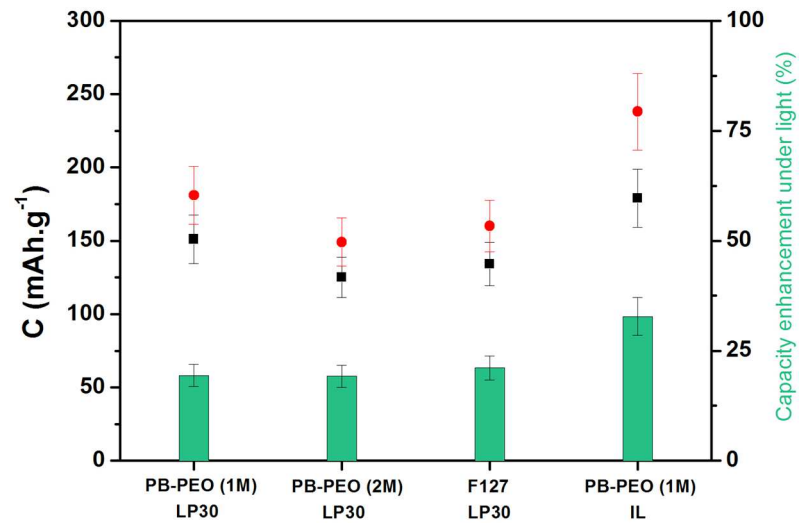


**Figure 13:** Capacity calculated from CV experiments at 0.5 mV.s<sup>-1</sup> under dark (black) and light (red) conditions compared in LP30 and in ionic liquid (IL) for 230 nm-thick mesoporous anatase electrodes.

Interestingly, capacities enhancement under light are also significantly more intense in ionic liquid than in LP30 for the same film architecture (PB-PEO, 1M in  $\text{TiCl}_4$ , 4 dipped layers). Comparison of dark and light capacities showed that intensities under illumination are  $\approx 33\%$  higher than under dark conditions in ionic liquid, against 20% in LP30 for the same electrode architecture (**Figure 13**).

Hence, intensity of photo-induced phenomena seems to be higher in ionic liquid (LiTFSI, 0.2M) than in EC/DMC carbonates solvent ( $\text{LiPF}_6$ , 1M).

This observation was confirmed by potentiostatic experiments under chopped illumination. Results obtained for sequences of 30 sec. in dark / 30 sec. in light were compared for LP30 and ionic liquid electrolytes. The shape of the photo-current curve suggests that periods of 30 sec. of illumination are too short in ionic liquid to reach a saturated photocurrent at the end of the transitory regime, which leads the photo-current to its maximal intensity value (**Figure 14**). By realizing the same experiment for a chopped illumination every 90 sec., shape of the photo-current became comparable to the one in LP30 experiment for 30 sec. of illumination. In this case, transitory regime is long enough to reach maximal values of photo-current (**Figure 15**). Calculated intensities of photo-currents confirmed the bigger light effect when using LiTFSI (0.2M) in ionic liquids instead of LP30 as solvent (**Figure 16**).

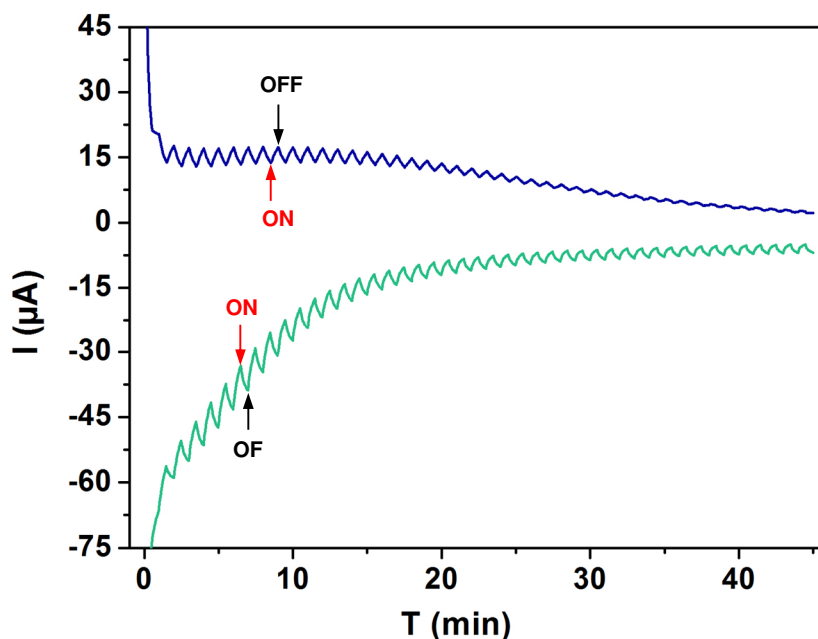


**Figure 14:** Potentiostatic experiments under chopped illumination, light is switched on/off every 30 sec. for E set at 1.90 V (blue) and 1.72 V (green).

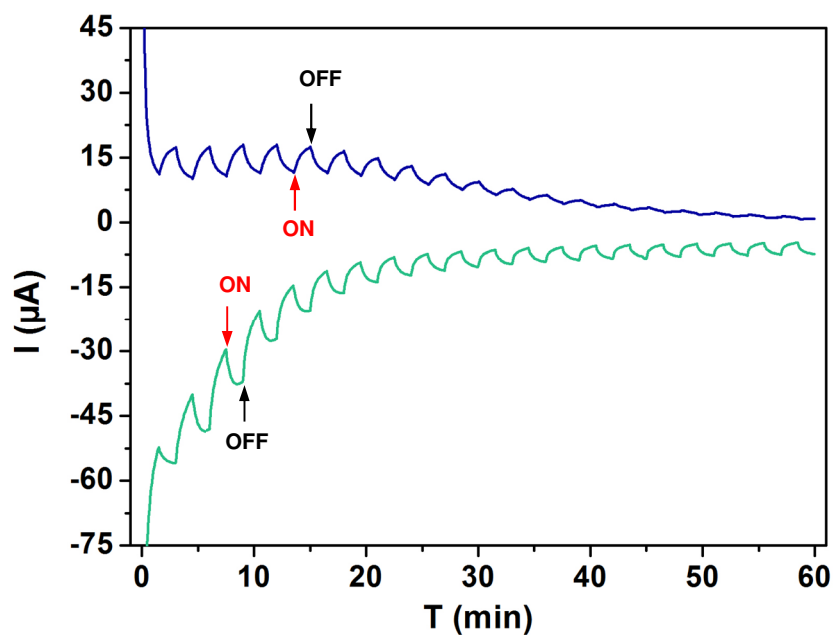


**Figure 15:** Potentiostatic experiments under chopped illumination, light is switched on and off every 90 sec for E set at 1.90 V (blue) and 1.72 V (green).

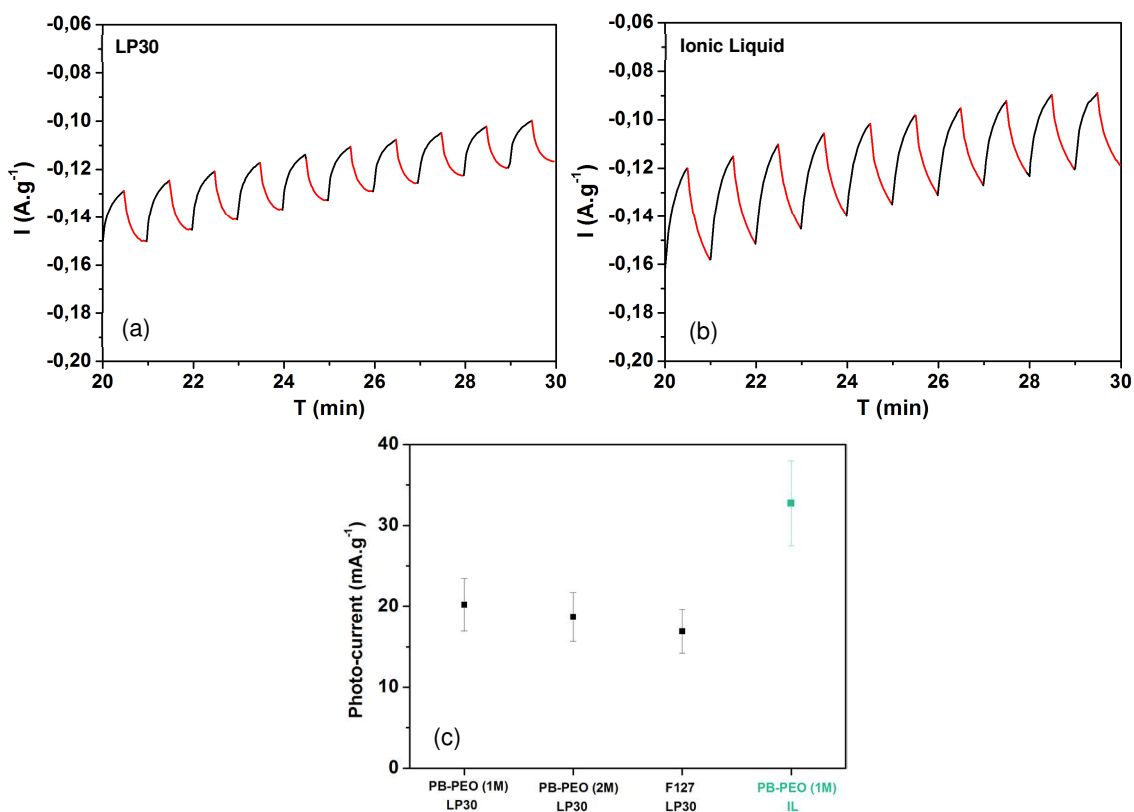


**Figure 16:** Potentiostatic experiments under chopped illumination, light is switched on (red) and off (dark) every 30 sec for E set at 1.72 V, in LP30 (a) and  $\text{PYR}_{13}\text{TFSI}$  (LiTFSI 0.2M) (b). Resulting photo-currents were compared in LP30 and in ionic liquid for 230 nm-thick mesoporous anatase electrodes (c).

In order to better understand these observations, stability of the electrolytes were first electrochemically tested in a 3-cell configuration using a Pt wire as working electrode and metallic Li as counter- and reference electrodes.

CV experiments showed electrochemical stability of both LP30 and LiTFSI (0.2M) in  $\text{PYR}_{13}\text{TFSI}$  electrolytes between 1 V and 4 V vs.  $\text{Li}^+/\text{Li}^0$  under dark conditions and also under illumination (**Figure 17**). Stability of the electrolytes under illumination is an important starting point for this study. It was expected because it is coherent with the theoretical stability range of ionic liquids, which is generally between 4-6 V ( $\approx 6$  V for pyrrolidinium-based ionic liquid).<sup>9,14–16</sup>

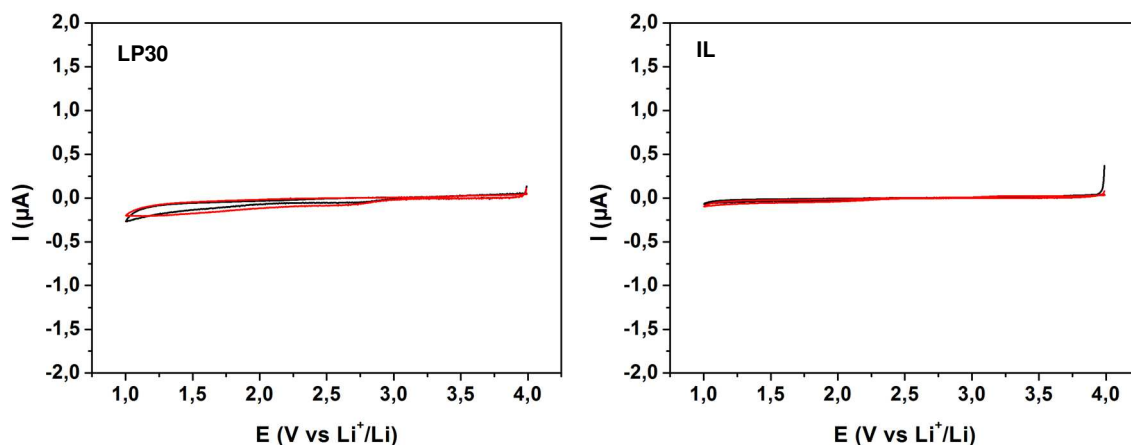


**Figure 17:** CV ( $0.5 \text{ mV.s}^{-1}$ ) under dark (black) and light (red) conditions in LP30 (left) and  $\text{PYR}_{13}\text{TFSI}$ , 0.2M LiTFSI (right) using Pt as working electrode and Li as counter- and reference electrodes.

In order to check if the higher photo-currents in ionic liquids could eventually be due to a concomitant degradation of the ionic liquid under illumination,  $\text{PYR}_{13}\text{TFSI}$  was then electrochemically tested without any lithium salt, using  $\text{TiO}_2$  as working electrode. Linear sweep voltammetry experiments under chopped illumination (**Figure 18**) were performed in lithium salt-free ionic liquid.

If  $\text{TiO}_2$  had had a catalytic effect on the degradation of the ionic liquid explaining higher reductive photo-currents during the potentiostatic under chopped illumination at 1.72 V (**Figure 16**), we would have expected a reductive photo-current at this potential when illuminating the  $\text{TiO}_2$  electrode in  $\text{PYR}_{13}\text{TFSI}$ . On the contrary, results of the experiment in lithium salt-free ionic liquid showed oxidative photo-currents, regardless of the potential.

The increasing positive photo-currents above 2.4V are characteristic of the  $\text{TiO}_2$  photo-catalytic response as n-type semiconductor<sup>17–21</sup> (reactive photo-generated holes at the electrode surface). These photo-currents could be attributed to the photo-oxidation of

residual water molecules, which are often unavoidable in ionic liquids due to atmospheric water sorption<sup>22–25</sup>.

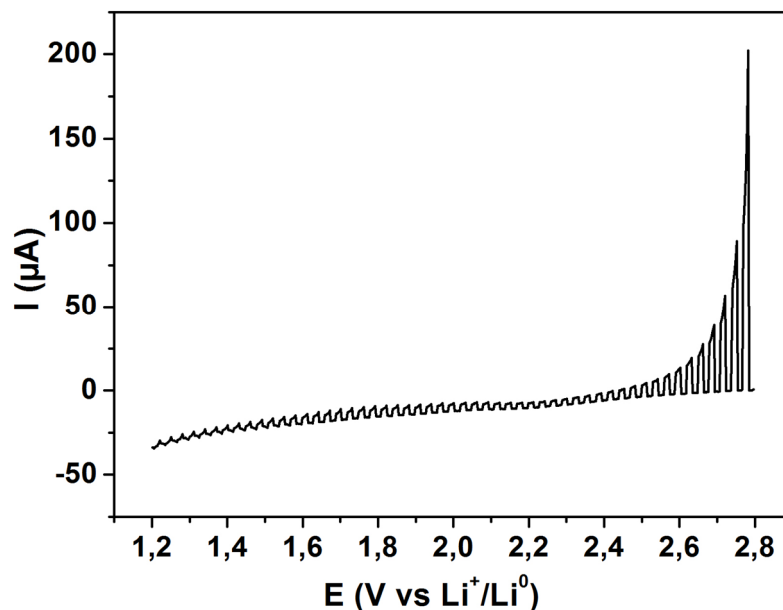


**Figure 18:** Linear sweep voltammetry ( $0.5 \text{ mV.s}^{-1}$ ) under chopped illumination (30 sec. off / 30 sec. on) from 2.8V to 1.2V in  $\text{PYR}_{13}\text{TFSI}$  using  $\text{TiO}_2$  (PB-PEO,  $\text{TiCl}_4$  2M, 530 nm) as working electrode and metallic Li as counter- and reference electrodes.

Now, for the experiments in  $\text{PYR}_{13}\text{TFSI}$ ,  $\text{LiTFSI}$  (0.2M), we suggest that in presence of lithiated anatase, holes could react preferentially within the electrode (rather than with water), *i.e.* directly with the  $\text{Ti(III)}$  of  $\text{Li}_x\text{TiO}_2$ , with no need to diffuse at the electrode/electrolyte interface. Significant water oxidation should indeed take place at potentials higher than  $\approx 2.0 \text{ V vs. Li}^+/\text{Li}^0$ , that is the observed potential for the oxidation of  $\text{Ti(III)}$  under light. Thus, even in presence of water, in the potential range where lithiated  $\text{TiO}_2$  phase is present ( $\approx 1.8 \text{ V}$  to  $\approx 1.4 \text{ V}$  in reduction,  $\approx 1.4 \text{ V}$  to  $\approx 2.2 \text{ V}$  in oxidation, based on CVs experiments, **Figure 11**) the photo-oxidation reaction with  $\text{Ti(III)}$  sites should appear to be the best option.

In absence of  $\text{Ti(III)}$  sites, water molecules could then become the preferential target of the action of photo-holes. This is typically what should happen in the described experiment in  $\text{PYR}_{13}\text{TFSI}$  (without any lithium salt) described in (**Figure 18**), or in  $\text{PYR}_{13}\text{TFSI}$ ,  $\text{LiTFSI}$  (0.2M) for potentials higher than  $\approx 2.2 \text{ V}$  (**Figure 11**), which could explain the increase of the oxidation intensities beyond  $\approx 2.2 \text{ V}$  under illumination.

By analyzing the energy diagram **Figure 19**, one might wonder whether water could also be reduce by photo-generated electrons. If this phenomenon effectively occurs, it

could compete the electrons and holes recombination, thus promoting holes reactions with Ti(III) when lithiated titania phase is present.  $\text{Li}^+$  photo-extraction could thereby be more important when photo-electrons are used for an other reaction (*e.g.* here, reaction with water).

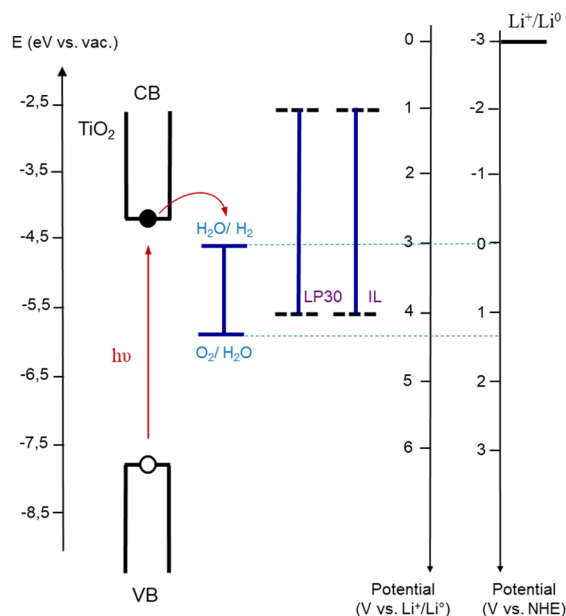


**Figure 19:** Schematic energy diagram of  $\text{TiO}_2$  (deducted from our UV-Vis and Mott-Schottky experiments). Stability range of LP30 and  $\text{PYR}_{13}\text{TFSI}$  (0.2M  $\text{LiTFSI}$ ) deducted from our CV's experiment between 1 V and 4 V vs.  $\text{Li}^+/\text{Li}$  (here underestimated).

In order to verify which photo-oxidation could be the most likely in simultaneous presence of Ti(III) sites and water, and test our mechanistic hypothesis in a third electrolyte,  $\text{TiO}_2$  photo-electrode was tested in a “water-in-salt” electrolyte.

## II.2.2 – $\text{TiO}_2$ photo-electrode in a “water-in-salt” electrolyte

Aqueous electrolyte could resolve safety issues (flammable solvent,  $\text{LiPF}_6$  thermal instability and toxicity), but their electrochemical stability window (1.23 V) is too narrow to support most of the electrochemical couples used in Li-ion batteries. In 2015, Suo et al.<sup>26</sup> proposed a highly concentrated aqueous electrolyte based on mixtures of  $\text{LiTFSI}$  ( $>20 \text{ mol.kg}^{-1}$ ) in water, yielding an expanded voltage stability of 3.0 V, which has become very interesting for Li-ion storage applications (**Figure 20**).<sup>27</sup> This high voltage stability has been attributed to the electrochemical reduction of TFSI<sup>-</sup> at the anode surface, which forms a protective SEI layer consisting primarily of  $\text{LiF}$ , and is accompanied by a shift in the oxygen evolution reaction to higher voltages.<sup>27,28</sup> This particular reduction of the TFSI<sup>-</sup> anion has been explained by analyzing the relationship between the solution structure and the electrochemical properties from

molecular dynamics simulations. For dilute solutions ( $< 5 \text{ mol.kg}^{-1}$ ), Suo et al.<sup>26</sup> showed that  $\text{Li}^+$  remains well hydrated in its primary solvation sheath with sufficient free water molecules available. The authors explained that in such electrolytes, attempts to lithiate the anode, whose lithiation potential is below that of water reduction, would lead to preferential reduction of water in hydrogen, which would prevent  $\text{Li}^+$  intercalation and any possible reduction of TFSI<sup>-</sup>. However, when LiTFSI concentrations beyond  $20 \text{ mol.kg}^{-1}$  are employed<sup>i</sup>, molecular dynamics simulation predicts that on average two TFSI<sup>-</sup> anions would be observed in each  $\text{Li}^+$  primary solvation sheath, and such a high probability of presence of TFSI<sup>-</sup> would lead to an interphase chemistry dominated by the reduction of TFSI<sup>-</sup> (see **Figure 20**).<sup>26,28</sup>

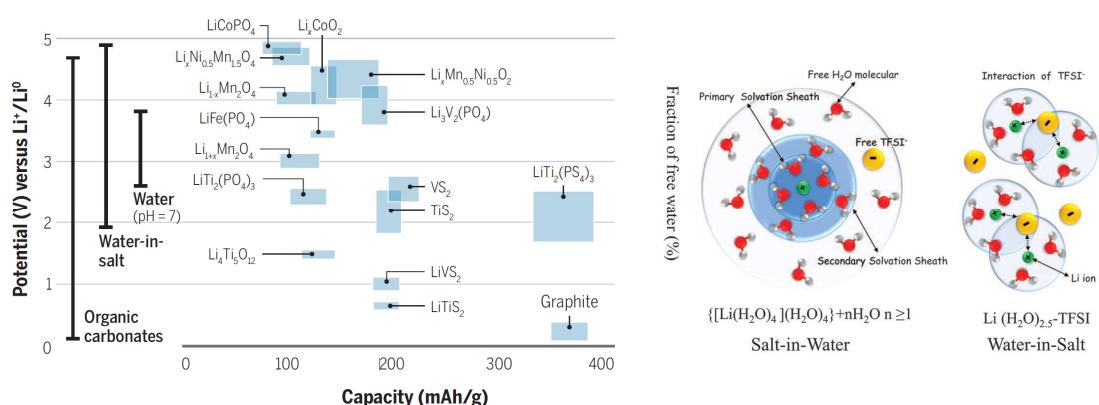


**Figure 20:** Voltage stability limits of organic, water-in-salt, and aqueous electrolytes compared to the chemical potential of various lithium intercalation materials (left).<sup>27</sup> Illustration of the evolution of the  $\text{Li}^+$  primary solvation sheath in diluted and water-in-salt solutions (right).<sup>26</sup>

In this work, this electrolyte is studied above all with the aim of investigating the fate of the photo-charges in presence of a different electrode/electrolyte interfacial environment. “Water-in-salt” electrolyte presents the advantage of containing both LiTFSI salt and water to test our mechanistic hypothesis about the preferential photo-oxidation of Ti(III) above water. Besides, for high LiTFSI concentration, our system could be tested in conditions where electrochemical  $\text{Li}^+$  intercalation/extraction is enough quantitative (in comparison to a classical “salt-in-water” electrolyte) to be comparable to our previous experiments in LP30 and IL.

CV experiments ( $0.5 \text{ mV.s}^{-1}$ ) were obtained in a three-electrode configuration using mesoporous  $\text{TiO}_2$  (PB-PEO, 2M in  $\text{TiCl}_4$ , 2 layers) as working electrode, Pt wire as counter-electrode and saturated  $\text{Ag}/\text{AgCl}$  as reference electrode. Water-in-salt

<sup>i</sup> the molality in  $[\text{mol.kg}^{-1}]$ , will be referred as “m”. Molality is more adapted than concentration (in  $[\text{mol.L}^{-1}]$ , “M”) to describe high concentrated water-in-salt electrolyte, where the volume of the added salt is often higher than volume of water.



electrolytes were prepared by dissolving LiTFSI salts in water, for 3 different concentrations (2.1, 10.5 and 21 mol.kg<sup>-1</sup>).

CVs presented in **Figure 21** show that the reduction of water is progressively shifted to lower potentials when the proportion of free water in the electrolyte decreases (dark curves). At low LiTFSI concentration (2.1 mol.kg<sup>-1</sup>), TiO<sub>2</sub> electrochemical response does not show any well-defined peaks for the Ti(IV) reduction or the Ti(III) oxidation, and is logically more comparable to the kind of CV obtained in classical diluted conditions in water (a). At 21 mol.kg<sup>-1</sup>, the proportion of free water seems low enough to observe reduction ( $\approx 1.5$  V vs. Li<sup>+</sup>/Li<sup>0</sup>) and oxidation ( $\approx 1.9$  V vs. Li<sup>+</sup>/Li<sup>0</sup>) peaks of TiO<sub>2</sub> (which began to be visible at 10.5 m).

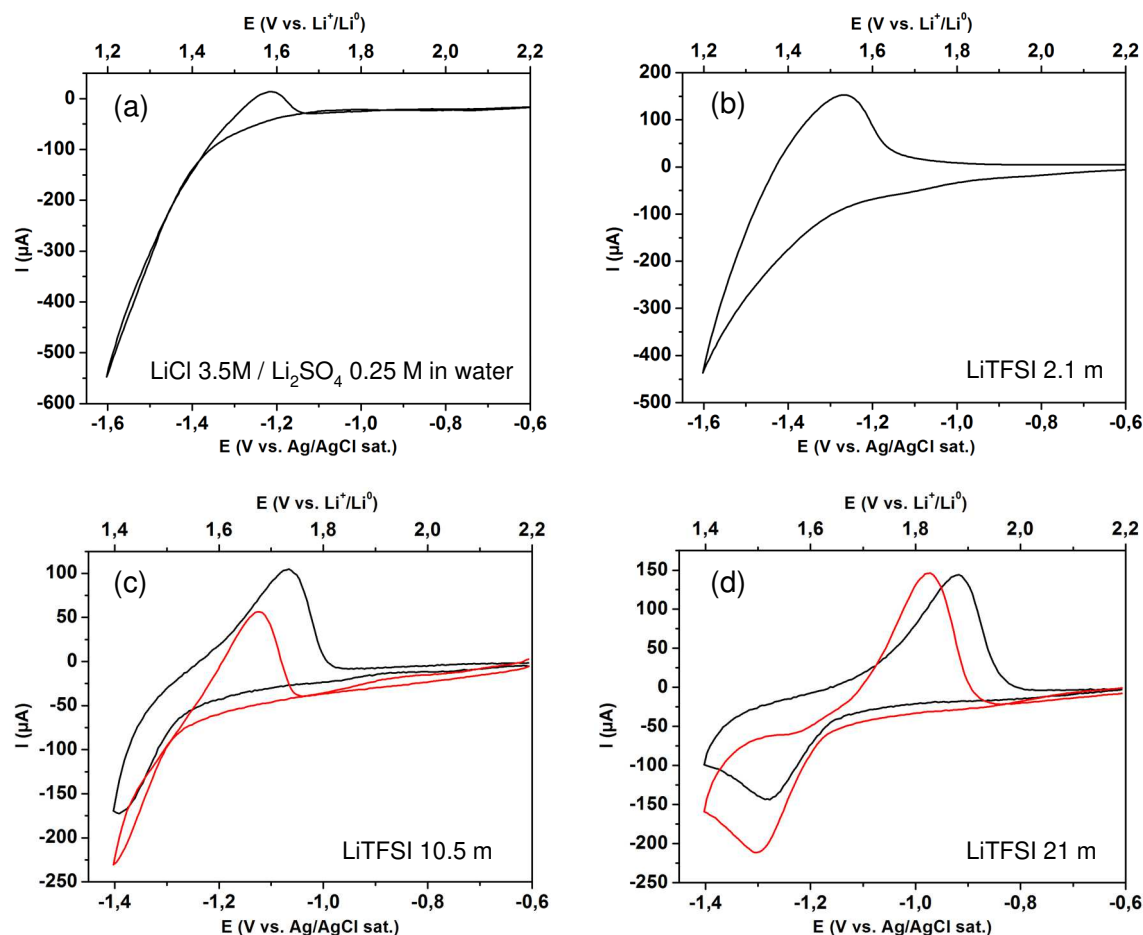


**Figure 21:** CVs (0.5 mV.s<sup>-1</sup>) for TiO<sub>2</sub> (PB-PEO, 2M in TiCl<sub>4</sub>, 2 layers), using Pt and sat. Ag/AgCl as counter and ref. electrodes, in water with: a dissolved mixture of LiCl (3.5M)/Li<sub>2</sub>SO<sub>4</sub>(0.25M) (a), LiTFSI at 2.1 (b), 10.5 (c) and 21 mol.kg<sup>-1</sup> (d). Cycling under dark conditions (black) and under illumination (red).

In comparison to identical experiments in IL or in LP30, CVs in light conditions (red curves) seem to be globally shifted to more negative intensities and more particularly during the reverse oxidation scan. Regardless of this intensity shift, usual intensity

increase and shift of the oxidation peaks can be guessed. At this point, we do not know yet the reason of the intensity shift phenomenon. One of the difficulties in analyzing such system, in this range of potentials, is to succeed in de-correlating phenomena associated with water reduction, from phenomena related to ions ( $\text{Li}^+$ , as well as  $\text{H}^+$ ) intercalation/extraction/adsorption. Protons are also known to adsorb on- or even intercalate in-  $\text{TiO}_2$  electrode depending on the applied bias and pH conditions.<sup>29–35</sup> Under illumination,  $\text{H}^+$  as well as  $\text{Li}^+$ , could therefore directly contribute to the observed photo-currents, depending on the applied potentials and the water-in-salt electrolyte concentration (pH notion here are also uneasy to define).

Linear sweep voltammetry (LSV) experiment at  $0.5 \text{ mV.s}^{-1}$  (from 0 V to -1.9 V vs. saturated Ag/AgCl) under chopped illumination confirms the delayed water reduction in more concentrated water-in-salt ( $E \lesssim -1.65 \text{ V}$  vs. Ag/AgCl at  $21 \text{ mol.kg}^{-1}$ ) in comparison to diluted electrolyte ( $E \lesssim -1.5 \text{ V}$  vs. Ag/AgCl at  $2.1 \text{ mol.kg}^{-1}$ ) (**Figure 22**).

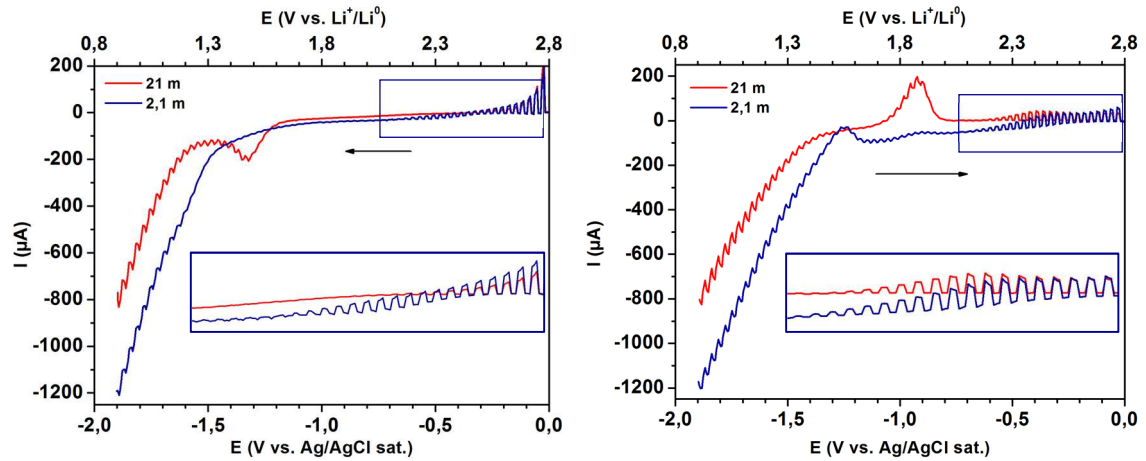


**Figure 22:** (LSV) experiment at  $0.5 \text{ mV.s}^{-1}$  under chopped illumination (30 sec. on/off) with **initial scan 1** (from 0 V to -1.9 V vs. Ag/AgCl) (left) and **reverse scan 2** (from -1.9 V to 0 V vs. Ag/AgCl) (right) for LiTFSI in water at 21 m (red) and 2.1 m (blue). Zooms corresponding to the oxidation potentials in blue frame.

This experiment also highlights two kinds of photo-responses that  $\text{TiO}_2$  electrode can exhibit (photo-oxidation of  $\text{Ti(III)}$  or of water) depending on the applied potential, and consequently on its lithium content. Let's consider the experiment at  $21 \text{ mol.kg}^{-1}$  (red curve):

- when  $\text{TiO}_2$  is in its intercalated state (from  $E \lesssim -1.2 \text{ V}$  vs. Ag/AgCl in **initial scan 1** (left) to  $E \lesssim -0.8 \text{ V}$  in the **reverse scan 2** (right)), in presence  $\text{Ti(III)}$  sites, the photo-current, which has “triangular” shape as in LP30 or IL during  $\text{Li}^+$  photo-

extraction, could be attributed to Ti(III) photo-oxidation. In the presence of Ti(III) sites, photo-generation could therefore lead to preferential  $\text{Li}^+/\text{H}^+$  photo-extraction through Ti(III) photo-oxidation. This is the photo-response, which has already been typically observed in LP30 and  $\text{PYR}_{13}\text{TFSI}$  (0.2M  $\text{LiTFSI}$ ) when the electrode is lithiated.

- when  $\text{TiO}_2$  is ‘unlithiated’ ( $E \gtrsim -1.2\text{ V}$  in **initial scan 1** (left), then  $E \gtrsim -0.8\text{ V}$  in the **reverse scan 2** (right)), in absence of Ti(III) sites, holes photo-generation lead to photo-oxidation of available water molecules. These water molecules can be more or less available, as in water-in-salt, depending on the concentrated or diluted nature of the electrolyte. They can also simply be residual water molecules, as observed in absence of  $\text{LiTFSI}$  in hygroscopic  $\text{PYR}_{13}\text{TFSI}$ . In this case, the photo-current has a “rectangular” shape (see the blue frames), which are more characteristic of the  $\text{TiO}_2$  photo-catalytic response during the water oxidation in solar watersplitting systems.<sup>17–21</sup>

The difference between the two different shapes of photo-current (“triangular” for the  $\text{Li}^+$  photo-extraction/“rectangular” for the water oxidation) could also give an information about the kinetics of both phenomena. In fact, photo-stimulated reaction are usually expected to happen very fast, as suggested by the rectangular photo-current observed in solar watersplitting systems<sup>14–18</sup> for example. In the case of  $\text{Li}^+$  photo-extraction, photo-induced processes could be limited by the  $\text{Li}^+$  diffusion in the electrode, which could explain the “triangular” shape of the photo-current.

In this section, mechanistic hypothesis has been drawn to explain the fate of the photo-generated charges depending on the presence, or not, of Ti(III) sites. In particular, in ionic liquids-based electrolyte, we have proposed that photo-holes could react preferentially within the Ti(III) of  $\text{Li}_x\text{TiO}_2$  (rather than with residual water). Photo-electrons could also potentially be scavenged by residual water. This phenomenon could compete the electrons and holes recombination, thus promoting holes reactions with Ti(III) when lithiated titania phase is present, and eventually contributing to the higher photo-currents observed in ionic liquids.

In the case of LP30 electrolyte, questions about the fate of the photo-charges should also be addressed by considering the potential reaction with the electrolyte.

To get more insight about the possible species formed under illumination by reaction with the photo-generated charges, we will focus in the next section on the *post mortem* analysis of the electrode surfaces and of the electrolytes (LP30 and  $\text{PYR}_{13}\text{TFSI}$ -based ionic liquid).

### III – *Post mortem* analysis of the photo-electrode

In the previous section, we have suggested that  $\text{PYR}_{13}\text{TFSI}$  (0.2M  $\text{LiTFSI}$ ) is protected from an eventual photo-degradation due to the presence of residual water molecules; in the case of LP30, questions about the fate of the photo-charges should also be addressed by considering the potential reaction with the electrolyte.

In order to get more insight about the possible species formed under illumination by reaction with the photo-generated charges in the case of LP30, and confirm non degradation of  $\text{PYR}_{13}\text{TFSI}$  (0.2M  $\text{LiTFSI}$ ) under illumination, electrode surfaces are probed in this section by means of FEG-SEM, EDX and XPS techniques. Analysis of the electrolytes (LP30 and  $\text{PYR}_{13}\text{TFSI}$ -based ionic liquid) will also be addressed by NMR spectroscopy as complementary study. In particular, it could confirm or not the presence of residual water in  $\text{PYR}_{13}\text{TFSI}$  (0.2M  $\text{LiTFSI}$ ), as well as the possible degradation products formed in LP30.

#### III.1 – FEG-SEM and complementary EDX analysis

In order to detect potential traces of electrolyte degradation at the electrode surface, FEG-SEM photos were taken at different steps of the electrode (photo)-electrochemical cycling. For this *post mortem* analysis, electrodes were cleaned by manually shaking them for 1-2 minutes in a beaker containing dimethyl carbonate, in order to wash the remaining lithium salts or solvent present at their surface.  $\text{TiO}_2$  electrodes (PB-PEO, 2M in  $\text{TiCl}_4$ , 2 dipped layers) were analyzed regarding their interaction with  $\text{PYR}_{13}\text{TFSI}$  (at 0.2M in  $\text{LiTFSI}$ ):

- (a) after 1 night in the solvent without any electrochemical cycling
- (b) after 10 CVs (2.6 V to 1.4 V vs.  $\text{Li}^+/\text{Li}^0$ , 0.5  $\text{mV.s}^{-1}$ ) under dark conditions
- (c) after 10 CVs (2.6 V to 1.4 V vs.  $\text{Li}^+/\text{Li}^0$ , 0.5  $\text{mV.s}^{-1}$ ) under continuous illumination
- (d) after 45 CVs (2.6 V to 1.4 V vs.  $\text{Li}^+/\text{Li}^0$ , 0.5  $\text{mV.s}^{-1}$ ) under dark conditions.

For each of these different steps, no visible differences were observed at the electrode surface.  $\text{PYR}_{13}\text{TFSI}$  (0.2M  $\text{LiTFSI}$ ) seemed thus electrochemically stable between 2.6V and 1.4V vs.  $\text{Li}^+/\text{Li}^0$  in dark conditions as well as under illumination (**Figure 23**).

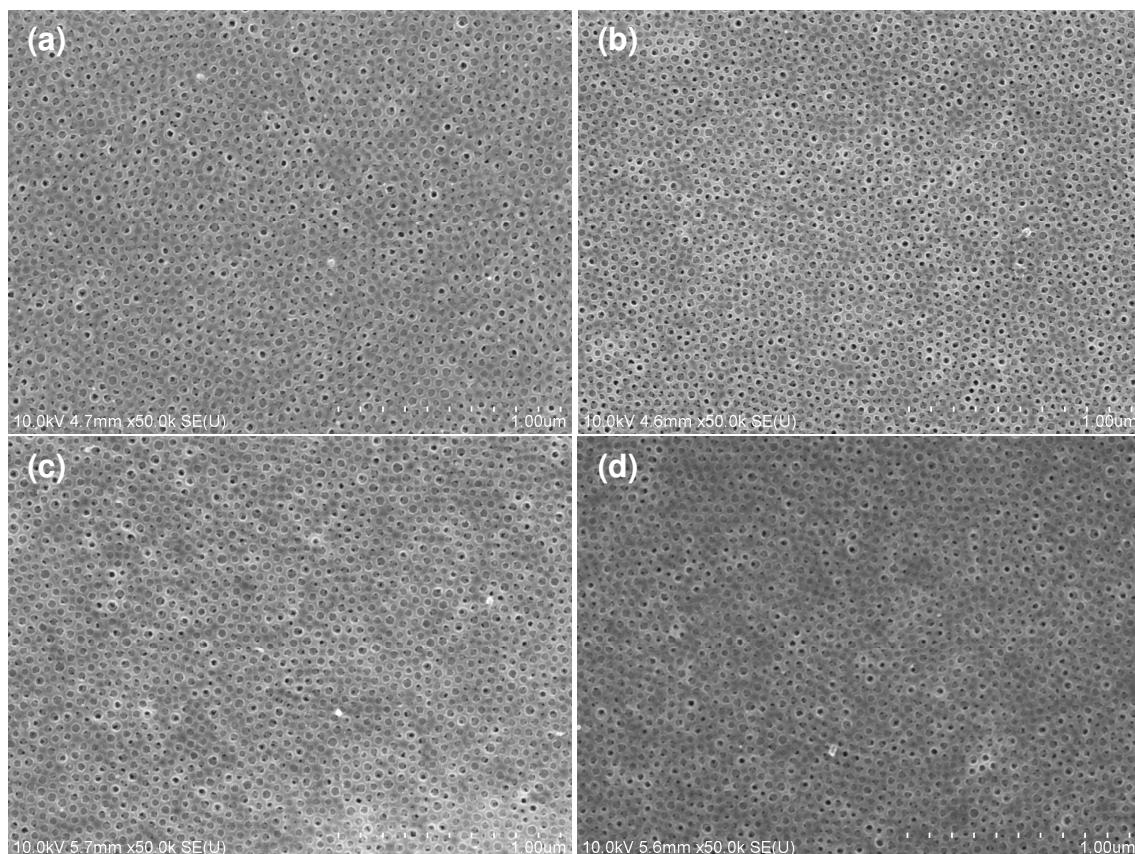


**Figure 23:** FEG-SEM photos of planar  $\text{TiO}_2$  sections use in  $\text{PYR}_{13}\text{TFSI}$  (0.2M  $\text{LiTFSI}$ ) after 1 night with no cycling (a), after 10 CV's (2.6V to 1.4V vs.  $\text{Li}^+/\text{Li}^0$ ,  $0.5 \text{ mV.s}^{-1}$ ) in dark (b) and in light (c), and after 45 CV's (2.6V to 1.4V vs.  $\text{Li}^+/\text{Li}^0$ ,  $0.5 \text{ mV.s}^{-1}$ ) in dark (d).

By contrast, important changes were observed during cycling in LP30 (**Figure 24** and **Figure 25**) In this electrolyte,  $\text{TiO}_2$  films (PB-PEO, 2M in  $\text{TiCl}_4$ , 2 dipped layers) were analyzed:

- (a) after 1 night in the solvent without any electrochemical cycling (green)
- (b) after the first CV (2.6 V to 1.4 V vs.  $\text{Li}^+/\text{Li}^0$ ,  $0.5 \text{ mV.s}^{-1}$ ) under dark conditions (yellow)
- (c) after 10 CVs (2.6 V to 1.4 V vs.  $\text{Li}^+/\text{Li}^0$ ,  $0.5 \text{ mV.s}^{-1}$ ) under dark conditions (orange)
- (d) after 10 CVs (2.6 V to 1.4 V vs.  $\text{Li}^+/\text{Li}^0$ ,  $0.5 \text{ mV.s}^{-1}$ ) under continuous illumination (red)
- (e) after 20 CVs (2.6 V to 1.4 V vs.  $\text{Li}^+/\text{Li}^0$ ,  $0.5 \text{ mV.s}^{-1}$ ) under dark conditions (blue).



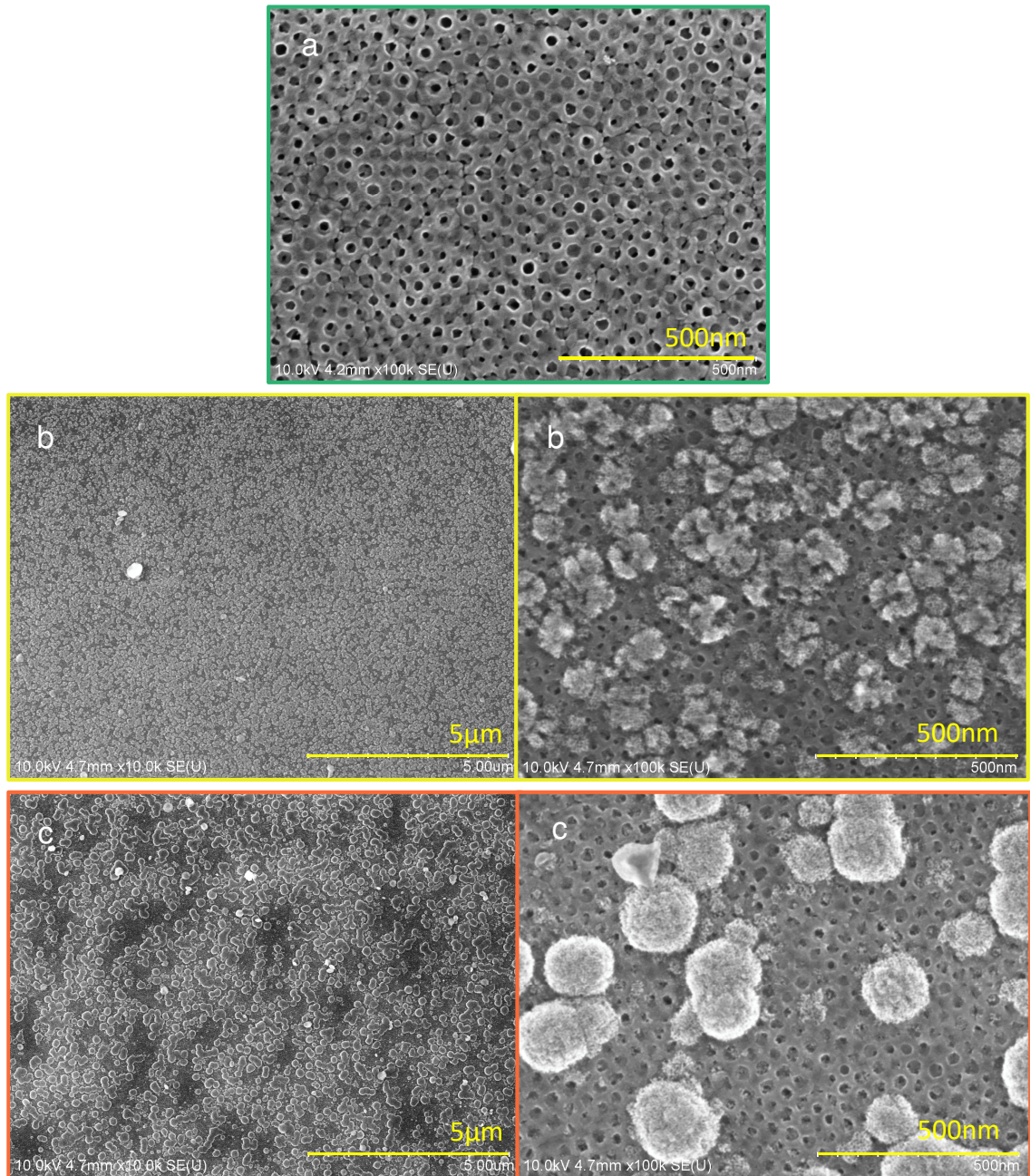


**Figure 24:** FEG-SEM photos corresponding to cycling steps (a), (b) and (c).



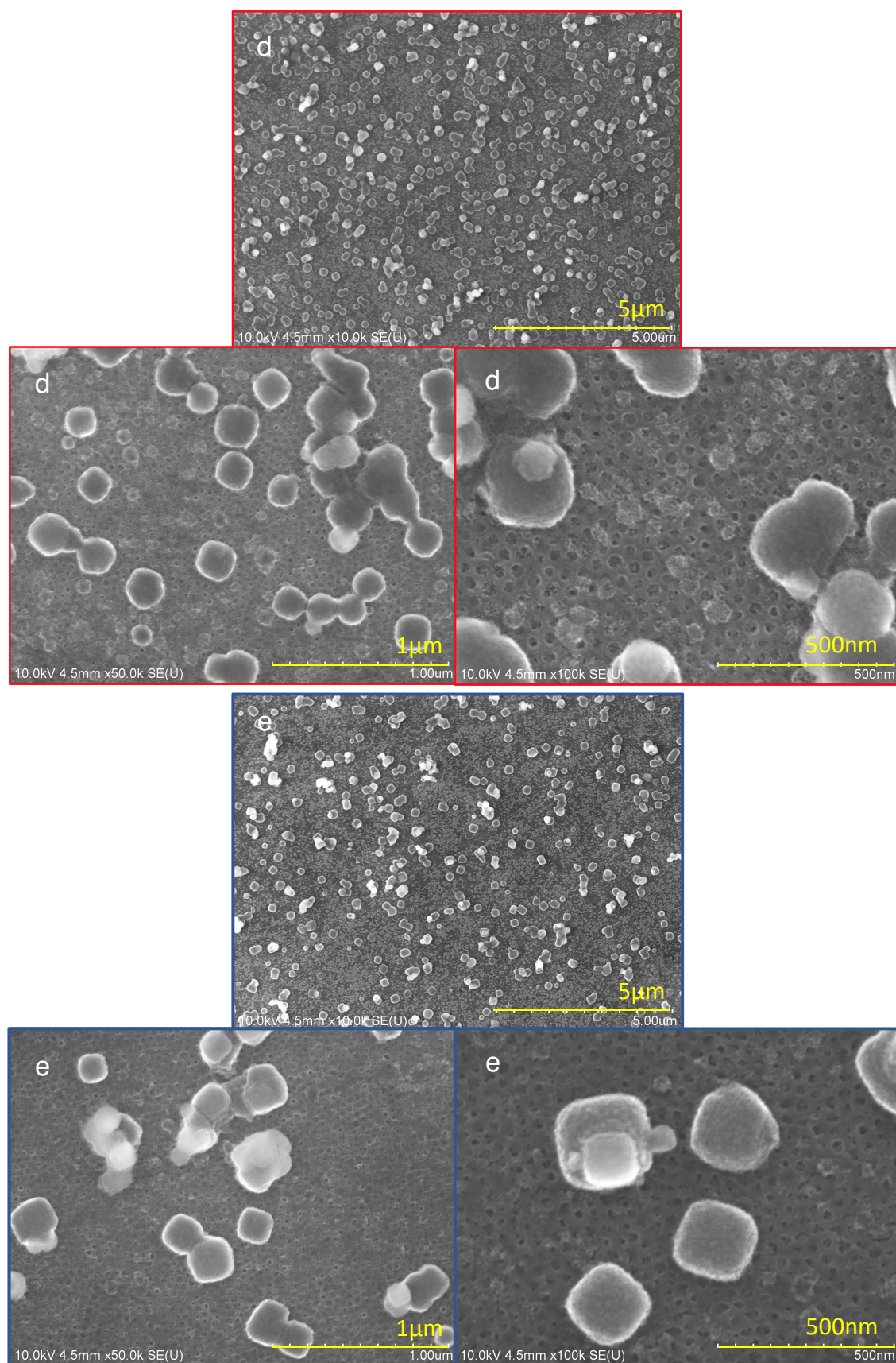


**Figure 25:** FEG-SEM photos corresponding to cycling steps (d) and (e).

FEG-SEM photos showed presence of flakes due to electrochemical cycling (absent in (a), present in (b)). Their presence after the first CV is concomitant with the large reduction current observed typically around 2.05V vs.  $\text{Li}^+/\text{Li}^0$  of the first CV (see Chapter 3 III **Figure 2**) and could witness  $\text{LiPF}_6$  salt degradation products at the electrode surface.

It is commonly considered that  $\text{TiO}_2$  is an SEI film-free anode in lithium-ion batteries. In fact, the reduction potential of most carbonate-based electrolytes is expected at  $\simeq 1.0 - 0.8$  V on carbonaceous materials, and  $\text{TiO}_2$  end discharge potential is usually at 1 V.<sup>36,37</sup>

In our case, the observation of these flakes (whose nature is still unknown) could however be in agreement with Ventosa et al.<sup>38</sup> and Han et al.<sup>39</sup> works, which both showed the formation of an SEI at reduction potential higher than 1V vs.  $\text{Li}^+/\text{Li}^0$  on anatase  $\text{TiO}_2$  (mix of anatase nanoparticles/carbon black/PvDF binder deposited by doctor blade on copper in Ventosa *et al.* study.<sup>38</sup> Mix of hollow spheres (diameter 410 nm, shell thickness 65 nm)/acetylene black/PvDF in Han et al.<sup>39</sup> work).

In dark conditions, these flakes progressively evolved from a « water-lily-like » shape ((b), yellow) to well-defined crystals ((e), blue). The important SEI evolution during the first 10 CVs probably explains the need for an aging step before obtention of a stable electrochemical signal.

Chemical nature of these flakes was investigated using Energy Dispersive X-ray spectroscopy (EDX). Qualitative results showed concomitant presence of Fluor with these flakes (see in **Annex Figure I.6**). It could suggest the formation of  $\text{LiF}$  at the electrode surface, which is known as a usual degradation product formed in LP30.

Comparison of the electrode surface after 10 CVs under dark ((c), orange) and light ((d), red) conditions suggests for the illuminated electrode a more advanced ripening stage of the flakes, compared than in the dark, as they looked like those observed after 20 CVs under dark ((e), blue).

As  $\text{LiF}$  has already been reported as reduction product of  $\text{LiPF}_6$ ,<sup>40</sup> an accelerated formation of  $\text{LiF}$  under illumination could witness the participation of photo-electrons to the  $\text{LiPF}_6$  salt degradation. Besides, as the used cell for the experiment under illumination was not water-cooled, this formation could also be due to the temperature increase of the cell, which is known to accelerate the LP30 degradation.<sup>41,42</sup>



### III.2 – Probing the electrode surface with XPS

Complementary analyses were then performed by means of X-ray photoelectron spectroscopy (XPS). Electrode surface characterization of  $\text{TiO}_2$  films (PB-PEO, 2M  $\text{TiCl}_4$ , 2 dipped layers) were conducted for both the LP30 and the 0.2M LiTFSI  $\text{PYR}_{13}\text{TFSI}$  electrolytes. Before analysis, films were cleaned by manually shaking them for 1-2 minutes in a beaker containing dimethyl carbonate, using a glove bag under argon atmosphere to limit possible surface contamination under air exposure.

In both electrolytes, the XPS spectra were compared for different conditions:

- (a) after 1 night in the solvent without any electrochemical cycling (green)
- (b) after 10 CVs (2.6V to 1.4V vs.  $\text{Li}^+/\text{Li}^0$ ,  $0.5 \text{ mV.s}^{-1}$ ) under dark conditions (yellow)
- (c) after 10 CVs (2.6V to 1.4V vs.  $\text{Li}^+/\text{Li}^0$ ,  $0.5 \text{ mV.s}^{-1}$ ) under continuous illumination (orange)
- (d) after 45 CVs (2.6V to 1.4V vs.  $\text{Li}^+/\text{Li}^0$ ,  $0.5 \text{ mV.s}^{-1}$ ) under dark conditions (red).

A  $\text{TiO}_2$  film (no polymer, 1M in  $\text{TiCl}_4$ , 1 dipped layer, 135 nm-thick) was also analyzed as reference without having been in contact with any electrolyte (**ref**).

General survey exhibited regions characteristic for the C1s, O1s, Ti2p and F1s regions (**Figure 26** for LP30 and **Figure 27** for ionic liquid).

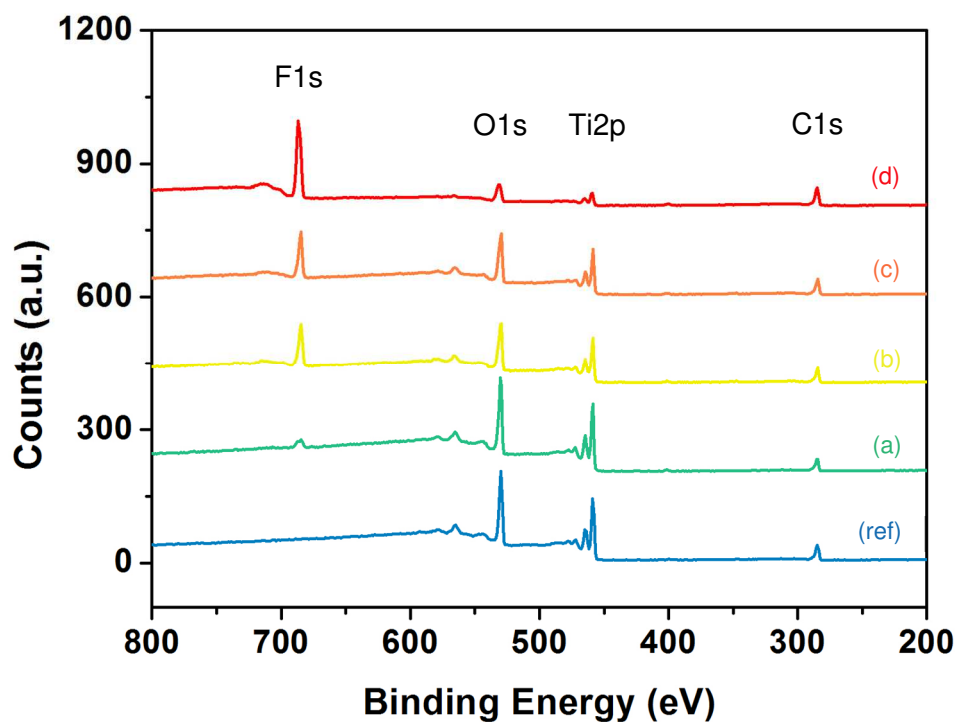


**Figure 26:** XPS survey spectra for the surface of  $\text{TiO}_2$  films (PB-PEO, 2M  $\text{TiCl}_4$ , 2 dipped layers) in LP30 electrolyte for cycling steps (a)-(d).

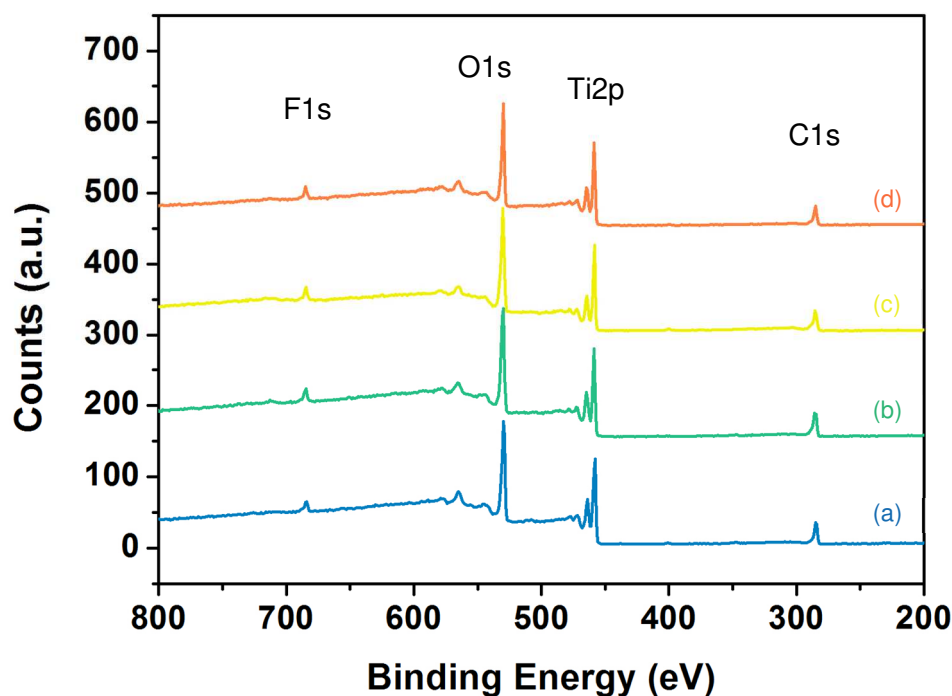


**Figure 27:** XPS survey spectra for the surface of  $\text{TiO}_2$  films (PB-PEO, 2M  $\text{TiCl}_4$ , 2 dipped layers) in  $\text{PYR}_{13}\text{TFSI}$  (0.2M  $\text{LiTFSI}$ ) for cycling steps (a)-(d).

In LP30, XPS spectra showed important evolution in the F1s regions (**Figure 28**). Peak at 684.8 eV is attributed to the fluor of the FTO substrate (**FTO**) by comparison to Xu et al. study.<sup>43</sup> The peak position of this signal is different from the one expected for the fluor in  $\text{LiPF}_6$ <sup>44,45</sup> or  $\text{LiF}$ .<sup>46</sup> A FTO substrate annealed for 1h at 500°C was analyzed as reference and effectively showed a single peak in the F 1s region at the same energy. The presence of peak characteristic of FTO substrate was at first sight unexpected for the  $\text{TiO}_2$  films, as XPS should only probe the first nanometers of the surface of the films. Because  $\text{TiO}_2$  films are porous and quite thin (around 200 nm), X-Rays could probably go across the film and hit the substrate. Analysis of a denser  $\text{TiO}_2$  (ref) film prepared with no polymer (135 nm-thick) showed absence of peak in this region, thus confirming this attribution.

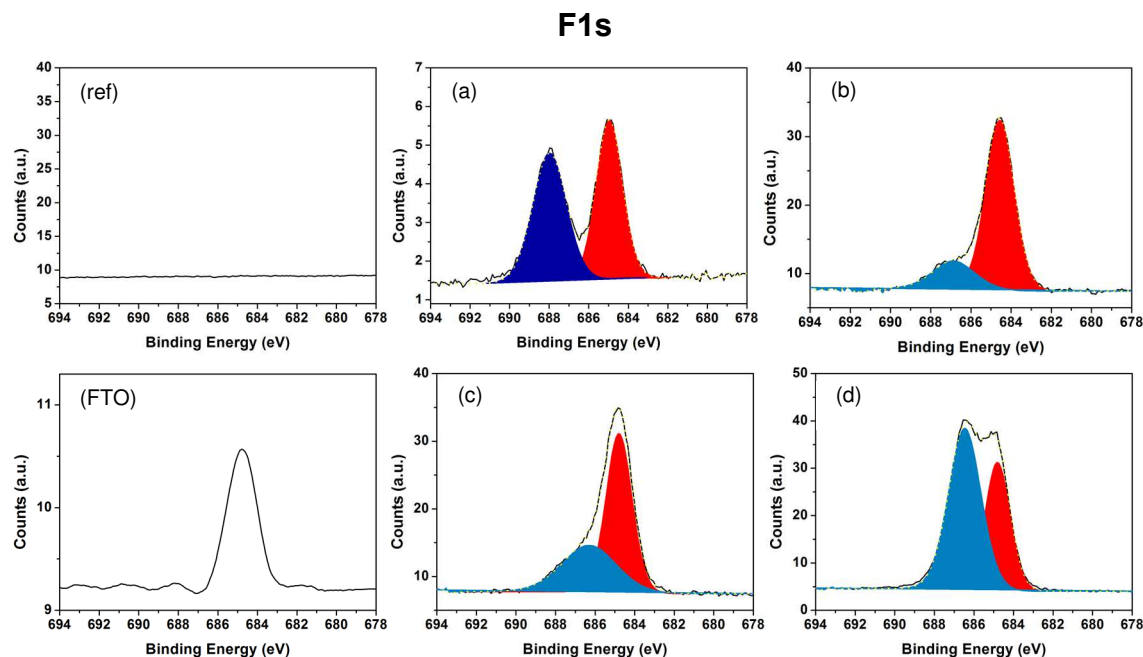


**Figure 28:** F1s XPS for the surface of TiO<sub>2</sub> films (PB-PEO, 2M TiCl<sub>4</sub>, 2 dipped layers) in LP30 for cycling steps (a)-(d), for the surface of a FTO substrate annealed for 1h at 500°C (FTO) and for the surface of a TiO<sub>2</sub> film prepared without polymer (ref).

The peak observed at 688.0 eV after 1 night in LP30 without any electrochemical cycling ((a), dark blue) is absent on a native TiO<sub>2</sub> electrode, which was not in contact with the electrolyte (ref). This peak is characteristic for the F1s electron binding energy of remaining native LiPF<sub>6</sub> salt at the electrode surface.<sup>44,45</sup>

After cycling, this peak is shifted at 686.2 – 686.5 eV ((b), (c), (d), light blue). It witnesses the presence of LiF (reported at 685.0,<sup>45,47</sup> 685.5,<sup>44</sup> 686<sup>38</sup> and from 685.9 to 686.5 eV in Verma et al. review<sup>46</sup>) as degradation product of LP30. It could confirm the nature of the previously observed growing flakes during the FEG-SEM and EDX experiments described in the previous section. Progressive electrolyte degradation upon electrochemical cycling is confirmed by the increase of the peak intensity after 45 CVs (d) in comparison to the intensity after 10 CVs.

Increase of the characteristic peak for LiF after 10 CVs under illumination (c) compared to the same experiment in dark conditions (b) also tends to confirm the accelerated LP30 degradation under illumination.

The XPS spectra of O1s region showed a two-band structure (**Figure 29**). The dominant peak 529.8 - 529.9 eV is characteristic of the O1s electron binding energy in TiO<sub>2</sub>.<sup>48</sup> The second O1s peak around 531.1 - 531.2 eV may be attribute to different oxidized hydrocarbons<sup>48</sup> and/or to OH-groups from chemisorbed H<sub>2</sub>O at the electrode surface.<sup>49</sup>

After long electrochemical cycling in dark conditions (d), the secondary peak significantly increased. It can be attributed to additional presence of carbonates like  $\text{Li}_2\text{CO}_3$  or  $\text{ROCO}_2\text{Li}$ , which have already been proposed as SEI components on anatase  $\text{TiO}_2$  Li-ion battery electrode surface<sup>38,39</sup> and in the SEI composition of  $\text{LiPF}_6$ -based electrolytes.<sup>44,46</sup> This secondary peak is very comparable between dark (b) and light (c) experiments.

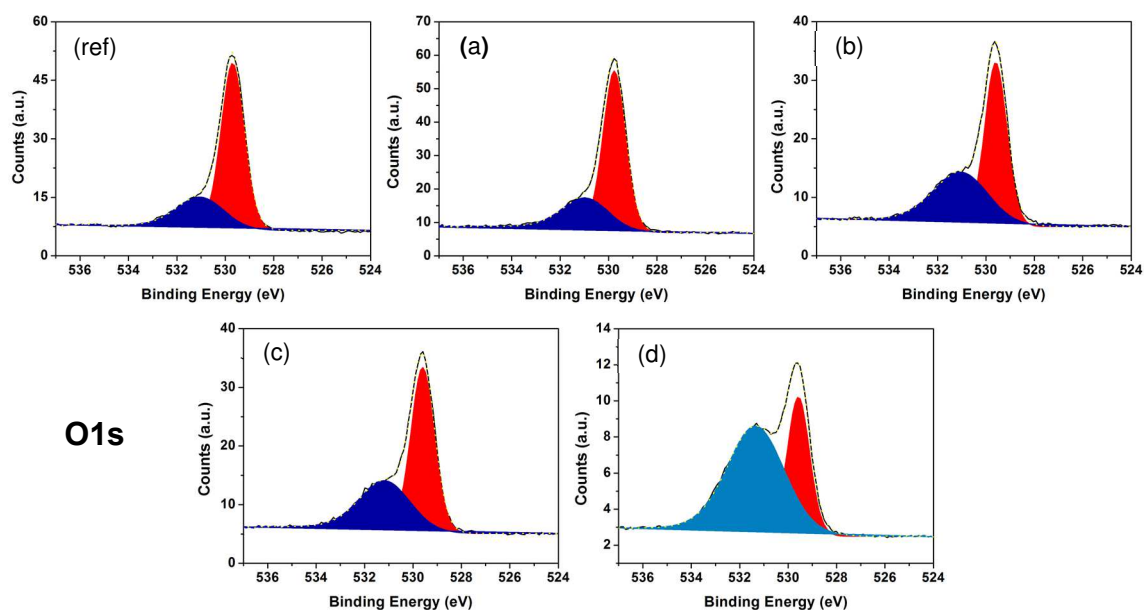


**Figure 29:** O1s XPS for the surface of  $\text{TiO}_2$  films (PB-PEO, 2M  $\text{TiCl}_4$ , 2 dipped layers) in LP30 for cycling steps (a)-(d) and for the surface of a  $\text{TiO}_2$  film prepared without polymer (ref).

In the C1s regions (see **Figure 30**), XPS spectra displayed three components, which were already present in the native  $\text{TiO}_2$  before any contact with the electrolyte (ref). These observed carbon peaks are probably due to incomplete decomposition of the carbon in the starting mesoporous thin film. The dominant peak at 284.4 - 284.5 eV can be attributed to C-C binding from hydrocarbon species.<sup>48</sup> The second and third smaller peaks at  $\approx 285.9$  eV and  $\approx 288.5$  eV correspond to hydroxyl groups (C-OH) and carboxyl groups (O=C-OH).<sup>38,47,48</sup>

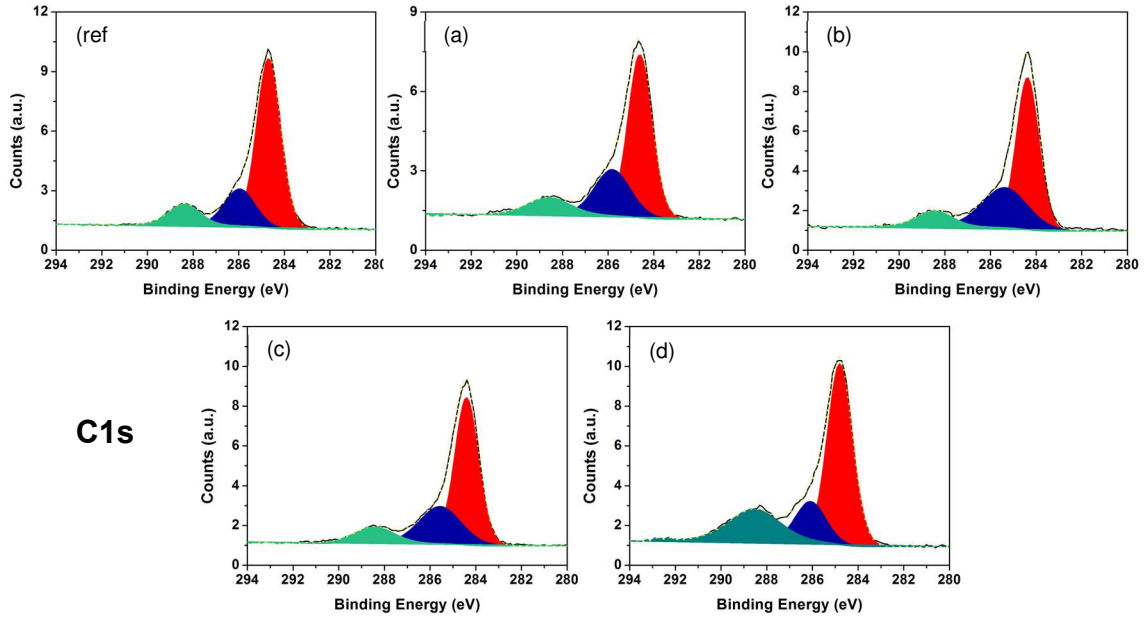


**Figure 30:** C1s XPS for the surface of TiO<sub>2</sub> films (PB-PEO, 2M TiCl<sub>4</sub>, 2 dipped layers) in LP30 for cycling steps (a)-(d) and for the surface of a TiO<sub>2</sub> film prepared without polymer (ref).

These peaks did not show significant evolution upon cycling in dark (b) and under illumination (c) after 10 CVs. For longer cycling time (d), observed slight increase of the peak area at  $\approx 285.9$  eV may witnesses the formation of Li<sub>2</sub>CO<sub>3</sub> or ROCO<sub>2</sub>Li carbonates,<sup>38,46</sup> which is coherent with observations in the O 1s region.

In the Ti 2p region (see **Figure 31**), expected XPS signals for the Ti2p<sub>1/2</sub> ( $\approx 464.3$  eV) and Ti2p<sub>3/2</sub> ( $\approx 458.5$  eV) were observed.<sup>47,50</sup> The oxidation state of Ti(IV) can be verified by comparison with Södergren et al. work,<sup>50</sup> and confirmed the delithiated state of all the probed TiO<sub>2</sub> electrodes before XPS analysis.

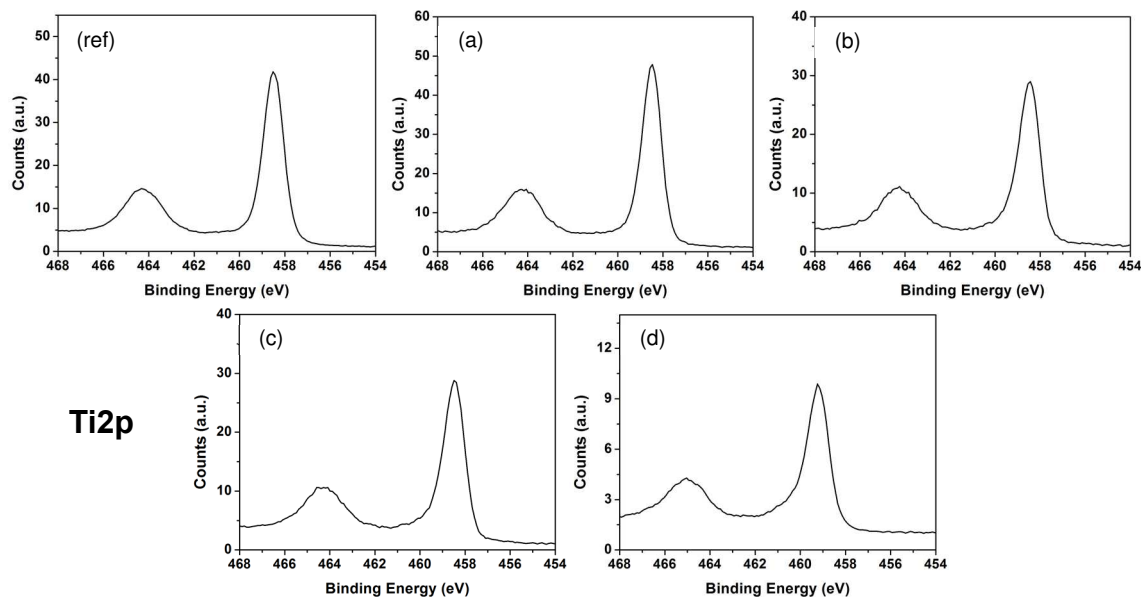


**Figure 31:** Ti2p XPS for the surface of TiO<sub>2</sub> films (PB-PEO, 2M TiCl<sub>4</sub>, 2 dipped layers) in LP30 for cycling steps (a)-(d) and for the surface of a TiO<sub>2</sub> film prepared without polymer (ref).

Comparatively, in PYR<sub>13</sub>TFSI (0.2M LiTFSI) ionic liquid, XPS spectra showed no significant evolution for the F1s, O1s, Ti2p and C1s, regions (see **Figure 32** and **Figure 33**).

In particular, in the F1s region, XPS peak at 688.8 - 688.9 eV is characteristic for the C-F<sub>3</sub> binding from the native TFSI<sup>-</sup> anion.<sup>45</sup> This peak did not shift upon cycling, in dark as well as under light conditions. By opposition to what happened in LP30, characteristic XPS signal for Li-F is absent, which is coherent with the observed unmodified electrode surface after use in ionic liquid (see section III.1). Hence, no sign of electrolyte degradation was observed at the electrode surface in PYR<sub>13</sub>TFSI (0.2M LiTFSI) in these cycling conditions.

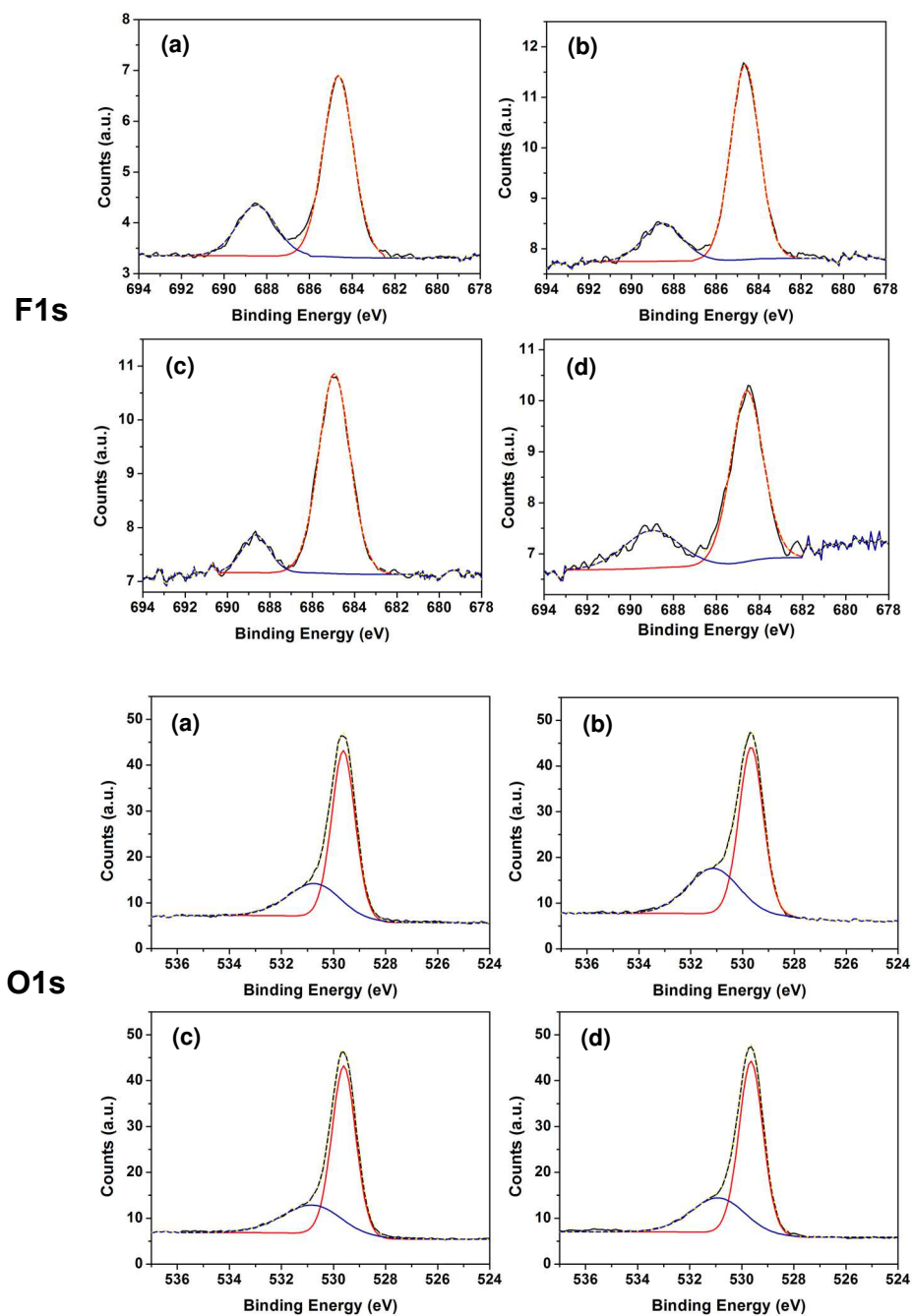


**Figure 32:** F1s and O1s XPS for the surface of  $\text{TiO}_2$  films (PB-PEO, 2M  $\text{TiCl}_4$ , 2 dipped layers) in  $\text{PYR}_{13}\text{TFSI}$  (0.2M  $\text{LiTFSI}$ ) for cycling steps (a)-(d).

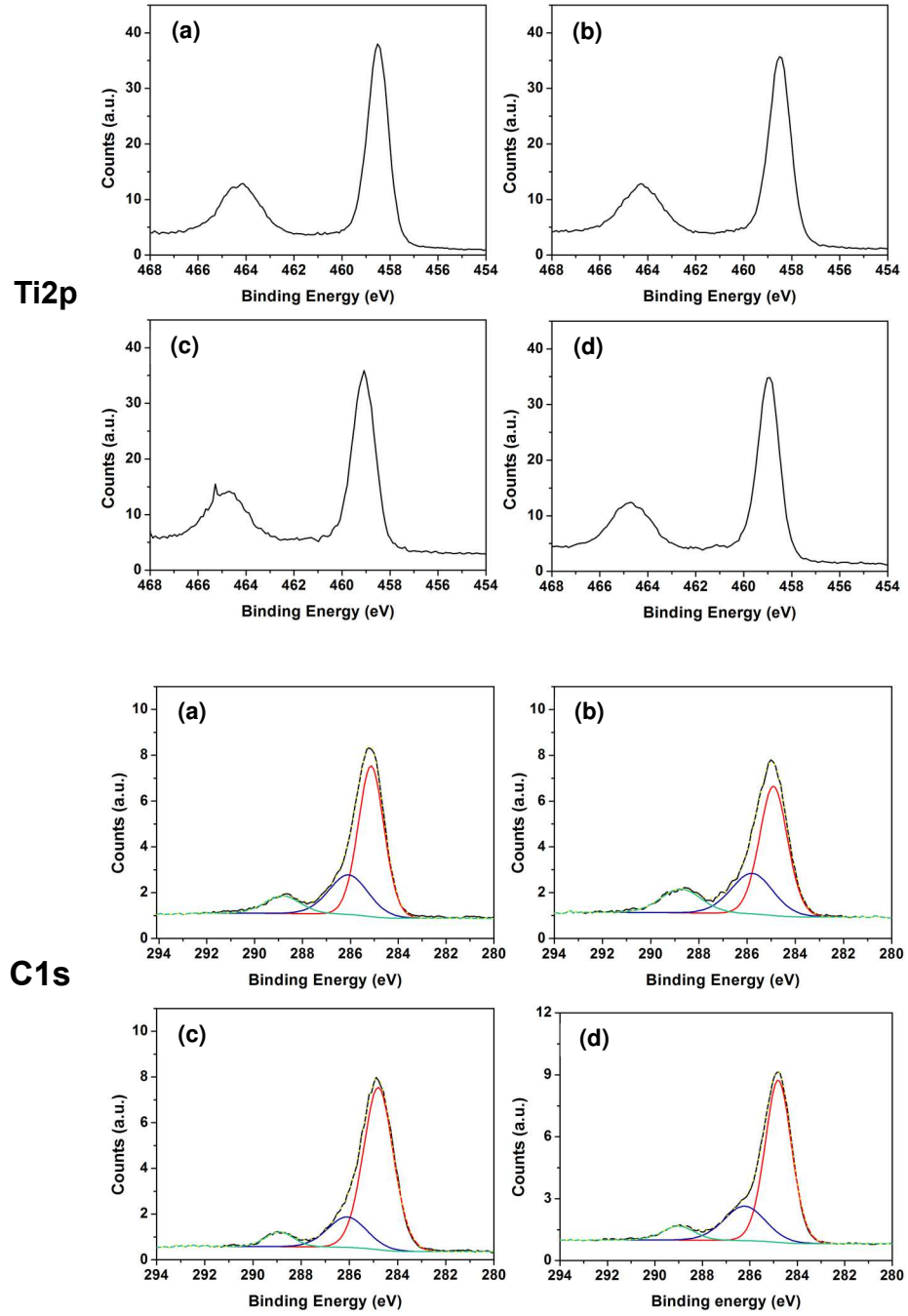


**Figure 33:** Ti<sub>2</sub>p and C1s XPS for the surface of TiO<sub>2</sub> films (PB-PEO, 2M TiCl<sub>4</sub>, 2 dipped layers) in PYR<sub>13</sub>TFSI (0.2M LiTFSI) for cycling steps (a)-(d).



### III.3 –Analysing the electrolyte by NMR spectroscopy

NMR spectroscopy can be used as a complementary study to confirm the possible degradation products formed in LP30 and confirms the absence of degradation of  $\text{PYR}_{13}\text{TFSI}$ , as well as the presence of residual water in the ionic liquid-based electrolyte.  $^{19}\text{F}$  and  $^{31}\text{P}$  NMR spectroscopy will be used for LP30, and  $^1\text{H}$  NMR spectroscopy for  $\text{PYR}_{13}\text{TFSI}$ .

In **Figure 34** is presented  $^{19}\text{F}$  NMR spectra of native LP30 solution prepared under argon atmosphere. The  $^{19}\text{F}$  spectra consists of typical doublets with chemical shifts  $\delta_{\text{F}} = -72.9$  ppm [ $J(\text{P},\text{F}) = 708$  Hz] (int. = 100) that is assigned to  $\text{PF}_6^-$  and  $\delta_{\text{F}} = -84.9$  ppm [ $J(\text{P},\text{F}) = 930$  Hz] (int. = 0.1) that is assigned to a small quantity of  $\text{OPF}_2\text{O}^-$ . A not very well-defined signal is also observed with  $\delta_{\text{F}} = -183.5$  ppm, which is probably due to the presence of trace of HF. The  $^{31}\text{P}$  NMR spectra contains a septet with  $\delta_{\text{P}} = -144.6$  ppm [ $J(\text{P},\text{F}) = 708$  Hz] belonging to  $\text{PF}_6^-$ . Amount of  $\text{OPF}_2\text{O}^-$  was still too low to be clearly detected on  $^{31}\text{P}$  NMR spectra. The signal assignments are based on literature data.<sup>6,51</sup>

$\text{OPF}_2\text{O}^-$ , is one of the species found in the LP30 initial degradation process (see **Annex Figure I.7**).<sup>51</sup> It is formed by the reaction between water and  $\text{POF}_3$ , which is, with HF, hydrolysis products of  $\text{PF}_5$  (themselves arising from the decomposition of  $\text{LiPF}_6$  salt).<sup>4,6,7</sup>

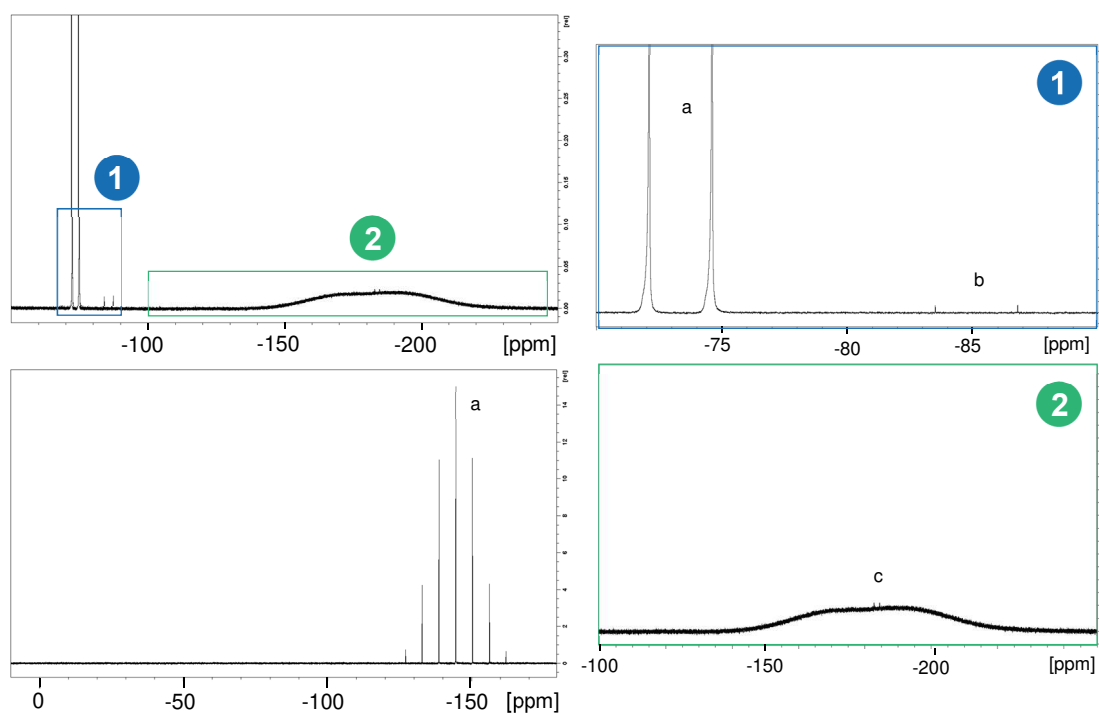


**Figure 34:**  $^{19}\text{F}$  (upper left with zoom to the right) and  $^{31}\text{P}$  (down left) NMR spectra of native LP30 electrolyte in  $\text{CD}_3\text{CN}$ . Signals a, b, c are assigned to  $\text{PF}_6^-$ ,  $\text{OPF}_2\text{O}^-$ , and HF, respectively.

After 10 CVs (2.6 V to 1.4 V vs.  $\text{Li}^+/\text{Li}^0$ ,  $0.5 \text{ mV.s}^{-1}$ ) under dark (**Figure 35**) and light (**Figure 36**) conditions using  $\text{TiO}_2$  (PB-PEO,  $\text{TiCl}_4$  at 2M, 2 dipped layers) as working electrode and  $\text{Li}^\circ$  at reference and counter electrodes, NMR signals belonging to  $\text{PF}_6^-$  and  $\text{OPF}_2\text{O}^-$  were also observed on  $^{19}\text{F}$ . Ratios between  $\text{PF}_6^-$  and  $\text{OPF}_2\text{O}^-$  deduced from  $^{19}\text{F}$  NMR integration signals are (100/0.4) in dark and (100/0.5) under light, versus (100/0.1) in the native LP30. At the time scale of our experiments (time of full illumination less than 14h), the electrochemical cycling of the electrode is thus the predominant phenomenon responsible for the electrolyte degradation. If it is significant, the slight increase of  $\text{OPF}_2\text{O}^-$  amount under light in comparison to dark conditions is coherent with the increasing formation under illumination of  $\text{LiF}$  at the electrode surface, observed through SEM-FEG and EDX analysis in section III.1. In fact, in the LP30 degradation process, formation of  $\text{LiF}$  is concomitant with formation of  $\text{PF}_5$ , which is a precursor for the formation of  $\text{OPF}_2\text{O}^-$  (**Annex Figure I.7**).

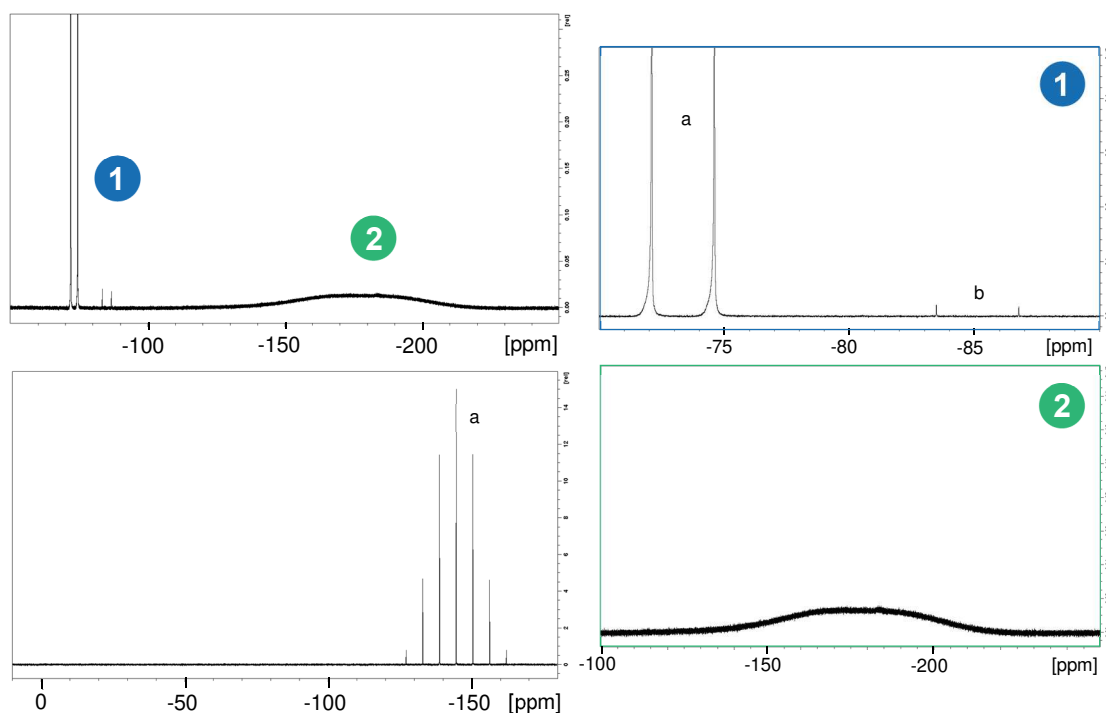


**Figure 35:**  $^{19}\text{F}$  (upper left with zoom to the right) and  $^{31}\text{P}$  (down left) NMR spectra of LP30 electrolyte in  $\text{CD}_3\text{CN}$  after 10 CV (2.6 V to 1.4 V vs.  $\text{Li}^+/\text{Li}^0$ ,  $0.5 \text{ mV.s}^{-1}$ ) under dark conditions. Signals a and b are assigned to  $\text{PF}_6^-$ ,  $\text{OPF}_2\text{O}^-$ , respectively.

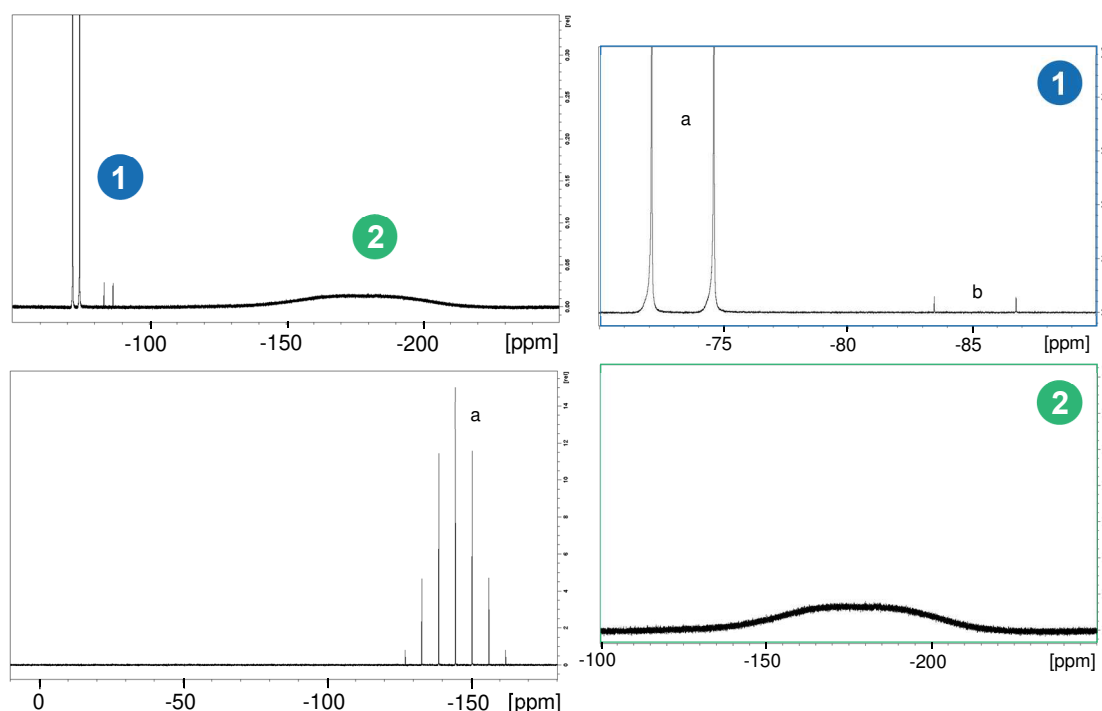


**Figure 36:**  $^{19}\text{F}$  (upper left with zoom to the right) and  $^{31}\text{P}$  (down left) NMR spectra of LP30 electrolyte in  $\text{CD}_3\text{CN}$  after 10 CV (2.6 V to 1.4 V vs.  $\text{Li}^+/\text{Li}^0$ ,  $0.5 \text{ mV}\cdot\text{s}^{-1}$ ) under illumination. Signals a and b are assigned to  $\text{PF}_6^-$ ,  $\text{OPF}_2\text{O}^-$ , respectively.

Electrolytes have also been analyzed after one and two weeks of cycling experiments to see the evolution of LP30 for longer experiment times (**Figure 37**).

After one week,  $^{19}\text{F}$  spectra shows increase of the amount of  $\text{OPF}_2\text{O}^-$  (ratio between  $\text{PF}_6^-/\text{OPF}_2\text{O}^-$  is 100/1.7) and characteristic singlet with  $\delta_{\text{F}} = -184.6 \text{ ppm}$  belonging to HF.

After two weeks, an additional doublet attributed to  $\text{OPFO}^{2-}$  is observed with  $\delta_{\text{F}} = -77.2 \text{ ppm}$  [ $J(\text{P},\text{F}) = 924 \text{ Hz}$ ] (ratio between  $\text{PF}_6^-/\text{OPF}_2\text{O}^-/\text{OPFO}^{2-}$  is 100/17/1.4)  $\text{OPFO}^{2-}$  is known to form in a second step in the degradation process by reaction of  $\text{OPF}_2\text{O}^-$  with water, which releases additional  $\text{HF}^{51}$  (**Annex Figure I.7**). In the meantime, amount of HF kept increasing, whereas a quintuplet belonging to an unknown species appears at 132.4 ppm.

$^{31}\text{P}$  NMR spectra confirmed the presence of both  $\text{OPF}_2\text{O}^-$  and  $\text{OPFO}^{2-}$  by the triplet with  $\delta_{\text{P}} = -19.2 \text{ ppm}$  [ $J(\text{P},\text{F}) = 942 \text{ Hz}$ ] and the doublet with  $\delta_{\text{P}} = 9.1 \text{ ppm}$  [ $J(\text{P},\text{F}) = 925 \text{ Hz}$ ], respectively.

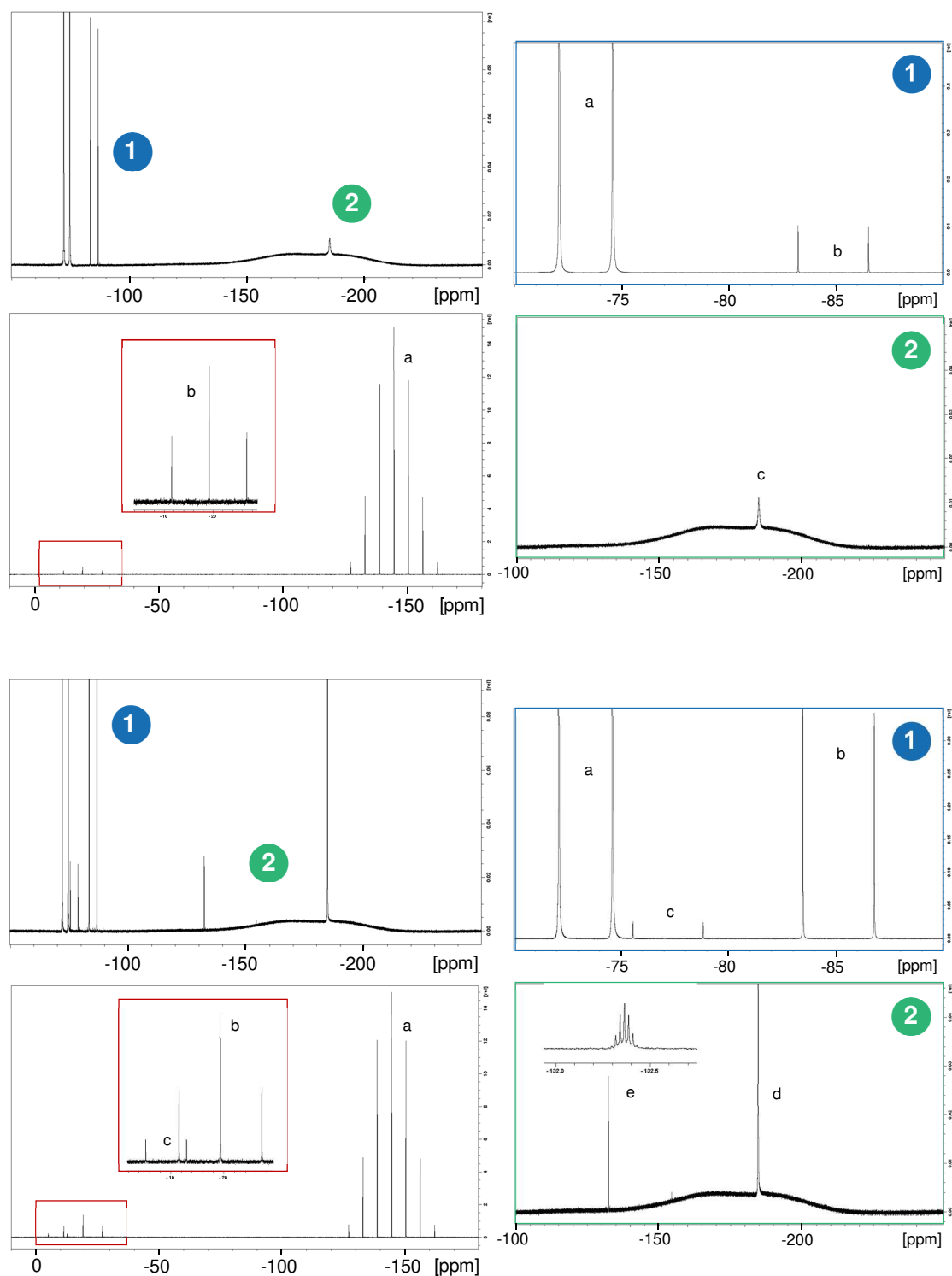


**Figure 37:**  $^{19}\text{F}$  and  $^{31}\text{P}$  NMR spectra of LP30 electrolyte in  $\text{CD}_3\text{CN}$  after 1 week (up) and 2 weeks (down) in electrochemical cell. Signals a, b, c and d are assigned to  $\text{PF}_6^-$ ,  $\text{OPF}_2\text{O}^-$ ,  $\text{OPFO}^{2-}$  and  $\text{HF}$ , respectively.

Using the same methodology, NMR measurements were also performed on  $\text{PYR}_{13}\text{TFSI}$  (0.2M in  $\text{LiTFSI}$ ) after different steps of electrode cycling. Comparatively,  $^1\text{H}$  NMR spectra do not show any difference between the native electrolyte, or when cycled for 10 CVs (2.6V to 1.4V vs.  $\text{Li}^+/\text{Li}^0$ ,  $0.5 \text{ mV.s}^{-1}$ ) in dark or in light conditions, as well as after 2 weeks under cycling conditions (including light exposure) (**Figure 38**). Attribution of the  $^1\text{H}$  signals are in good agreement with expected chemical shift and integration for  $\text{PYR}_{13}\text{TFSI}$ ,<sup>52</sup> and are described in (**Figure 39**). The peak at 2.2 ppm confirms the non-negligible presence of water in the electrolyte, as suggested in our previous analysis in section II.2.

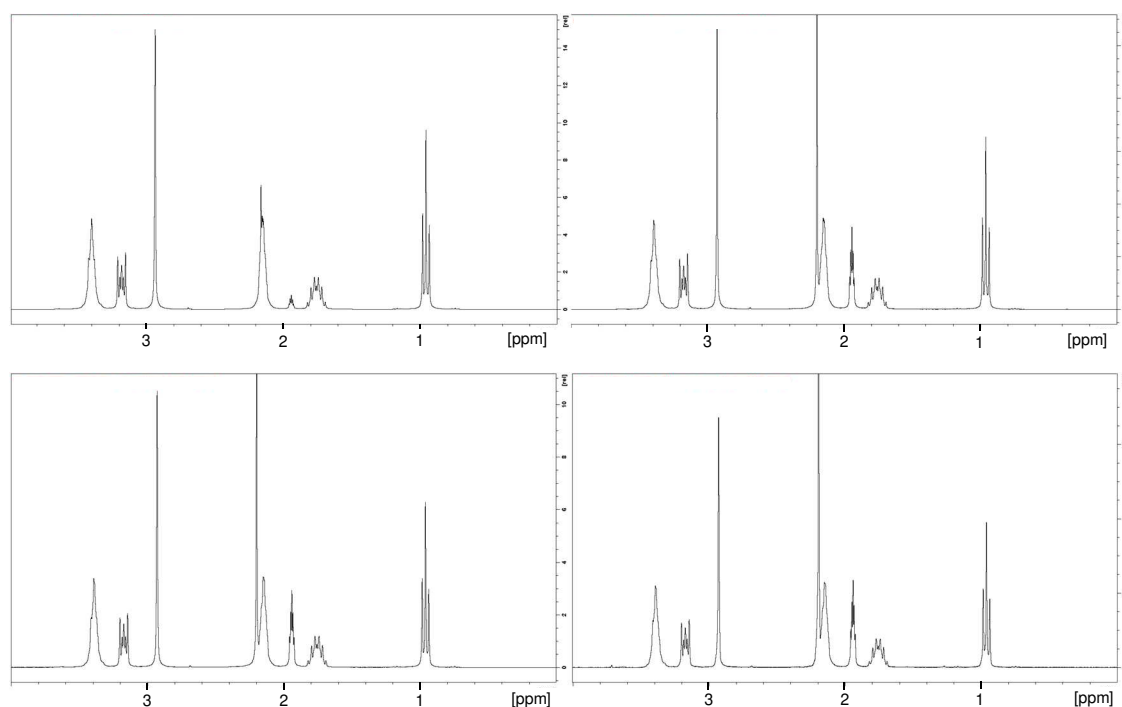


**Figure 38:**  $^1\text{H}$  NMR spectra of  $\text{PYR}_{13}\text{TFSI}$  (0.2M  $\text{LiTFSI}$ ) electrolyte in  $\text{CD}_3\text{CN}$ , native (upper left), after 10 CVs (2.6 V to 1.4 V vs.  $\text{Li}^+/\text{Li}^0$ ,  $0.5 \text{ mV.s}^{-1}$ ) in dark (upper right), in light conditions (down left) and after 2 weeks of cycling including light exposure (down right).

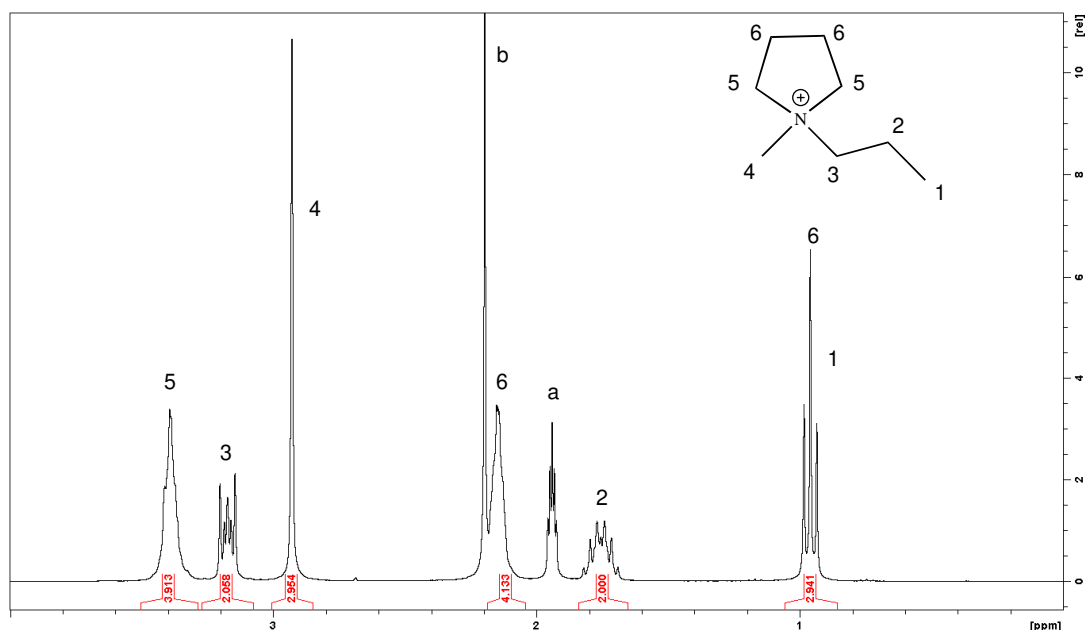


**Figure 39:** Peak assignments for  $\text{PYR}_{13}\text{TFSI}$ . Peak (a) corresponds to the deuterated solvent impurity, peak (b) to water.<sup>53</sup>

In this section, questions about the fate of the photo-charges have been addressed by considering their potential reaction with the electrolyte.

In the case of LP30, under dark conditions, usual electrolyte degradation products were found on the electrode surface ( $\text{LiF}$ ) and in the electrolyte ( $\text{OPF}_2\text{O}^-$ ,  $\text{OPFO}^{2-}$  and  $\text{HF}$ ). Possible accelerated formation of  $\text{LiF}$  under illumination and cycling conditions (10 CVs between 2.6 V to 1.4 V vs.  $\text{Li}^+/\text{Li}^0$ ,  $0.5 \text{ mV}\cdot\text{s}^{-1}$ ) could (1) be due to an eventual temperature increase of the non water-cooled cell under continuous illumination, and/or (2) witness the participation of photo-electrons to the  $\text{LiPF}_6$  salt reduction.

In the case of  $\text{PYR}_{13}\text{TFSI}$  (0.2M  $\text{LiTFSI}$ ), no degradation product, neither from TFSI anion, nor from the pyrrolidinium cation, were observed during electrochemical cycling in dark conditions as well as under illumination. Presence of residual water molecules, which has been suggested in the previous section, was confirmed by NMR study.

In order to further investigate the properties of the system, we now propose to study  $\text{TiO}_2$  materials by means of *operando* techniques. In the next section, EIS measurements will be performed in order to probe the electrical properties of the material in dark and light conditions.

## IV – TiO<sub>2</sub> photo-electrode: *operando* characterizations

### IV.1 – Electrochemical Impedance Spectroscopy (EIS)

Electrochemical Impedance Spectroscopy (EIS) is an analytical technique, which allows to study electrochemical and electrical properties of a material (*e.g.* the conduction properties, the corrosion, or the chemical reaction occurring at its surface or interfaces). In particular, EIS measurements can provide qualitative information about the resistive, capacitive or diffusive phenomena at an electrode/electrolyte interface, and can be helpful in order to distinguish their origin depending on the frequency range (*e.g.* electrolyte or material intrinsic resistance, resistance due to intern interfaces, resistance due to the processes at the electrode/electrolyte interfaces, *etc.*).

EIS analysis consists in (1) applying a sinusoidal perturbation with constant amplitude and variable frequency ( $v(t) = V_m \cdot \cos(\omega t)$ ) to the studied system, and (2) monitoring its answer ( $i(t) = I_m \cdot \cos(\omega t - \phi)$ ).

- At the applied tension,  $v(t)$ , is associated the complex number  $\underline{v(\omega)} = V_m \cdot e^{j\omega t}$ .
- At the resulting intensity,  $i(t)$ , is associated the complex number  $\underline{i(\omega)} = I_m \cdot e^{j(\omega t - \phi)}$ .

The complex impedance is then defined as  $Z(\omega) = \underline{v(\omega)} / \underline{i(\omega)}$ , with the notation  $Z(\omega) = Z' + jZ''$ , where  $Z' = \text{Re}(Z)$  and  $Z'' = \text{Im}(Z)$ . The representation mode associated to the formalism where  $-Z'' = f(Z')$  is called Nyquist diagram. For each pulsation  $\omega$ , only the extremity of the  $\vec{Z}(\omega)$  vector is represented. The combination of all the reunited points forms the characteristic curve of the studied system.

#### IV.1.1 – Nyquist plots and equivalent circuits

Anatase electrode (PB-PEO, 2M in TiCl<sub>4</sub>, 2 layers) was analyzed using impedance measurements in order to follow the evolution of electrical properties of the electrochemical cell upon cycling using the usual 3-electrode configuration in LP30 electrolyte.

**Figure 40** and **Figure 41** represent the Nyquist diagrams obtained at different potentials during a galvanostatic discharge (-30  $\mu\text{A}$ )/charge (30  $\mu\text{A}$ ) experiment under dark (black curve) and light (red curve) conditions. Prior to this experiment, 10 CVs (2.6 V to 1.4 V vs. Li<sup>+</sup>/Li<sup>0</sup>, 0.5 mV.s<sup>-1</sup>) were applied to the TiO<sub>2</sub> electrode in order to reach stable electrochemical response.

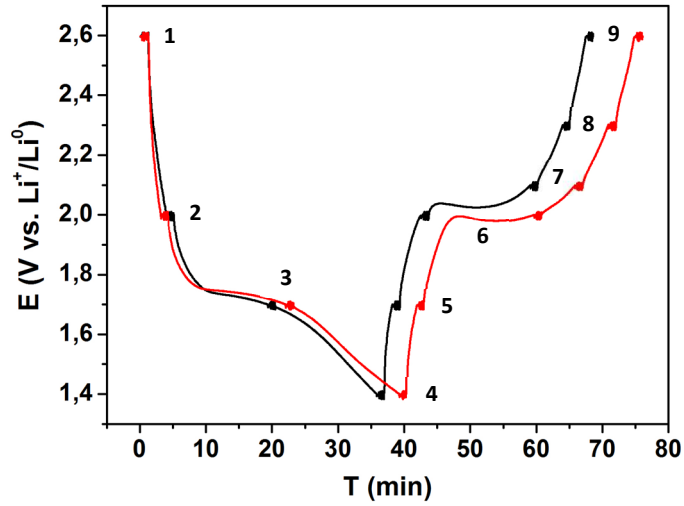


**Figure 40:** Galvanostatic discharge ( $-30 \mu\text{A}$ )/charge ( $30 \mu\text{A}$ ) experiment under dark (black curve) and light (red curve) conditions with simultaneous EIS measurements at different potentials corresponding to Nyquist plots in **Figure 41**.

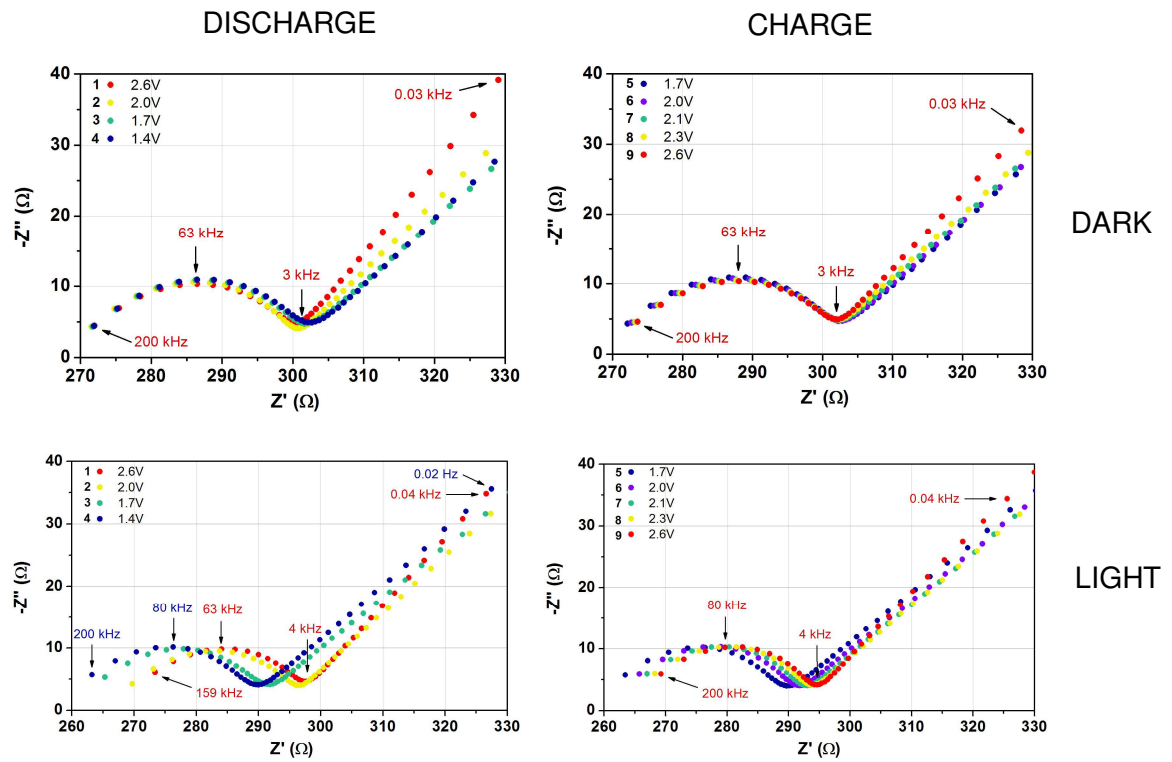


**Figure 41:** Nyquist diagrams (200 kHz to 0.1 Hz, amplitude 10 mV, orthonormal diagrams) obtained at different potentials during the galvanostatic discharge presented in **Figure 40** in dark conditions (up). Same experiment under light (down). Discharges are plotted to the left, and charges to the right.



Different equivalent circuits were successively tested to simulate the impedance spectra (**Figure 42**).

In the equivalent circuit (a), an ohmic resistance ( $R_\Omega$ ) was used to describe the cumulative resistance of the electrolyte and cell components. A parallel circuit combining a capacitance and a resistance was taken for the double-layer capacitance ( $C_{DL}$ ) and the charge transfer resistance ( $R_{CT}$ ). A Warburg element ( $Z_W$ ) is added to describe the diffusion of  $\text{Li}^+$  into the electrode. The as-described Randles circuit is a commonly used equivalent circuit for the interpretation of impedance spectra at an electrode/electrolyte interface.<sup>54</sup> In particular, it has already been used to describe lithium diffusion in nano-sized rutile  $\text{TiO}_2$ ,<sup>55</sup> rutile  $\text{MnO}_2$ <sup>56</sup> or  $\text{WO}_3$  thin films.<sup>57</sup>

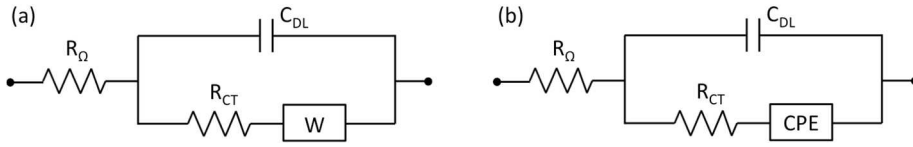


**Figure 42:** Equivalent circuits used for EIS data fits. Randles circuit (a), modified Randles circuit constant phase element (b).

In our case, this model was insufficient to properly fit the impedance data (**Annex Figure A.I.8**). In fact, upon cycling, the Nyquist plots mostly evolve in the diffusion zone (low frequencies zone) described by the Warburg element. As the Warburg element has constant phase at  $45^\circ$  from the real  $Z$  axis, it was not completely well suited in our case to fit and compare Nyquist plots presenting curves with changing slopes (slightly different from  $45^\circ$ ) in the diffusion area.

Thus, a second equivalent circuit (b) was proposed by replacing the Warburg element by a constant-phase element (CPE). Models invoking CPEs are more often used to replace the double-layer capacitance, when solid/electrolyte interfaces reveal non-capacitive double layer properties, which arises in a broad range of experimental systems.<sup>58-61</sup> However, it has also been used in replacement of the Warburg element to describe diffusion phenomena (*e.g.*  $\text{Na}^+$  diffusion in  $\text{MnO}_2$ ,<sup>62</sup>  $\text{Li}^+$  diffusion in rutile  $\text{TiO}_2$ ,<sup>63</sup> or in  $\text{MnO}_2$  supercapacitors<sup>61</sup>).

The CPE impedance is expressed in terms of model parameters  $\alpha$  and  $Q$  as:

$$Z_{CPE} = \left( \frac{1}{(j\omega)^\alpha Q} \right) \quad (1)$$

where  $\alpha$  is the CPE exponent and  $Q$  [ $F \cdot s^{-(1-\alpha)}$  or  $\Omega^{-1} s^\alpha$ ] the CPE parameter.

The physical interpretation of the CPE remains a matter of controversy. It was initially attributed to a dispersion of the capacity or a change of capacity with the frequency and for that reason it was referred to as “capacitive dispersion” or “frequency dispersion of capacitance”. This phenomenon is generally believed to be due to interface inhomogeneities (surface disorder and roughness, electrode porosity, surface adsorption, normal-to surface distributions characteristics in films and coatings, *etc.*),<sup>58</sup> which cause a distribution of time-constants.<sup>59</sup>

In this study, CPE element is mathematically used to fit properly and compare the slopes of the Nyquist plots in the diffusive zones. Slope of the curves in low frequency zone can be linked to  $\alpha$ . In fact, the Bode representation of the complex capacitance function defined as  $C(\omega) = [i\omega \cdot (Z(\omega) - Z(\omega \rightarrow \infty))]^{-1}$  should give a straight line with slope  $\alpha - 1$ . A decreasing  $\alpha$  thus gives a more and more tilted curve in the diffusion region.

#### IV.1.2 – Results of the fits and analysis

In dark conditions as well as under illumination, fitted curves (**Annex Figure A.I.9** and **Figure A.I.10**) and parameters (**Table 2**) obtained with equivalent circuit (b) showed that  $R_\Omega$ ,  $C_{DL}$  and  $R_{CT}$  are globally invariant in discharge as well as in charge.

E (vs. Li <sup>+</sup> /Li)	dark	$R_\Omega$ ( $\Omega$ )	$C_{DL}$ ( $\mu F$ )	$R_{CT}$ ( $\Omega$ )	Q ( $\Omega^{-1}s^\alpha$ )	$\alpha$	light	$R_\Omega$ ( $\Omega$ )	$C_{DL}$ ( $\mu F$ )	$R_{CT}$ ( $\Omega$ )	Q ( $\Omega^{-1}s^\alpha$ )	$\alpha$
2.6		275	0,12	23	0,0008	0,58		274	0,13	21	0,0011	0,52
2		274	0,11	24	0,0020	0,49		272	0,12	21	0,0022	0,48
1.7		275	0,11	24	0,0021	0,46		267	0,10	21	0,0027	0,44
1.4		275	0,12	25	0,0020	0,50		265	0,010	22	0,0024	0,47
1.7		275	0,12	24	0,0022	0,47		265	0,09	22	0,0028	0,44
2		276	0,12	24	0,0020	0,49		267	0,09	22	0,0024	0,46
2.1		276	0,12	24	0,0017	0,49		269	0,09	22	0,0022	0,47
2.3		276	0,11	23	0,0016	0,49		270	0,09	22	0,0019	0,47
2.6		276	0,11	23	0,0012	0,51		270	0,08	21	0,0013	0,50

**Table 2:** Parameters from fits of Nyquist plots using equivalent circuit (b) during the discharge (2.6 V to 1.4 V vs. Li<sup>+</sup>/Li<sup>0</sup>) (green) and the following charge (1.4 V to 2.6 V vs. Li<sup>+</sup>/Li<sup>0</sup>) (blue) in dark (left) and under illumination (right).

In order to verify that the CPE (added to describe the diffusion) did not artificially distort resistances and capacitance values,  $R_\Omega$ ,  $C_{DL}$  and  $R_{CT}$  were also fitted using usual Randles circuit and RC in the semi-circle frequencies zones. Very similar values were found for these three parameters using the 3 equivalent-circuits (**Annex Figure A.I.8**).

As the lithium content  $x$  in our electrodes is  $< 0.5$  in our electrode, The value of  $R_{CT}$  ( $\approx 20 \Omega$ ) and its relative invariance upon cycling is comparable with previous studies (a different evolution could be observed for higher lithium content).<sup>55,56,63</sup>

In dark as in light conditions,  $\alpha$  globally decreased during the discharge, then progressively re-increased during the charge.

It is however not easy to directly interpret the physical meaning of  $\alpha$  coefficient. For example, in Pfanzelt *et al.* study,<sup>63</sup> which uses the same equivalent circuit to describe rutile  $\text{TiO}_2$  during discharge and charge, authors observed the same trend for  $\alpha$  as in our study, but do not comment the evolution of the CPE coefficient.

In Bach *et al.* study,<sup>56</sup> it has been shown for nano-size rutile  $\text{TiO}_2$  that chemical diffusion coefficient decreased vs. the lithium content. This analysis was made from a Randles equivalent circuit by determining the Warburg impedance prefactor  $A$  (defined by  $-\text{Im}(Z) = A\omega^{-1/2}$ ), which is inversely proportional to the square root of diffusion coefficient.<sup>55,57</sup>

In order to try to use in a simple way this  $\alpha$  coefficient (which could be simply used as the parameter allowing to fit the slope of the Nyquist plot in the diffusion zone), we have attempted to exploit the EIS fits in the diffusion area, by treating them as a “Warburg-like” element with a slight correction of the exponent  $\alpha$  with a range  $0.46 < \alpha < 0.58$  instead  $\alpha = 0.5$  (ideal Warburg element is a CPE  $\alpha = 0.5$ ).

In this approximation, the “Warburg-like” diffusion coefficient is the slope of the  $-\text{Im}(Z)$  curve plotted as a function of  $\omega^{-\alpha}$ . Results presented in (**Figure 43**) showed that “Warburg-like” coefficient, referred as  $A_\alpha$ , decreases with increasing lithium content until  $E = 1.7 \text{ V}$  ( $\approx \text{Li}_{0.2}\text{TiO}_2$ , with Li content evaluated through the galvanostatic discharge), but is then higher at  $1.4 \text{ V}$  ( $\approx \text{Li}_{0.5}\text{TiO}_2$ ).

At this point, we will not risk to over-interpret our results due to difficulty that represents the interpretation of the  $\alpha$  coefficient. But if the analysis by means of this model is correct, it could potentially mean that the diffusion of  $\text{Li}^+$  is facilitated at relative low lithium content ( $x \lesssim 0.2$  in  $\text{Li}_x\text{TiO}_2$ , in discharge) then becomes harder at higher lithium content ( $x \gtrsim -0.2$ , in discharge). This trend would be in part consistent with Bach *et al.*<sup>55</sup> ‘s analysis for the high lithium content, but differs from their observations at small lithium content, as they described a continuous decrease of the apparent chemical diffusion with lithium insertion. It is also to mention that we have compared here the “Warburg-like” coefficients and not directly the diffusion coefficient of lithium  $D_{\text{Li}}$ . In fact, the determination of the absolute value of diffusion coefficient of lithium  $D_{\text{Li}}$  is based on multiple parameters (*e.g.* slope  $(dE/dx)_x$  of equilibrium potential

function as a function of the lithium content  $x$ , applied current density, geometrical parameters), which should necessitate a more careful investigation.<sup>55,57</sup>

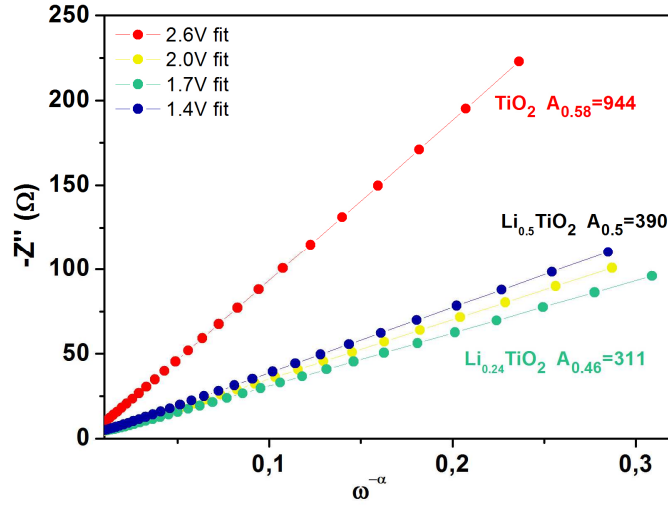


**Figure 43:** determination of  $A_\alpha$  from  $-\text{Im}(Z''(\omega^{-\alpha}))$  plot as a function of the potential during the discharge. Lithium content is estimated through galvanostatic discharge capacity

From this study in dark conditions, we will first remember that the charge transfer resistance is globally invariant with the lithium content (for  $0 < x < 0.5$  in  $\text{Li}_x\text{TiO}_2$ ).

Under illumination,  $\text{TiO}_2$  electrode has very similar behavior. Results presented in **Table 2** do not seem significantly different from those in dark. The comparison between dark and light experiment could also be complicated by the fact that lithium content is not necessarily the same at a given potential between dark and light. From this experiment, we could suggest that light does not significantly influence the diffusion of  $\text{Li}^+$ . Experiments realized on thicker electrodes or reaching more important lithium contents could be interesting for the future investigations.

In the next section, we propose to further study the system using *operando* measurements. A preliminary work is dedicated to the analysis of the gravimetric response of a  $\text{TiO}_2$ -coated piezoelectric substrate ( $\text{GaPO}_4$ ) when coupled to electrochemical and photo-electrochemical measurements. A specially designed experimental setup is thereby developed to study the nature of species involved at the electrode/electrolyte interface upon photo-electrochemical cycling.

## IV.2 – Investigations by means of Electrochemical Quartz Crystal Microbalance (EQCM)

### IV.2.1 – Principle of Quartz Crystal Microbalance (QCM)

The piezoelectric effect is a property of certain materials that become electrically charged when a mechanical stress is applied. Conversely, these materials can be deformed under the action of an external electrical field.<sup>64</sup> Consequently, by applying an electrical potential, dipoles reorganize in the acentric material causing its deformation.<sup>65</sup> Quartz (empirical formula  $\text{SiO}_2$ ) and  $\text{GaPO}_4$  are some of the members of a family of crystals that experience the piezoelectric effect, where quartz is the most commonly used one. The specific cut of the quartz crystal, with respect to its crystallographic axes, as well as its thickness, determine the mode of vibration and its frequency domain.<sup>64</sup> By depositing electrodes on each side of a quartz crystal disk, alternative voltage can be applied between the two electrodes. Consequently, the upper and the lower faces of the active zone oscillate parallel to each other (**Figure 44**). A stationary acoustic wave is generated throughout the quartz crystal. The frequency of this wave is called the resonant frequency of the quartz resonator.<sup>66</sup> This resonant frequency then varies under the effect of changes in the mass, viscoelasticity and shape of the electrode surface. This constitutes the basic principle of the microbalance operation.

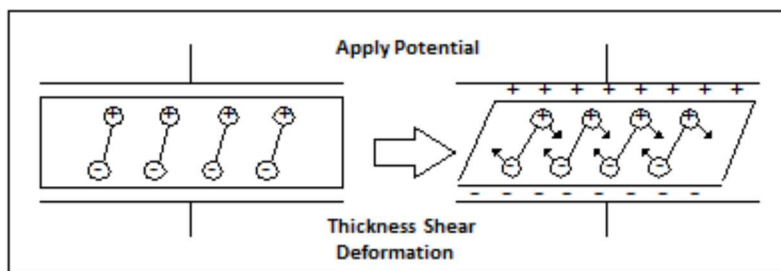


**Figure 44:** Schematic representation of the converse piezoelectric effect for shear motion. Direction of shear is dependent upon the applied potential while the extent of shear strain depends on the magnitude of the applied potential.<sup>65</sup>

A quartz crystal microbalance (QCM) is based on a thin quartz crystal linked to an electrical circuit that is strong enough to create vibrational motion of the crystal at its resonant frequency.<sup>65</sup> The microbalance frequency may be followed over time, the precision depending on the measuring parameters and the stability of the microbalance.<sup>67</sup> This high precision instrument permits the measurement of a mass

sample deposited on the surface of a quartz resonator through the change of its resonance frequency, using Sauerbrey equation<sup>68</sup> (2):

$$\Delta f = \frac{K_S \cdot \Delta m}{S} = - \left( \frac{2n f_0^2}{S \sqrt{\rho_q \mu_q}} \right) \cdot \Delta m \quad (2)$$

where  $\Delta f$  is the measured shift in frequency (Hz),  $\Delta m$  is the mass change (g),  $\rho_q$  is the quartz density (2.648 g.cm<sup>-3</sup>),  $\mu_q$  is the shear modulus of a shear AT quartz crystal (2.947 x 10<sup>11</sup> g.s<sup>-2</sup>.cm<sup>-1</sup>),  $f_0$  is the fundamental resonant frequency of the quartz (Hz),  $S$  is the active surface on the quartz corresponding to the metal electrode surface deposited on it (cm<sup>2</sup>),  $n$  is the overtone number ( $n = 1$  in our case) and  $K_S$  is the theoretical sensitivity factor (Hz.g<sup>-1</sup>.cm<sup>2</sup>). For example for a 6 MHz quartz resonator, theoretical sensitivity factor is 8.14 x 10<sup>7</sup> Hz.g<sup>-1</sup>.cm<sup>2</sup>.<sup>69</sup>

## IV.2 – EQCM and [F(Δm/ΔQ)] function

The electrochemical quartz crystal microbalance (EQCM) has emerged as a very powerful “*in situ*” technique to complement electrochemical experiments. It is based on the coupling of the electrochemical methods (cyclic voltammetry or galvanostatic charge/discharge) and gravimetric measurements through a QCM. This method has been used to investigate diverse phenomena, for example, metal electrodeposition,<sup>70–72</sup> and any mass changes associated with the electrolyte-ion movement, such as electrochromic reactions,<sup>73</sup> intercalation,<sup>74</sup> and electro-adsorption.<sup>75,76</sup> Basically, a metal-patterned quartz crystal resonator (the metal being used as electrode) is inserted in an electrochemical cell (called electrogravimetric cell) and connected to a specific electronic circuit, the whole system being called an oscillator. Thus, it is possible to monitor the evolution of microbalance frequency in the course of electrochemical measurements in real time.

The simultaneous measurement of  $\Delta m$  and of the electrochemical charge  $\Delta Q$  gives the mass per mole of electrons (MPE) exchanged in distinct electrochemical processes. This MPE can be converted into equivalent weights of specific surface species that are inserted, expelled, deposited or dissolved *via* a single or multi electron processes. Specifically, it is possible to quantify small mass changes (of the order of a few nanograms<sup>64</sup>) occurring at the electrode/electrolyte interface during an electrochemical process. During an interval of time, where the mass changes and the electrical charge passed is  $\Delta Q$ , then the apparent mass of the ions involved in the charge compensation can be estimated by means of the mass/charge ratio [F(Δm/ΔQ)],<sup>77</sup> where F is the Faraday constant (96 500 C.mol<sup>-1</sup>), using equation (3):

$$MPE = F \cdot \frac{\Delta m}{\Delta Q} \quad (3)$$

The same analysis can be done punctually at any potential by<sup>77</sup>:

$$MPE = F \cdot \frac{dm}{dQ} = F \cdot \frac{dm/dt}{dQ/dt} = F \cdot \frac{dm/dt}{I} \quad (4)$$

These functions are negative for mass increase during cathodic processes ( $dm > 0$ ,  $dQ < 0$ ) or mass decrease during anodic processes ( $dm < 0$ ,  $dQ > 0$ ) and positive for mass increase during anodic processes ( $dm > 0$ ,  $dQ > 0$ ) or mass decrease during cathodic processes ( $dm < 0$ ,  $dQ < 0$ ).

The  $MPE = F(\Delta m/\Delta Q)$  calculated from the EQCM data can provide indications of the nature of transferred species during cycling. If only one species is involved in the charge storage process, the value of  $MPE$  would be its molar mass. The cation and anion contributions lead to negative and positive signs of  $MPE$  values, respectively.

That way, the function  $[F(\Delta m/\Delta Q)]$  can give information about the species that participate in the charge compensation reaction at different potentials.<sup>78</sup>

Demonstration of this relation<sup>64,79</sup> is given considering the insertion reaction of a monovalent cation  $C^+$  in an electrode free site. When a potential variation,  $\Delta E$ , is applied to the electrochemical system, mass and charge variations may occur according to the equation (5):

$$F = \frac{dQ}{dn} = \frac{dQ}{dm} M_{C^+} \quad (5)$$

where  $dQ$  is the charge variation during the insertion of  $C^+$  and  $dn$  the variation of the number of moles of  $C^+$ . It implies equation (6):

$$M_{C^+} = F \frac{dm}{dQ} \quad (6)$$

This proof was made considering only one cation contribution. The same methodology can be applied when only one anion is involved in the electrochemical process. If there are other species participating in the charge compensation process, the limitation of this method appears as only an average molar mass that represents the contribution of all species can be estimated.

However, in electrochemical systems, it is also important to consider uncharged species such as the free solvent molecules that may participate indirectly in the electrochemical process. This participation could produce mass changes but their motion does not cause an electrical charge flux and, therefore, no faradaic current is associated. Nonetheless, the participation of these species could modify the obtained mass/charge ratio.<sup>80</sup> Conversely, other reactions associated with a faradaic current could take place in the outer medium without implying a mass change at the electrode.<sup>77</sup>

### IV.2.3 – EQCM study for Li-ion photo-battery electrode

The remarkable sensitivity of the EQCM technique has attracted particular attention in the energy storage community (super-capacity, Li-ion battery), since “discrete” events like intercalation (and/or adsorption of ions in/on active materials) can be detected.<sup>75,81</sup> EQCM has already been employed to investigate the electrolyte/electrode interface for Li-ion batteries<sup>82–84</sup> and in particular to analyze the solid electrolyte interface (SEI).<sup>46</sup> However, to the best of our knowledge, EQCM has not been reported yet as an *operando* technique to investigate photo-induced phenomena at the electrode/electrolyte interface of a Li-ion photo-battery. This section presents a preliminary study towards developing *operando* EQCM measurements applied for the analysis of TiO<sub>2</sub> photo-electrode. Results presented in this section were obtained in collaboration with Ozlem Sel and Hubert Perrot from the Laboratoire Interfaces et Systèmes Electrochimiques (LISE).

#### IV.2.3.1 – Electrode fabrication

Anatase TiO<sub>2</sub> electrodes were prepared by adapting the dip-coating process described in Chapter 2 to EQCM substrates. As the final step of the anatase electrode fabrication requires a heat treatment at 500°C for 1h, precautions should be taken with the substrate. In fact, the absolute limit temperature for the microbalance measurements with a quartz crystal is the Curie point at 573 °C. The quartz crystal irreversibly loses all its piezoelectric properties above this point.<sup>69</sup> Therefore, a more robust piezoelectric crystal, gallium orthophosphate (GaPO<sub>4</sub>), was used instead of quartz. GaPO<sub>4</sub> is a quartz structure analogue, Si atoms being replaced by Ga and P atoms in the quartz structure. GaPO<sub>4</sub> shows outstanding thermal properties, as it can be used up to a Curie transition temperature of 930 °C.<sup>69</sup>

The suitable electrode layers were deposited on the neat GaPO<sub>4</sub> resonators in the LISE laboratory. Two different types of electrode geometries are used (**Figure 45**). The resonators were prepared by depositing platinum keyhole electrodes (surface area of



0.4 cm<sup>2</sup> (a) or 1.2 cm<sup>2</sup> (b)) by evaporation techniques on both sides of the GaPO<sub>4</sub> with a titanium adhesion sublayer. TiO<sub>2</sub> mesoporous active material (PB-PEO, 2M in TiCl<sub>4</sub>, 1 dipped layer) was then deposited, by dip-coating, on only one side of the Pt electrodes (face A). The rest of the crystal (not covered with Pt) and the entire face B were immediately cleaned with an ethanol soaked cotton bud. Heat treatment of 500°C was finally applied to obtain the TiO<sub>2</sub>/Pt/GaPO<sub>4</sub> electrodes for EQCM measurements, where TiO<sub>2</sub> is deposited only on the Pt electrode of the selected face of the resonator.

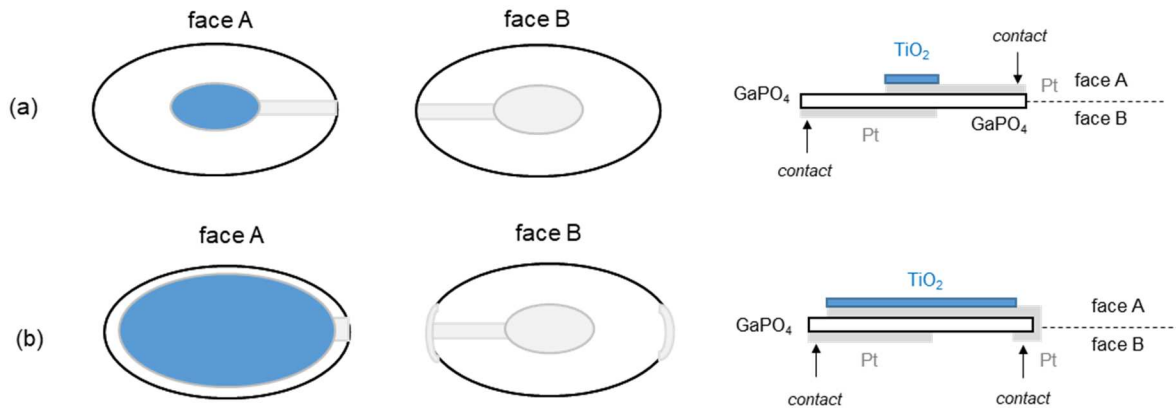


**Figure 45:** Schematic representation of the TiO<sub>2</sub>/Pt/GaPO<sub>4</sub> substrates (surface area of 0.4 cm<sup>2</sup> (a) or 1.2 cm<sup>2</sup> (b)). Electrical contact points for EQCM measurements are indicated by arrows.

FEG-SEM analysis in **Figure 46** show the expected mesoporous structure with a formation of 240 nm-thick  $\text{TiO}_2$  electrode. In comparison to FTO substrate, the surface of the substrate is hillier, due to the rough Ti interlayer.

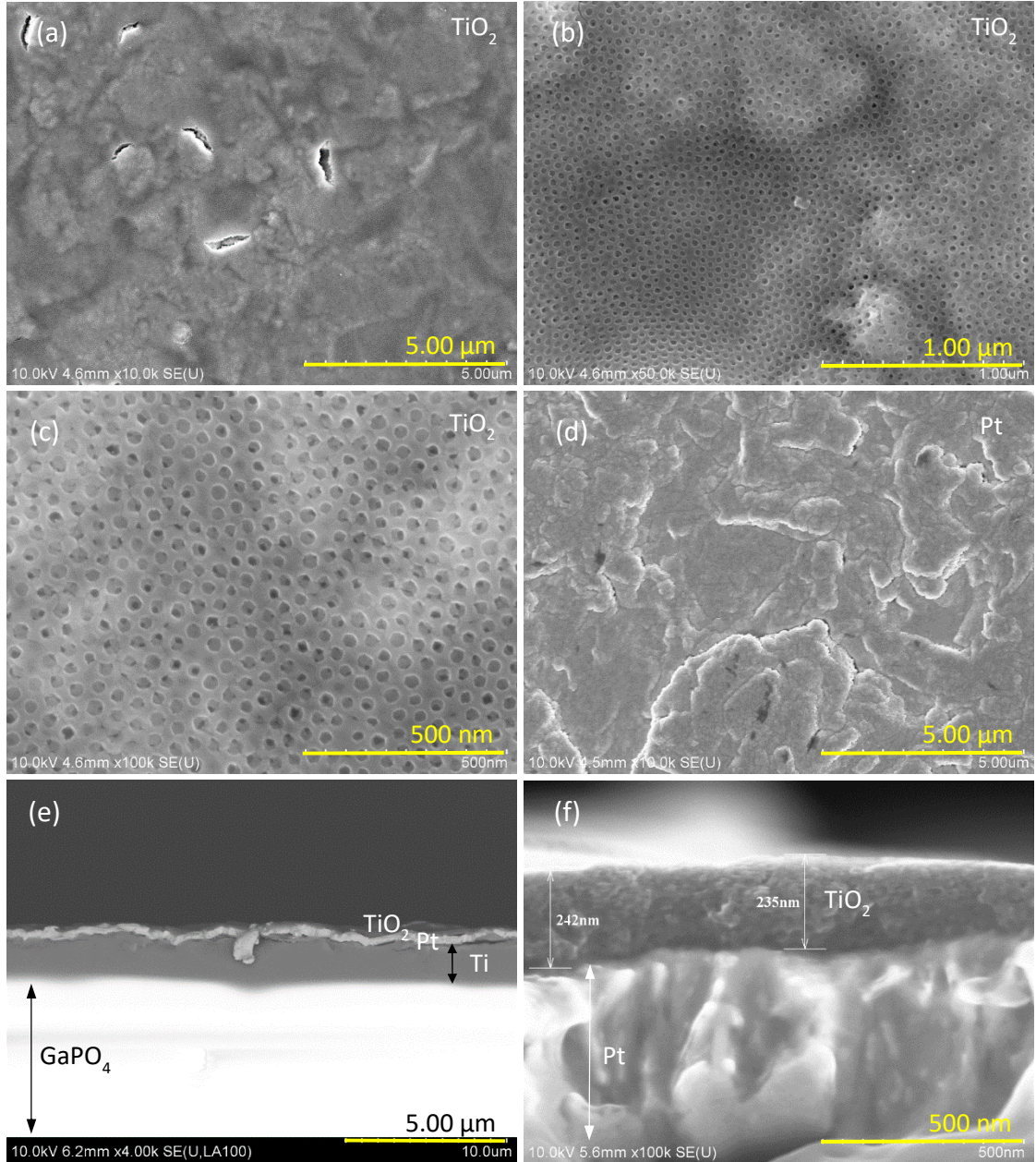


**Figure 46:** FEG SEM planar sections of  $\text{TiO}_2/\text{Pt}/\text{GaPO}_4$  at different magnifications (a)-(c) and  $\text{Pt}/\text{GaPO}_4$  before the  $\text{TiO}_2$  deposit dip (d).  $\text{TiO}_2/\text{Pt}/\text{GaPO}_4$  cross section (e)-(f).

### IV.2.3.2 – Design of the electrogravimetric cell

In comparison to EQCM cells working under ambient conditions, the *operando* EQCM measurements applied for the analysis of TiO<sub>2</sub> photo-electrode requires a specific cell design. The electrogravimetric cell has to be both water-tight and air-tight to avoid electrode and solvent degradation, *e.g.*, metallic lithium and LP30. It should also possess a transparent window to allow illumination of the substrate.

A lab-made “first generation” EQCM cell was fabricated by adapting a quartz window on a pre-existing electrogravimetric cell. The obtained cell allowed electrochemical measurements coupled with EQCM measurements to test the electrochemical and gravimetric responses of the prepared TiO<sub>2</sub> electrodes, using an optical fiber as source of illumination.

In this first-generation cell, good electrical contact between Pt electrodes of the resonator and electrogravimetric cell were assured only by using tin weld and silver lacquer by the user, which was not satisfactory considering the delicacy of the system. Besides, the set-up was not perfectly water- or air-tight because of the specific configuration of the O-rings. It therefore required optimizations for the reproducibility of the measurements. Due to these practical reasons given above, a “second generation” cell was designed to meet the experimental requirements and the first-generation cell set the base for the improvements achieved in the latter. It was fabricated by the AWS Company in Spain, and used for the first time in this Ph.D. thesis (**Figure 47**).

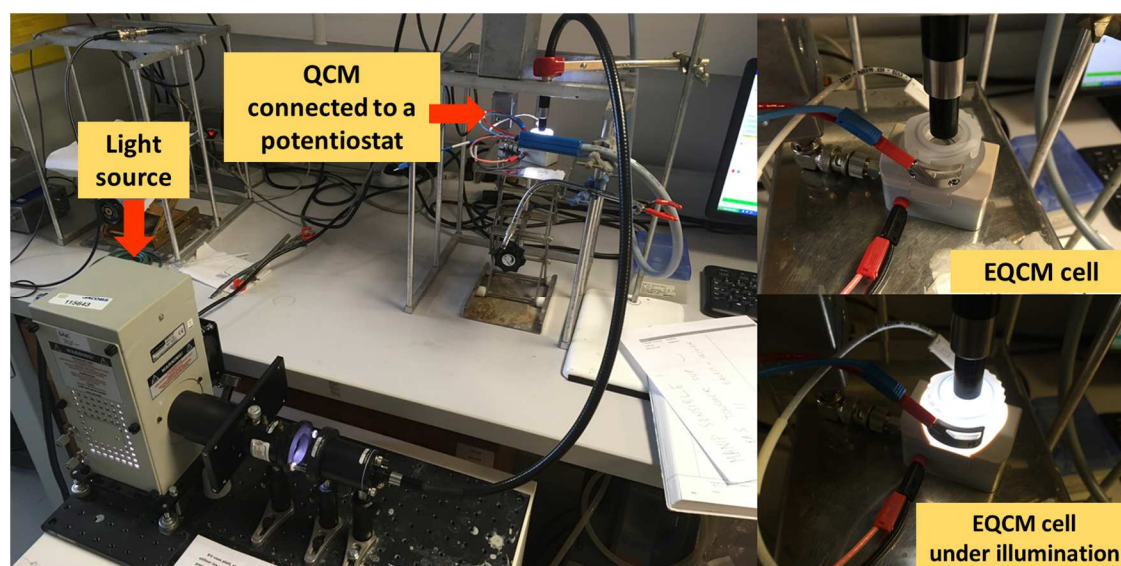


**Figure 47:** « Second generation » air- and water-tight EQCM cell allowing the measurements under illumination.

### IV.2.3.3 – EQCM and EQCM under illumination: preliminary work

#### a) Reference EQCM experiments without illumination in LP30

The EQCM coupling CV (from 2.6V to 1.4V vs.  $\text{Li}^+/\text{Li}^0$ ,  $0.5 \text{ mV.s}^{-1}$ ) with QCM measurements of the  $\text{TiO}_2/\text{Pt}$  modified  $\text{GaPO}_4$  resonators were performed using a three-electrode configuration in LP30 electrolyte. The modified resonators are used as working electrodes and two lithium foils served as reference and counter electrodes in this configuration. The sealed EQCM cell designed for this experiments was mounted in an Argon-filled glove-box and the experiments were performed under ambient conditions as shown in **Figure 47**. Prior to the experiments under illumination, reference EQCM measurements were done as follows.

**Figure 48** presents the charge and frequency profiles as a function of time during 10 CV cycles after stabilization step.

During  $\text{Li}^+$  insertion ( $dq/dt < 0$ , i.e.  $i < 0$ ), the modified resonators' frequency decreases ( $df/dt < 0$ ). Conversely, during  $\text{Li}^+$  extraction ( $dq/dt > 0$ , i.e.  $i > 0$ ), the frequency increases ( $df/dt > 0$ ).

Due to the rigid and electro-acoustically thin nature of the  $\text{TiO}_2$  layers in this study, the frequency variations were converted to the mass variations using Sauerbrey equation, i.e., the gravimetric regime is kept. The effects such as viscoelastic changes and the surface roughness of the electrodes were considered to have a negligible effect on the gravimetric responses.

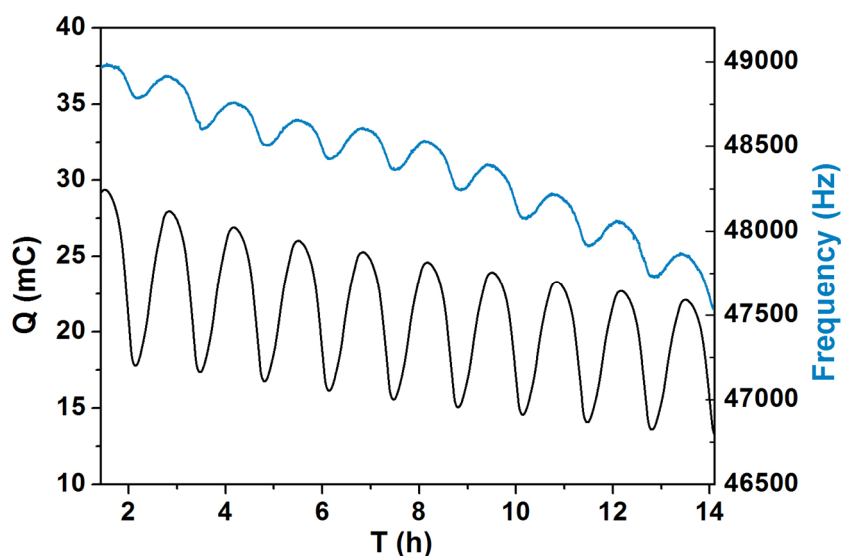


**Figure 48:** Charge (black) and frequency (blue) variations as a function of the time during 10 CV cycles (2.6V to 1.4V vs.  $\text{Li}^+/\text{Li}^0$ ,  $0.5 \text{ mV.s}^{-1}$ ) in LP30 using  $\text{TiO}_2$  (PB-PEO,  $\text{TiCl}_4$  at 2M, 1 layer)/Pt modified  $\text{GaPO}_4$  electrode as working electrode, (blue). Cycles are presented after 10 CVs of electrode stabilization.



As mass and frequency evolve in opposite directions according to Sauerbrey equation (eq. 2), we thus observe an expected mass uptake at the electrode surface during  $\text{Li}^+$  insertion and mass loss during  $\text{Li}^+$  extraction.

An average molecular weight of the inserted species (when  $dQ/dt < 0$ ) and of the extracted species when ( $dQ/dt > 0$ ) can first be roughly estimated by calculating the  $F(\Delta m/\Delta Q)$  function for an entire time period where  $i < 0$  or where  $i > 0$ .

In average, for the 10 cycles presented in **Figure 48**:

- during discharge,  $\Delta Q \simeq -9.8$  mC for a frequency variation  $\Delta f \simeq -280$  Hz.
- during charge,  $\Delta Q \simeq -9.1$  mC for a frequency variation  $\Delta f \simeq -150$  Hz.

Corresponding mass variations  $\Delta m$  can then be calculated using Sauerbrey equation for  $\text{GaPO}_4$  substrates with a theoretical sensitivity factor,  $K_s = 8.14 \times 10^7$  Hz.g<sup>-1</sup>.cm<sup>2</sup> ( $\rho = 3.570$  g.cm<sup>-3</sup>,  $f_0 = 5.8$  MHz,  $\mu = 2.147 \times 10^{11}$  g.s<sup>-2</sup>.cm<sup>-1</sup>, and  $S = 0.4$  cm<sup>2</sup>).

Thus, it is found that:

- average molecular weight of species inserted during discharge is  $\simeq 14$  g.mol<sup>-1</sup>
- average molecular weight of species extracted during charge is  $\simeq 8$  g.mol<sup>-1</sup>.

$F(\Delta m/\Delta Q)$  value obtained for the species extracted during oxidation ( $\simeq 8$  g.mol<sup>-1</sup>) is in a good agreement with the molecular weight of lithium ion, which is 7 g.mol<sup>-1</sup>. However, during reduction, a higher average molecular weight ( $\simeq 14$  g.mol<sup>-1</sup>) was obtained which indicates that lithium ions may not be the only species inserted or deposited at the electrode surface. An SEI formation during the reduction process may be the origin of the deviation of the  $F(\Delta m/\Delta Q)$  value from the exact molecular weight of  $\text{Li}^+$ . It is very likely that due to electrolyte degradation (LP30) during reduction, the formation of  $\text{LiF}$  and carbonates on the electrode surface may result in this additional mass variation (see **Figure 49** for the microscopy images of the electrodes before and after the cycling in LP30), as seen in section II.

The instantaneous analysis of EQCM data by means of the  $F(\Delta m/\Delta Q)$  function can give a more precise vision of the evolution of the average molecular weight of species involved in the charge compensation. This representation presents the advantage to give the instantaneous M.P.E. at each potential during a voltammetric scan. As the asymptotic behavior of the  $F(\Delta m/\Delta Q)$  function near the zero current zones affects the interpretation of molecular weight,<sup>77</sup> no conclusion can be drawn in this zones (**Annex Figure I.11**).

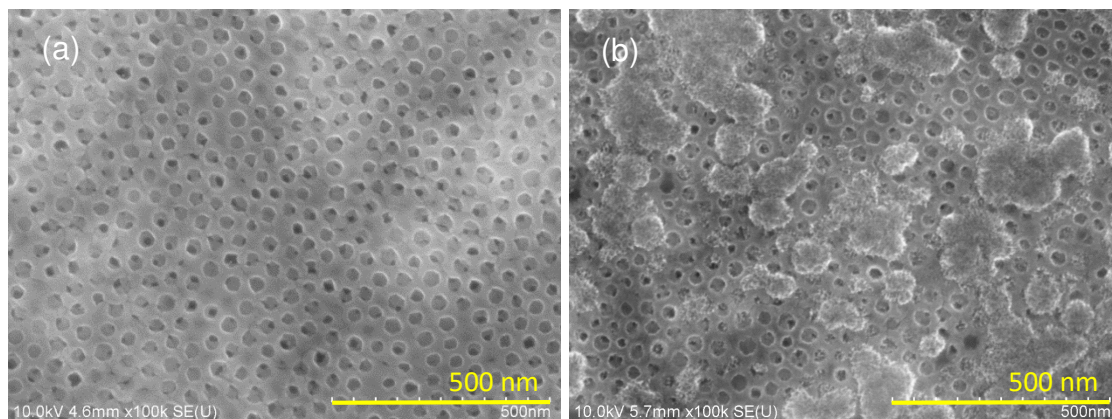


**Figure 49:** FEG SEM planar sections of  $\text{TiO}_2/\text{Pt}/\text{GaPO}_4$  before (a) and after (b) use in LP30.

**Figure 50** presents the  $F(\Delta m/\Delta Q)$  function for 2 successive CVs of a EQCM experiment in LP30 between 2.6V and 1.4V vs.  $\text{Li}^+/\text{Li}^0$  at  $0.5 \text{ mV.s}^{-1}$  (cycles n°12 and n°13 corresponding to time experiment between 3h30 to 6h in **Figure 48** and **Annex Figure I.11**). Curves **1** and **2** correspond to the first charge and first discharge, respectively. Curves **3** and **4** correspond to the second charge and second discharge, respectively. The experiments under electrochemical oxidation ( $\text{Li}^+$  extraction) are plotted in green, and the experiment under electrochemical reduction ( $\text{Li}^+$  insertion) are plotted in blue. Plots do not include uninterpretable zones near zero current.

These results confirm that species extracted during the charge has a molecular weight, which is in very good agreement with that of  $\text{Li}^+$  (green curves). Conversely, the higher average molecular weight ( $\approx 13 \text{ g.mol}^{-1}$ ) persistently observed during discharges (blue curves) shows that  $\text{Li}^+$  is not the only species inserted at the electrode surface during the reduction. This value of average molecular weight stays relatively constant during all potential range where reduction takes place, showing that  $\text{LiF}$  and carbonates are deposited continuously on the electrode upon  $\text{Li}^+$  insertion. This indicates that the degradation of the electrolyte does not seem to be triggered at a particular low potential, and seems to occur continuously for the reductive potential range (at least between 1.9 V and 1.5 V).

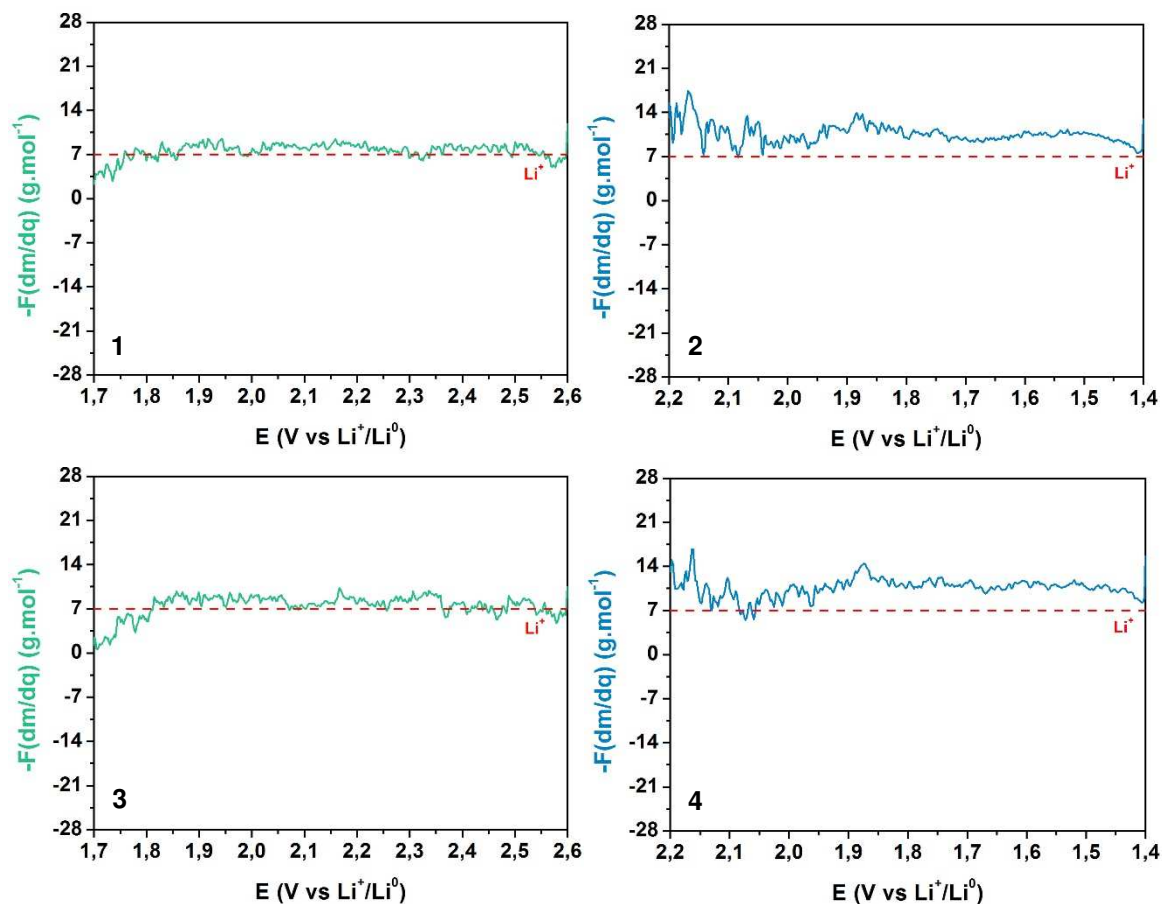


**Figure 50:**  $-F(\Delta m/\Delta Q)$  function calculated from the EQCM data corresponding to the average molecular weight of the species involved in the charge compensation as a function of the potential for a mesoporous  $\text{TiO}_2$  film (PB-PEO,  $\text{TiCl}_4$  at 2M, 1 layer) deposited on the  $\text{GaPO}_4$  resonators. The measurements were done in LP30 and showing 2 successive CVs (n°12 and n°13) at 2.6V and 1.4V vs.  $\text{Li}^+/\text{Li}^0$  ( $0.5 \text{ mV.s}^{-1}$ ). First “charge” (1)-“discharge” (2) / second “charge” (3)-“discharge” (4). Molecular weight of lithium is drawn in red.

The fact that the SEI formation has been suspected which resulted in the additional mass variation during reduction of each cycle and continuous mass increase during cycling (**Figure 48**), the initial 10 CV cycles of the EQCM necessary to obtain a stabilized electrochemical response merits deeper analysis (see **Figure 51**).

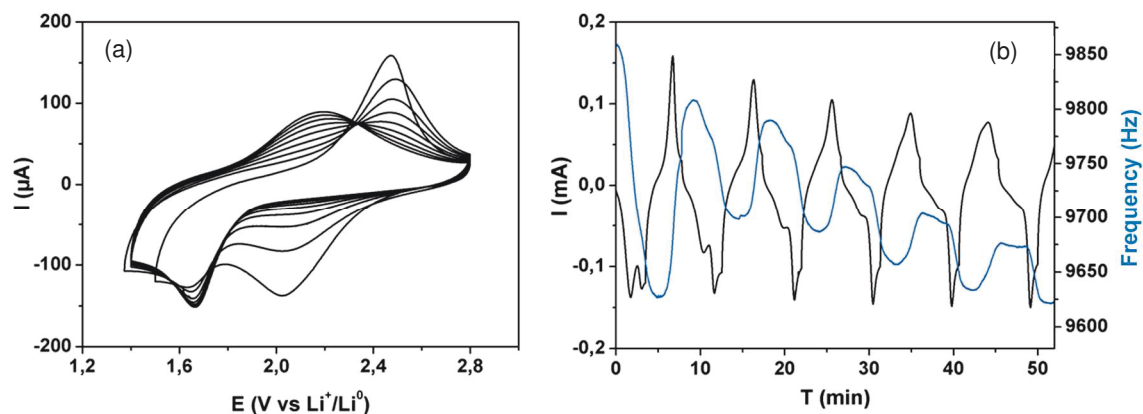


**Figure 51:** Initial CVs at  $2 \text{ mV.s}^{-1}$  for a  $\text{TiO}_2/\text{Pt}/\text{GaPO}_4$  electrode (PB-PEO,  $\text{TiCl}_4$  at 2M, 1 layer) in LP30 (a). Associated frequency changes of the resonator as a function of the time and plotted for the 5 first cycles (b).

As on FTO substrate, large reduction peak observed around 2 V can be attributed to the electrolyte decomposition and thus initial SEI formation during the first reduction cycle. It is concomitant with an important frequency diminution. If all the mass uptake observed during the first cycle between 2.8 V and 1.5 V is attributed to initial SEI formation, the calculated mass change of the electrode is found as  $m \simeq 3.4 \text{ } \mu\text{g}$  (using Sauerbrey equation with an electrode surface of  $S = 1.2 \text{ cm}^2$ ). If we correct this value by subtracting the mass of inserted  $\text{Li}^+$  during this first cycle (assuming that the same amount of  $\text{Li}^+$  is inserted during this 1<sup>st</sup> cycle and during the 10<sup>th</sup> cycle for example), the calculated mass corresponds to a SEI layer thickness of  $h \simeq 10 \text{ nm}$ .<sup>i</sup>

Then, during the first oxidation (from 5 to 10 min), the calculated average molecular weight of released species is  $-F(\Delta m/\Delta Q) \simeq 25 \text{ g.mol}^{-1}$ . This value is about 3 times higher than the one obtained during the other oxidation steps after the stabilization ( $\simeq 8 \text{ g.mol}^{-1}$ ). It could suggest that the SEI formed during the first reduction (from 0 to 5 min) is partially reversible or mechanically removed during lithium extraction. This SEI then continues to form during 4-5 CV cycles, as suggested by the presence of the reduction peak around 2 V for 4-5 cycles.

<sup>i</sup> Calculated as  $h = m/(\rho.S)$  with a value for  $\rho \simeq 2 \text{ g.cm}^{-3}$  corresponding to an average molecular mass of the possible SEI products deposited in LP30 electrolyte referred in Trahey study,<sup>85</sup> with  $S = 1.2 \text{ cm}^2$ .



These experiments without illumination has allowed to better identify the species involved during the charge and discharge of  $\text{TiO}_2$  electrode. It has also permitted to test for the first time the newly designed EQCM cell, and the strict criteria of air- and water-tightness were validated which is also a prerequisite for an *operando* study under illumination.

The preliminary experiments which also validated of the EQCM cell led us to study photo-rechargeable electrode under illumination to get more precise information about the effect of light on the species' insertion/extraction in/from the electrode. It is important to highlight the specifications of these electrogravimetric measurements in comparison to the substantial photo-electrochemical characterization performed until here. In addition to the geometrical configuration changes inherent to the EQCM cell, Pt metal has replaced FTO and illumination is here mediated by an optical fiber. In this configuration, the light power was found to be about 10 times smaller than on the optical bench (see **Annex III.8**).

#### b) EQCM experiments under illumination in LP30

In order to test the  $\text{TiO}_2/\text{Pt}/\text{GaPO}_4$  response under illumination in LP30 electrolyte, EQCM measurements were performed. During CVs (after stabilization step,  $2 \text{ mV.s}^{-1}$  between 2.8 V and 1.4 V vs.  $\text{Li}^+/\text{Li}^0$ ), simultaneous frequency changes of the resonator were monitored under light for 1 cycle and compared to experiment without illumination (see **Figure 52**).

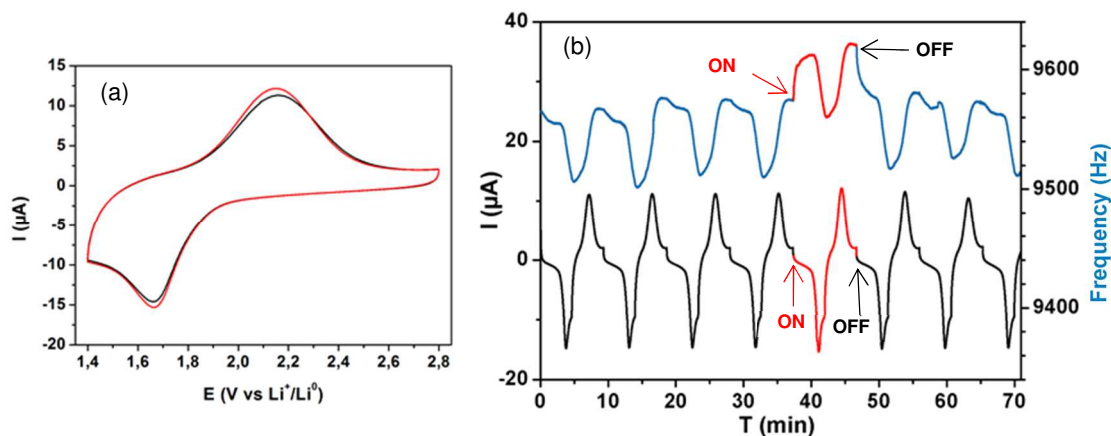


**Figure 52:** CVs at  $2 \text{ mV.s}^{-1}$  for a  $\text{TiO}_2/\text{Pt}/\text{GaPO}_4$  electrode (PB-PEO,  $\text{TiCl}_4$  at 2M, 1 layer) in LP30 in dark (black) and under light (red) (a) after stabilization step. Associated frequency changes of the resonator as a function of the time with cycle under illumination (red) (b).

Under illumination (curves in red), frequencies undergo an immediate increase ( $\Delta f \simeq +40$  Hz). When the illumination is stopped, frequencies undergo an immediate decrease ( $\Delta f \simeq -40$  Hz). This frequency change was found too fast and too important (the global frequencies variations between the charge and discharge states is only about 70 Hz) to be attributed to an effective important and quick mass change at the  $\text{TiO}_2$  electrode surface.

Then, the frequencies variation of a neat  $\text{Pt}/\text{GaPO}_4$  substrate was thus monitored during an open circuit voltage (OCV) experiment under illumination (**Figure 53**). The frequency increase/decrease ( $\simeq 150$  Hz) were also observed immediately when the light is switched ON/OFF. This transitory response observed during the experiment could thus be attributed the response of  $\text{Pt}/\text{GaPO}_4$  substrate under illumination.

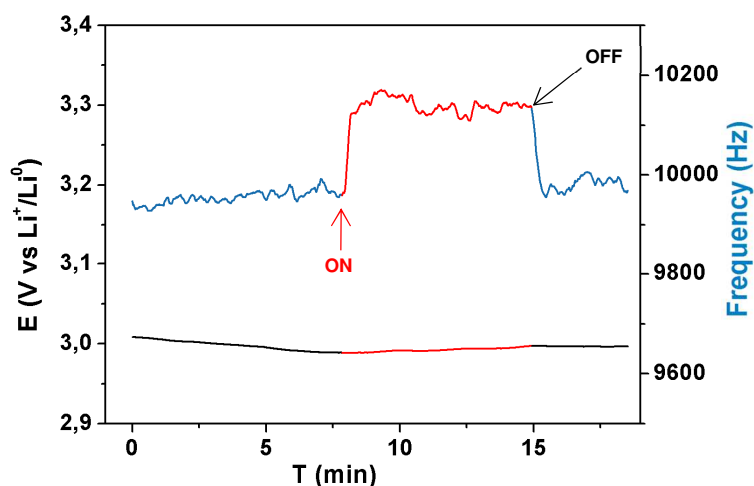


**Figure 53:** Frequencies variations of  $\text{GaPO}_4$  substrate at OCV under illumination.

Gravimetric response of  $\text{TiO}_2/\text{Pt}/\text{GaPO}_4$  electrode was then tested when coupled to a galvanostatic discharge/discharge measurement (**Figure 54**). With these kinds of experiments, the possible changes of the frequency variation were followed and plotted as a function of time during illumination of the electrode.

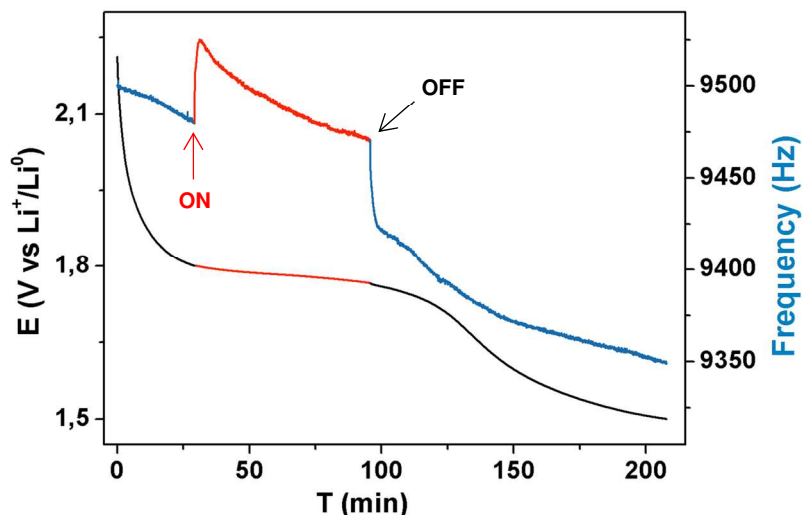


**Figure 54:** Galvanostatic discharge at  $-3 \mu\text{A}$  for a  $\text{TiO}_2/\text{Pt}/\text{GaPO}_4$  electrode (PB-PEO,  $\text{TiCl}_4$  at 2M, 1 layer) in LP30. Associated frequency changes of the resonator as a function of the time. Curves are plotted in red during the illumination.

During galvanostatic experiments at  $-3 \mu\text{A}$ , the electrode underwent mass uptake (frequency diminution) due to the electrode lithiation.

$\text{TiO}_2/\text{Pt}/\text{GaPO}_4$  electrode was illuminated during the potential plateau region (curves in red). The fast transitory response ( $\Delta f \simeq +50 \text{ Hz}$ ) was also observed in this measurements with similar magnitude of  $\Delta f$  changes as in **Figure 52**. A closer look at the frequency response region plotted in red (**Figure 54**) indicates that the absolute value of the slope of the frequency plotted as a function of time gradually increased. This slope change may suggest that the mass uptake progressively decreases under illumination when the film gets progressively lithiated.

Further experiments are required to confirm that this change is significant and not due, for example, to the end of the transitory response of the  $\text{GaPO}_4$  under illumination. If so, this slope change could be attributed to the simultaneous  $\text{Li}^+$  photo-extraction phenomenon, which is effectively expected to become more significant when the film gets progressively lithiated.

It is also important to mention that, for a complete analysis, additional effects that may contribute to the gravimetric response should be pondered, *i.e.*, mass loss due to photo-extraction can be counterbalanced by the possible mass uptake due to the expected increased formation of  $\text{LiF}$  (decomposition product of the LP30) under illumination.

When the light was switched off, after the transitory response of the  $\text{GaPO}_4$  substrate ( $\Delta f \simeq -50 \text{ Hz}$ ), absolute value of the slope immediately increased: in absence of  $\text{Li}^+$  photo-extraction to compensate the imposed  $\text{Li}^+$  galvanostatic-insertion, more  $\text{Li}^+$

should be effectively inserted into the electrode and mass uptake become bigger at the end of the plateau without the illumination.

### c) EQCM experiments: first tests in ionic liquid

Preliminary experiments have been realized by changing the electrolyte from LP30 to  $\text{PYR}_{13}\text{TFSI}$  ( $\text{LiTFSI}$  at 0.2M). EQCM is less frequently conducted in ionic liquid electrolyte mainly due to their high viscosity which may interface with the gravimetric measurements. Nonetheless, certain ILs have already been employed to study the ionic dynamics in nanoporous carbons,<sup>75</sup> electrodeposition,<sup>86</sup> or electropolymerization.<sup>87</sup>

The choice of ionic liquid type electrolyte in EQCM measurements of our study is considered to be highly relevant as it may constitute a system free from the SEI formation, and allow to focus the analysis on the  $\text{Li}^+$  insertion/extraction mechanisms under illumination.

The EQCM data in the absence of illumination are presented in **Figure 55** as a reference. First of all, the large reduction peak observed around 2 V which was attributed to the electrolyte decomposition and thus initial SEI formation during the first reduction cycle in LP30 (**Figure 51**) is absent when cycled in  $\text{PYR}_{13}\text{TFSI}$  ( $\text{LiTFSI}$  at 0.2M). The corresponding charge and frequency profile as a function of time is shown in **Figure 55-b**). First rough estimation of the  $-F(\Delta m/\Delta Q)$  function for two cycles of the CVs ( $2 \text{ mV.s}^{-1}$ ) gives an average molecular weight of about  $5 \text{ g.mol}^{-1}$ , in reduction as well as in oxidation, which is slightly inferior but not far from the expected value for  $\text{Li}^+$  in a first approximation.

Although there is no significant irreversible mass was detected during cycling, one can notice that frequency response is delayed from the current response. This delay can be attributed to the slower kinetics of ions movement in comparison to the kinetics of the faradic processes, maybe due to relatively high viscosity of the ionic liquid.<sup>14</sup>

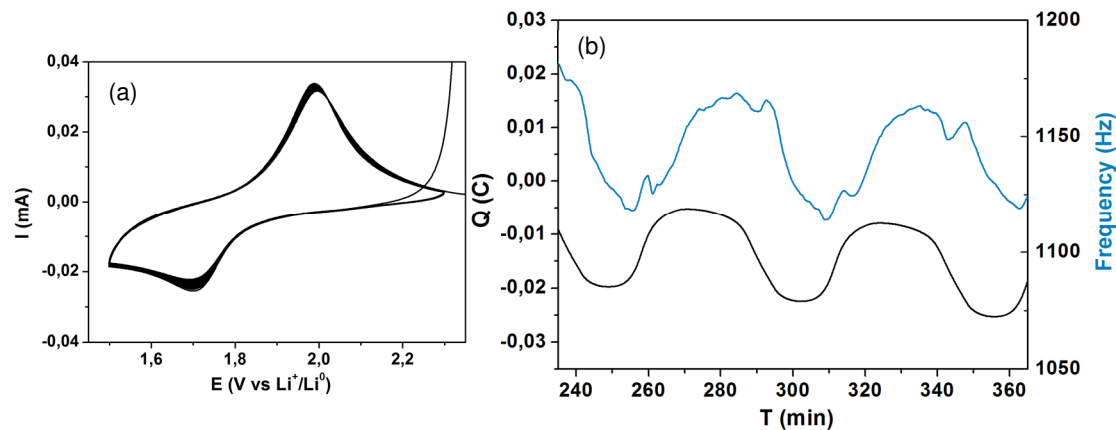


**Figure 55:** Initial 10 CVs at  $2 \text{ mV.s}^{-1}$  for a  $\text{TiO}_2/\text{Pt}/\text{GaPO}_4$  electrode (PB-PEO,  $\text{TiCl}_4$  at 2M, 1 layer) in  $\text{PYR}_{13}\text{TFSI}$  ( $\text{LiTFSI}$  0.2M) (a). Associated frequency changes of the resonator as a function of the time and plotted for 2 cycles ( $n^\circ 6$  and  $n^\circ 7$ ) (b).

First tests under illumination during galvanostatic discharge/charge at  $5 \mu\text{A}$  showed similar transitory response of the  $\text{GaPO}_4$  substrate under illumination but with a larger magnitude ( $\Delta f \approx 200 \text{ Hz}$ ) (**Figure 56**). During these experiments, only a short period of illumination was tested ( $\approx 5 \text{ min}$ ) to first confirm that the transitory response of the  $\text{GaPO}_4$  substrate is not specific to the LP30 electrolyte.

Further experiments are necessary for longer periods of illumination to clarify the behavior of the substrate under illumination in comparison to that of in LP30. Nonetheless, these preliminary results obtained in two different electrolytes strengthens the idea that *operando* EQCM is a suitable complementary tool for the investigation of photo-induced ion insertion/extraction mechanisms of photo-electrodes.

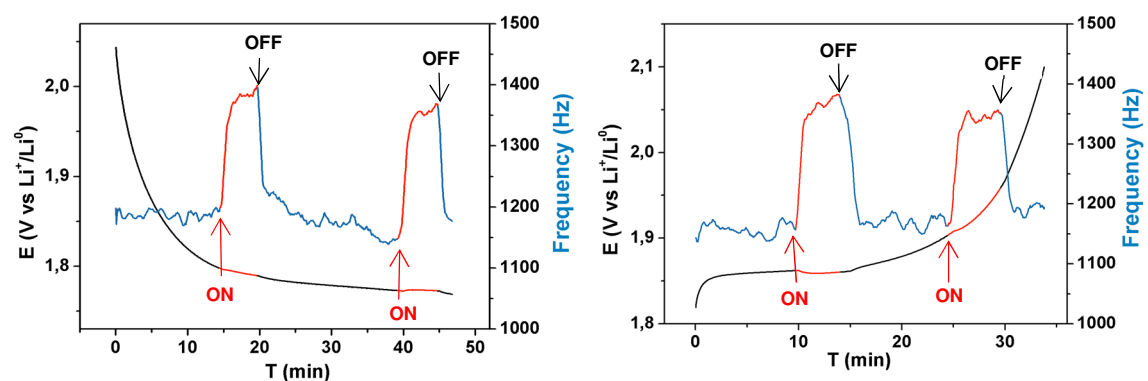


**Figure 56:** Frequency changes for the  $\text{TiO}_2/\text{Pt}/\text{GaPO}_4$  substrate (PB-PEO,  $\text{TiCl}_4$  at 2M, 1 layer) in  $\text{PYR}_{13}\text{TFSI}$  ( $\text{LiTFSI}$  0.2M). Curves are plotted in red during the illumination.

## V – Conclusion

In this chapter, photo-induced mechanisms were studied by means of different approaches.

First, we have played with the electrode architecture (mesoporous structure and thickness) in order to see how much it could impact the photo-induced mechanisms. Thinner films were found to present the more interesting mass capacities, whereas thicker one (above 500 nm) allowed to obtain higher photo-current intensities. No drastic differences were observed in the range of mesoporous architectures used in this work.

We have then compared the photo-electrochemical behavior of the electrode in LP30 and in  $\text{PYR}_{13}\text{TFSI}$  (0.2M  $\text{LiTFSI}$ ), with complementary tests in “water-in-salt” electrolyte. With the support of *post mortem* analysis, we have tried to picture the possible fate of generated-excitons at the electrode/electrolyte interface. Here are our main conclusions:

- In the case of LP30, under dark conditions, usual electrolyte degradation products were found on the electrode surface ( $\text{LiF}$ ) and in the electrolyte ( $\text{OPF}_2\text{O}^\cdot$ ,  $\text{OPFO}^{2-}$  and  $\text{HF}$ ). Possible accelerated formation of  $\text{LiF}$  under illumination and cycling conditions (10 CVs between 2.6 V to 1.4 V vs.  $\text{Li}^+/\text{Li}^0$ ,  $0.5 \text{ mV.s}^{-1}$ ) (1) could be due to an eventual temperature increase of the non-water-cooled cell under continuous illumination, and/or (2) could witness the participation of photo-electrons to the  $\text{LiPF}_6$  salt reduction.
- In the case of ( $\text{PYR}_{13}\text{TFSI}$ , 0.2M  $\text{LiTFSI}$ ), comparison of the electrochemical studies performed under light and dark conditions showed a behavior qualitatively comparable to the one in LP30 electrolyte. In simultaneous presence of  $\text{Ti(III)}$  sites and water in the electrolyte (both susceptible to be photo-oxidized), study of  $\text{TiO}_2$  electrode in a “water-in-salt” electrolyte suggested that photo-generation should lead to preferential cations photo-extraction through  $\text{Ti(III)}$  photo-oxidation. Photo-electrons could for their part eventually be scavenged by water molecules (whose presence in ionic liquid was confirm by NMR study). This phenomenon could eventually limit the photo-charges recombination and promoting the holes reaction with  $\text{Ti(III)}$ , thereby participating to the higher photo-currents observed in ionic liquid in comparison to LP30.

In the last section, photo-induced mechanisms were then further investigated by means of *operando* measurements.

From the EIS study in dark conditions, we observed that the charge transfer resistance of the electrode is globally invariant with the lithium content (for  $0 < x < 0.5$  in  $\text{Li}_x\text{TiO}_2$ ). The comparison between dark and light experiments for  $\text{TiO}_2$  (PB-PEO, 2M in  $\text{TiCl}_4$ , 2 layers) suggests that light does not significantly influence the diffusion of  $\text{Li}^+$ .

We then performed a preliminary work dedicated to the analysis of the gravimetric response of a  $\text{TiO}_2$ -coated piezoelectric substrate ( $\text{GaPO}_4$ ) when coupled to electrochemical and photo-electrochemical measurements. A new specially designed experimental setup was therefore proposed to study the nature of species involved at the electrode/electrolyte interface upon photo-electrochemical cycling.

In LP30 electrolyte, results under dark conditions confirmed that species extracted during the charge has a molecular weight very closed from the one of  $\text{Li}^+$ . Conversely, the higher average molecular weight ( $\simeq 13 \text{ g.mol}^{-1}$ ) observed during discharges shows that  $\text{Li}^+$  is not the only species inserted/deposited at the electrode surface during the reduction. The cell design was then tested and found adapted for *operando* measurements under illumination. First results showed in particular that transitory response arising from the  $\text{GaPO}_4$  substrate under illumination should be de-correlated from the one of  $\text{TiO}_2$  for a proper analysis of the photo-induced mechanisms using these substrates.

## Bibliography

1. Nguyen, O. *et al.* Shedding light on the light-driven lithium ion de-insertion reaction: towards the design of a photo-rechargeable battery. *J. Mater. Chem. A* **5**, 5927–5933 (2017).
2. Ardo, S. & Meyer, G. J. Photodriven heterogeneous charge transfer with transition-metal compounds anchored to TiO<sub>2</sub> semiconductor surfaces. *Chem Soc Rev* **38**, 115–164 (2009).
3. Salvador, P. Hole diffusion length in *n*-TiO<sub>2</sub> single crystals and sintered electrodes: Photoelectrochemical determination and comparative analysis. *J. Appl. Phys.* **55**, 2977–2985 (1984).
4. Aurbach, D. *et al.* Design of electrolyte solutions for Li and Li-ion batteries: a review. *Electrochimica Acta* **50**, 247–254 (2004).
5. Xu, K. Electrolytes and Interphases in Li-Ion Batteries and Beyond. *Chem. Rev.* **114**, 11503–11618 (2014).
6. Plakhotnyk, A. V., Ernst, L. & Schmutzler, R. Hydrolysis in the system LiPF<sub>6</sub>—propylene carbonate—dimethyl carbonate—H<sub>2</sub>O. *J. Fluor. Chem.* **126**, 27–31 (2005).
7. Sloop, S. E., Pugh, J. K., Wang, S., Kerr, J. B. & Kinoshita, K. Chemical Reactivity of PF<sub>5</sub> and LiPF<sub>6</sub> in Ethylene Carbonate/Dimethyl Carbonate Solutions. *Electrochem. Solid-State Lett.* **4**, A42 (2001).
8. Aurbach, D. *et al.* The Study of Surface Phenomena Related to Electrochemical Lithium Intercalation into Li<sub>x</sub>MO<sub>y</sub> Host Materials (M = Ni, Mn). *J. Electrochem. Soc.* **147**, 1322–1331 (2000).
9. Armand, M., Endres, F., MacFarlane, D. R., Ohno, H. & Scrosati, B. Ionic-liquid materials for the electrochemical challenges of the future. *Nat. Mater.* **8**, 621–629 (2009).
10. Tarascon, J.-M. & Armand, M. Issues and challenges facing rechargeable lithium batteries. in *Materials for Sustainable Energy* 171–179 (2010).
11. Kim, G. T. *et al.* Use of natural binders and ionic liquid electrolytes for greener and safer lithium-ion batteries. *J. Power Sources* **196**, 2187–2194 (2011).
12. Appetecchi, G. B., Montanino, M. & Passerini, S. Ionic Liquid-Based Electrolytes for High Energy, Safer Lithium Batteries. in *Ionic Liquids: Science and Applications* **1117**, 67–128 (American Chemical Society, 2012).
13. Mun, J. *et al.* Electrochemical stability of bis(trifluoromethanesulfonyl)imide-based ionic liquids at elevated temperature as a solvent for a titanium oxide bronze electrode. *J. Power Sources* **194**, 1068–1074 (2009).
14. Lewandowski, A. & Świdorska-Mocek, A. Ionic liquids as electrolytes for Li-ion batteries—An overview of electrochemical studies. *J. Power Sources* **194**, 601–609 (2009).
15. Kazemiabnavi, S., Zhang, Z., Thornton, K. & Banerjee, S. Electrochemical Stability Window of Imidazolium-Based Ionic Liquids as Electrolytes for Lithium Batteries. *J. Phys. Chem. B* **120**, 5691–5702 (2016).



16. Appetecchi, G. B., Montanino, M. & Passerini, S. Ionic liquid-based electrolytes for high-energy lithium batteries. *Ion. Liq. Sci. Appl.* (2013).
17. Abe, R. Recent progress on photocatalytic and photoelectrochemical water splitting under visible light irradiation. *J. Photochem. Photobiol. C Photochem. Rev.* **11**, 179–209 (2010).
18. Zhang, Z., Zhang, L., Hedhili, M. N., Zhang, H. & Wang, P. Plasmonic Gold Nanocrystals Coupled with Photonic Crystal Seamlessly on TiO<sub>2</sub> Nanotube Photoelectrodes for Efficient Visible Light Photoelectrochemical Water Splitting. *Nano Lett.* **13**, 14–20 (2013).
19. Pu, Y.-C. *et al.* Au Nanostructure-Decorated TiO<sub>2</sub> Nanowires Exhibiting Photoactivity Across Entire UV-visible Region for Photoelectrochemical Water Splitting. *Nano Lett.* **13**, 3817–3823 (2013).
20. Hejazi, S., Nguyen, N. T., Mazare, A. & Schmuki, P. Aminated TiO<sub>2</sub> nanotubes as a photoelectrochemical water splitting photoanode. *Catal. Today* **281**, 189–197 (2017).
21. Mazare, A., Paramasivam, I., Lee, K. & Schmuki, P. Improved water-splitting behaviour of flame annealed TiO<sub>2</sub> nanotubes. *Electrochem. Commun.* **13**, 1030–1034 (2011).
22. Cao, Y., Chen, Y., Sun, X., Zhang, Z. & Mu, T. Water sorption in ionic liquids: kinetics, mechanisms and hydrophilicity. *Phys. Chem. Chem. Phys.* **14**, 12252 (2012).
23. Cuadrado-Prado, S. *et al.* Experimental measurement of the hygroscopic grade on eight imidazolium based ionic liquids. *Fluid Phase Equilibria* **278**, 36–40 (2009).
24. Francesco, F. D. *et al.* Water sorption by anhydrous ionic liquids. *Green Chem.* **13**, 1712 (2011).
25. Reid, J. E. S. J., Walker, A. J. & Shimizu, S. Residual water in ionic liquids: clustered or dissociated? *Phys. Chem. Chem. Phys.* **17**, 14710–14718 (2015).
26. Suo, L. *et al.* ‘Water-in-salt’ electrolyte enables high-voltage aqueous lithium-ion chemistries. *Science* **350**, 938–943 (2015).
27. Smith, L. & Dunn, B. Opening the window for aqueous electrolytes. *Science* **350**, 918–918 (2015).
28. Suo, L. *et al.* ‘Water-in-Salt’ electrolytes enable green and safe Li-ion batteries for large scale electric energy storage applications. *J. Mater. Chem. A* **4**, 6639–6644 (2016).
29. Berger, T., Monllor-Satoca, D., Jankulovska, M., Lana-Villarreal, T. & Gómez, R. The Electrochemistry of Nanostructured Titanium Dioxide Electrodes. *ChemPhysChem* **13**, 2824–2875 (2012).
30. Kim, Y.-S. *et al.* Evidencing Fast, Massive, and Reversible H<sup>+</sup> Insertion in Nanostructured TiO<sub>2</sub> Electrodes at Neutral pH. Where Do Protons Come From? *J. Phys. Chem. C* **121**, 10325–10335 (2017).
31. Berger, T., Anta, J. A. & Morales-Flórez, V. Spectroscopic properties of electrochemically populated electronic states in nanostructured TiO<sub>2</sub> films: anatase versus rutile. *Phys. Chem. Chem. Phys.* **15**, 13790–13795 (2013).

32. Berger, T., Anta, J. A. & Morales-Flórez, V. Electrons in the Band Gap: Spectroscopic Characterization of Anatase TiO<sub>2</sub> Nanocrystal Electrodes under Fermi Level Control. *J. Phys. Chem. C* **116**, 11444–11455 (2012).
33. Fabregat-Santiago, F. *et al.* High Carrier Density and Capacitance in TiO<sub>2</sub> Nanotube Arrays Induced by Electrochemical Doping. *J. Am. Chem. Soc.* **130**, 11312–11316 (2008).
34. Chen, B., Hou, J. & Lu, K. Formation Mechanism of TiO<sub>2</sub> Nanotubes and Their Applications in Photoelectrochemical Water Splitting and Supercapacitors. *Langmuir* **29**, 5911–5919 (2013).
35. Meekins, B. H. & Kamat, P. V. Got TiO<sub>2</sub> nanotubes? Lithium ion intercalation can boost their photoelectrochemical performance. *ACS Nano* **3**, 3437–3446 (2009).
36. Bryngelsson, H., Stjerndahl, M., Gustafsson, T. & Edström, K. How dynamic is the SEI? *J. Power Sources* **174**, 970–975 (2007).
37. Zampardi, G., La Mantia, F. & Schuhmann, W. Determination of the formation and range of stability of the SEI on glassy carbon by local electrochemistry. *RSC Adv.* **5**, 31166–31171 (2015).
38. Ventosa, E. *et al.* Solid Electrolyte Interphase (SEI) at TiO<sub>2</sub> Electrodes in Li-Ion Batteries: Defining *Apparent* and *Effective* SEI Based on Evidence from X-ray Photoemission Spectroscopy and Scanning Electrochemical Microscopy. *ACS Appl. Mater. Interfaces* **9**, 3123–3130 (2017).
39. Han, C. *et al.* Hollow titanium dioxide spheres as anode material for lithium ion battery with largely improved rate stability and cycle performance by suppressing the formation of solid electrolyte interface layer. *J. Mater. Chem. A* **3**, 13340–13349 (2015).
40. Parimalam, B. S. & Lucht, B. L. Reduction Reactions of Electrolyte Salts for Lithium Ion Batteries: LiPF<sub>6</sub>, LiBF<sub>4</sub>, LiDFOB, LiBOB, and LiTFSI. *J. Electrochem. Soc.* **165**, A251–A255 (2018).
41. Campion, C. L., Li, W. & Lucht, B. L. Thermal Decomposition of LiPF<sub>6</sub>-Based Electrolytes for Lithium-Ion Batteries. *J. Electrochem. Soc.* **152**, A2327 (2005).
42. Lux, S. F. *et al.* The mechanism of HF formation in LiPF<sub>6</sub> based organic carbonate electrolytes. *Electrochem. Commun.* **14**, 47–50 (2012).
43. Xu, J., Ao, Y., Fu, D. & Yuan, C. Low-temperature preparation of F-doped TiO<sub>2</sub> film and its photocatalytic activity under solar light. *Appl. Surf. Sci.* **254**, 3033–3038 (2008).
44. Ensling, D., Stjerndahl, M., Nyten, A., Gustafsson, T. & Thomas, J. O. A comparative XPS surface study of Li<sub>2</sub>FeSiO<sub>4</sub>/C cycled with LiTFSI- and LiPF<sub>6</sub>-based electrolytes. *J. Mater. Chem.* **19**, 82–88 (2008).
45. Yamada, Y. *et al.* Hydrate-melt electrolytes for high-energy-density aqueous batteries. *Nat. Energy* **1**, 16129 (2016).
46. Verma, P., Maire, P. & Novák, P. A review of the features and analyses of the solid electrolyte interphase in Li-ion batteries. *Electrochimica Acta* **55**, 6332–6341 (2010).

47. Steiner, D., Auer, A., Portenkirchner, E. & Kunze-Liebhäuser, J. The role of surface films during lithiation of amorphous and anatase TiO<sub>2</sub> nanotubes. *J. Electroanal. Chem.* **812**, 166–173 (2018).
48. Atashbar, M. Z., Sun, H. T., Gong, B., Wlodarski, W. & Lamb, R. XPS study of Nb-doped oxygen sensing TiO<sub>2</sub> thin films prepared by sol-gel method. *Thin Solid Films* **326**, 238–244 (1998).
49. Sham, T. K. & Lazarus, M. S. X-ray photoelectron spectroscopy (XPS) studies of clean and hydrated TiO<sub>2</sub> (rutile) surfaces. *Chem. Phys. Lett.* **68**, 426–432 (1979).
50. Södergren, S. *et al.* Lithium intercalation in nanoporous anatase TiO<sub>2</sub> studied with XPS. *J. Phys. Chem. B* **101**, 3087–3090 (1997).
51. Wiemers-Meyer, S., Winter, M. & Nowak, S. Mechanistic insights into lithium ion battery electrolyte degradation – a quantitative NMR study. *Phys. Chem. Chem. Phys.* **18**, 26595–26601 (2016).
52. Nicotera, I., Oliviero, C., Henderson, W. A., Appetecchi, G. B. & Passerini, S. NMR Investigation of Ionic Liquid–LiX Mixtures: Pyrrolidinium Cations and TFSI<sup>-</sup> Anions. *J. Phys. Chem. B* **109**, 22814–22819 (2005).
53. Fulmer, G. R. *et al.* NMR Chemical Shifts of Trace Impurities: Common Laboratory Solvents, Organics, and Gases in Deuterated Solvents Relevant to the Organometallic Chemist. *Organometallics* **29**, 2176–2179 (2010).
54. Orazem, M. E. & Tribollet, B. *Electrochemical Impedance Spectroscopy*. (John Wiley & Sons, 2017).
55. Bach, S., Pereira-Ramos, J. P. & Willman, P. Investigation of lithium diffusion in nano-sized rutile TiO<sub>2</sub> by impedance spectroscopy. *Electrochimica Acta* **55**, 4952–4959 (2010).
56. Bach, S., Pereira-Ramos, J. P. & Willmann, P. A kinetic study of electrochemical lithium insertion in nanosized rutile  $\beta$ -MnO<sub>2</sub> by impedance spectroscopy. *Electrochimica Acta* **56**, 10016–10022 (2011).
57. Ho, C., Raistrick, D. & Huggins, A. Application of A-C Techniques to the Study of Lithium Diffusion in Tungsten Trioxide Thin Films. *J. Electrochem. Soc.* **127**, 343 (1980).
58. Hirschorn, B. *et al.* Constant-Phase-Element Behavior Caused by Resistivity Distributions in Films. *J. Electrochem. Soc.* **157**, C452 (2010).
59. Córdoba-Torres, P. *et al.* On the intrinsic coupling between constant-phase element parameters  $\alpha$  and Q in electrochemical impedance spectroscopy. *Electrochimica Acta* **72**, 172–178 (2012).
60. Tröltzsch, U., Kanoun, O. & Tränkler, H.-R. Characterizing aging effects of lithium ion batteries by impedance spectroscopy. *Electrochimica Acta* **51**, 1664–1672 (2006).
61. Roberts, A. J. & Slade, R. C. T. Effect of specific surface area on capacitance in asymmetric carbon/ $\alpha$ -MnO<sub>2</sub> supercapacitors. *Electrochimica Acta* **55**, 7460–7469 (2010).
62. Yoon, S.-B., Jegal, J.-P., Roh, K. C. & Kim, K.-B. Electrochemical Impedance Spectroscopic Investigation of Sodium Ion Diffusion in MnO<sub>2</sub> Using a Constant

- Phase Element Active in Desired Frequency Ranges. *J. Electrochem. Soc.* **161**, H207–H213 (2014).
63. Pfanzelt, M., Kubiak, P., Fleischhammer, M. & Wohlfahrt-Mehrens, M. TiO<sub>2</sub> rutile. An alternative anode material for safe lithium-ion batteries. *J. Power Sources* **196**, 6815–6821 (2011).
  64. Escobar Teran, F. D. A new approach towards understanding the ion transfer dynamics in nanostructured carbon-based thin films for energy storage applications. (Université Pierre et Marie Curie).
  65. Buttry, D. A. & Ward, M. D. Measurement of interfacial processes at electrode surfaces with the electrochemical quartz crystal microbalance. *Chem. Rev.* **92**, 1355–1379 (1992).
  66. Perrot, H. Piezoelectric Transduction (QCM). in *Chemical Sensors and Biosensors* 71–91 (Wiley-Blackwell, 2013).
  67. Rodriguez-Pardo, L., Rodriguez, J. F., Gabrielli, C., Perrot, H. & Brendel, R. Sensitivity, noise, and resolution in QCM sensors in liquid media. *IEEE Sens. J.* **5**, 1251–1257 (2005).
  68. Sauerbrey, G. Verwendung von Schwingquarzen zur Wägung dünner Schichten und zur Mikrowägung. *Z. Für Phys.* **155**, 206–222 (1959).
  69. Jakab, S. *et al.* Study of the Dissolution of Thin Films of Cerium Oxide by Using a GaPO<sub>4</sub> Crystal Microbalance. *Anal. Chem.* **81**, 5139–5145 (2009).
  70. Hepel, M., Kanige, K. & Bruckenstein, S. In situ underpotential deposition study of lead on silver using the electrochemical quartz crystal microbalance: Direct evidence for lead(II) adsorption before spontaneous charge transfer. *J. Electroanal. Chem. Interfacial Electrochem.* **266**, 409–421 (1989).
  71. Hepel, M. & Bruckenstein, S. Tracking anion expulsion during underpotential deposition of lead at silver using the quartz microbalance. *Electrochimica Acta* **34**, 1499–1504 (1989).
  72. Bruckenstein, S. & Swathirajan, S. Potential dependence of lead and silver underpotential coverages in acetonitrile using a piezoelectric crystal oscillator method. *Electrochimica Acta* **30**, 851–855 (1985).
  73. Ostrom, G. S. & Buttry, D. A. Quartz crystal microbalance studies of deposition and dissolution mechanisms of electrochromic films of diheptylviologen bromide. *J. Electroanal. Chem. Interfacial Electrochem.* **256**, 411–431 (1988).
  74. Arias, C. R. *et al.* New Insights into Pseudocapacitive Charge-Storage Mechanisms in Li-Birnessite Type MnO<sub>2</sub> Monitored by Fast Quartz Crystal Microbalance Methods. *J. Phys. Chem. C* **118**, 26551–26559 (2014).
  75. Tsai, W.-Y., Taberna, P.-L. & Simon, P. Electrochemical Quartz Crystal Microbalance (EQCM) Study of Ion Dynamics in Nanoporous Carbons. *J. Am. Chem. Soc.* **136**, 8722–8728 (2014).
  76. Sigalov, S., Levi, M. D., Salitra, G., Aurbach, D. & Maier, J. EQCM as a unique tool for determination of ionic fluxes in microporous carbons as a function of surface charge distribution. *Electrochem. Commun.* **12**, 1718–1721 (2010).
  77. Agrisuelas, J. *et al.* Usefulness of F(dm/dQ) Function for Elucidating the Ions Role in PB Films. *J. Electrochem. Soc.* **154**, F134 (2007).

78. Benito, D. *et al.* Study by EQCM on the voltammetric electrogeneration of poly(neutral red). The effect of the pH and the nature of cations and anions on the electrochemistry of the films. *Electrochimica Acta* **48**, 4039–4048 (2003).
79. Giménez-Romero, D., García-Jareño, J. & Vicente, F. Materiales y Procesos Electrónicos (I), Chap. 3, Burjassot (2002).
80. Giménez-Romero, D. *et al.* Mechanism for Interplay between Electron and Ionic Fluxes in  $K_hFe_k[Fe(CN)_6]_l \cdot mH_2O$  Compounds. *J. Phys. Chem. B* **110**, 2715–2722 (2006).
81. Levi, M. D., Salitra, G., Levy, N., Aurbach, D. & Maier, J. Application of a quartz-crystal microbalance to measure ionic fluxes in microporous carbons for energy storage. *Nat. Mater.* **8**, 872–875 (2009).
82. Kwon, K., Kong, F., McLarnon, F. & Evans, J. W. Characterization of the SEI on a Carbon Film Electrode by Combined EQCM and Spectroscopic Ellipsometry. *J. Electrochem. Soc.* **150**, A229–A233 (2003).
83. Li, J.-T., Chen, S.-R., Fan, X.-Y., Huang, L. & Sun, S.-G. Studies of the Interfacial Properties of an Electroplated Sn Thin Film Electrode/Electrolyte Using in Situ MFTIRS and EQCM. *Langmuir* **23**, 13174–13180 (2007).
84. Pralong, V. Electrochemical study of nanometer  $Co_3O_4$ , Co,  $CoSb_3$  and Sb thin films toward lithium. *Solid State Ion.* **166**, 295–305 (2004).
85. Yang, Z., Dixon, M. C., Erck, R. A. & Trahey, L. Quantification of the Mass and Viscoelasticity of Interfacial Films on Tin Anodes Using EQCM-D. *ACS Appl. Mater. Interfaces* **7**, 26585–26594 (2015).
86. Borisenko, N. *et al.* In situ STM and EQCM studies of tantalum electrodeposition from TaF5 in the air- and water-stable ionic liquid 1-butyl-1-methylpyrrolidinium bis(trifluoromethylsulfonyl)amide. *Electrochimica Acta* **54**, 1519–1528 (2009).
87. Schneider, O. *et al.* An EQCM Study of the Electropolymerization of Benzene in an Ionic Liquid and Ion Exchange Characteristics of the Resulting Polymer Film. *J. Phys. Chem. B* **109**, 7159–7168 (2005).

## **GENERAL CONCLUSION**



## General Conclusion

In this work, we have studied another approach to harvest and store solar energy simultaneously into a single device, using a  $\text{TiO}_2$  bi-functional Li-ion battery photo-electrode.

The apprehension of an electrode undergoing simultaneous light absorption and  $\text{Li}^+$  intercalation/extraction is very rich in terms of potentialities. However, at the same time, the various facets of the electrode evolution are very challenging to track and understand. For this reason, we have chosen to work with a model electrode, whose composition is as simple as possible (carbon and dye-free electrode): a mesoporous  $\text{TiO}_2$  anatase thin film electrode. It was prepared by combining the sol-gel chemistry with the dip-coating process, using the “evaporation induced self-assembly” (EISA) approach to obtain the mesoporosity. The careful control of the porous architecture and the electrode thickness (typically between 100 nm and 1500 nm) provided a well-defined and highly reproducible active material in terms of crystallite size and interconnection, and also in terms of electrode/electrolyte interface. All these parameters are known to dictate the electrode behavior, their fine control will then allow for trustworthy interpretation.

Mesoporous  $\text{TiO}_2$  thin films deposited on FTO substrate were studied as a positive (photo)-electrode in a classical Li-ion battery configuration, using LP30 as an electrolyte, either Li foil or C as counter-electrode, and Li foil as reference electrode.

The  $\text{TiO}_2$ -electrode behaviour was first investigated in dark conditions. The thinner  $\text{TiO}_2$  electrode exhibited the expected capacities ( $\simeq 160 \text{ mAh.g}^{-1}$  for an electrochemical range between 1.4 V and 2.6 V vs.  $\text{Li}^+/\text{Li}^0$ ). Mass capacities were nonetheless found to decrease when increasing the film thickness, which was probably due to the harder electrolyte penetration and/or harder electrons diffusion throughout the inorganic network.

During the first cycles, a SEI was found to be formed at the electrode surface (CVs) at reductive potentials. The analysis of the  $F(dm/dQ)$  function in EQCM measurements confirmed an important mass gain after the first reduction sweep. SEM pictures after the first cycle also exhibits the presence of a layer at the surface of the electrode, partially covering the porous structure. Elemental analyses, like XPS performed on the electrode surface and liquid NMR ( $^1\text{H}$ ,  $^{19}\text{F}$ ,  $^{31}\text{P}$ ) recorded on the electrolyte solution, after cycling, could highlight the presence of LiF on the electrode surface and of  $\text{OPF}_2\text{O}^-$ ,  $\text{OPFO}^{2-}$  and HF in solution. It is however difficult to clearly address their origin, in particular for LiF (SEI related or simple hydrolysis product).



The illumination of the cell then allowed to highlight the photo-induced processes. A first observation was that light enhances the electrochemical charge and discharge capacities. These results lead to a first conclusion that the mechanism previously suggested by Tributsch *et al.*,<sup>1,2</sup> reporting a photo-induced  $\text{Li}^+$  de-insertion, is actually taking place for the here-studied carbon- and dye-free  $\text{TiO}_2$  based mesoporous film electrode. Light induces the formation of electron/hole pairs and those charge carriers could participate in the oxidation of  $\text{Ti}^{3+}$  and facilitate  $\text{Li}^+$  de-insertion. The most striking proof of  $\text{Li}^+$  photo-extraction was provided for a galvanostatic discharge experiment under light by adjusting the electrochemical discharge rate ( $\text{Li}^+$ -electrochemical insertion) to the estimated kinetics of the photo-charge ( $\text{Li}^+$ -photo-extraction). The capacity obtained under light largely exceeded the theoretical capacity of  $\text{TiO}_2$ . Continuing to illuminate in these conditions, we could hope for an apparent “infinite” capacity. Order of magnitude of photo-currents intensities ( $I_{\text{light}} \sim 30 \text{ mA.g}^{-1}$  for a 500 nm-thick electrode of  $1 \text{ cm}^2$  using titania precursor solution at 2M and PB-PEO) has been estimated through potentiostatic experiments under chopped illumination and have been confirmed by OCV experiments and galvanostatic experiments under light.

From *post mortem* analysis of both the electrode and the electrolyte, usual electrolyte degradation products were found on the electrode surface ( $\text{LiF}$ ) and in the electrolyte ( $\text{OPF}_2\text{O}^-$ ,  $\text{OPFO}^{2-}$  and  $\text{HF}$ ). Possible accelerated formation of  $\text{LiF}$  under illumination and cycling conditions (10 CVs between 2.6 V to 1.4 V vs.  $\text{Li}^+/\text{Li}^0$ ,  $0.5 \text{ mV.s}^{-1}$ ) (1) could be due to an eventual temperature increase of the non-water-cooled cell under continuous illumination, and/or (2) could witness the participation of photo-electrons to the  $\text{LiPF}_6$  salt reduction. The exact fate of the electrons still remains unknown. As suggested in Zaghib study on  $\text{LiFePO}_4$  photo-electrode,<sup>3</sup> photo-electrons could also possibly be involved in the reduction of dissolved  $\text{O}_2$ , leading to peroxide generation and thereby to an SEI formation at the counter-electrode. Probing the counter-electrode by *post mortem* analysis or the formation of radicals through electron paramagnetic resonance could give valuable information for future investigations.

In order to investigate in real time the nature of species involved at the electrode/electrolyte interface upon photo-electrochemical cycling, a preliminary work was dedicated to the analysis of the gravimetric response of a  $\text{TiO}_2$ -coated  $\text{GaPO}_4$  when coupled to photo-electrochemical measurements. First results showed that transitory response arising from the  $\text{GaPO}_4$  substrate under illumination should be de-correlated from the one of  $\text{TiO}_2$  for a proper analysis of the photo-induced mechanisms using these substrates. Besides, LP30 might not be the simplest electrolyte to analyze the photo-

induced phenomena due to the  $\text{LiPF}_6$  salt degradation and the resulting gravimetric changes that are uneasy to de-correlate from  $\text{Li}^+$  insertion/extraction phenomena.

Mesoporous  $\text{TiO}_2$  thin film electrode was also studied in a different electrolyte, using ( $\text{PYR}_{13}\text{TFSI}$ , 0.2M  $\text{LiTFSI}$ ) ionic liquid.

In dark conditions, no SEI formation was detected on  $\text{TiO}_2$  electrode (CVs, EQCM) for a potential range between 2.6 V and 1.4 V. Under illumination, no degradation product was found, neither from TFSI $^-$  anion at the electrode surface (FEG-SEM, XPS), nor from the pyrrolidinium cation in the electrolyte (NMR).

The potential of the bifunctional electrode was also tested in ionic liquid. Results showed that it behaves qualitatively the same as in LP30 electrolyte, but higher photo-currents were observed. Water, whose presence in ionic liquid was confirmed by NMR, could possibly act as a scavenger for photo-electrons and explain the higher photocurrent. Water photo-oxidation is not likely to interfere with Ti(III) as shown by tests performed in “water-in-salt” electrolyte. In comparison to the study in LP30, this work in ionic liquid has allowed to confirm the mechanism of photo-extraction in the absence of electrolyte degradation, which is unavoidable in LP30 electrolyte. This system also presents the advantage to not present any SEI, this could highly facilitate the *operando* analysis of  $\text{Li}^+$  insertion/extraction mechanisms under illumination using EQCM measurements.

We also investigate electrode architecture (mesoporous structure and film thickness) in order to understand how it could impact the photo-induced mechanism. In comparison to the changes obtained by switching the electrolytes, no critical differences were observed in the range of architecture used in this study. Study using the cheaper F127 polymers could therefore be considered for further investigations.

In this work, we focused our attention on one electrode trying to understand how photo-holes could trigger the reaction of photo-recharge. In order to design a complete photo-rechargeable system, it is now necessary to investigate how photo-generated electrons could be wisely used to trigger the complementary charging reaction at the counter-electrode.

To that aim, more insight should be provided on the exact nature of the electronic transitions involved within  $\text{Li}_x\text{TiO}_2$  semiconductor under illumination. In fact, as the photo-active phase is the lithiated anatase (since it is active under visible light), more attention should be paid to the energy levels occupied by the injected electrons, and how they can behave upon cycling and under illumination. The transport of the photo-

generated species is even more interesting and complicated to apprehend since the material is composed of a gradient of  $\text{Li}_{0.5}\text{TiO}_2\text{-TiO}_2$  with dynamic boundaries. UV-Vis NIR *operando* measurements could therefore be performed to better understand the electronic transitions involved within  $\text{Li}_x\text{TiO}_2$  semiconductor under illumination. Dynamics of the charge carriers could also be studied by time-resolved microwave conductivity to get information about life-time and diffusion length of the photo-generated charges.

At this very early stage of the development of bifunctional electrode for energy conversion and storage, there is still much progress to be made in order to fully control the fate of the photo-generated charges, and obtain a complete photo-rechargeable system. Search for new electrode candidates amongst the existing semiconductor electrodes able to intercalate  $\text{Li}^+$  ( $\text{WO}_3$ ,  $\text{Nb}_2\text{O}_5$ ,  $\text{LiMn}_2\text{O}_4$ , *etc.*) could therefore be very helpful in order to develop this challenging technology. In association with  $\text{TiO}_2$  or another photo-electrode, the combination could indeed allow to study the photo-electrodes in a complete photo-rechargeable system, which is key in the development of the future of photo-rechargeable Li-ion battery.

## Bibliography

1. Tributsch, H. Photo-intercalation: Possible application in solar energy devices. *Appl. Phys.* **23**, 61–71 (1980).
2. Sauvage, F., Andriamiadamanana, C. & Laberty-Robert, C. Photorechargeable battery: turning light energy into chemical energy and then electric energy, French patent. (FR1361775).
3. Paolella, A. *et al.* Light-assisted delithiation of lithium iron phosphate nanocrystals towards photo-rechargeable lithium ion batteries. *Nat. Commun.* **8**, 14643 (2017).



## **ANNEX**



**TABLE of CONTENTS**

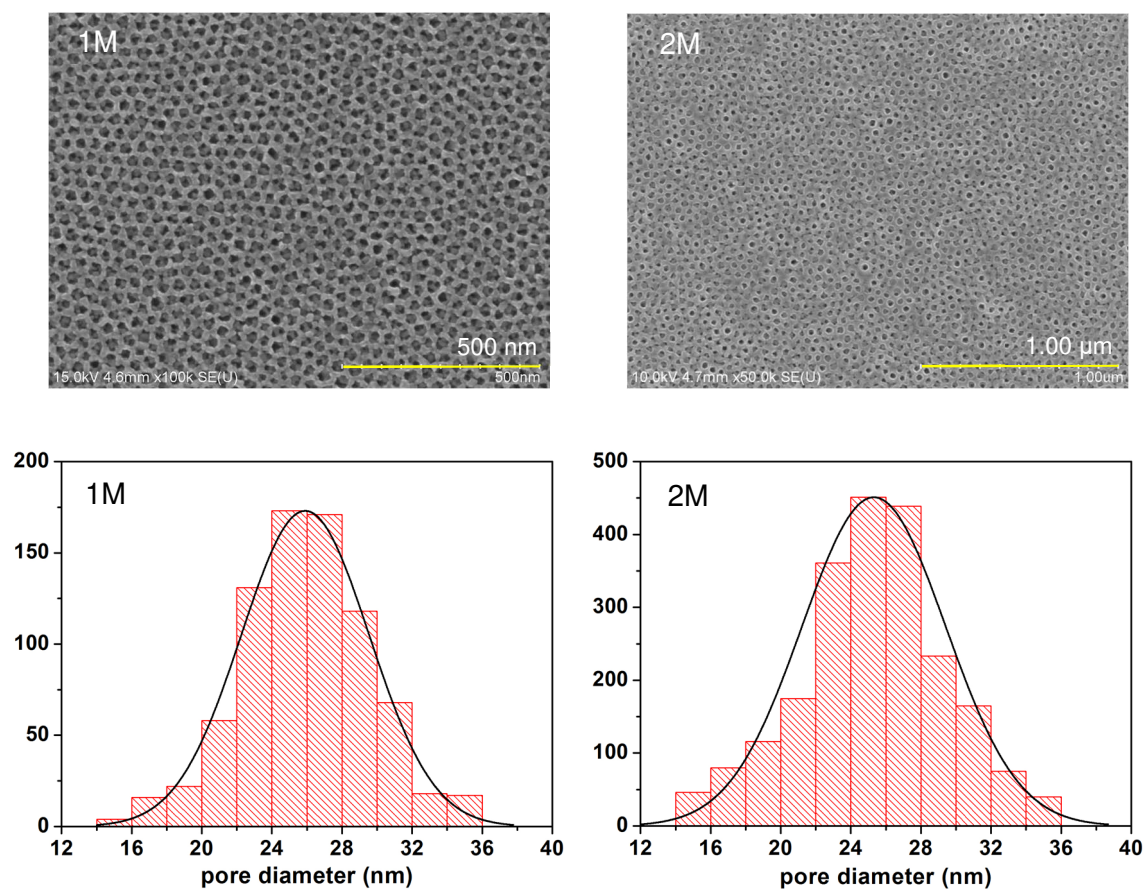
Annex I –Figures .....	V
Annex I.1 – TiO <sub>2</sub> (PB-PEO, TiCl <sub>4</sub> 1M/2M) pore size distribution.....	V
Annex I.2 – FTO and LP30 UV-Visible absorption spectra .....	VI
Annex I.3 – In situ evolution of UV-Vis absorption spectra for anatase TiO <sub>2</sub> electrode (PB-PEO, 2M in TiCl <sub>4</sub> , 10 dipped layers).....	VII
Annex I.4 – CVs in dark and light for different film architecture .....	VIII
Annex I.5 – Chopped potentiostatic experiment in dark and light for different film architecture .....	IX
Annex I.6 – EDX qualitative analysis of TiO <sub>2</sub> electrode surface for different cycling conditions in LP30 electrolyte.....	X
Annex I.7 – Reaction scheme of LiPF <sub>6</sub> degradation suggested by Wiemers-Meyers <i>et al.</i> NMR study .....	XI
Annex I.8 – Nyquist plots fits using RC and Randles circuits.....	XI
Annex I.9 – Nyquist plots fits using equivalent circuit with CPE (dark) .....	XII
Annex I.10 – Nyquist plots fits using equivalent circuit with CPE (light) .....	XIII
Annex I.11 – F(dm/dq) function for TiO <sub>2</sub> film during CVs in LP30 .....	XIV
Annex II – Anatase thin film fabrication .....	XV
Annex III – Technics of characterization .....	XVII
III.1 - Electrochemical and Photo-Electrochemical measurements.....	XVII
III.2 – Glancing Angle X-Ray Diffraction .....	XX
III.3 - Ellipsometry .....	XX
III.4 - Field-Emission-Gun Scanning-Electron-Microscopy and Energy-dispersive X- Ray Spectroscopy .....	XXI
III.5 - X-Ray Photoelectron Spectroscopy .....	XXI
III.6 - Nuclear Magnetic Resonance Spectroscopy .....	XXI
III.7 - UV-Visible spectroscopy .....	XXII
III.8 - Electrochemical Quartz Crystal Microbalance .....	XXIII
Bibliography .....	XXV





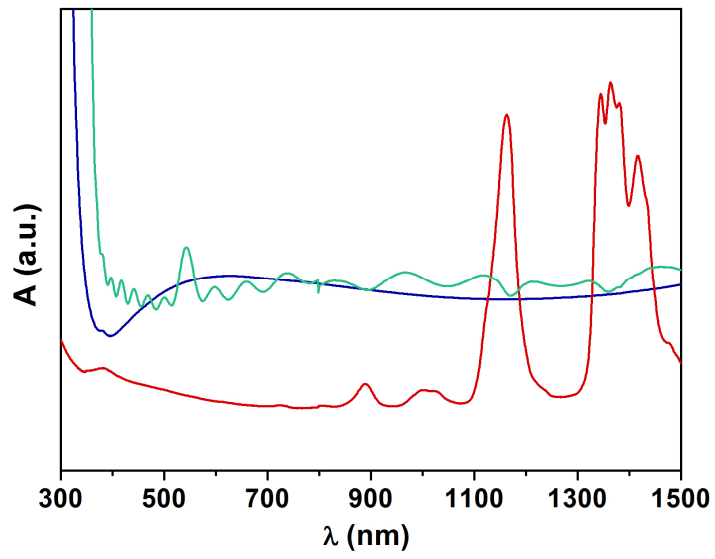
## Annex I –Figures

### Annex I.1 – TiO<sub>2</sub> (PB-PEO, TiCl<sub>4</sub> 1M/2M) pore size distribution



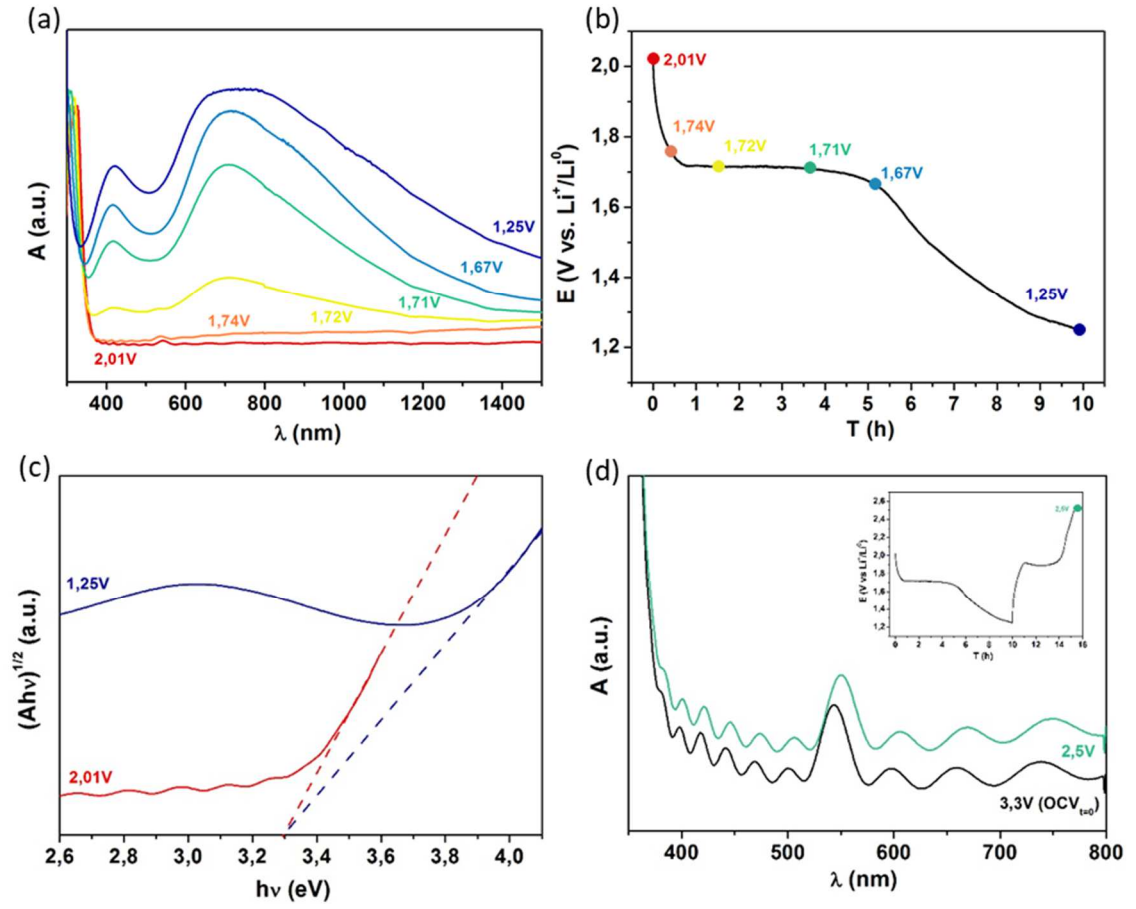
**Figure A.I.1:** Pore size distribution of TiO<sub>2</sub> mesoporous thin films prepared with PB-PEO polymers with TiCl<sub>4</sub> at 1M (left) and 2M (right). Distribution were obtained by analyzing SEM-FEG pictures with IMAGE-J (analysis in contrast) for samples of 623 points (1M) and 2181 points (2M).

## Annex I.2 – FTO and LP30 UV-Visible absorption spectra



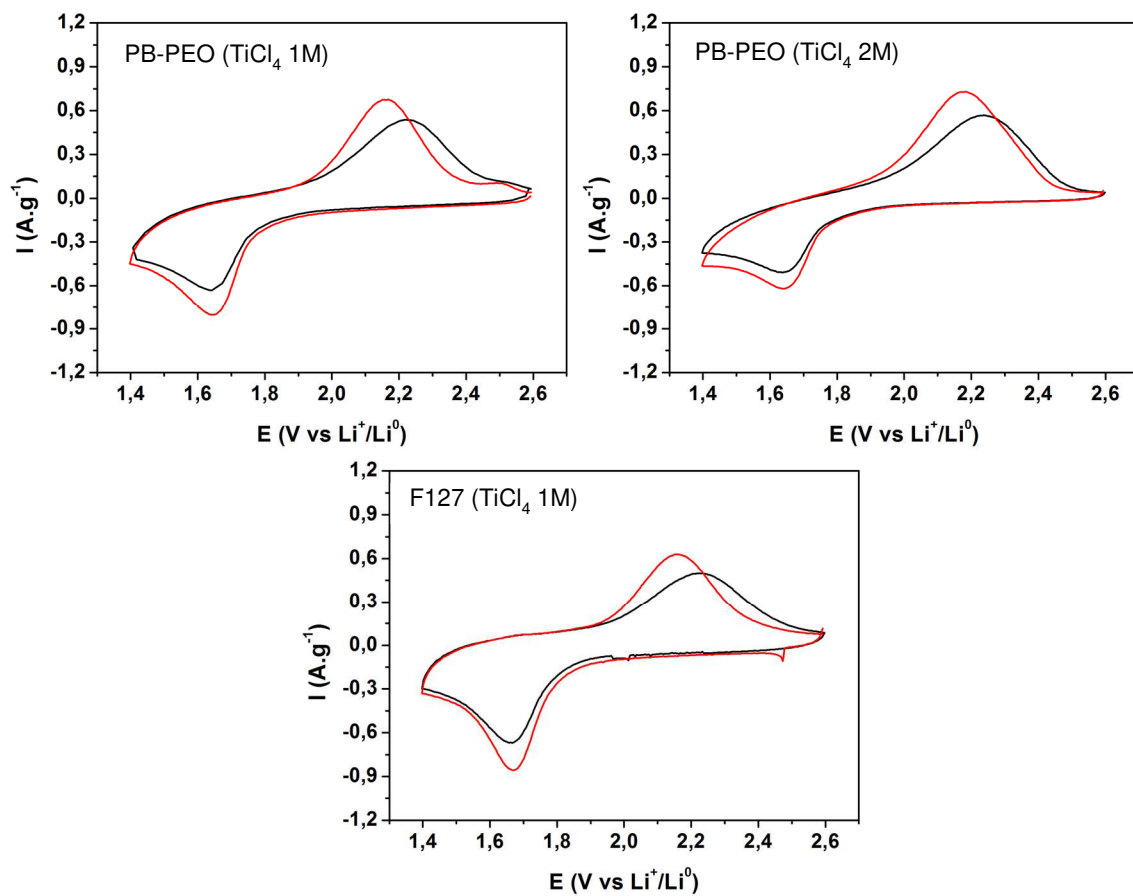
**Figure A.I.2:** UV-Vis absorption spectra of FTO/glass substrate (blue), LP30 (orange) compared anatase TiO<sub>2</sub> electrode (PB-PEO, 2M in TiCl<sub>4</sub>, 10 dipped layers) absorption spectra (green).

### Annex I.3 – In situ evolution of UV-Vis absorption spectra for anatase TiO<sub>2</sub> electrode (PB-PEO, 2M in TiCl<sub>4</sub>, 10 dipped layers)



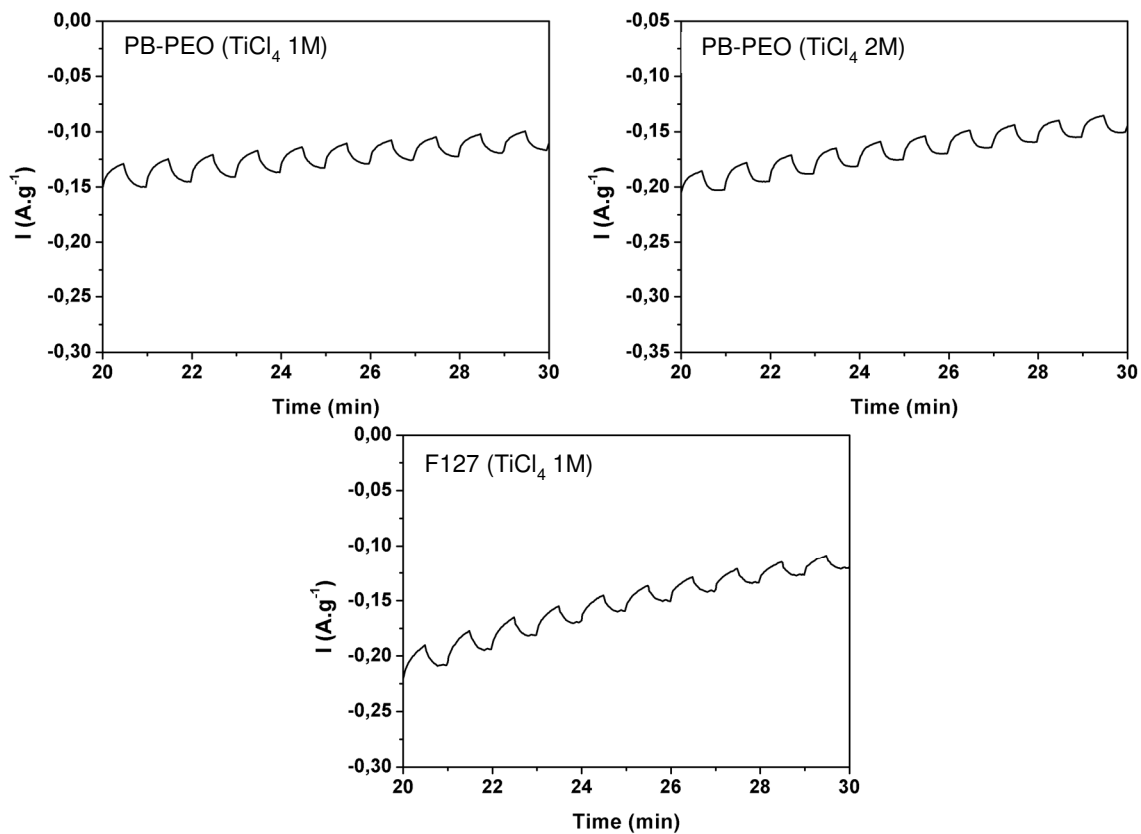
**Figure A.I.3:** In situ evolution of UV-Vis absorption spectra (a) for anatase TiO<sub>2</sub> electrode (PB-PEO, 2M in TiCl<sub>4</sub>, 10 dipped layers) during galvanostatic discharge (-15  $\mu$ A) in PYR<sub>13</sub>TFSI (0.2M in LiTFSI) (b). Associated Tauc plots (c). Comparison between absorbance at initial OCV (3.3 V) and after discharge (-15  $\mu$ A) / charge (30  $\mu$ A) (d).

## Annex I.4 – CVs in dark and light for different film architecture



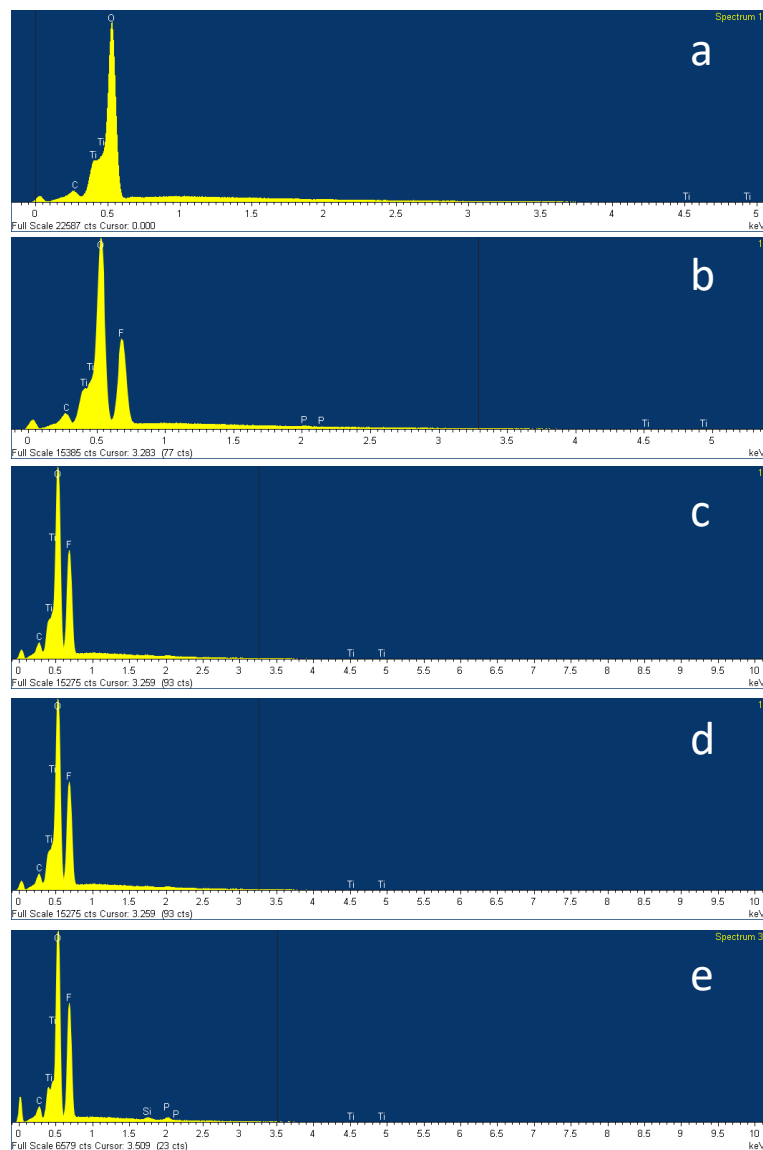
**Figure A.I.4:** CVs at 0.5 mV.s<sup>-1</sup> in LP30 electrolyte under dark (black) and light (red) conditions for 230 nm-thick anatase films prepared with PB-PEO (1M and 2M in TiCl<sub>4</sub>) and with F127. Counter and reference electrodes are metallic Li foils.

### Annex I.5 – Chopped potentiostatic experiment in dark and light for different film architecture



**Figure A.I.5:** Chopped potentiostatic experiment (1.72 V vs.  $\text{Li}^+/\text{Li}^0$ , on/off every 30 s) in LP30 electrolyte under dark (black) and light (red) conditions for 230 nm-thick anatase films prepared with PB-PEO (1M and 2M in  $\text{TiCl}_4$ ) and with F127. Counter- and reference electrodes are metallic Li foils.

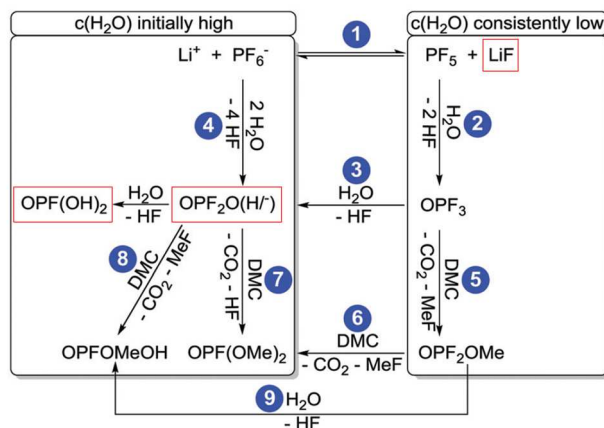
## Annex I.6 – EDX qualitative analysis of $\text{TiO}_2$ electrode surface for different cycling conditions in LP30 electrolyte



**Figure A.I.6:** EDX spectra corresponding to the following steps:

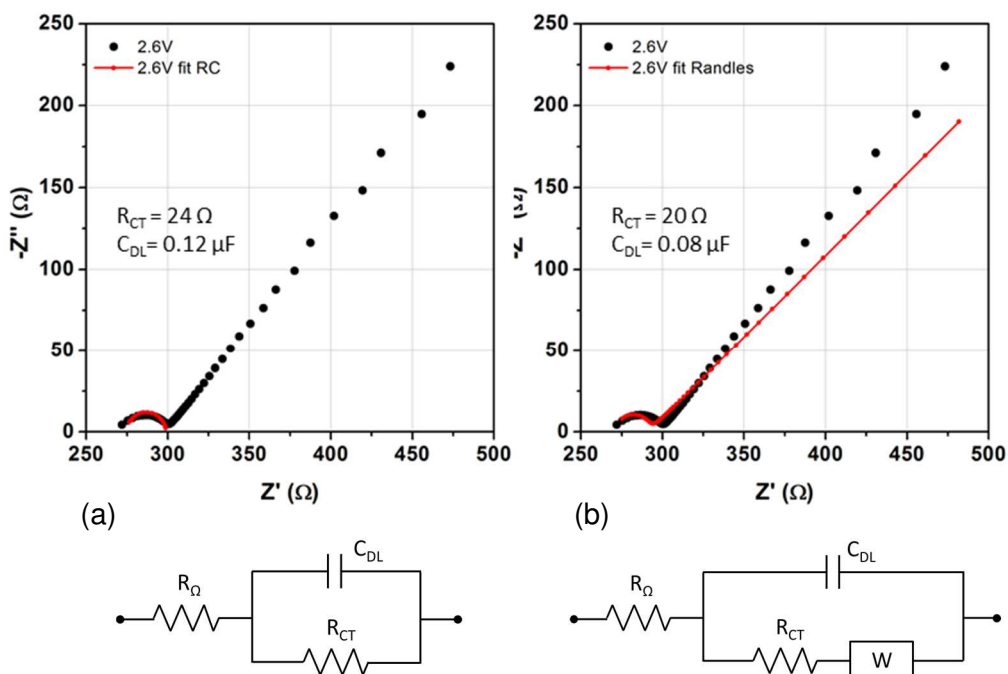
- (a) after 1 night in the solvent without any electrochemical cycling
- (b) after the first CV (2.6 V to 1.4 V vs.  $\text{Li}^+/\text{Li}^0$ ,  $0.5 \text{ mV.s}^{-1}$ ) under dark conditions
- (c) after 10 CV's (2.6 V to 1.4 V vs.  $\text{Li}^+/\text{Li}^0$ ,  $0.5 \text{ mV.s}^{-1}$ ) under dark conditions
- (d) after 10 CV's (2.6 V to 1.4 V vs.  $\text{Li}^+/\text{Li}^0$ ,  $0.5 \text{ mV.s}^{-1}$ ) under continuous illumination
- (e) after 20 CV's (2.6 V to 1.4 V vs.  $\text{Li}^+/\text{Li}^0$ ,  $0.5 \text{ mV.s}^{-1}$ ) under dark conditions

### Annex I.7 – Reaction scheme of $\text{LiPF}_6$ degradation suggested by Wiemers-Meyers *et al.* NMR study



**Figure A.I.7:** Proposed reaction scheme of  $\text{PF}_6^-$  degradation by Wiemers-Meyers *et al.*<sup>1</sup> NMR study. Species detected in our study are indicated in red frame.

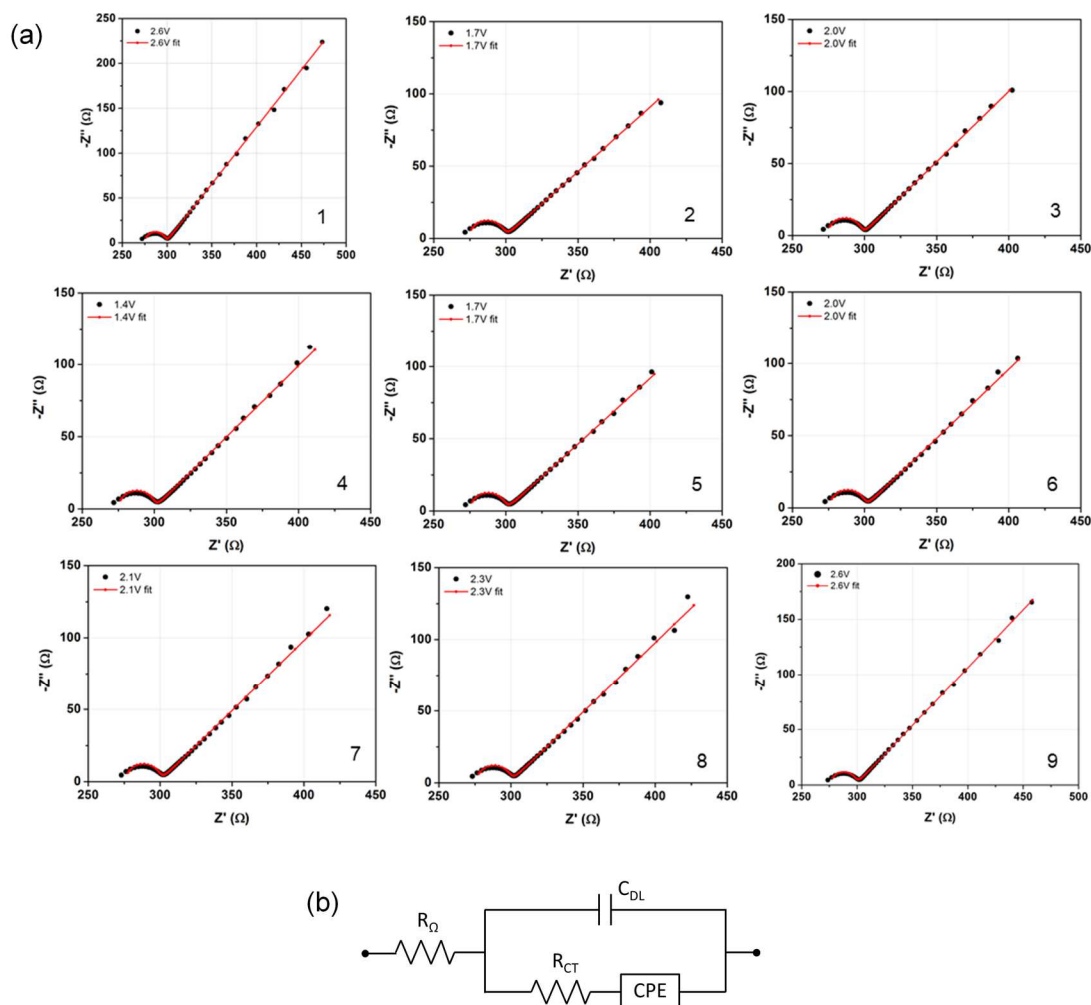
### Annex I.8 – Nyquist plots fits using RC and Randles circuits



**Figure A.I.8:** Fits of the Nyquist plots using equivalent RC circuit (a) (left) and Randles circuit (b) (right) for anatase electrode (PB-PEO, 2M in  $\text{TiCl}_4$ , 2 layers) in dark at 2.6 V.

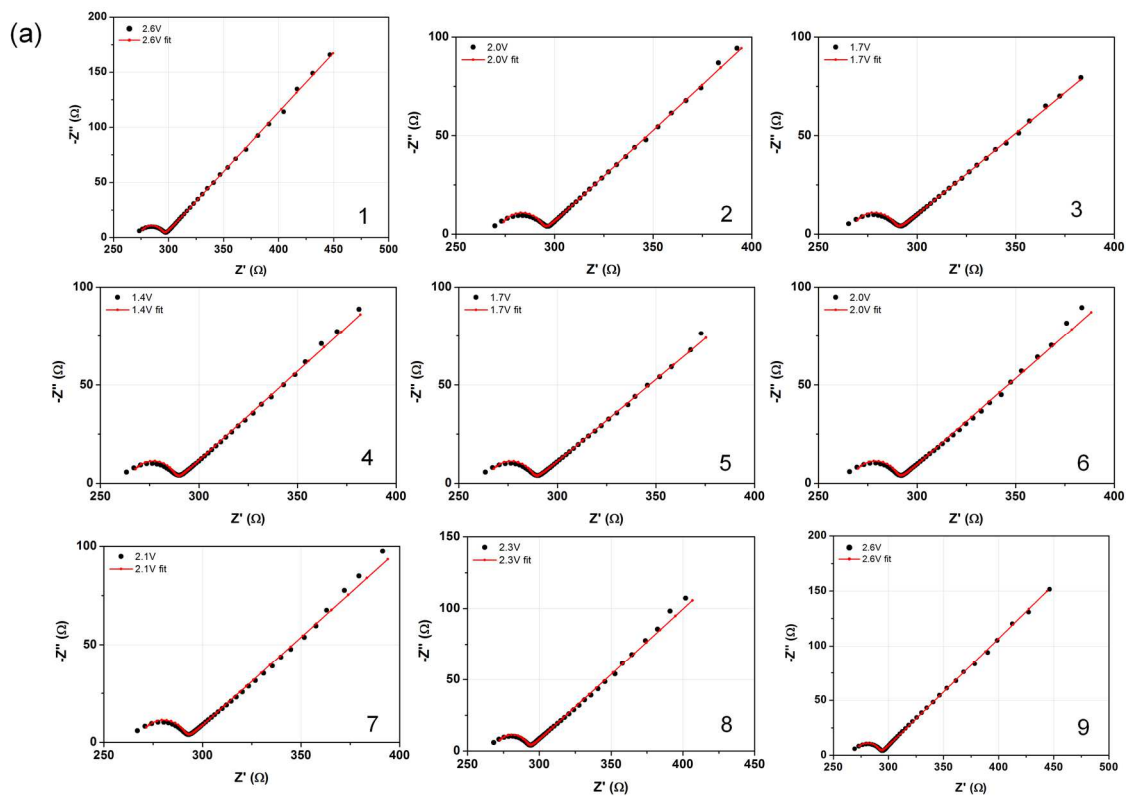


## Annex I.9 – Nyquist plots fits using equivalent circuit with CPE (dark)

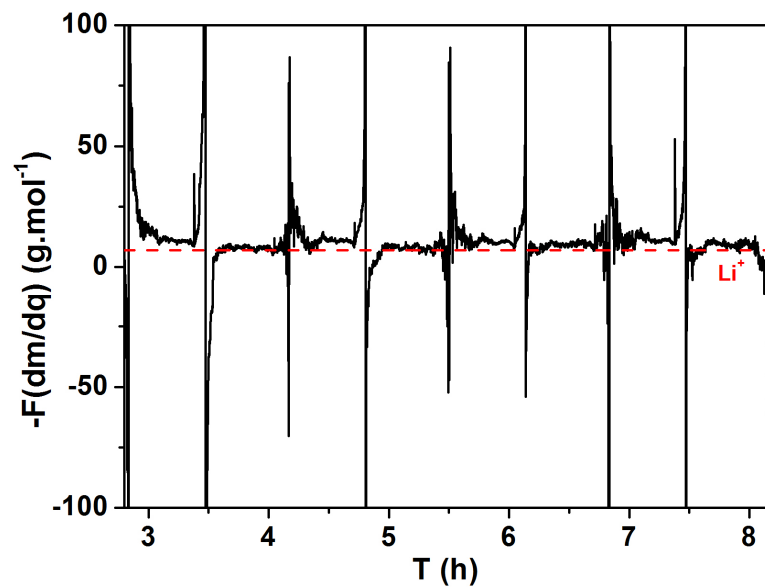


**Figure A.I.9:** Fits of the Nyquist plots (a) using equivalent circuit with CPE element (b) of anatase electrode (PB-PEO, 2M in  $\text{TiCl}_4$ , 2 layers) during galvanostatic discharge ( $-30 \mu\text{A}$ ) (1-4) / charge ( $30 \mu\text{A}$ ) (4-9) under dark conditions.

# Annex I.10 – Nyquist plots fits using equivalent circuit with CPE (light)



**Figure A.I.10:** Fits of the Nyquist plots (a) using equivalent circuit with CPE element (b) of anatase electrode (PB-PEO, 2M in  $\text{TiCl}_4$ , 2 layers) during galvanostatic discharge ( $-30 \mu\text{A}$ ) (1-4) / charge ( $30 \mu\text{A}$ ) (4-9) under light conditions.

Annex I.11 –  $F(dm/dq)$  function for  $TiO_2$  film during CVs in LP30

**Annex Figure A.I.11:**  $-F(dm/dq)$  function corresponding to the average molecular weight of the species involved in the charge compensation as a function of the time for a mesoporous  $TiO_2$  film (PB-PEO,  $TiCl_4$  at 2M, 1 layer) in LP30 obtained from CVs (2.6V and 1.4V vs.  $Li^+/Li^0$ , 0.5 mV.s<sup>-1</sup>).

## Annex II – Anatase thin film fabrication

### *FTO Substrates:*

Fluorine-doped tin oxide (FTO) - coated pre-cut substrates were purchased from SOLEMS (YSUB/ASASHI 120/1: 10 x 30 mm / resistivity:  $80 \Omega \cdot \text{cm}^{-2}$ , thickness of the FTO layer: 80 nm). The substrates are cleaned with EtOH and acetone before being dipped.

### *Titania “precursor solution”:*

Product	Amount	Supplier	Information
ethanol	28.1 g	VWR	AnalaR NORMAPUR® ACS, Reag. Ph. Eur. analytical reagent (99.9%)
Titanium tetrachloride	23.2 g	Sigma Aldrich	≥99.9% trace metals basis

A solution containing the  $\text{TiCl}_4$  precursor is first prepared by mixing  $\text{TiCl}_4$  and ethanol with a molar ratio 1( $\text{TiCl}_4$ ):5(EtOH), and is referred as “precursor solution”. When stored at 4°C, this precursor solution can be used for several months.

### *PB-b-PEO dip-coating solutions:*

Product	Amount	Supplier	Information
ethanol	5.0 g	Sigma Aldrich	≥99.9% trace metals basis
water	0.4 g		Distilled water
“Precursor solution”	0.8 g (1M) 1.6 g (2M)	See “precursor solution”	See “precursor solution”
Poly(1,4-butadiene)-b-poly(ethylene oxide)	0.1 g	Polymer Source	PB-b-PEO:P4515-BdEO M.W.(PB)=11800 g.mol <sup>-1</sup> M.W.(PEO)=13500 g.mol <sup>-1</sup>

100 mg of polymers (PB-b-PEO) is dissolved in a mixture of 5.0 g EtOH and 0.4 g  $\text{H}_2\text{O}$ . A heat treatment of 70°C for 1 hour is necessary to complete the dissolution. After cooling at room temperature, the titania “precursor solution” containing  $\text{TiCl}_4$  precursor is added dropwise into the solution of PB-PEO. The concentration of inorganic salts in the final solution is 1M (0.8 g of “precursor solution” or 2M (1.6 g of “precursor solution”). The  $\text{TiO}_2$  mesoporous films were obtained using the dip-coating process at a withdrawal speed  $2.5 \text{ mm} \cdot \text{s}^{-1}$  in dry atmosphere ( $< 5\%$  relative humidity). Back side of the dipped FTO substrate is cleaned with an ethanol soaked paper. The

hybrid film is then placed for 1h in a furnace pre-heated at 500°C in air (static atmosphere) to (i) induce crystallization of the anatase and (ii) decompose the block-copolymer to obtain the TiO<sub>2</sub>/FTO electrode.

For the multilayered process, between each layer dipped layer, an intermediate heat treatment of 3 min in the furnace pre-heated at 350°C is necessary. After the final dipped layer, final heat treatment at 500°C is applied.

***Pluronic F127 dip-coating solutions:***

Product	Amount	Supplier	Information
ethanol	8.1 g	Sigma Aldrich	≥99.9% trace metals basis
water	0.9 g		Distilled water
“Precursor solution”	2.1 g	See “precursor solution”	See “precursor solution”
Pluronic F-127	0.335 g	Sigma Aldrich	BioReagent, suitable for cell culture

335 mg of polymers (F127) is dissolved in a mixture of 8.1 g EtOH and 0.9 g H<sub>2</sub>O. A heat treatment of 70°C for 1 hour is necessary to complete the dissolution. After cooling at room temperature, the titania “precursor solution” containing TiCl<sub>4</sub> precursor (2.1 g) is added dropwise into the solution of F127. The TiO<sub>2</sub> mesoporous films were obtained using the dip-coating process at a withdrawal speed 2.5 mm.s<sup>-1</sup> in dry atmosphere (< 5% relative humidity). Back side of the dipped FTO substrate is cleaned with an ethanol soaked paper. The hybrid film is then placed for 1h in a furnace pre-heated at 500°C in air (static atmosphere) to (i) induce crystallization of the anatase and (ii) decompose the block-copolymer to obtain the TiO<sub>2</sub>/FTO electrode.

For the multilayered process, between each layer dipped layer, an intermediate heat treatment of 3 min in the furnace pre-heated at 350°C is necessary. After the final dipped layer, final heat treatment at 500°C is applied.

## Annex III – Technics of characterization

### III.1 - Electrochemical and Photo-Electrochemical measurements

#### *Cell preparation:*

Bottom of the  $\text{TiO}_2$  electrode is cut when needed to eliminate the inhomogeneous part of the  $\text{TiO}_2$  film (final meniscus, which is usually obtained by dip coating process). Contacts of the working electrode were made by placing the denuded part of a WCT30 wire (Radiospare) directly onto the FTO (top part, which is not recovered by the  $\text{TiO}_2$ ) with copper Radiospare tape (1 cm width,  $4.5 \text{ N.cm}^{-1}$  / RS 542-5460).

For the counter- and reference electrodes, 2 lithium foils (Sigma Aldrich) are directly placed on the denuded part of a WCT30 wire (Radiospare).

The three-electrode cell is made of a sealed glass container (transparent in the visible range) or of a sealed water-cooled glass cell (**Figure 1**). It is assembled in an Ar-glovebox using silicon caps (Saint-Gobain, Versilic). Electrolyte is added in order to cover  $\simeq 1 \text{ cm}^2$  of the  $\text{TiO}_2$  electrode. All the electrolytes are used without any further purification.

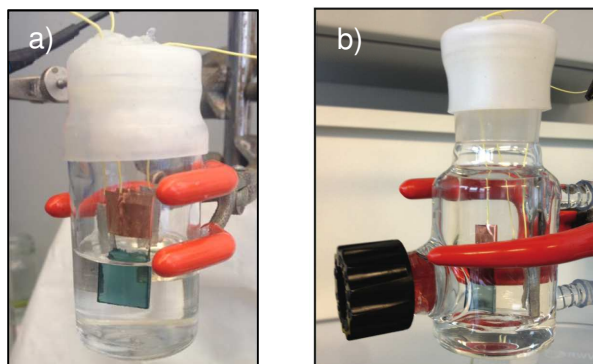


**Figure 1** : cell made of sealed glass container (a) or sealed water-cooled glass cell (b)

#### *Electrolytes and lithium salts:*

Product	Supplier	Information
1M $\text{LiPF}_6$ in EC:DMC “LP30”	Sigma Aldrich	battery grade <15 ppm $\text{H}_2\text{O}$ , <50 ppm HF
N-Propyl-N-methyl-pyrrolidinium bis(trifluoromethanesulfonyl)imide “PYR <sub>13</sub> TFSI”	Solvionic	99.9%, <20 ppm $\text{H}_2\text{O}$
Bis(trifluoromethane)sulfonamide lithium salt “LiTFSI”	Solvionic	99.9% extra dry <20 ppm $\text{H}_2\text{O}$
Lithium chloride	Sigma Aldrich	>99.9%
Lithium sulfate	Sigma Aldrich	>99.99%

**Potentiostat:**

AMETEK Solartron pstat 1 MS/s, Bio-logic SP300 and Princeton 273A were used for electrochemical characterization. AMETEK Solartron pstat 1 MS/s was used for all the photo-electrochemical measurements and electrochemical impedance spectroscopy measurements. Princeton 273A was used for all the electrochemical UV-Visible coupled measurements.

**Lamp:**

A Newport xenon arc lamp was used throughout photo-electrochemical experiments (spectrum in **Figure 2-a**). Newport model 6258 300 W ozone free lamp working was used at 280 W for photo-electrochemical measurements in an Arc Lamp Housing enclosure, model 67001. This was powered by a Newport power supply 69911 in junction with an Oriel liquid filter 61945 (250-950 nm transmission) filled with water in order to filter the IR light and resultant heat (spectrum in **Figure 2-b**).

All photo-electrochemical measurements were done 45 cm away from the arc lamp source. Light output was verified by a 1918-R Newport power meter 918D-UV-OD3R, UV Silicon Detector (200 – 1100 nm) in two configurations: through direct lightning or through optical fiber lightning (see **Figure 3**).

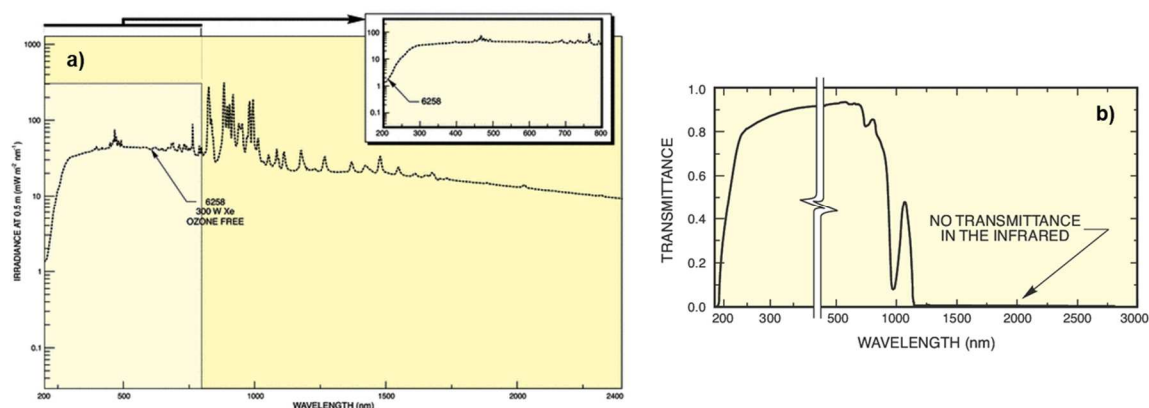


**Figure 2:** Newport 300W Xe arc lamp ozone free spectrum (model 6258) (a) and Oriel liquid filter 61945 transmission (250-950 nm) (b).

In **Table 1** are reported the light output verified by the Silicon Detector in these two configurations. Complementary measurements using Oriel PV Reference Cell System (911150V) with a 20BPF10-450 filter bandpass (Newport) gives an equivalent of 2.2 SUN in the direct lightning configuration.

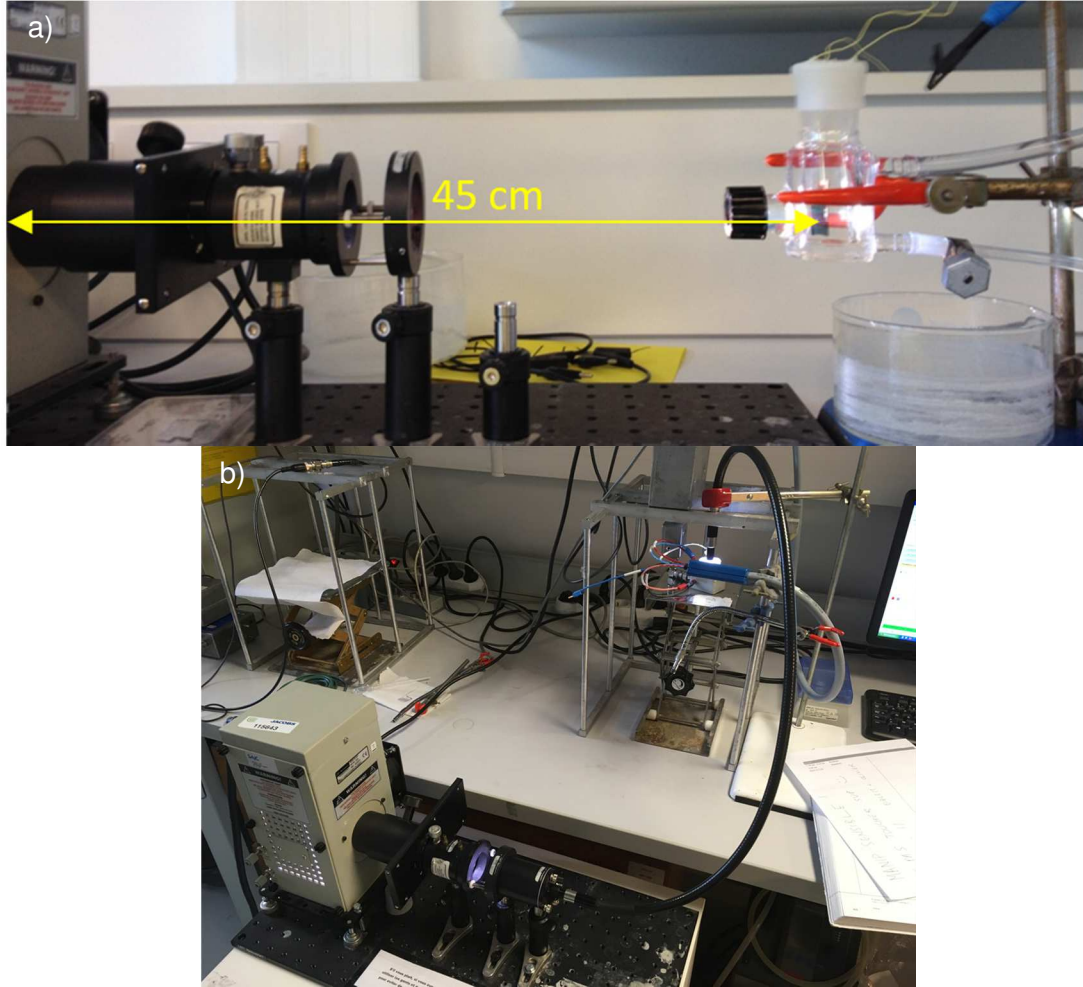


**Figure 3** : direct lightning (a) and optical fiber lightning (b).

$\lambda$ (nm)	450	500	550	600	650	700	750	800	850	900	950	1000	1050	1100
P direct (mW/cm <sup>2</sup> )	490	375	288	281	288	274	260	237	216	198	184	182	245	567
P fiber (mW/cm <sup>2</sup> )	44	34	26	25	26	25	24	22	20	18	16	16	22	50

**Table 1** : Light output verified by a 1918-R Newport power meter 918D-UV-OD3R, UV Silicon Detector (200 – 1100 nm) in two configurations: through direct lightning and through optical fiber lightning (without other filters than the Oriel liquid filter 61945).



### ***Electrochemical Impedance Spectroscopy:***

Mott Schottky measurements were performed with  $\text{TiO}_2/\text{FTO}$  as working electrode, and lithium foils at counter- and reference-electrodes in LP30 electrolyte. Scans were done between 3.5 V and 2.3 V vs.  $\text{Li}^+/\text{Li}^0$  with 10 mV amplitude from 3.5 V to 2.3 V at frequencies varying from 0.1 kHz to 10 kHz.

Nyquist diagrams were obtained during galvanostatic discharge/charge (30  $\mu\text{A}$ ) under dark and light conditions at different potentials (2.6 V, 2.0 V, 1.7 V, 1.4 V, 1.7 V, 2.1 V, 2.3 V, 2.6 V) for frequencies between 200 kHz to 0.1 Hz, for an amplitude of 10 mV. Fits were obtained from BioLogic using the Z-Fit software.

All the EIS measurements were performed on AMETEK Solartron pstat 1 MS/s.

## **III.2 – Glancing Angle X-Ray Diffraction**

The structure of the mesoporous thin films was studied by using a Bruker AXS D8 Discover X-ray diffractometer. The measurements in glancing geometry were performed using a line focus copper X-ray tube and a parabolic multilayer Göbel mirror to obtain an almost parallel X-ray  $\text{CuK}\alpha$  impinging beam. A primary slit of 0.1 mm x 6 mm was used to obtain a square footprint on the sample for a  $1^\circ$  glancing angle. The samples were mounted on a motorized X, Y, Z stage, supported by an Eulerian cradle, to obtain an accurate alignment of the samples at the goniometer center. A 1D position sensitive detector Lyn- xEye ( $2^\circ$  angular opening) was used to speed up the data collection. Diagrams were analyzed by Rietveld method using the XND software. This study was performed in collaboration with BALDINOZZI Gianguido from the Laboratoire de Structure, Propriétés et Modélisation des Solides, UMR CNRS CEA 8580 (SPMS), Commissariat de l'Energie Atomique de Saclay.

## **III.3 - Ellipsometry**

Ellipsometry measurements were performed on a UV-visible (from 240 to 1000 nm) variable angle spectroscopic ellipsometer (VASE – 2000 U Woollam), and the data analyses were performed with the CompleteEASE software using Cauchy models. Environmental ellipsometric porosimetry was performed through a water adsorption/desorption isotherm using an atmospheric control chamber as described in Boissiere et al.<sup>2</sup> Pore size dimensions were calculated using a model based on spherical geometry in the adapted Kelvin's equation. The specific surface area evaluation takes into account both mesopores and micropores, it is based on the pore dimensions and total porous volume obtained by EEP analysis.

### **III.4 - Field-Emission-Gun Scanning-Electron-Microscopy and Energy-dispersive X-Ray Spectroscopy**

The microstructure of the films and film thickness were observed by Field Emission Gun Scanning Electron Microscopy (FEG- SEM) on a SU-70 Hitachi FEG-SEM, instruments facilitated by the IMPC (Institut des Matériaux de Paris Centre FR2482) financially supported by the C'Nano projects of the Region Ile-de-France. FEG-SEM images were collected under 10 kV tension.

EDX measurements were performed on a X-Max Oxford EDX detector using 5 kV with a silicon standard for quantification. Measurements under 1% atomic were considered below the limit of detection and therefore considered unreliable.

Measurements were performed with MONTERO David from the IMPC (Institut des Matériaux de Paris Centre FR2482).

### **III.5 - X-Ray Photoelectron Spectroscopy**

Films were prepared in Ar-glovebox in cells made of a sealed glass container. After cycling, cells were de-assembled in a glove bag under argon atmosphere to limit possible surface contamination under air exposure. films were cleaned by manually shaking them for 1-2 minutes in a beaker containing dimethyl carbonate (Sigma Aldrich, >99.9%), and conserved if needed before analysis in Ar-glovebox.

XPS measurements were done using an ESCA+ d'Omicron Nano Technology with an Al K $\alpha$  ( $h\nu = 1486.6$  eV) X-ray source. These measurements were completed at the Université de Pierre et Marie Curie (Paris VI) Laboratoires de l'Institut des Matériaux de Paris Centre (IMPC, FR 2482) in association by the Centre national de la recherche scientifique (CNRS) at Laboratoire de Réactivité de Surface (LRS) by MICHE Antoine.

### **III.6 - Nuclear Magnetic Resonance Spectroscopy**

Cells made of a sealed glass container were prepared in Ar-glovebox, with about 2 mL of electrolytes (LP30 or PYR<sub>13</sub>TFSI, 0,2M LiTFSI). Cells were de-assembled in a glove bag under argon atmosphere to limit possible surface contamination under air exposure. For LP30 electrolyte, 50 or 200  $\mu$ L of electrolyte was completed with 550 or 400  $\mu$ L of deuterated CD<sub>3</sub>CN (Sigma Aldrich, >99.8% atom % D) in NMR tubes for the <sup>19</sup>F and <sup>31</sup>P analysis.

For PYR<sub>13</sub>TFSI, 0,2M LiTFSI electrolyte, 50  $\mu$ L of LP30 was completed with 550  $\mu$ L of deuterated CD<sub>3</sub>CN in NMR tubes for the <sup>1</sup>H analysis.

NMR measurements were performed in a Bruker AVIII 300 spectrometer (7.05 T).

### III.7 - UV-Visible spectroscopy

Agilent Technologies Cary Series UV-vis-NIR 5000 spectrometer was used for absorbance and transmittance measurements. Double beam measurements were taken with glass/FTO substrates as a zero/baseline and scans were completed between 300 – 800 nm or 300 – 1500 nm with a data point at every nanometer. The optical band gap of  $\text{TiO}_2$  was extrapolated by Tauc plots using  $m = 1/2$  for direct semiconductors and  $m = 2$  and for indirect semiconductors.  $\text{TiO}_2$  were considered to be indirect semiconductor.<sup>3</sup>

Experiments were performed in in 2x1 cm quartz cell. The cell was sealed with a cap, which included 2 contacts for the coupled electrochemical measurements (see **Figure 4**). The cap (Teflon) was designed for the experiment and fabricated by DESNOYERS DE MARBAIX Axel from the Laboratoire Interfaces et Systèmes Electrochimiques (LISE), UMR 8235, Sorbonne Université. Electrochemical UV-Visible coupled measurements were performed in a two-electrode configuration using Princeton 273A potentiostat.

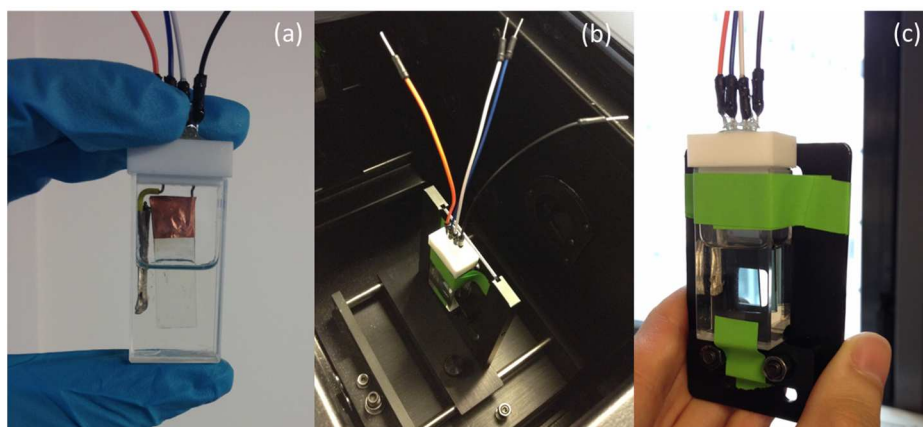


**Figure 4** :  $\text{TiO}_2$  thin film (used as working electrode) and Li foil (used as counter- and ref. electrode) in argon-tight cuvette containing LP30 electrolyte (a) same cell in UV-Vis spectrophotometer (b).

### III.8 - Electrochemical Quartz Crystal Microbalance

#### *TiO<sub>2</sub> film preparation:*

Pt-patterned GaPO<sub>4</sub> crystal resonator substrates (6 MHz, diameter of 1.5 cm, purchased as neat crystals from TEMEX, France or AWS, Spain) were prepared by depositing platinum keyhole electrodes by evaporation techniques on both sides of the GaPO<sub>4</sub> with a titanium adhesion sublayer. Pt active surface area is 0.4 cm<sup>2</sup> or 1.2 cm<sup>2</sup> depending on the pattern (see **Figure 5**).

TiO<sub>2</sub> mesoporous films were then deposited on Pt-patterned GaPO<sub>4</sub> substrate using the “evaporation induced micelles packing” process. First, a solution containing the TiCl<sub>4</sub> precursor is prepared by mixing TiCl<sub>4</sub> and ethanol (EtOH) (molar ratio 1:5). Then, 100 mg of poly(1,4-butadiene)-b-poly(ethylene oxide) (PB-b-PEO:P4515-BdEO, M.W. (PB)=11800 g.mol<sup>-1</sup> and M.W. (PEO)=13500 g.mol<sup>-1</sup>) is dissolved in a mixture of 5.0 g EtOH and 0.4 g H<sub>2</sub>O. A heat treatment of 70°C for 1 hour is necessary to complete the dissolution. After cooling at room temperature, the titania “precursor solution” containing TiCl<sub>4</sub> precursor (2.1 g) is added dropwise into the solution of PB-PEO. The concentration of inorganic salts in the final solution was 2 mol.l<sup>-1</sup>. The TiO<sub>2</sub> mesoporous films were obtained using the dip-coating process<sup>22</sup> at a withdrawal speed of 2.5 mm.s<sup>-1</sup> in dry atmosphere (< 5% relative humidity). Deposit of TiO<sub>2</sub> on a selected Pt surface is assured by cleaning the Pt-uncovered surface of the chosen face as well as the entire rear face with an ethanol soaked cotton bud. The hybrid film was then placed for 1h in a furnace pre-heated at 500°C in air (static atmosphere) to (i) induce crystallization of the anatase and (ii) decompose the block-copolymer template to obtain the mesoporous TiO<sub>2</sub>/Pt/GaPO<sub>4</sub> electrodes for EQCM measurements.

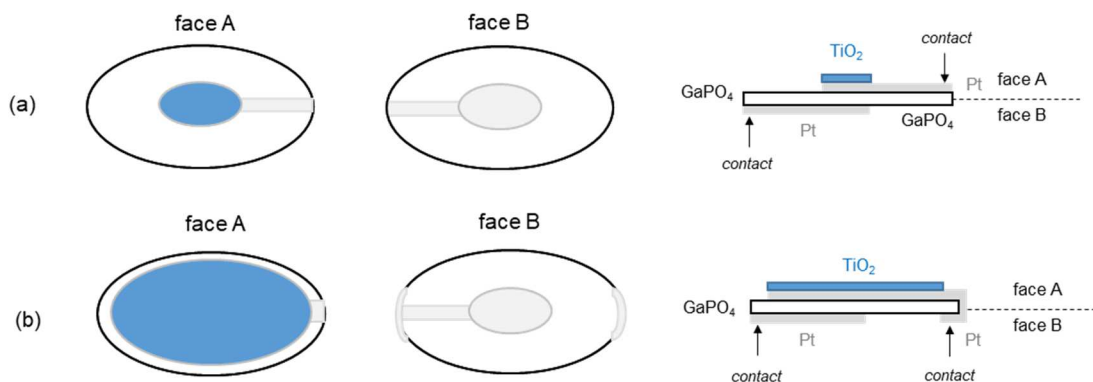


**Figure 5:** Schematic representation of the TiO<sub>2</sub>/Pt/GaPO<sub>4</sub> substrates (surface area of 0.4 cm<sup>2</sup> (a) or 1.2 cm<sup>2</sup> (b)). Electrical contact points for EQCM measurements are indicated by arrows.

**EQCM set-up:**

EQCM tests were conducted by coupling cyclic voltammetry (CV) and galvanostatic charge/discharge (GCD) with QCM to track the simultaneous microbalance frequency changes of the electrode during cycling. The set-up used for measuring gravimetric changes is a lab made microbalance developed at the LISE laboratory (UMR8235, SU) (see **Figure 6**). The  $\text{TiO}_2/\text{Pt}/\text{GaPO}_4$  modified crystal resonators were used as working electrode in an electrochemical cell designed in our group (collaboration between LCMCP and LISE) and fabricated by AWS Company (Spain). This air-tight electrochemical cell, used for the first time in this Ph.D. thesis, contains a quartz window dedicated for a front illumination of the  $\text{TiO}_2$  electrode through the electrolyte. Two lithium foils were used as counter- and reference electrode, using either LP30 or  $\text{PYR}_{13}\text{TFSI}$  (0.2M  $\text{LiTFSI}$ ) as electrolytes.

The electrochemical measurements were performed by using a potentiostat (Biologic SP200) and the frequency changes of the modified crystal ( $\text{GaPO}_4$  in these measurements) were monitored by a frequencymeter (Yokogawa).

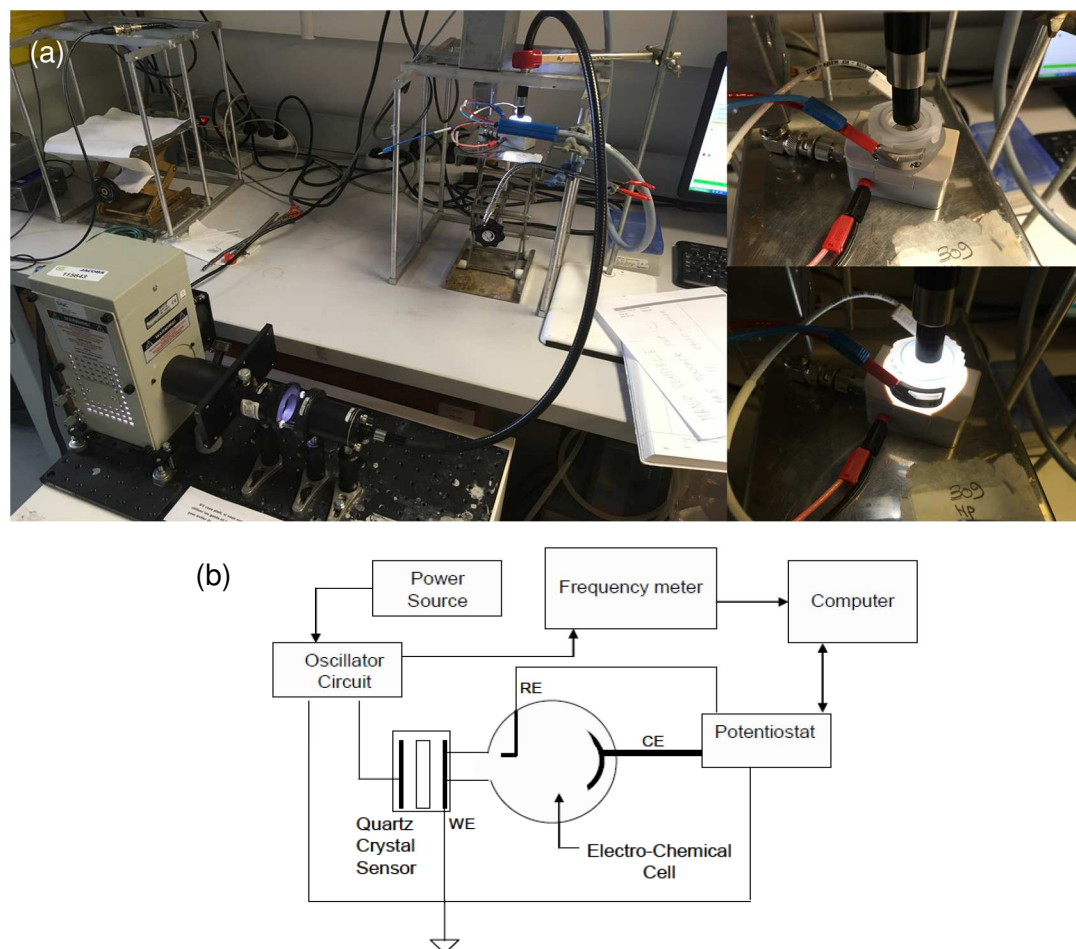


**Figure 6:** « Second generation » air- and water-tight EQCM cell allowing the measurements under illumination (a). Sketch of the EQCM set-up (b).<sup>4</sup>

## Bibliography

1. Wiemers-Meyer, S., Winter, M. & Nowak, S. Mechanistic insights into lithium ion battery electrolyte degradation – a quantitative NMR study. *Phys. Chem. Chem. Phys.* **18**, 26595–26601 (2016).
2. Boissiere, C. *et al.* Porosity and Mechanical Properties of Mesoporous Thin Films Assessed by Environmental Ellipsometric Porosimetry. *Langmuir* **21**, 12362–12371 (2005).
3. Ardo, S. & Meyer, G. J. Photodriven heterogeneous charge transfer with transition-metal compounds anchored to TiO<sub>2</sub> semiconductor surfaces. *Chem Soc Rev* **38**, 115–164 (2009).
4. Vives, A. A. *Piezoelectric Transducers and Applications*. (Springer Science & Business Media, 2008).